

Special Issue Reprint

Numerical Simulation and Computational Methods in Engineering and Sciences

Edited by
Zhuojia Fu, Yiqian He and Hui Zheng

mdpi.com/journal/mathematics

Numerical Simulation and Computational Methods in Engineering and Sciences

Numerical Simulation and Computational Methods in Engineering and Sciences

Editors

Zhuojia Fu

Yiqian He

Hui Zheng



Basel • Beijing • Wuhan • Barcelona • Belgrade • Novi Sad • Cluj • Manchester

Editors

Zhuojia Fu
College of Mechanics and
Engineering Science,
Hohai University
Nanjing
China

Yiqian He
Dalian University of
Technology
Dalian
China

Hui Zheng
Nanchang University
Nanchang
China

Editorial Office

MDPI
St. Alban-Anlage 66
4052 Basel, Switzerland

This is a reprint of articles from the Special Issue published online in the open access journal *Mathematics* (ISSN 2227-7390) (available at: https://www.mdpi.com/si/mathematics/Numerical_Simulation_Comput_Method_Engin_Sci).

For citation purposes, cite each article independently as indicated on the article page online and as indicated below:

Lastname, A.A.; Lastname, B.B. Article Title. <i>Journal Name</i> Year , Volume Number, Page Range.
--

ISBN 978-3-7258-0955-4 (Hbk)

ISBN 978-3-7258-0956-1 (PDF)

doi.org/10.3390/books978-3-7258-0956-1

© 2024 by the authors. Articles in this book are Open Access and distributed under the Creative Commons Attribution (CC BY) license. The book as a whole is distributed by MDPI under the terms and conditions of the Creative Commons Attribution-NonCommercial-NoDerivs (CC BY-NC-ND) license.

Contents

About the Editors	ix
Jia-Wei Mao and Dong-Liang Hu Vibrational Resonance and Electrical Activity Behavior of a Fractional-Order FitzHugh–Nagumo Neuron System Reprinted from: <i>Mathematics</i> 2022 , <i>10</i> , 87, doi:10.3390/math10010087	1
Qiang Wang, Pyeoungkee Kim and Wenzhen Qu A Hybrid Localized Meshless Method for the Solution of Transient Groundwater Flow in Two Dimensions Reprinted from: <i>Mathematics</i> 2022 , <i>10</i> , 515, doi:10.3390/math10030515	11
Lin Chen, Wenzhi Xu and Zhuojia Fu A Novel Spatial–Temporal Radial Trefftz Collocation Method for 3D Transient Wave Propagation Analysis with Specified Sound Source Excitation Reprinted from: <i>Mathematics</i> 2022 , <i>10</i> , 897, doi:10.3390/math10060897	25
Yang Wu, Junli Zhang, Shuang Ding and Yan-Cheng Liu Localized Boundary Knot Method for Solving Two-Dimensional Inverse Cauchy Problems Reprinted from: <i>Mathematics</i> 2022 , <i>10</i> , 1324, doi:10.3390/math10081324	40
Maoxiong Liao, Tao Zhang and Jinggu Cao “Mixed” Meshless Time-Domain Adaptive Algorithm for Solving Elasto-Dynamics Equations Reprinted from: <i>Mathematics</i> 2022 , <i>10</i> , 1722, doi:10.3390/math10101722	57
Jing Wan, Jiehui Huang, Zhiyuan Liao, Chunquan Li and Peter X. Liu A Multi-View Ensemble Width-Depth Neural Network for Short-Term Wind Power Forecasting Reprinted from: <i>Mathematics</i> 2022 , <i>10</i> , 1824, doi:10.3390/math10111824	81
Yuqi Shang, Dezhong Kong, Shijiang Pu, Yu Xiong, Qiang Li and Zhanbo Cheng Study on Failure Characteristics and Control Technology of Roadway Surrounding Rock under Repeated Mining in Close-Distance Coal Seam Reprinted from: <i>Mathematics</i> 2022 , <i>10</i> , 2166, doi:10.3390/math10132166	101
Qi Jiang, Yuxin Cheng, Haozhe Le, Chunquan Li and Peter X. Liu A Stacking Learning Model Based on Multiple Similar Days for Short-Term Load Forecasting Reprinted from: <i>Mathematics</i> 2022 , <i>10</i> , 2446, doi:10.3390/math10142446	119
Yuquan Zhang, Zhiqiang Liu, Chengyi Li, Xuemei Wang, Yuan Zheng, Zhi Zhang, et al. Fluid–Structure Interaction Modeling of Structural Loads and Fatigue Life Analysis of Tidal Stream Turbine Reprinted from: <i>Mathematics</i> 2022 , <i>10</i> , 3674, doi:10.3390/math10193674	139
Liyuan Lan, Suifu Cheng, Xiatao Sun, Weiwei Li, Chao Yang and Fajie Wang A Fast Singular Boundary Method for the Acoustic Design Sensitivity Analysis of Arbitrary Two- and Three-Dimensional Structures Reprinted from: <i>Mathematics</i> 2022 , <i>10</i> , 3817, doi:10.3390/math10203817	154
Dongdong Liu, Xing Wei, Chengbin Li, Chunguang Han, Xiayi Cheng and Linlin Sun Transient Dynamic Response Analysis of Two-Dimensional Saturated Soil with Singular Boundary Method Reprinted from: <i>Mathematics</i> 2022 , <i>10</i> , 4323, doi:10.3390/math10224323	167

Noman Iqbal, Jinwoong Choi, Changkyu Lee, Hafiz Muhammad Uzair Ayub, Jinho Kim, Minseo Kim, et al. Effects of Diffusion-Induced Nonlinear Local Volume Change on the Structural Stability of NMC Cathode Materials of Lithium-Ion Batteries Reprinted from: <i>Mathematics</i> 2022 , <i>10</i> , 4697, doi:10.3390/math10244697	186
Wei Zang, Yuan Zheng, Yuquan Zhang, Xiangfeng Lin, Yanwei Li and Emmanuel Fernandez-Rodriguez Numerical Investigation on a Diffuser-Augmented Horizontal Axis Tidal Stream Turbine with the Entropy Production Theory Reprinted from: <i>Mathematics</i> 2023 , <i>11</i> , 116, doi:10.3390/math11010116	203
Mumin Zhang, Yuzhi Wang, Haochen Zhang, Zhiyun Peng and Junjie Tang A Novel and Robust Wind Speed Prediction Method Based on Spatial Features of Wind Farm Cluster Reprinted from: <i>Mathematics</i> 2023 , <i>11</i> , 499, doi:10.3390/math11030499	221
Cong Liu, Shaosong Min, Yandong Pang and Yingbin Chai The Meshfree Radial Point Interpolation Method (RPIM) for Wave Propagation Dynamics in Non-Homogeneous Media Reprinted from: <i>Mathematics</i> 2023 , <i>11</i> , 523, doi:10.3390/math11030523	238
Yasir Ali, Noman Iqbal, Imran Shah and Seungjun Lee Mechanical Stability of the Heterogenous Bilayer Solid Electrolyte Interphase in the Electrodes of Lithium–Ion Batteries Reprinted from: <i>Mathematics</i> 2023 , <i>11</i> , 543, doi:10.3390/math11030543	265
German Solorzano and Vagelis Plevris DNN-MLVEM: A Data-Driven Macromodel for RC Shear Walls Based on Deep Neural Networks Reprinted from: <i>Mathematics</i> 2023 , <i>11</i> , 2347, doi:10.3390/math11102347	284
Fakrudeen Ali Ahamed J and Pandivelan Chinnaiyan Studies on Finite Element Analysis in Hydroforming of Nimonic 90 Sheet Reprinted from: <i>Mathematics</i> 2023 , <i>11</i> , 2437, doi:10.3390/math11112437	303
Hillary Muzara and Stanford Shateyi Magnetohydrodynamics Williamson Nanofluid Flow over an Exponentially Stretching Surface with a Chemical Reaction and Thermal Radiation Reprinted from: <i>Mathematics</i> 2023 , <i>11</i> , 2740, doi:10.3390/math11122740	318
Jialin Liu, Chen Gong, Suhua Chen and Nanrun Zhou Multi-Step-Ahead Wind Speed Forecast Method Based on Outlier Correction, Optimized Decomposition, and DLinear Model Reprinted from: <i>Mathematics</i> 2023 , <i>11</i> , 2746, doi:10.3390/math11122746	336
Seitkerim Bimurzaev, Seil Sautbekov and Zerde Sautbekova Calculation of the Electrostatic Field of a Circular Cylinder with a Slot by the Wiener–Hopf Method Reprinted from: <i>Mathematics</i> 2023 , <i>11</i> , 2933, doi:10.3390/math11132933	362
Maria Fernandes, Luisa C. Sousa, Carlos A. Conceição António and Sónia I. S. Pinto Modeling the Five-Element Windkessel Model with Simultaneous Utilization of Blood Viscoelastic Properties for FFR Achievement: A Proof-of-Concept Study Reprinted from: <i>Mathematics</i> 2023 , <i>11</i> , 4877, doi:10.3390/math11244877	373

Igor Reznichenko, Primož Podržaj and Aljoša Peperko Calculation of Stationary Magnetic Fields Based on the Improved Quadrature Formulas for a Simple Layer Potential Reprinted from: <i>Mathematics</i> 2024 , <i>12</i> , 21, doi:10.3390/math12010021	392
Rabea Jamil Mahfoud, Nizar Faisal Alkayem, Emmanuel Fernandez-Rodriguez, Yuan Zheng, Yonghui Sun, Shida Zhang and Yuquan Zhang Evolutionary Approach for DISCO Profit Maximization by Optimal Planning of Distributed Generators and Energy Storage Systems in Active Distribution Networks Reprinted from: <i>Mathematics</i> 2024 , <i>12</i> , 300, doi:10.3390/math12020300	409
Mohammed Nabil, Fengqi Guo, Lizhong Jiang, Zhiwu Yu and Qiuliang Long Numerical Investigation of Wind Flow and Speedup Effect at a Towering Peak Extending out of a Steep Mountainside: Implications for Landscape Platforms Reprinted from: <i>Mathematics</i> 2024 , <i>12</i> , 467, doi:10.3390/math12030467	442

About the Editors

Zhuojia Fu

Zhuojia Fu is a professor at the College of Mechanics and Engineering Science, Hohai University. His research interests include semi-analytical and numerical methods in computational mechanics, numerical modeling of wave propagation, and structural vibration.

Yiqian He

Yiqian He is a professor at the State Key Lab of Structural Analysis for Industrial Equipment, Department of Engineering Mechanics, International Research Centre for Computational Mechanics, Dalian University of Technology. His research interests include computational mechanics, biomechanics for soft tissues, and inverse problems.

Hui Zheng

Hui Zheng is a Professor at the Institute of Aerospace, School of Infrastructure Engineering, Nanchang University. His research interests include computational solid mechanics, biomechanics, and phononic crystals.

Article

Vibrational Resonance and Electrical Activity Behavior of a Fractional-Order FitzHugh–Nagumo Neuron System

Jia-Wei Mao and Dong-Liang Hu *

College of Mechanics and Materials, Hohai University, Nanjing 211100, China; 191308040019@hhu.edu.cn

* Correspondence: dlhu@hhu.edu.cn

Abstract: Making use of the numerical simulation method, the phenomenon of vibrational resonance and electrical activity behavior of a fractional-order FitzHugh–Nagumo neuron system excited by two-frequency periodic signals are investigated. Based on the definition and properties of the Caputo fractional derivative, the fractional L1 algorithm is applied to numerically simulate the phenomenon of vibrational resonance in the neuron system. Compared with the integer-order neuron model, the fractional-order neuron model can relax the requirement for the amplitude of the high-frequency signal and induce the phenomenon of vibrational resonance by selecting the appropriate fractional exponent. By introducing the time-delay feedback, it can be found that the vibrational resonance will occur with periods in the fractional-order neuron system, i.e., the amplitude of the low-frequency response periodically changes with the time-delay feedback. The weak low-frequency signal in the system can be significantly enhanced by selecting the appropriate time-delay parameter and the fractional exponent. In addition, the original integer-order model is extended to the fractional-order model, and the neuron system will exhibit rich dynamical behaviors, which provide a broader understanding of the neuron system.

Keywords: fractional-order system; time-delay feedback; vibrational resonance; FitzHugh–Nagumo neuron; numerical simulation

Citation: Mao, J.-W.; Hu, D.-L.

Vibrational Resonance and Electrical Activity Behavior of a

Fractional-Order FitzHugh–Nagumo Neuron System. *Mathematics* **2022**, *10*, 87. <https://doi.org/10.3390/math10010087>

Academic Editors: Yiqian He, Zhuojia Fu and Hui Zheng

Received: 13 December 2021

Accepted: 23 December 2021

Published: 27 December 2021

Publisher’s Note: MDPI stays neutral with regard to jurisdictional claims in published maps and institutional affiliations.



Copyright: © 2021 by the authors. Licensee MDPI, Basel, Switzerland. This article is an open access article distributed under the terms and conditions of the Creative Commons Attribution (CC BY) license (<https://creativecommons.org/licenses/by/4.0/>).

1. Introduction

Vibrational resonance (VR) has attracted considerable attention in the field of nonlinear sciences in the last twenty years. Based on the study of stochastic resonance (SR) [1], VR is firstly proposed by Landa and McClintock [2]. When replacing the noise in SR with an appropriate high-frequency signal, the weak low-frequency signal can be greatly amplified, which is similar to the typical “Inverted Bell” resonance phenomenon in SR, and is named as VR. Compared with the noise in SR, the high-frequency signal in VR is more controllable. Biharmonic signals are common in various fields, such as acoustics [3], optics [4], engineering [5], neuroscience [6], etc. Recently, the research hotspots of VR have changed from classic bistable systems [7–9] to fractional-order systems [10], delay systems [11], and network dynamical systems [12].

Due to the complex definition and lack of corresponding application background, the research on fractional calculus has been limited to the field of mathematics for a long time. However, compared with integer calculus, the power-law characteristic of complex social and physical phenomena can be accurately approximated through fractional calculus. Hence, this theory is gradually used in viscoelastic materials [13], electrification process [14], control theory [15], and neuron models [16], etc. To the best of our knowledge, the research on VR for fractional-order systems is quite few, and most of which are limited to bistable and multi-stable systems [17–19]. However, it is found that fractional calculus has its own unique advantages in describing certain neuronal characteristics. For example, fractional-order differentiation can be used to account for the firing rate of neocortical pyramidal neurons when stimulated by sinusoidal current [20]. Anastasio et al. [21] thought that the

net output of the motor neurons in the visual system is consistent with fractional-order differentiation relative to eye position. Therefore, it is of great significance to study VR in the fractional-order neuron system.

In this study, we consider the FitzHugh–Nagumo (FHN) neuron model. As one of the simplest mathematical models for disclosing the dynamical behavior of neurons, the FHN model is widely used in integer-order systems for studying VR [22,23]. In brain activities [24], the neurons may exhibit two quite different time scales, and then, it is reasonable to reveal the mechanism of weak signal detection of neuron by VR. Since time delay is inherent in the neuron system, great progress has been made in the research on the effect of time delay on VR. Adding the time-delay feedback to the recovery variable of the FHN neuron model, the phenomenon of multiple VR can be induced in the neuron [25]. It is found that the bifurcation point and equilibrium point change periodically with the increase of time delay in a fractional order quantic oscillator system, and the output can be enhanced by selecting appropriate time delay [26].

Inspired by the above-mentioned ideas, the effects of fractional order and time delay on VR and dynamical behavior are studied in the fractional-order FHN neuron model. The VR can be induced in the fractional-order neuron model without strict requirement for the amplitude of high-frequency signal. It can be found that multiple VR occurs in the neuron with the increase of delay. Compared with integer-order model, the fractional-order FHN neuron exhibits rich electrical activities. The remainder of this paper is organized as follows: In Section 2, the fractional-order FHN neuron model excited by two periodic signals is briefly introduced. In Section 3, the VR in the fractional-order FHN model without and with time delay is studied. In Section 4, the effects of fractional exponent and time delay on the dynamical behavior in the fractional-order FHN model are discussed. Several conclusions are given in Section 5.

2. Fractional-Order FitzHugh–Nagumo Neuron Model

There are three common definitions of fractional calculus, namely Riemann–Liouville (R-L) definition, Grünwald–Letnikov (G-L) definition, and the Caputo definition. With the property of supersingularity, R-L definition is mainly used for the analysis of mathematical theory and is not convenient for engineering and physical modeling. G-L definition can be regarded as the extension of the limit form of integral calculus difference definition, which is widely applied to early numerical calculation. As its initial condition is the form of integer calculus, and it has clear physical meaning, the Caputo definition is used in this paper.

The fractional derivative of univariate function $f(t)$ is defined as

$$\frac{d^\alpha f(t)}{dt^\alpha} = {}_{t_0}D_t^\alpha f(t) = \frac{1}{\Gamma(n - \alpha)} \int_{t_0}^t \frac{f^{(n)}(\tau) d\tau}{(t - \tau)^{\alpha - n + 1}}, \quad (n - 1 < \alpha < n), \quad (1)$$

where $\Gamma(n - \alpha)$ is the gamma function, t_0 and t are the lower limit and upper limit of the definite integral, n is the minimum positive integer greater than α , and $f^{(n)}(\tau)$ is the n th derivative of the function $f(\tau)$. Under the joint excitation of harmonic signals, the fractional-order FHN neuron model with time delay (the model comes from the model involved in Ref. [27]) is given by the following form:

$$\begin{aligned} \varepsilon \frac{d^\alpha x}{dt^\alpha} &= x(t) - \frac{x(t)^3}{3} - y(t), \\ \frac{d^\alpha y}{dt^\alpha} &= x(t) + a + f \cos(\omega t) + F \cos(\Omega t) + K(y(t - \tau) - y(t)), \end{aligned} \quad (2)$$

where $x(t)$ and $y(t)$ represent the fast-varying membrane potential and the slow-varying recovery variable of neuronal cells, respectively; $\alpha(0 < \alpha \leq 1)$ is the fractional exponent; K is the strength of time-delay feedback. $\tau \geq 0$ is the delay parameter, and Equation (2) degenerates into the fractional-order FHN neuron model without delay when $\tau = 0$. $\varepsilon = 0.05$ is the time scale ratio, which is chosen to ensure that the membrane potential

$x(t)$ evolves faster than the recovery variable $y(t)$. $f \cos(\omega t)$ and $F \cos(\Omega t)$ represent the low-frequency signal and the high-frequency signal, respectively, which satisfy $f \ll 1$, $\omega \ll \Omega$. The value of a determines the behavior of the system under the conditions that $f = F = \tau = 0$ and $\alpha = 1$. If $|a| > 1.0$, the system is excitable and has only a stable fixed point; if $|a| < 1.0$, a limit cycle in the system arises. Here, the parameter $a = 1.05$ is chosen to make the system in the excitable state [28]. The variables in the model are dimensionless.

We consider the fractional derivative of $x(t)$ defined with the Caputo fractional derivative,

$$\frac{d^\alpha x(t)}{dt^\alpha} = f(x, t). \tag{3}$$

The discrete format of fractional-order L1 algorithm is [29]:

$$\frac{d^\alpha x(t)}{dt^\alpha} \approx \frac{(dt)^{-\alpha}}{\Gamma(2-\alpha)} \left[\sum_{k=0}^{N-1} [x(t_{k+1}) - x(t_k)] \left[(N-k)^{1-\alpha} - (N-1-k)^{1-\alpha} \right] \right], \tag{4}$$

where $t_k = k\Delta t$. Combining the right sides of Equations (3) and (4) and solving for x at time t_N , it can be concluded that the discrete format of Equation (3) is

$$x(t_N) \approx (dt)^\alpha \Gamma(2-\alpha) f(x, t) + x(t_{N-1}) - \left[\sum_{k=0}^{N-2} [x(t_{k+1}) - x(t_k)] \left[(N-k)^{1-\alpha} - (N-1-k)^{1-\alpha} \right] \right]. \tag{5}$$

where the Markov term weighted by the gamma function is given by

$$(dt)^\alpha \Gamma(2-\alpha) f(x, t) + x(t_{N-1}) \tag{6}$$

and the memory trace is given by

$$\sum_{k=0}^{N-2} [x(t_{k+1}) - x(t_k)] \left[(N-k)^{1-\alpha} - (N-1-k)^{1-\alpha} \right] \tag{7}$$

The memory trace integrates information of all the previous activities and has a memory effect, which is the typical property of fractional-order system. When $\alpha = 1$, the memory trace has no effect, and Equation (5) degenerates into classical Euler algorithm.

According to Equation (5), the discrete format of Equation (2) can be obtained as follows:

$$\begin{aligned} x(t_N) &\approx \frac{1}{2} (dt)^\alpha \Gamma(2-\alpha) \left(x(t_{N-1}) - \frac{(x(t_{N-1}))^3}{3} - y(t_{N-1}) \right) + x(t_{N-1}) \\ &\quad - \left[\sum_{k=0}^{N-2} [x(t_{k+1}) - x(t_k)] \left[(N-k)^{1-\alpha} - (N-1-k)^{1-\alpha} \right] \right], \\ y(t_N) &\approx (dt)^\alpha \Gamma(2-\alpha) \left(x(t_{N-1}) + a + f \cos(\omega t_{N-1}) + F \cos(\Omega t_{N-1}) + K(y(t_{N-m}) - y(t_{N-1})) \right) + y(t_{N-1}) \\ &\quad - \left[\sum_{k=0}^{N-2} [y(t_{k+1}) - y(t_k)] \left[(N-k)^{1-\alpha} - (N-1-k)^{1-\alpha} \right] \right], \end{aligned} \tag{8}$$

where m is the number of discrete points caused by time delay.

3. Vibrational Resonance in the Fractional-Order FHN Neuron Model

3.1. VR in the Fractional-Order FHN Neuron Model without Time Delay

The response amplitude Q at the low-frequency signal is usually used as the index to measure the VR, which is defined by:

$$Q = \sqrt{Q_s^2 + Q_c^2}, \tag{9}$$

with

$$\begin{aligned}
 Q_s &= \frac{2}{nT} \int_0^{nT} x(t) \sin(\omega t) dt, \\
 Q_c &= \frac{2}{nT} \int_0^{nT} x(t) \cos(\omega t) dt,
 \end{aligned}
 \tag{10}$$

where $T = 2\pi/\omega$ and n is a positive integer. For the numerical simulation, the parameters are selected as $\varepsilon = 0.05$, $K = 0.2$, $f = 0.01$, $n = 50$.

Under fixed parameters $\omega = 0.5$, $\Omega = 5$, the curves of VR in the fractional-order FHN neuron without time delay are plotted in Figure 1a. It can be seen that different fractional exponents correspond to different phenomena of the VR. In Figure 1b, with the decrease of α , the region of the VR in the neuron changes, and the amplitude of low-frequency Q corresponding to the optimal F gradually decreases. Compared with the integer-order FHN neuron model, it is found that the low-frequency signal can also be amplified without strict requirement for the amplitude of high-frequency F in the fractional-order neuron. For example, in Figure 1b, the integer-order FHN neuron model fails to reach the state of the VR for $F = 0.15$, while for $\alpha = 0.96$, the VR occurs for the same value of F . Hence, it is shown that the VR in the FHN neuron can be induced by adjusting appropriate fractional exponent and the high-frequency force.

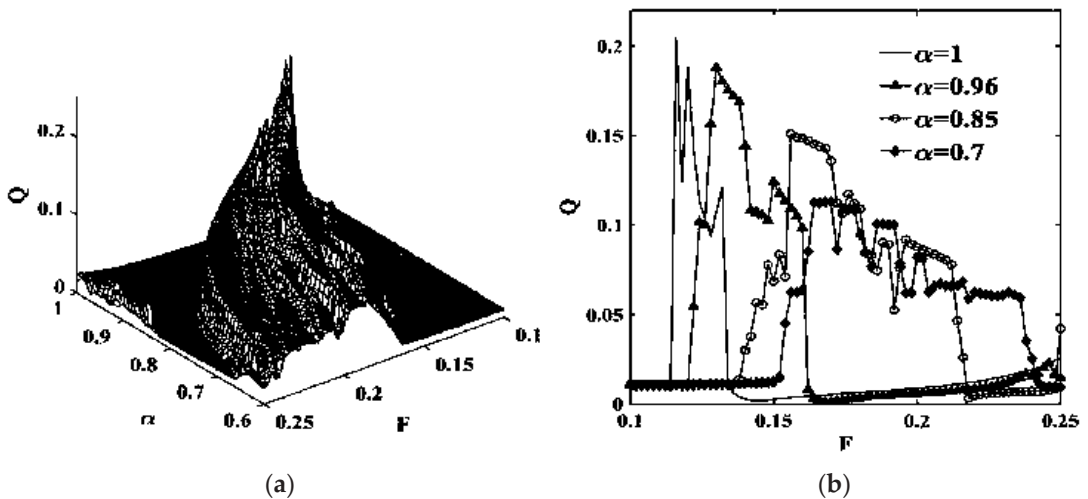


Figure 1. Response amplitude Q as a function of α and F . (a) The three-dimensional surface of response amplitude Q versus α and F ; (b) response amplitude Q versus F for different values of α .

In order to further discuss the effect of α on the VR, the response amplitude Q_{\max} versus α for $F \in [0.1, 0.25]$ is depicted in Figure 2a. For a certain range of F , although the response amplitude Q_{\max} is not a strictly monotonic increasing function of α , in general, with the increase of α , the response amplitude Q can be optimized under the appropriate high-frequency force. However, when the value of F is fixed, the function of Q versus α shows different monotonic characteristics, as shown in Figure 2b. For $F = 0.11$, the curve of response amplitude is approximately a straight line, which indicates that VR does not occur with the change of α , while for $F = 0.15$ or $F = 0.2$, the response amplitude Q is a nonlinear function of α , and the low-frequency signal can be significantly enhanced by selecting an appropriate fractional-order α compared with the integer-order system.

3.2. Multiple VR in Fractional-Order FHN Neuron Model with Delay

For the fractional-order FitzHugh–Nagumo neuron with time delay, the numerical result of functional curves of the response amplitude Q versus τ can be obtained by combining Equation (8) with Equation (9). The response amplitude Q versus time delay τ in the fractional-order FHN neuron excited by two frequency signals is given in Figure 3. Figure 3e,f are partial, enlarged views of Figure 3a,d, respectively. From Figure 3a–d, it is seen that multiple resonance occurs in the neuron with the increase of the time-delay parameter. Therefore, the response amplitude Q can reach the maximum by selecting appropriate time-delay parameters, and the response amplitude Q can be greatly amplified compared with the neuron without time delay. Another notable phenomenon is that the response amplitude Q is periodic with the change of τ . From Figure 3a–d, it is clear that that the period of response amplitude Q is $2\pi/\omega$, while Figure 3e,f shows that the response amplitude Q varies with another period of $2\pi/\Omega$. Therefore, the response amplitude Q in the fractional-order FHN neuron with time-delay feedback presents two different periods, namely fast period $2\pi/\Omega$ and slow period $2\pi/\omega$, which exactly correspond to the period of high-frequency signal and low-frequency signal. Utilizing the periodicity of response amplitude Q and selecting appropriate time-delay parameters are helpful to realizing the effective control of the fractional-order FHN neuron. The only regret is that the parameters involved in the system are difficult to be optimized quickly to satisfy the requirement of resonance, which is consistent with the conclusion in Ref. [30].

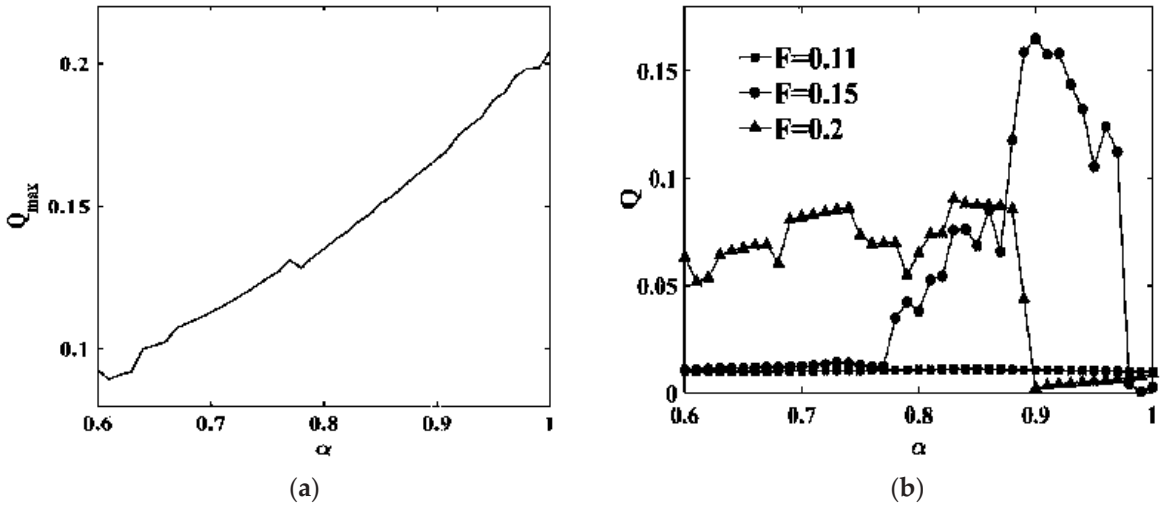


Figure 2. Relationship curve between response amplitude Q and fractional-order α . (a) Response amplitude Q_{\max} versus α ; (b) response amplitude Q versus α for three different values of F .

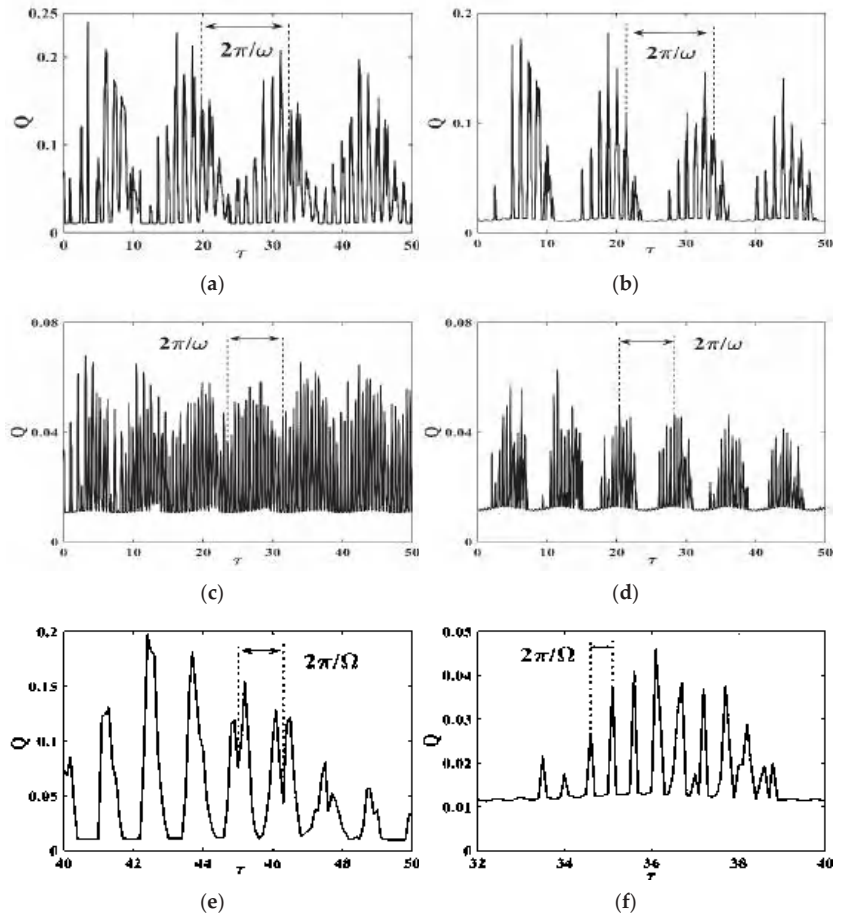


Figure 3. Relationship curve between response amplitude Q and τ : (a) $\omega = 0.5$, $\Omega = 5$, $\alpha = 0.96$, $F = 0.123$; (b) $\omega = 0.5$, $\Omega = 5$, $\alpha = 0.85$, $F = 0.138$; (c) $\omega = \pi/4$, $\Omega = 12$, $\alpha = 0.7$, $F = 0.395$; (d) $\omega = \pi/4$, $\Omega = 12$, $\alpha = 0.6$, $F = 0.298$; (e) $\omega = 0.5$, $\Omega = 5$, $\alpha = 0.96$, $F = 0.123$; (f) $\omega = \pi/4$, $\Omega = 12$, $\alpha = 0.6$, $F = 0.298$.

4. Dynamical Behavior of Fractional-Order FHN Neuron Model

4.1. Effect of the Fractional-Order

In this subsection, the dynamical behavior of the fractional-order FHN neuron without time-delay feedback is studied. Figure 4 shows the bifurcation diagram of interspike interval (ISI) of the neuron versus the fractional-order α , where $\alpha \in [0.6, 1]$. From Figure 4, when α is small, it can be seen that the fractional-order FHN neuron does not fire, and when the α is relatively large, various periodic and irregular firing patterns appear in the neuron. It can be found that the fractional-order FHN neuron displays complex dynamics by adjusting a single parameter α , which is also observed in other neurons [31,32].

In order to intuitively depict the effect of the fractional-order α on the dynamical behavior of the FHN neuron, the evolution of the membrane potential $x(t)$ is given in Figure 5. From Figure 5a, when $\alpha = 0.6$, the neuron is in the quiescent state. As can be seen from Figure 5b,c, when $\alpha = 0.792$ and $\alpha = 0.84$, the firing pattern of the neuron is period 1 bursting. Obviously, their interspike intervals are different, which are four times and two times $2\pi/\omega$, respectively. In Figure 5a, when $\alpha = 0.934$, the discharge rhythm of the FHN neuron alternates between period 1 and period 2. From Figure 5a–d, it is found that the

fractional-order FHN neuron is more active with the increase of α , which is consistent with that revealed in Figure 4.

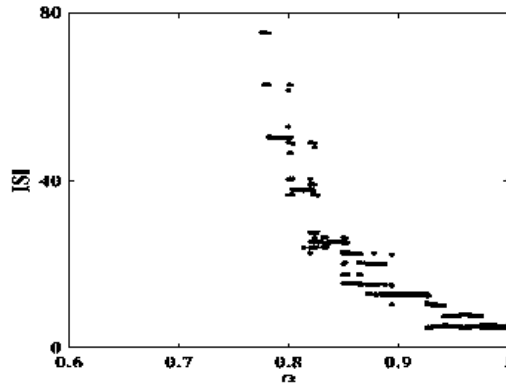


Figure 4. Bifurcation diagram of interspike interval (ISI) versus the fractional-order α ; other parameters are $\omega = 0.5$, $\Omega = 5$, $F = 0.15$.

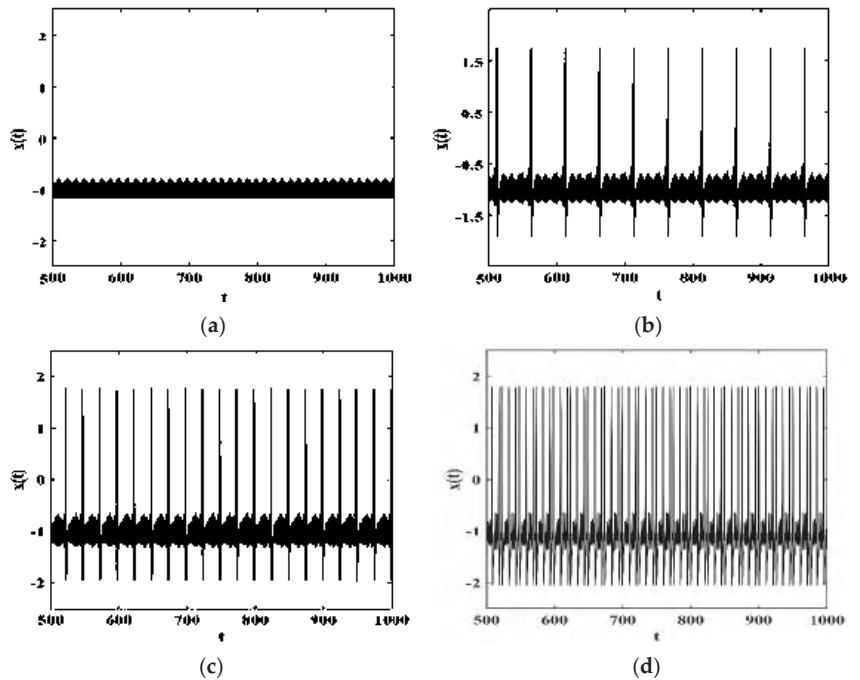


Figure 5. Time evolution of the membrane potential $x(t)$ for different values of α ; other parameters are $\omega = 0.5$, $\Omega = 5$, $F = 0.15$; (a) $\alpha = 0.6$; (b) $\alpha = 0.792$; (c) $\alpha = 0.84$; (d) $\alpha = 0.934$.

4.2. Effect of the Time Delay

In order to study the effect of time-delay feedback on the dynamical behavior of the fractional-order FHN neuron, $\alpha = 0.84$ in Figure 5c is selected. Figure 6 depicts the bifurcation diagram of interspike interval (ISI) of the neuron versus the time-delay parameter τ , from which it can be seen that the fractional-order FHN neuron with time-delay feedback exhibits rich dynamical behaviors. The time series of the membrane potential $x(t)$ for different values of τ are given in Figure 7. When $\tau = 0$, the neuron fires with period

1, which corresponds to the case of the neuron without time delay in Figure 5c. When $\tau = 5.6$, it is seen that the firing pattern of the neuron is period 2 bursting. It can be seen from Figure 7c that a new firing pattern appears in the neuron, which regularly alters between period 2 and period 1. The multiple spiking of the firing pattern also appears in the neuron, as shown in Figure 7d. Thus, bursting patterns and interspike intervals of the fractional-order FHN neuron can be controlled by adjusting α or τ .

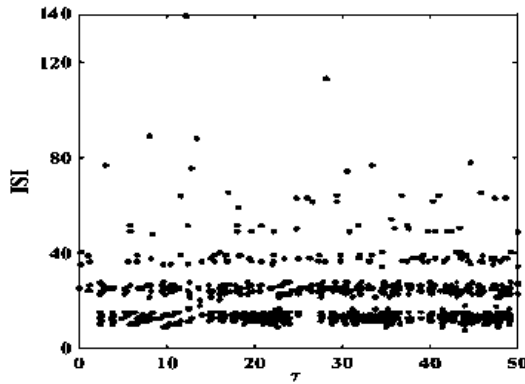


Figure 6. Bifurcation diagram of interspike interval (ISI) versus the time-delay τ ; other parameters are $\alpha = 0.84$, $\omega = 0.5$, $\Omega = 5$, $F = 0.15$.

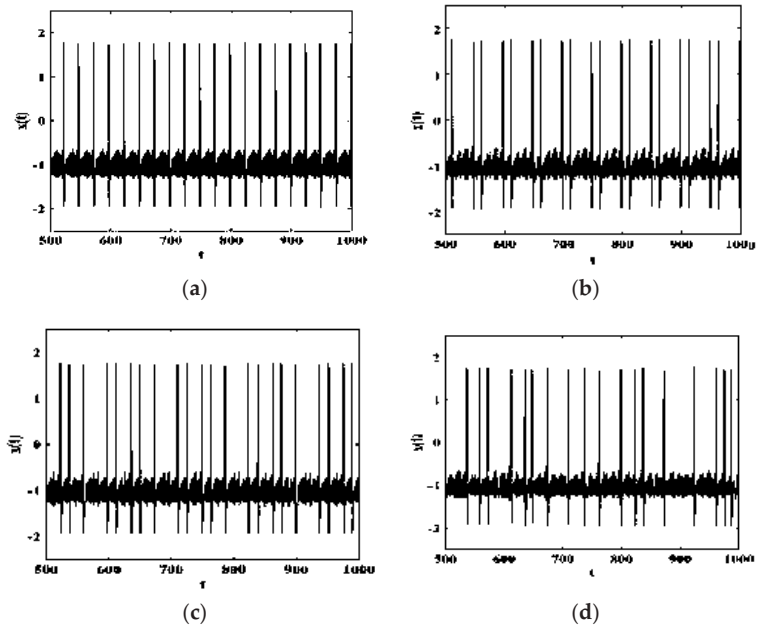


Figure 7. Time evolution of the membrane potential $x(t)$ for different values of τ ; other parameters are $\alpha = 0.84$, $\omega = 0.5$, $\Omega = 5$, $F = 0.15$; (a) $\tau = 0$; (b) $\tau = 5.6$; (c) $\tau = 25$; (d) $\tau = 31.8$.

5. Conclusions

The vibrational resonance and electrical activity behaviors in the fractional-order FHN neuron are studied in this paper. When the original integer-order model is extended to the fractional-order model, the region of the VR will be wider, so the requirement for the amplitude of high-frequency signal can be relaxed, and then, the VR phenomenon can be

induced by choosing the appropriate fractional-order α . Introducing time-delay feedback, it is found that the phenomenon of vibrational resonance appears with two different periods in the fractional FHN neuron, which are exactly equal to the periods of two frequency signals. The fractional-order FHN neuron exhibits rich electrical activities, and its bursting patterns and interspike interval can be controlled by adjusting α or τ .

Author Contributions: Conceptualization, J.-W.M. and D.-L.H.; methodology, J.-W.M. and D.-L.H.; validation, J.-W.M. and D.-L.H.; formal analysis, J.-W.M.; investigation, J.-W.M.; resources, D.-L.H.; data curation, J.-W.M.; writing—original draft preparation, J.-W.M.; writing—review and editing, D.-L.H.; visualization, D.-L.H.; supervision, D.-L.H.; project administration, D.-L.H.; funding acquisition, D.-L.H. All authors have read and agreed to the published version of the manuscript.

Funding: This work in the present paper was supported by the National Natural Science Foundation of China (Grant No. 11502067), and Natural Science Foundation of Jiangsu Province of China (Grant No. BK20191295).

Institutional Review Board Statement: Not applicable.

Informed Consent Statement: Not applicable.

Data Availability Statement: Not applicable.

Conflicts of Interest: The authors declare no conflict of interest. The funders had no role in the design of the study; in the collection, analyses, or interpretation of data; in the writing of the manuscript, or in the decision to publish the results.

References

1. Landa, P.S.; McClintock, P. Vibrational resonance. *J. Phys. A* **2000**, *33*, L433–L438. [CrossRef]
2. Mcnamara, B.; Wiesenfeld, K. Theory of stochastic resonance. *Phys. Rev. A* **1989**, *39*, 4854–4869. [CrossRef] [PubMed]
3. Maksimov, A.O. On the subharmonic emission of gas bubbles under two-frequency excitation. *Ultrasonics* **1997**, *35*, 79–86. [CrossRef]
4. Volkov, E.I.; Ullner, E.; Zaikin, A.A.; Kurths, J. Oscillatory amplification of stochastic resonance in excitable systems. *Phys. Rev. E* **2003**, *68*, 026214. [CrossRef] [PubMed]
5. Gherm, V.E.; Zernov, N.N.; Lundborg, B.; Västberg, A. The two-frequency coherence function for the fluctuating ionosphere: Narrowband pulse propagation. *J. Atmos. Sol.-Terr. Phys.* **1997**, *59*, 1831–1841. [CrossRef]
6. Victor, J.D.; Conte, M.M. Two-frequency analysis of interactions elicited by Vernier stimuli. *Vis. Neurosci.* **2000**, *17*, 959–973. [CrossRef]
7. Yao, C.; Liu, Y.; Zhan, M. Frequency-resonance-enhanced vibrational resonance in bistable systems. *Phys. Rev. E* **2011**, *83*, 061122. [CrossRef]
8. Abusoua, A.; Daqaq, M.F. Experimental evidence of vibrational resonance in a mechanical bistable twin-well oscillator. *J. Comput. Nonlinear Dyn.* **2018**, *3*, 061002. [CrossRef]
9. Chizhevsky, V.N. Vibrational higher-order resonances in an overdamped bistable system with biharmonic excitation. *Phys. Rev. E* **2014**, *90*, 042924. [CrossRef]
10. Yang, J.; Sanjuan, M.; Liu, H. Bifurcation and resonance in a fractional Mathieu-Duffing oscillator. *Eur. Phys. J. B* **2015**, *88*, 310. [CrossRef]
11. Yang, Z.; Ning, L. Vibrational resonance in a harmonically trapped potential system with time delay. *Pramana* **2019**, *92*, 1–12. [CrossRef]
12. Uzuntarla, M.; Yilmaz, E.; Wagemakers, A.; Ozer, M. Vibrational resonance in a heterogeneous scale free network of neurons. *Commun. Nonlinear Sci. Numer. Simul.* **2015**, *22*, 367–374. [CrossRef]
13. Meral, F.C.; Royston, T.J.; Magin, R. Fractional calculus in viscoelasticity: An experimental study. *Commun. Nonlinear Sci. Numer. Simul.* **2010**, *15*, 939–945. [CrossRef]
14. Matouk, A.E. Chaos, feedback control and synchronization of a fractional-order modified Autonomous Van der Pol–Duffing circuit. *Commun. Nonlinear Sci. Numer. Simul.* **2011**, *16*, 975–986. [CrossRef]
15. Chaudhary, N.I.; Raja, M.; Khan, A.R. Design of modified fractional adaptive strategies for Hammerstein nonlinear control autoregressive systems. *Nonlinear Dyn.* **2015**, *82*, 1811–1830. [CrossRef]
16. Khanday, F.A.; Kant, N.A.; Dar, M.R.; Zulkifli, T.Z.A.; Psychalinos, C. Low-Voltage low-power integrable CMOS circuit implementation of integer and fractional-order FitzHugh-Nagumo Neuron model. *IEEE Trans. Neural Netw. Learn. Syst.* **2019**, *30*, 2108–2122. [CrossRef]
17. Yang, J.H.; Zhu, H. Vibrational resonance in Duffing systems with fractional-order damping. *Chaos* **2012**, *22*, 013112. [CrossRef]
18. Mbong, T.L.M.D.; Siewe, M.S.; Tchawoua, C. The effect of the fractional derivative order on vibrational resonance in a special fractional quintic oscillator. *Mech. Res. Commun.* **2016**, *78*, 13–19. [CrossRef]

19. Qin, T.; Xie, T.; Luo, M.; Deng, K. Vibrational resonance in fractional-order overdamped multistable systems. *Chin. J. Phys.* **2017**, *55*, 546–555. [CrossRef]
20. Lundstrom, B.N.; Higgs, M.H.; Spain, W.J.; Fairhall, A.L. Fractional differentiation by neocortical pyramidal neurons. *Nat. Neurosci.* **2008**, *11*, 1335–1342. [CrossRef]
21. Anastasio, T.J. The fractional-order dynamics of brainstem vestibulo-oculomotor neurons. *Biol. Cybern.* **1994**, *72*, 69–79. [CrossRef]
22. Ullner, E.; Zaikin, A.; García-Ojalvo, J.; Bascones, R.; Kurths, J. Vibrational resonance and vibrational propagation in excitable systems. *Phys. Lett. A* **2003**, *312*, 348–354. [CrossRef]
23. Deng, B.; Wang, J.; Wei, X.; Tsang, K.M.; Chan, W.L. Vibrational resonance in neuron populations. *Chaos* **2010**, *20*, 013113. [CrossRef]
24. Izhikevich, E.M. Simple model of spiking neurons. *IEEE Trans. Neural Netw.* **2003**, *14*, 1569–1572. [CrossRef] [PubMed]
25. Hu, D.L.; Yang, J.H.; Liu, X.B. Delay-induced vibrational multiresonance in FitzHugh–Nagumo system. *Commun. Nonlinear Sci. Numer. Simul.* **2012**, *17*, 1031–1035. [CrossRef]
26. Guo, W.; Ning, L. Vibrational resonance in a fractional order quintic oscillator system with time delay feedback. *Int. J. Bifurc. Chaos* **2020**, *30*, 2050025. [CrossRef]
27. Abdelouahab, M.S.; Lozi, R.P.; Chen, G. Complex Canard Explosion in a Fractional-Order FitzHugh–Nagumo Model. *Int. J. Bifurc. Chaos* **2019**, *29*, 1950111. [CrossRef]
28. Wu, D.; Zhu, S. Stochastic resonance in FitzHugh–Nagumo system with time-delayed feedback. *Phys. Lett. A* **2008**, *372*, 5299–5304. [CrossRef]
29. Teka, W.; Marinov, T.M.; Santamaria, F. Neuronal spike timing adaptation described with a fractional leaky integrate-and-fire model. *PLoS Comput. Biol.* **2014**, *10*, e1003526. [CrossRef] [PubMed]
30. Wu, C.; Yang, J.; Huang, D.; Liu, H.; Hu, E. Weak signal enhancement by the fractional-order system resonance and its application in bearing fault diagnosis. *Meas. Sci. Technol.* **2019**, *30*, 035004. [CrossRef]
31. Teka, W.W.; Upadhyay, R.K.; Mondal, A. Spiking and bursting patterns of fractional-order Izhikevich model. *Commun. Nonlinear Sci. Numer. Simul.* **2018**, *56*, 161–176. [CrossRef]
32. Mondal, A.; Sharma, S.K.; Upadhyay, R.K.; Mondal, A. Firing activities of a fractional-order FitzHugh–Rinzel bursting neuron model and its coupled dynamics. *Sci. Rep.* **2019**, *9*, 15721. [CrossRef] [PubMed]

Article

A Hybrid Localized Meshless Method for the Solution of Transient Groundwater Flow in Two Dimensions

Qiang Wang ^{1,2}, Pyeoungkee Kim ^{1,*} and Wenzhen Qu ^{3,*}¹ Division of Computer Software Engineering, Silla University, Busan 612022, Korea; wangqiang@sdivc.edu.cn² Shandong Vocational College of Industry, Zibo 256414, China³ School of Mathematics and Statistics, Qingdao University, Qingdao 266071, China

* Correspondence: pkkim@silla.ac.kr (P.K.); quwz@qdu.edu.cn (W.Q.)

Abstract: In this work, a hybrid localized meshless method is developed for solving transient groundwater flow in two dimensions by combining the Crank–Nicolson scheme and the generalized finite difference method (GFDM). As the first step, the temporal discretization of the transient groundwater flow equation is based on the Crank–Nicolson scheme. A boundary value problem in space with the Dirichlet or mixed boundary condition is then formed at each time node, which is simulated by introducing the GFDM. The proposed algorithm is truly meshless and easy to program. Four linear or nonlinear numerical examples, including ones with complicated geometry domains, are provided to verify the performance of the developed approach, and the results illustrate the good accuracy and convergence of the method.

Keywords: groundwater flow; generalized finite difference method; Crank–Nicolson; transient

Citation: Wang, Q.; Kim, P.; Qu, W. A Hybrid Localized Meshless Method for the Solution of Transient Groundwater Flow in Two Dimensions. *Mathematics* **2022**, *10*, 515. <https://doi.org/10.3390/math10030515>

Academic Editors: Zhuojia Fu, Yiqian He and Hui Zheng

Received: 14 January 2022

Accepted: 3 February 2022

Published: 5 February 2022

Publisher's Note: MDPI stays neutral with regard to jurisdictional claims in published maps and institutional affiliations.



Copyright: © 2022 by the authors. Licensee MDPI, Basel, Switzerland. This article is an open access article distributed under the terms and conditions of the Creative Commons Attribution (CC BY) license (<https://creativecommons.org/licenses/by/4.0/>).

1. Introduction

As an important component of the hydrological cycle system, groundwater is a key source of domestic and industrial water supply. Therefore, the analysis of the groundwater flow has great significance for water supply security. Due to the complexity of the problem, an analytical solution is rarely available for most models of groundwater flow. With the development of computing techniques, more and more numerical approaches have been developed and applied to numerical simulations of science and engineering problems, such as the finite element method (FEM) [1–3], the boundary element method (BEM) [4,5], and the meshless method [6–10].

As a new approach in recent years, the meshless method is now widely applied in various fields [11–19], particularly in computational fluid dynamics (CFD). The developed meshless approaches can be classified into collocation-based and Galerkin-based methods. Compared with the latter, the meshless collocation methods have the advantages of no numerical quadrature and mesh generation, and some of these are the localized method of fundamental solutions (LMFS) [20–22], the generalized finite difference method (GFDM) [23–33], the localized Chebyshev collocation method [34], the singular boundary method (SBM) [35–43], and the localized knot method (LKM) [44].

The GFDM, as a popular localized meshless collocation method, employs the Taylor series expansions and moving least squares (MLS) approximations [45,46] to form the system of algebraic equations with a sparse matrix [47,48]. Thanks to this sparse system, this method is highly efficient and suitable for the numerical simulations of large-scale problems. Many physical applications have been addressed by the GFDM, such as the thin elastic plate bending analysis [49], the electroelastic analysis of 3D piezoelectric structures [50], the acoustic wave propagation [51], the inverse Cauchy problem in 2D elasticity [52], the heat conduction problems [53], and the stationary flow in a dam [54].

A hybrid localized meshless method is proposed in this paper for the solution of transient groundwater flow in a two-dimensional space by combining the Crank–Nicolson

scheme and the GFDM. As the first step, the Crank–Nicolson scheme is applied to the temporal discretization of the transient groundwater flow equation. At each time node, a boundary value problem in space is then formed and subsequently solved with the GFDM. Through the above process, a hybrid localized meshless approach is finally established, which is truly meshless and easy to program. The rest of the work is organized as follows. The governing equation of transient groundwater flow with boundary and initial conditions is described in Section 2. The formulations of the hybrid localized meshless method are derived in Section 3. Several linear and nonlinear numerical examples are provided in Section 4 to verify the performance of the developed method. Some conclusions are presented in Section 5.

2. Problem Definition

The movement of transient groundwater flow of a constant density in a homogeneous and anisotropic two-dimensional (2D) medium with the domain Ω can be described by using the following equation:

$$T_x \frac{\partial^2 H(x, y, t)}{\partial x^2} + T_y \frac{\partial^2 H(x, y, t)}{\partial y^2} + W(x, y, t) = u_s \frac{\partial H(x, y, t)}{\partial t}, \quad (x, y) \in \Omega, \quad t > 0, \quad (1)$$

where H denotes hydraulic head, W is the volumetric flow rate of a source or sink per unit volume, u_s means the specific aquifer storativity, T_x and T_y are hydraulic conductivities along the x - and y -axis, and t is the time.

To obtain the solution of Equation (1), the boundary and initial conditions are imposed as the following:

$$H(x, y, t) = g_1(x, y, t), \quad (x, y) \in \partial\Omega_D, \quad t \geq 0, \quad (2)$$

$$\frac{\partial H(x, y, t)}{\partial n(x, y)} = g_2(x, y, t), \quad (x, y) \in \partial\Omega_N, \quad t \geq 0, \quad (3)$$

$$H(x, y, 0) = g_3(x, y), \quad (x, y) \in \Omega, \quad (4)$$

where $g_i (i = 1, 2, 3)$ are given functions, $\partial\Omega_D \cup \partial\Omega_N = \partial\Omega$ ($\partial\Omega_D \cap \partial\Omega_N = \emptyset$), and \mathbf{n} is unit outward normal vector to $\partial\Omega_N$.

3. Hybrid Localized Meshless Method

To solve the transient groundwater flow of Equations (1)–(4), the temporal discretization of this system is first made by using the Crank–Nicolson scheme. The spatial equation is then formed at each time node. The GFDM is finally used for the solution of the spatial equation with corresponding boundary conditions.

3.1. Temporal Discretization by the Crank–Nicolson Scheme

We insert n nodes $\{t_1 = 0, t_2, \dots, t_n = T_f\}$ in the time domain $[0, T_f]$ where T_f is the final time. By using the Crank–Nicolson scheme, the governing Equation (1) at each time node t_{i+1} is then recast as the following:

$$\frac{1}{2} \left[T_x \frac{\partial^2 H(x, y, t_{i+1})}{\partial x^2} + T_y \frac{\partial^2 H(x, y, t_{i+1})}{\partial y^2} + W(x, y, t_{i+1}) + T_x \frac{\partial^2 H(x, y, t_i)}{\partial x^2} + T_y \frac{\partial^2 H(x, y, t_i)}{\partial y^2} + W(x, y, t_i) \right] = u_s \frac{H(x, y, t_{i+1}) - H(x, y, t_i)}{\Delta t_i}, \quad i = 1, 2, \dots, n - 1, \quad (5)$$

where the time step size $\Delta t_i = t_{i+1} - t_i$. Then we can reformulate Equation (5) as the following:

$$\frac{\Delta t_i}{2} \left[T_x \frac{\partial^2 H(x, y, t_{i+1})}{\partial x^2} + T_y \frac{\partial^2 H(x, y, t_{i+1})}{\partial y^2} \right] - u_s H(x, y, t_{i+1}) = -u_s H(x, y, t_i) - \frac{\Delta t_i}{2} \left[T_x \frac{\partial^2 H(x, y, t_i)}{\partial x^2} + T_y \frac{\partial^2 H(x, y, t_i)}{\partial y^2} + W(x, y, t_i) + W(x, y, t_{i+1}) \right], \quad i = 1, 2, \dots, n - 1, \quad (6)$$

As a result, a system of spatial equations with the boundary conditions (2) and (3) at time node t_{i+1} is formed and will be solved by using the GFDM.

3.2. Spatial Discretization by the GFDM

For the GFDM, some collocation nodes are first distributed in the computational domain Ω and its boundary Γ . A supporting domain called a star for each node $x_0 = (x_0, y_0)$ is defined by collecting m nearest nodes $x_j = (x_j, y_j) (j = 1, 2, \dots, m)$ as shown in Figure 1. In the star, x_0 and $x_j (j = 1, 2, \dots, m)$ are respectively named as the central node and the supporting nodes. This distance criterion is the simplest way of star selection. However, it should be noted that distorted (ill-conditioned) stars may be formed based on this distance criterion, particularly for cases with very irregular distributions of collocation nodes. To overcome the above drawback, the “cross” and the “Voronoi neighbours” criterions discussed in Refs. [55,56] can be used to form more reasonable stars.

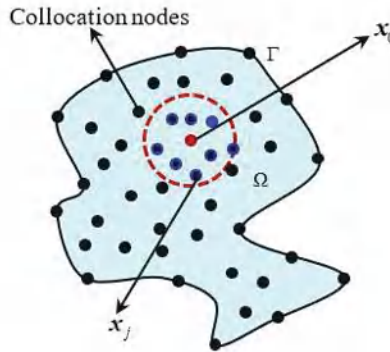


Figure 1. A star of collocation node x_0 .

To conveniently derive the system of algebraic equations, the $H_j (j = 0, 1, \dots, m)$ are employed to denote the values of hydraulic head at nodes $x_j (j = 0, 1, \dots, m)$ in the star of central node x_0 . Based on Taylor series expansions, H_j can be given as

$$H_j = H_0 + a_j \frac{\partial H_0}{\partial x} + b_j \frac{\partial H_0}{\partial y} + \frac{1}{2} \left(a_j^2 \frac{\partial^2 H_0}{\partial x^2} + b_j^2 \frac{\partial^2 H_0}{\partial y^2} \right) + a_j b_j \frac{\partial^2 H_0}{\partial x \partial y} + \dots, \quad j = 1, 2, \dots, m, \tag{7}$$

with

$$a_j = x_j - x_0, \text{ and } b_j = y_j - y_0. \tag{8}$$

By truncating the expansion (7) after second-order derivatives of hydraulic head H , we can define a residual function $R(H)$ as the following:

$$R(H) = \sum_{j=1}^m \left[\left(H_0 - H_j + a_j \frac{\partial H_0}{\partial x} + b_j \frac{\partial H_0}{\partial y} + \frac{a_j^2}{2} \frac{\partial^2 H_0}{\partial x^2} + \frac{b_j^2}{2} \frac{\partial^2 H_0}{\partial y^2} + a_j b_j \frac{\partial^2 H_0}{\partial x \partial y} \right) \kappa_j \right]^2, \tag{9}$$

with the following weighting function κ_j [57,58]:

$$\kappa_j = \frac{\exp(-\lambda_j^2) - \exp(-\lambda_m^2)}{1 - \exp(-\lambda_m^2)}, \quad j = 1, 2, \dots, m, \tag{10}$$

in which $\lambda_j = |x_j - x_0|$, and $\lambda_m = \max\{\lambda_j, j = 1, 2, \dots, m\}$. It should be noted that the weighting function in the GFDM should be a monotonic decreasing function of λ_j . Because the Taylor series approximation becomes more accurate when the distance λ_j is smaller, which should have a higher weight κ_j in residual function $R(H)$ of Equation (9). Some other weighting functions can be found in [53,59].

A vector P_H is defined by the following:

$$P_H = \left[\frac{\partial H_0}{\partial x}, \frac{\partial H_0}{\partial y}, \frac{\partial^2 H_0}{\partial x^2}, \frac{\partial^2 H_0}{\partial y^2}, \frac{\partial^2 H_0}{\partial x \partial y} \right]^T \tag{11}$$

Minimizing the residual function $R(H)$ with respect to each element in the vector P_H , i.e.,

$$\frac{\partial R(H)}{\partial \left\{ \frac{\partial H_0}{\partial x} \right\}} = 0, \frac{\partial R(H)}{\partial \left\{ \frac{\partial H_0}{\partial y} \right\}} = 0, \frac{\partial R(H)}{\partial \left\{ \frac{\partial^2 H_0}{\partial x^2} \right\}} = 0, \frac{\partial R(H)}{\partial \left\{ \frac{\partial^2 H_0}{\partial y^2} \right\}} = 0, \frac{\partial R(H)}{\partial \left\{ \frac{\partial^2 H_0}{\partial x \partial y} \right\}} = 0, \quad (12)$$

we can have a system of linear equations as the following:

$$AP_H = b, \quad (13)$$

with the following:

$$A = \sum_{j=1}^m \text{diag} \left(E_1^{(j)} \right) \text{II} \text{diag} \left(E_2^{(j)} \right), \quad (14)$$

$$b = BH = \left(-\sum_{j=1}^m \kappa_j E_2^{(j)}, \kappa_1 E_2^{(1)}, \kappa_2 E_2^{(2)}, \dots, \kappa_m E_2^{(m)} \right)_{5 \times (m+1)} \begin{pmatrix} H_0 \\ H_1 \\ H_2 \\ \vdots \\ H_m \end{pmatrix}_{(m+1) \times 1}, \quad (15)$$

where II is a 5×5 square matrix that all elements are one, $\text{diag} \left(E_1^{(j)} \right)$ and $\text{diag} \left(E_2^{(j)} \right)$ are both diagonal matrices with their diagonal elements as the following:

$$E_1^{(j)} = \kappa_j \begin{bmatrix} a_j & b_j & a_j^2 & b_j^2 & a_j b_j \end{bmatrix}^T, \text{ and } E_2^{(j)} = \frac{\kappa_j}{2} \begin{bmatrix} 2a_j & 2b_j & a_j^2 & b_j^2 & 2a_j b_j \end{bmatrix}^T, \quad (16)$$

and $H = [H_0, H_1, H_2, \dots, H_m]^T$.

With the help of Equation (13) and Equation (15), the vector P_H can be formulated as the following:

$$P_H = A^{-1}B[H_0, H_1, H_2, \dots, H_m]^T. \quad (17)$$

As a result, all the first- and second-order derivatives of hydraulic head H at central node x_0 are expressed as the linear combinations of values H_j ($j = 0, 1, \dots, m$). By substituting the corresponding second-order derivatives of Equation (17) into Equation (6), we can easily recast Equation (6) as the following:

$$\sum_{j=0}^m \alpha_j H_j = Q, \quad (18)$$

where α_j ($j = 0, 1, \dots, m$) and Q are obviously known and can be determined by Equations (6) and (17). For each collocation node excepting that of satisfying boundary condition (2), one equation can be obtained by using the above similar derivation. It should be noted that $H_0 = g(x_0, y_0, t_{i+1})$ is directly used as one equation for collocation nodes of satisfying boundary condition (2). Finally, by using the GFDM, the spatial equation with the corresponding boundary conditions has been transformed into a system of linearly algebraic equations with a sparse matrix. The values of hydraulic head H at all collocation nodes can be calculated once this system is solved.

In addition, we consider a case with a nonlinear volumetric flow rate in the following numerical example 4 to further verify the proposed approach. Through a similar derivation process, a nonlinear system of algebraic equations is established and solved by using "fsolve" function of MATLAB.

4. Numerical Examples

In this section, four numerical examples with square and complicated domains are given to test the accuracy and stability of the proposed method. To preferably estimate

the precision of numerical results, two different error definitions are provided as the following [60,61]:

$$\text{Global error} = \sqrt{\sum_{i=1}^N (\bar{H}_i - H_i)^2} / \sqrt{\sum_{i=1}^N H_i^2}, \tag{19}$$

$$\text{Max error} = \max_{1 \leq i \leq N} \left\{ \frac{|\bar{H}_i - H_i|}{|H_i|} \right\} \tag{20}$$

in which N denotes the number of collocation nodes, H_i and \bar{H}_i represents the exact and numerical results of hydraulic head at the i -th node. Unless otherwise specified, the number of supporting nodes in a star is set to $m = 12$ in all numerical examples.

4.1. Example 1: Hydraulic Head Distribution in a Square Domain

As the first numerical example, we consider the distribution of hydraulic heads in a unit square domain with its central point (0.5,0.5). The specific aquifer storativity is $u_s = 1$, and the hydraulic conductivities are $T_x = 1$ and $T_y = 3$. The volumetric flow rate W is given as the following:

$$W(x, y, t) = \sin(0.5\pi x) \sin(0.5\pi y) (\pi^2 \sin t + \cos t). \tag{21}$$

The Dirichlet boundary condition $H(x, y, t) = 0$ is imposed on the boundaries $x = 0$, and $y = 0$. The Neumann boundary condition $\frac{\partial H(x, y, t)}{\partial n} = 0$ is applied to the boundaries $x = 1$, and $y = 1$. The initial condition is $H(x, y, 0) = 0$. Based on these, the exact solution can be determined as the following:

$$H(x, y, t) = \sin(0.5\pi x) \sin(0.5\pi y) \sin t. \tag{22}$$

In the numerical simulation, the final time is set to $T_f = 2$, and the time step size is $\Delta t = 0.05$. For the spatial discretization, 396 collocation nodes are distributed in the domain and its boundary, which have the following two different patterns: regular distribution (case 1) and irregular distribution (case 2), as shown in Figure 2a. From $t = 0$ to $t = 2$, the variations of global and max errors of hydraulic head H calculated by the GFDM with the Crank–Nicolson scheme (CN-GFDM) are plotted in Figure 2b. As we can see from this figure, the developed method has good performance for two different collocation node distributions. We also find that errors obtained by employing the irregular distribution (case 2) are larger than those obtained by using the regular distribution (case 1).

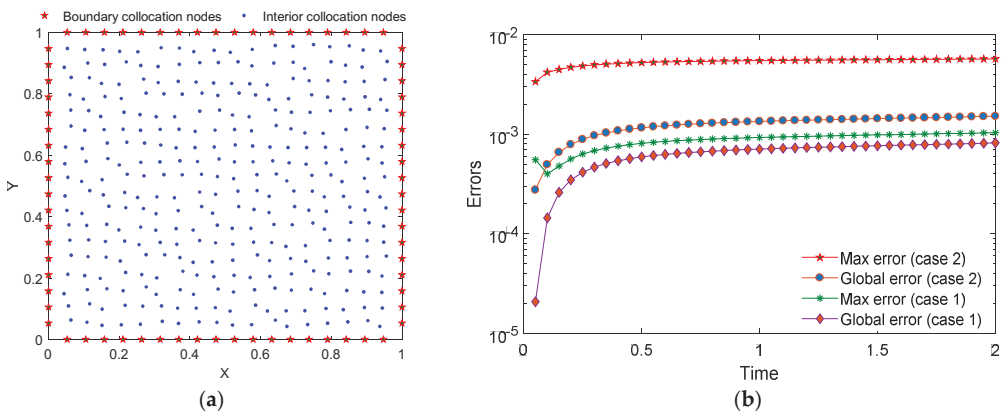


Figure 2. (a) Irregular distribution of 396 collocation nodes, (b) Global and max errors of hydraulic head H from $t = 0$ to $t = 2$.

To investigate the convergence behavior of the CN-GFDM, the program is rerun by only changing the number of collocation nodes compared with the previous setting. Here, the distribution of nodes is regular. By using the developed method with a different number of collocation nodes (or a different mean distance of collocation nodes), Table 1 provides the max and global errors of the numerical results of the hydraulic head at time $t = 2$. It can be obviously observed that the errors decay with an increasing collocation node number, which indicates the CN-GFDM has a good convergence property for this case.

Table 1. Max and global errors of hydraulic head H with different number of collocation nodes.

Number of collocation nodes	21	96	192	285	396
Mean distance of collocation nodes	2.50×10^{-1}	1.11×10^{-1}	7.69×10^{-2}	6.25×10^{-2}	5.26×10^{-2}
Max error	1.01×10^{-2}	3.75×10^{-3}	2.05×10^{-3}	1.42×10^{-3}	1.04×10^{-3}
Global error	5.94×10^{-3}	2.74×10^{-3}	1.57×10^{-3}	1.11×10^{-3}	8.18×10^{-4}

4.2. Example 2: Hydraulic Head Distribution in a Heart-Shaped Domain

The second numerical example is a hydraulic head distribution in a heart-shaped domain, and the dimension of this domain is shown in Figure 3. The specific aquifer storativity and hydraulic conductivity are assumed to be as the following:

$$u_s = 3, T_x = 2T_y = 2. \tag{23}$$

The volumetric flow rate is $W = 0$. In this case, the Dirichlet boundary and initial conditions are imposed as the following:

$$H(x, y, t) = e^{-t} \cos x \cos y + c, (x, y) \in \Gamma, \tag{24}$$

$$H(x, y, 0) = \cos x \cos y + c, (x, y) \in \Omega, \tag{25}$$

where $c = 0.2$. The exact solution for this example is determined as $H(x, y, t) = e^{-t} \cos x \cos y + c$.

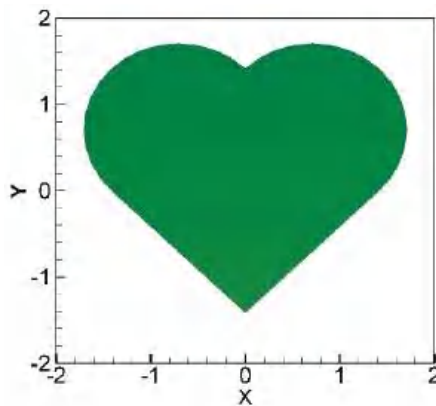


Figure 3. The dimension of a heart-shaped domain.

To simulate the solution from $t = 0$ to $t = 5$, the developed method employs 218,464 (see Figure 4), and 1700 collocation nodes. The time step size is set to $\Delta t = 0.05$. Figure 5 provides the contours of relative errors (RE) of the hydraulic head at final time $t = 5$ by using these three distributions of collocation nodes. It can be found that the max relative error of numerical results in the computational domain is less than 3×10^{-4} even only using

218 collocation nodes. Moreover, all numerical errors overall decreased with an increasing number of collocation nodes.

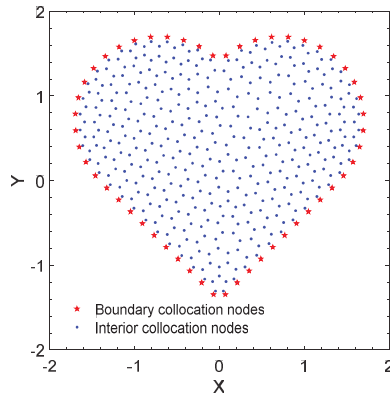


Figure 4. Distribution of 464 collocation nodes.

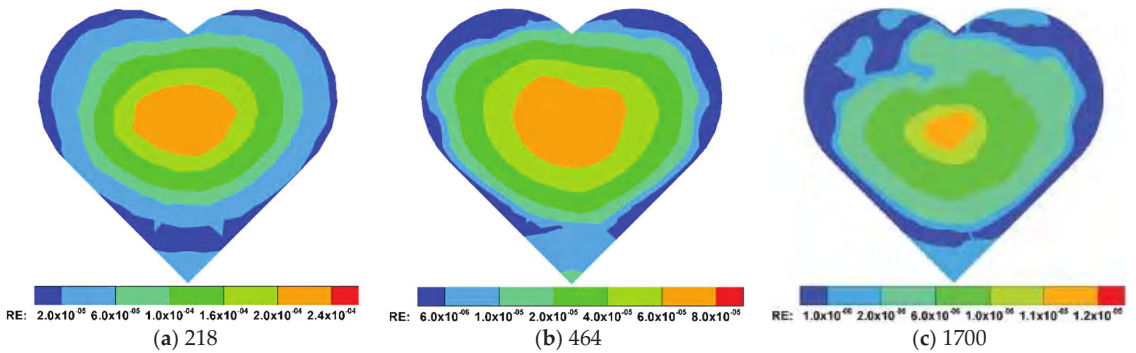


Figure 5. The contours of relative errors of hydraulic head H with three distributions of collocation nodes.

Next, we keep the above-mentioned setting and distribute 1700 collocation nodes. The mean distance of these nodes is 0.101. Table 2 lists the max and global errors of hydraulic head H at final time $t = 5$, which are calculated by the CN-GFDM with different time step sizes. As we can observe, the errors decay rapidly when decreasing the time step size.

Table 2. Max and global errors of hydraulic head H with different time step size.

Time step size	0.625	0.50	0.25	0.125	0.05
Max error	2.51×10^{-3}	1.60×10^{-3}	4.05×10^{-4}	8.42×10^{-5}	1.17×10^{-5}
Global error	1.20×10^{-3}	7.80×10^{-4}	1.91×10^{-4}	3.89×10^{-5}	4.97×10^{-6}

Finally, we investigate the influence of supporting node number m on the precision and computational efficiency of the developed approach. The time step size is reset as $\Delta t = 0.25$. Table 3 provides the variations of two kinds of errors and CPU time with different numbers of supporting nodes. As we can observe, the accuracy of numerical results obtained by the present method is relatively insensitive to the number of supporting nodes. To have a higher computing efficiency of the CN-GFDM, we should choose a relatively small number of supporting nodes when the numerical results satisfy the accuracy requirement.

Table 3. Max and global errors of hydraulic head H and CPU time with different supporting node numbers.

m	12	16	20	24	28
Max error	4.05×10^{-4}	3.53×10^{-4}	3.45×10^{-4}	3.38×10^{-4}	3.23×10^{-4}
Global error	1.91×10^{-4}	1.71×10^{-4}	1.66×10^{-4}	1.61×10^{-4}	1.55×10^{-4}
CPU time (s)	0.27	0.34	0.38	0.44	0.49

4.3. Example 3: Hydraulic Head Distribution in a Complicated Domain

As the third numerical example, the distribution of hydraulic head in a complicated domain is considered. The dimension of this domain is 2.7×1.4 , as shown in Figure 6. The specific aquifer storativity is set to $u_s = 0.3$, and hydraulic conductivities are assumed to be functions as the following:

$$T_x = e^{|x|}, \text{ and } T_y = e^{|y|}. \tag{26}$$

The volumetric flow rate is given as the following:

$$W(x, y, t) = e^{x+y} [u_s \cos t - (T_x + T_y) \sin t] \tag{27}$$

The Dirichlet boundary condition is imposed as the following:

$$H(x, y, t) = e^{x+y} \sin t, \quad (x, y) \in \Gamma, \tag{28}$$

and initial condition is $H = 0$. The exact solution for this example is $H(x, y, t) = e^{x+y} \sin t$.

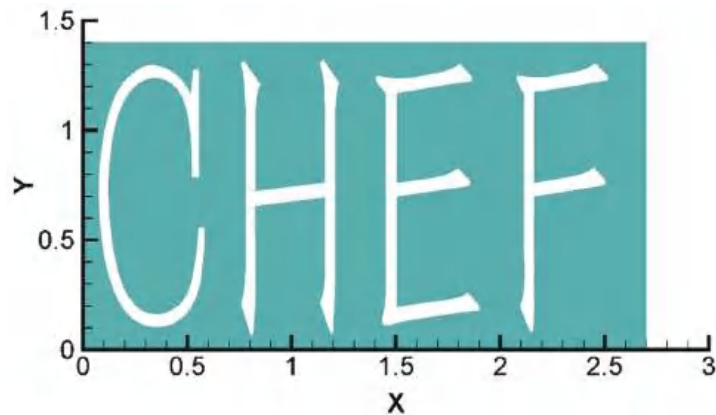


Figure 6. The dimension of a complicated domain.

We first consider the simulation from $t = 0$ to $t = 5$, and set the time step size as $\Delta t = 0.1$. By using the present approach with 3398 (see Figure 7) and 8918 collocation nodes, Figures 8 and 9 respectively plot the contours of relative errors of hydraulic head H and its flux $\frac{\partial H}{\partial x}$ at final time $t = 5$. The numerical results in these figures illustrate the availability and convergency of the developed CN-GFDM.

Finally, a long-time simulation of hydraulic head H from $t = 0$ to $t = 100$ is considered. The number of collocation nodes is 8918, and the time step size is $\Delta t = 0.1$. Figure 10 shows the max and global errors of hydraulic head H , which are changed as functions of time. As we can see from this figure, the two kinds of errors both remain stable in this simulation.

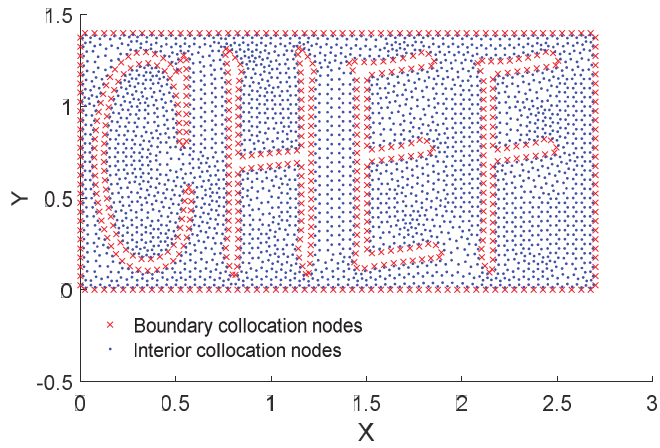


Figure 7. Distribution of 3398 collocation nodes.

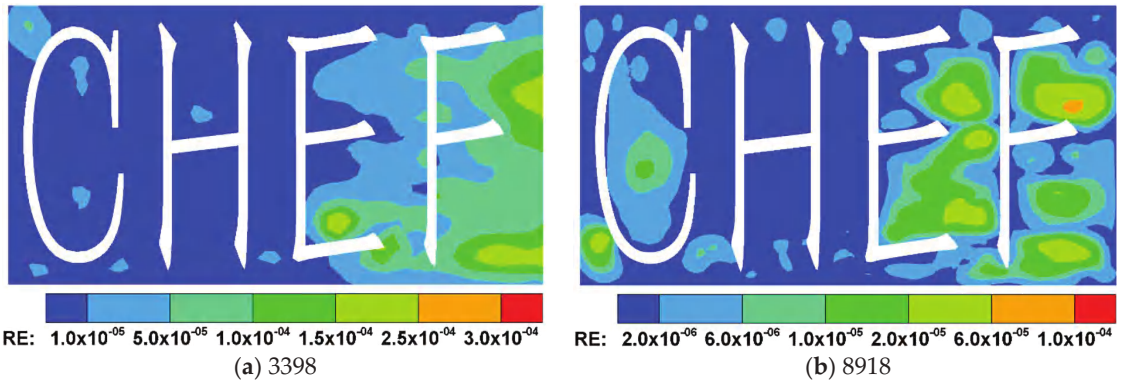


Figure 8. The contours of relative errors of hydraulic head H with two distributions of collocation nodes.

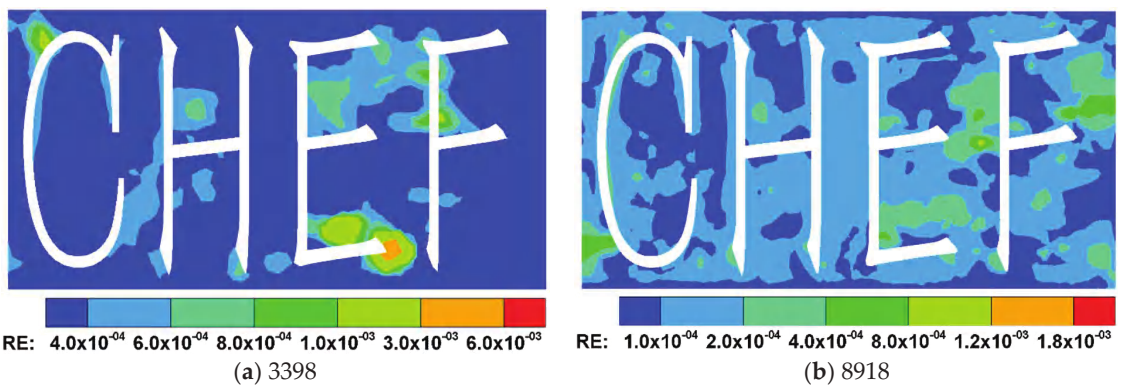


Figure 9. Relative error distributions of flux $\partial H / \partial x$ with different number of collocation nodes.

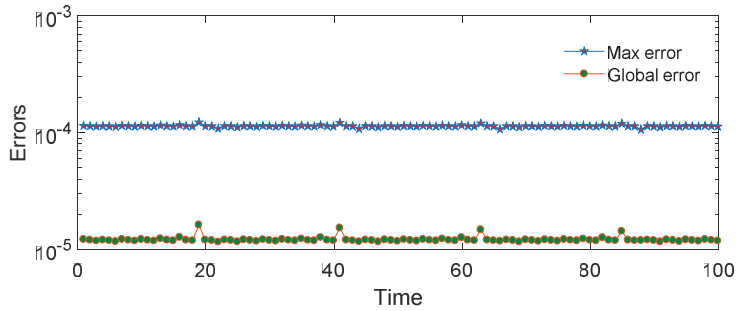


Figure 10. Two types of error curves of hydraulic head H from $t = 0$ to $t = 100$.

4.4. Example 4: Nonlinear Hydraulic Head Distribution in a Gear Domain

As the final numerical example, we consider the distribution of nonlinear hydraulic head in a gear domain. Figure 11 shows the dimension of the gear domain. The specific aquifer storativity is assumed to be $u_s = 1200$, and hydraulic conductivities are the following:

$$T_x = x^2, \text{ and } T_y = y^2. \tag{29}$$

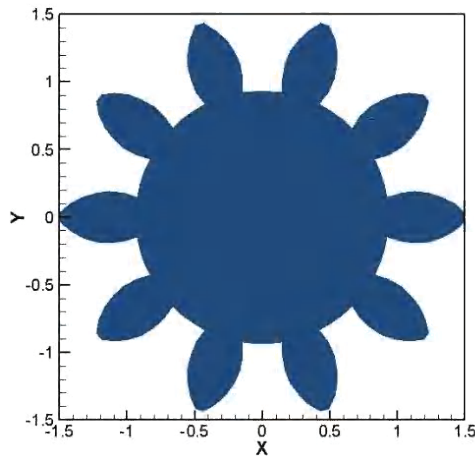


Figure 11. The dimension of a gear domain.

The volumetric flow rate is a nonlinear term given as the following:

$$W(x, y, t) = H^2(x, y, t) - \left[(x^4 + y^4) e^{\frac{t}{100}} + 0.1 \right]^2 \tag{30}$$

The Dirichlet boundary condition is imposed as the following:

$$H(x, y, t) = (x^4 + y^4) e^{\frac{t}{100}} + 0.1, \quad (x, y) \in \Gamma, \tag{31}$$

and initial condition is the following:

$$H(x, y, t) = x^4 + y^4 + 0.1, \quad (x, y) \in \Omega. \tag{32}$$

The exact solution for this case is determined as the following:

$$H(x, y, t) = (x^4 + y^4) e^{\frac{t}{100}} + 0.1 \tag{33}$$

The numerical simulation for this case is run from $t = 0$ to $t = 10$. The time step size is set to $\Delta t = 0.05$, and 1186 collocation nodes are distributed in the gear domain and its boundary as shown in Figure 12. The contours of relative errors of the hydraulic head H at $t = 5$ and $t = 10$ are plotted in Figure 13. As we can see from this figure, the present approach obtains the satisfied numerical results for this nonlinear case, and max relative error is less than 4×10^{-3} . Figure 14 provides the max and global errors of hydraulic head H at each time node, which illustrates that the developed CN-GFDM yields accurate numerical results as an increasing time.

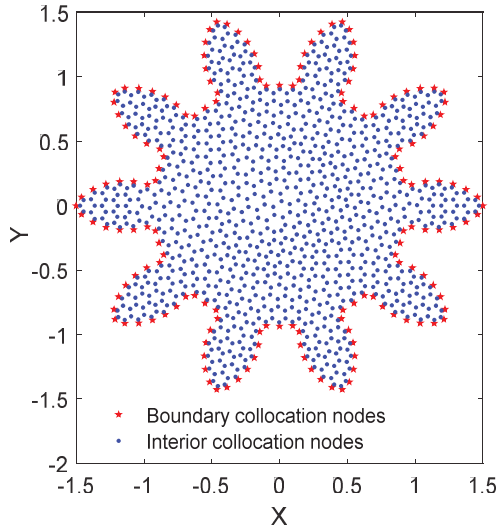


Figure 12. Distribution of 1186 collocation nodes.

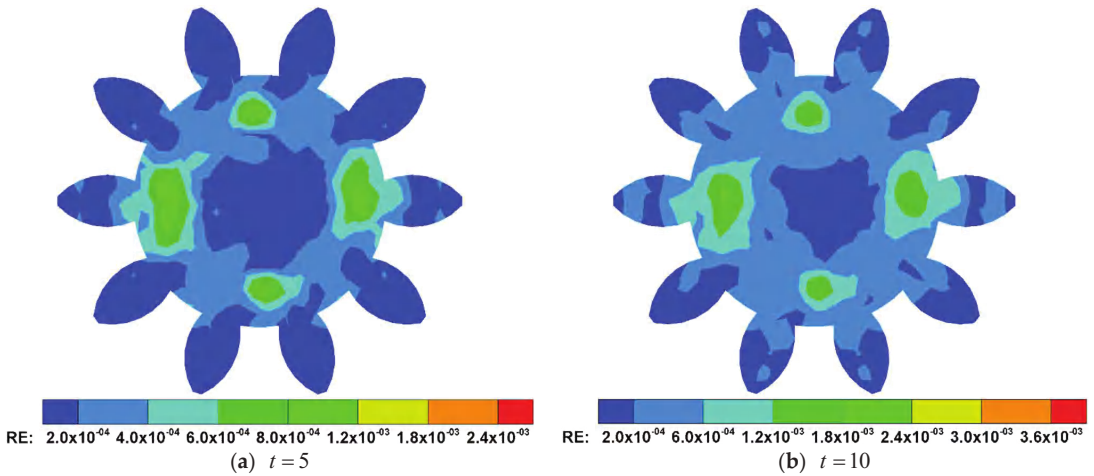


Figure 13. The contours of relative errors of hydraulic head H at $t = 5$ and $t = 10$.

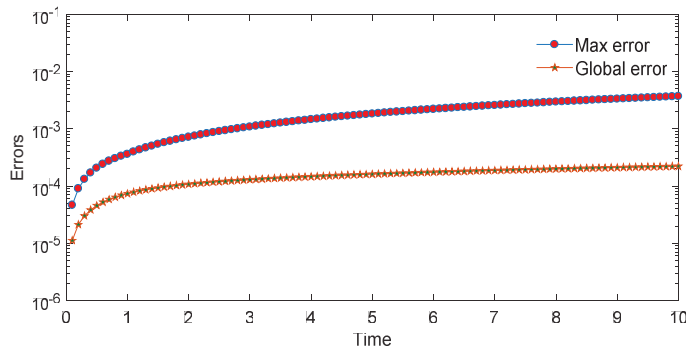


Figure 14. Two types of error curves of hydraulic head H from $t = 0$ to $t = 10$.

5. Concluding Remarks

To simulate the transient groundwater flow in homogeneous and anisotropic two-dimensional mediums, a hybrid localized meshless method is constructed based on the Crank–Nicolson scheme for temporal discretization and the GFDM for spatial discretization. The present approach is truly meshless and easy to program.

To fully investigate the performance of the developed method, the max and global errors of hydraulic head are both provided for numerical examples with different boundary conditions, complicated geometry domains, and several kinds of hydraulic conductivities. Numerical results indicate that the hybrid localized meshless method developed in this work obtains the satisfied accuracy and convergency in time and space.

Author Contributions: Conceptualization, Q.W. and W.Q.; methodology, W.Q.; software, Q.W. and P.K.; investigation, Q.W.; writing—original draft preparation, Q.W.; writing—review and editing, P.K. and W.Q.; visualization, Q.W.; supervision, P.K. and W.Q.; funding acquisition, Q.W. All authors have read and agreed to the published version of the manuscript.

Funding: The work described in this paper was supported by the Government of Shandong’s Education System for studying abroad, and the key R & D plan of Zibo city: Intelligent Water IoT cloud service platform of “Zishui Online” (NO. 2019ZBXC246).

Institutional Review Board Statement: Not applicable.

Informed Consent Statement: Not applicable.

Data Availability Statement: Not applicable.

Conflicts of Interest: The authors declare no conflict of interest.

References

1. Hughes, T.J. *The Finite Element Method: Linear Static and Dynamic Finite Element Analysis*; Courier Corporation: Chelmsford, MA, USA, 2012.
2. Chai, Y.; Li, W.; Liu, Z. Analysis of transient wave propagation dynamics using the enriched finite element method with interpolation cover functions. *Appl. Math. Comput.* **2022**, *412*, 126564. [CrossRef]
3. Li, W.; Zhang, Q.; Gui, Q.; Chai, Y. A coupled FE-meshfree triangular element for acoustic radiation problems. *Int. J. Comput. Methods* **2021**, *18*, 2041002. [CrossRef]
4. Qu, W.; Zhang, Y.; Liu, C.-S. Boundary stress analysis using a new regularized boundary integral equation for three-dimensional elasticity problems. *Arch. Appl. Mech.* **2017**, *87*, 1213–1226. [CrossRef]
5. Gu, Y.; Zhang, C. Fracture analysis of ultra-thin coating/substrate structures with interface cracks. *Int. J. Solids Struct.* **2021**, *225*, 111074. [CrossRef]
6. Zhang, X.; Liu, X.H.; Song, K.Z.; Lu, M.W. Least-squares collocation meshless method. *Int. J. Numer. Methods Eng.* **2001**, *51*, 1089–1100. [CrossRef]
7. Atluri, S.N.; Shen, S. *The Meshless Method*; Tech Science Press: Encino, CA, USA, 2002.
8. Wang, C.; Wang, F.; Gong, Y. Analysis of 2D heat conduction in nonlinear functionally graded materials using a local semi-analytical meshless method. *AIMS Math.* **2021**, *6*, 12599–12618. [CrossRef]

9. Xing, Y.; Song, L.; Fan, C.-M. A generalized finite difference method for solving elasticity interface problems. *Eng. Anal. Bound. Elem.* **2021**, *128*, 105–117. [CrossRef]
10. Li, X.; Dong, H. An element-free Galerkin method for the obstacle problem. *Appl. Math. Lett.* **2021**, *112*, 106724. [CrossRef]
11. Xi, Q.; Fu, Z.; Wu, W.; Wang, H.; Wang, Y. A novel localized collocation solver based on Trefftz basis for potential-based inverse electromyography. *Appl. Math. Comput.* **2021**, *390*, 125604. [CrossRef]
12. Tang, Z.; Fu, Z.; Chen, M.; Ling, L. A localized extrinsic collocation method for Turing pattern formations on surfaces. *Appl. Math. Lett.* **2021**, *122*, 107534. [CrossRef]
13. Xi, Q.; Fu, Z.; Rabczuk, T.; Yin, D. A localized collocation scheme with fundamental solutions for long-time anomalous heat conduction analysis in functionally graded materials. *Int. J. Heat Mass Transf.* **2021**, *180*, 121778. [CrossRef]
14. Lin, J.; Zhang, Y.; Reutskiy, S.; Feng, W. A novel meshless space-time backward substitution method and its application to nonhomogeneous advection-diffusion problems. *Appl. Math. Comput.* **2021**, *398*, 125964. [CrossRef]
15. Qiu, L.; Hu, C.; Qin, Q.-H. A novel homogenization function method for inverse source problem of nonlinear time-fractional wave equation. *Appl. Math. Lett.* **2020**, *109*, 106554. [CrossRef]
16. Sun, L.; Zhang, C.; Yu, Y. A boundary knot method for 3D time harmonic elastic wave problems. *Appl. Math. Lett.* **2020**, *104*, 106210. [CrossRef]
17. Sun, L.; Chen, Z.; Zhang, S.; Chu, L. A wave based method for two-dimensional time-harmonic elastic wave propagation in anisotropic media. *Appl. Math. Lett.* **2021**, *120*, 107292. [CrossRef]
18. García, Á.; Negreanu, M.; Ureña, F.; Vargas, A.M. A Note on a Meshless Method for Fractional Laplacian at Arbitrary Irregular Meshes. *Mathematics* **2021**, *9*, 2843. [CrossRef]
19. Rao, X.; Zhan, W.; Zhao, H.; Xu, Y.; Liu, D.; Dai, W.; Gong, R.; Wang, F. Application of the least-square meshless method to gas-water flow simulation of complex-shape shale gas reservoirs. *Eng. Anal. Bound. Elem.* **2021**, *129*, 39–54. [CrossRef]
20. Qu, W.; Fan, C.-M.; Li, X. Analysis of an augmented moving least squares approximation and the associated localized method of fundamental solutions. *Comput. Math. Appl.* **2020**, *80*, 13–30. [CrossRef]
21. Gu, Y.; Fan, C.-M.; Fu, Z. Localized Method of Fundamental Solutions for Three-Dimensional Elasticity Problems: Theory. *Adv. Appl. Math. Mech.* **2021**, *13*, 1520–1534.
22. Li, W. Localized method of fundamental solutions for 2D harmonic elastic wave problems. *Appl. Math. Lett.* **2021**, *112*, 106759. [CrossRef]
23. Qu, W.; Gao, H.; Gu, Y. Integrating Krylov deferred correction and generalized finite difference methods for dynamic simulations of wave propagation phenomena in long-time intervals. *Adv. Appl. Math. Mech.* **2021**, *13*, 1398–1417.
24. Qu, W.; He, H. A spatial-temporal GFDM with an additional condition for transient heat conduction analysis of FGMs. *Appl. Math. Lett.* **2020**, *110*, 106579. [CrossRef]
25. Song, L.; Li, P.-W.; Gu, Y.; Fan, C.-M. Generalized finite difference method for solving stationary 2D and 3D Stokes equations with a mixed boundary condition. *Comput. Math. Appl.* **2020**, *80*, 1726–1743. [CrossRef]
26. Shao, M.; Song, L.; Li, P.-W. A generalized finite difference method for solving Stokes interface problems. *Eng. Anal. Bound. Elem.* **2021**, *132*, 50–64. [CrossRef]
27. Xing, Y.; Song, L.; Li, P.-W. A generalized finite difference method for solving biharmonic interface problems. *Eng. Anal. Bound. Elem.* **2022**, *135*, 132–144. [CrossRef]
28. Li, P.-W. Space-time generalized finite difference nonlinear model for solving unsteady Burgers' equations. *Appl. Math. Lett.* **2021**, *114*, 106896. [CrossRef]
29. Li, Y.-D.; Tang, Z.-C.; Fu, Z.-J. Generalized Finite Difference Method for Plate Bending Analysis of Functionally Graded Materials. *Mathematics* **2020**, *8*, 1940. [CrossRef]
30. Fan, C.-M.; Chu, C.-N.; Šarler, B.; Li, T.-H. Numerical solutions of waves-current interactions by generalized finite difference method. *Eng. Anal. Bound. Elem.* **2019**, *100*, 150–163. [CrossRef]
31. Ureña, F.; Gavete, L.; Garcia, A.; Benito, J.J.; Vargas, A.M. Solving second order non-linear parabolic PDEs using generalized finite difference method (GFDM). *J. Comput. Appl. Math.* **2019**, *354*, 221–241. [CrossRef]
32. Salet, E.; Vargas, A.M.; Garcia, Á.; Negreanu, M.; Benito, J.J.; Ureña, F. Complex Ginzburg–Landau Equation with Generalized Finite Differences. *Mathematics* **2020**, *8*, 2248. [CrossRef]
33. Huang, J.; Lyu, H.; Fan, C.-M.; Chen, J.-H.; Chu, C.-N.; Gu, J. Wave-Structure Interaction for a Stationary Surface-Piercing Body Based on a Novel Meshless Scheme with the Generalized Finite Difference Method. *Mathematics* **2020**, *8*, 1147. [CrossRef]
34. Wang, F.; Zhao, Q.; Chen, Z.; Fan, C.-M. Localized Chebyshev collocation method for solving elliptic partial differential equations in arbitrary 2D domains. *Appl. Math. Comput.* **2021**, *397*, 125903. [CrossRef]
35. Li, J.; Gu, Y.; Qin, Q.-H.; Zhang, L. The rapid assessment for three-dimensional potential model of large-scale particle system by a modified multilevel fast multipole algorithm. *Comput. Math. Appl.* **2021**, *89*, 127–138. [CrossRef]
36. Li, J.; Fu, Z.; Gu, Y.; Qin, Q.-H. Recent Advances and Emerging Applications of the Singular Boundary Method for Large-Scale and High-Frequency Computational Acoustics. *Adv. Appl. Math. Mech.* **2021**, *14*, 315–343. [CrossRef]
37. Li, W.; Chen, W.; Pang, G. Singular boundary method for acoustic eigenanalysis. *Comput. Math. Appl.* **2016**, *72*, 663–674. [CrossRef]
38. Lin, J.; Qiu, L.; Wang, F. Localized singular boundary method for the simulation of large-scale problems of elliptic operators in complex geometries. *Comput. Math. Appl.* **2022**, *105*, 94–106. [CrossRef]

39. Qiu, L.; Wang, F.; Lin, J. A meshless singular boundary method for transient heat conduction problems in layered materials. *Comput. Math. Appl.* **2019**, *78*, 3544–3562. [CrossRef]
40. Wei, X.; Luo, W. 2.5D singular boundary method for acoustic wave propagation. *Appl. Math. Lett.* **2021**, *112*, 106760. [CrossRef]
41. Wei, X.; Huang, A.; Sun, L. Singular boundary method for 2D and 3D heat source reconstruction. *Appl. Math. Lett.* **2020**, *102*, 106103. [CrossRef]
42. Qu, W.; Chen, W. Solution of two-dimensional stokes flow problems using improved singular boundary method. *Adv. Appl. Math. Mech.* **2015**, *7*, 13–30. [CrossRef]
43. Li, W.; Wang, F. Precorrected-FFT Accelerated Singular Boundary Method for High-Frequency Acoustic Radiation and Scattering. *Mathematics* **2022**, *10*, 238. [CrossRef]
44. Wang, F.; Wang, C.; Chen, Z. Local knot method for 2D and 3D convection–diffusion–reaction equations in arbitrary domains. *Appl. Math. Lett.* **2020**, *105*, 106308. [CrossRef]
45. Li, X.; Zhao, Q.; Long, K.; Zhang, H. Multi-material topology optimization of transient heat conduction structure with functional gradient constraint. *Int. Commun. Heat Mass Transf.* **2022**, *131*, 105845. [CrossRef]
46. Li, X.; Li, S. On the stability of the moving least squares approximation and the element-free Galerkin method. *Comput. Math. Appl.* **2016**, *72*, 1515–1531. [CrossRef]
47. Liszka, T. An interpolation method for an irregular net of nodes. *Int. J. Numer. Methods Eng.* **1984**, *20*, 1599–1612. [CrossRef]
48. Liszka, T.; Orkisz, J. The finite difference method at arbitrary irregular grids and its application in applied mechanics. *Comput. Struct.* **1980**, *11*, 83–95. [CrossRef]
49. Qu, W.; He, H. A GFDM with supplementary nodes for thin elastic plate bending analysis under dynamic loading. *Appl. Math. Lett.* **2022**, *124*, 107664. [CrossRef]
50. Xia, H.; Gu, Y. Generalized finite difference method for electroelastic analysis of three-dimensional piezoelectric structures. *Appl. Math. Lett.* **2021**, *117*, 107084. [CrossRef]
51. Qu, W. A high accuracy method for long-time evolution of acoustic wave equation. *Appl. Math. Lett.* **2019**, *98*, 135–141. [CrossRef]
52. Li, P.-W.; Fu, Z.-J.; Gu, Y.; Song, L. The generalized finite difference method for the inverse Cauchy problem in two-dimensional isotropic linear elasticity. *Int. J. Solids Struct.* **2019**, *174*, 69–84. [CrossRef]
53. Qu, W.; Gu, Y.; Zhang, Y.; Fan, C.M.; Zhang, C. A combined scheme of generalized finite difference method and Krylov deferred correction technique for highly accurate solution of transient heat conduction problems. *Int. J. Numer. Methods Eng.* **2019**, *117*, 63–83. [CrossRef]
54. Chávez-Negrete, C.; Santana-Quinteros, D.; Domínguez-Mota, F. A Solution of Richards’ Equation by Generalized Finite Differences for Stationary Flow in a Dam. *Mathematics* **2021**, *9*, 1604. [CrossRef]
55. Orkisz, J. Finite Difference Method; Part III. In *Handbook of Computational Solid Mechanics*; Kleiber, M., Ed.; Springer: Berlin/Heidelberg, Germany, 1998; pp. 336–432.
56. Milewski, S. Meshless finite difference method with higher order approximation—Applications in mechanics. *Arch. Comput. Methods Eng.* **2012**, *19*, 1–49. [CrossRef]
57. Belytschko, T.; Krongauz, Y.; Organ, D.; Fleming, M.; Krysl, P. Meshless methods: An overview and recent developments. *Comput. Methods Appl. Mech. Eng.* **1996**, *139*, 3–47. [CrossRef]
58. Zhou, Y.; Qu, W.; Gu, Y.; Gao, H. A hybrid meshless method for the solution of the second order hyperbolic telegraph equation in two space dimensions. *Eng. Anal. Bound. Elem.* **2020**, *115*, 21–27. [CrossRef]
59. Gavete, L.; Ureña, F.; Benito, J.J.; García, A.; Ureña, M.; Salet, E. Solving second order non-linear elliptic partial differential equations using generalized finite difference method. *J. Comput. Appl. Math.* **2017**, *318*, 378–387. [CrossRef]
60. Qu, W.; Chen, W.; Gu, Y. Fast multipole accelerated singular boundary method for the 3D Helmholtz equation in low frequency regime. *Comput. Math. Appl.* **2015**, *70*, 679–690. [CrossRef]
61. Qu, W.; Fan, C.-M.; Zhang, Y. Analysis of three-dimensional heat conduction in functionally graded materials by using a hybrid numerical method. *Int. J. Heat Mass Transf.* **2019**, *145*, 118771. [CrossRef]

Article

A Novel Spatial–Temporal Radial Trefftz Collocation Method for 3D Transient Wave Propagation Analysis with Specified Sound Source Excitation

Lin Chen, Wenzhi Xu * and Zhuojia Fu *

College of Mechanics and Materials, Hohai University, Nanjing 211100, China; chenlin@hhu.edu.cn

* Correspondence: xwz@hhu.edu.cn (W.X.); paul212063@hhu.edu.cn (Z.F.)

Abstract: In this paper, a novel semi-analytical collocation solver, the spatial–temporal radial Trefftz collocation method (STRTCM) is proposed to solve 3D transient wave equations with specified sound source excitations. Unlike the traditional time discretization strategies, the proposed numerical scheme introduces the spatial–temporal radial Trefftz functions (STRTFs) as the basis functions for the spatial and temporal discretization of the transient wave equations. The STRTFs are constructed in the spatial–temporal domain, which is a combination of 3D Euclidean space and time into a 4D manifold. Moreover, since the initial and boundary conditions are imposed on the spatial–temporal domain boundaries, the original transient wave propagation problem can be converted to an inverse boundary value problem. To deal with the specified time-dependent sound source excitations, the composite multiple reciprocity technique is extended from the spatial domain to the spatial–temporal domain, which transforms the original problem with a source term into a high-order problem without a source term. By deriving the related STRTFs for the considered high-order problem, the proposed scheme only requires the node discretization on the spatial–temporal domain boundaries. The efficiency of the proposed method is numerically verified by four benchmark examples under 3D transient wave equations with specified time-dependent sound source excitation.

Keywords: meshless collocation method; semi-analytical; radial Trefftz basis functions; transient wave propagation analysis

MSC: 65M70; 35L05

Citation: Chen, L.; Xu, W.; Fu, Z. A Novel Spatial–Temporal Radial Trefftz Collocation Method for 3D Transient Wave Propagation Analysis with Specified Sound Source Excitation. *Mathematics* **2022**, *10*, 897. <https://doi.org/10.3390/math10060897>

Academic Editor: Efstratios Tzirtzilakis

Received: 25 January 2022

Accepted: 8 March 2022

Published: 11 March 2022

Publisher's Note: MDPI stays neutral with regard to jurisdictional claims in published maps and institutional affiliations.



Copyright: © 2022 by the authors. Licensee MDPI, Basel, Switzerland. This article is an open access article distributed under the terms and conditions of the Creative Commons Attribution (CC BY) license (<https://creativecommons.org/licenses/by/4.0/>).

1. Introduction

As is well known, the phenomenon of wave propagation [1–7] widely exists in various areas of science and engineering, such as acoustics, elastodynamics, electromagnetics, and fluid dynamics. Numerical simulation plays an important role in understanding and mastering the fundamental laws of such wave propagation. Traditional numerical methods [8–10], such as the finite difference method and finite element method (FEM), have been widely used in wave propagation analysis. However, they usually have the problems of low computational efficiency and poor computational accuracy due to the use of universal polynomial functions. To overcome these drawbacks, several basis functions, including wave characteristics, have been introduced, and then a series of semi-analytical numerical methods have been constructed, such as the wave-based method [11], scaled boundary finite element method [12] and boundary element method [13–15], and so on. The aforementioned numerical methods belong to the mesh-based methods, which are sensitive to the mesh quality. To eliminate the effect of mesh generation, a group of meshless methods is developed. Similarly, by introducing the basis functions including the wave characteristics, several boundary-type meshless methods are proposed. They can be divided into two categories: weak-form boundary meshless methods and strong-form boundary meshless methods. The weak-form boundary meshless methods mainly

include the local boundary integral equation method [16], boundary node method [17], hybrid boundary node method [18], boundary face method [19], null-field boundary integral equation method [20], and so on. The strong-form boundary meshless methods mainly include the wave superposition method [21,22], method of fundamental solutions (MFS) [23,24], regularized meshless method [25], boundary distributed source method [26], singular boundary method (SBM) [27–31], collocation Trefftz method (CTM) [32,33], and so on. Due to their simpler form, integral-free and easy-to-use merits, this study focused on the strong-form boundary meshless methods based on the semi-analytical basis functions.

A broader and more challenging problem in wave propagation analysis is the simulation of wave propagation in the time domain. The following three popular approaches have been widely used to treat transient wave propagation problems: (1) Time-stepping methods (TSM) [23,34] transform the transient wave propagation problem into a series of time-independent problems, and the accuracy and stability of this method highly depend on the time-step size. (2) Frequency domain techniques (FDT) [35,36] use the transformation technique to eliminate the time derivative leading to a time-independent equation in the frequency domain, and then employ a numerical inversion scheme to invert the frequency domain solutions back into the time-dependent solutions. The FDT does not require time stepping, and thus avoids the effect of the time step on numerical accuracy. However, for systems with no intrinsic damping and mismatched initial and ending responses, the numerical inversion transformation fails to produce accurate results. This is why in practical calculations often small artificial damping is added to the model. (3) Spatial–temporal semi-analytical basis function methods [37–39] employ the spatial–temporal semi-analytical basis function a priori to satisfy the transient wave equation and then solve it directly. Among these three time-discretization schemes, the first two have been widely used for transient wave propagation analysis; the last one has not been widely used because the time-dependent semi-analytical basis functions are not easy to construct, in particular, the transient wave equation, including the source excitations.

Fortunately, the composite multiple reciprocity method (CMRM) [40] has been proposed and applied to deal with some specified source terms in time-independent nonhomogeneous PDEs. In this study, the CMRM is extended from the spatial domain to the spatial–temporal domain, which transforms the original transient wave propagation problem with a source term into the high-order time-dependent problem without a source term. Then a group of spatial–temporal semi-analytical basis functions and spatial–temporal radial Trefftz functions are derived to satisfy the governing equation of such high-order time-dependent problem in advance. Correspondingly, the so-called spatial–temporal radial Trefftz collocation method (STRTCM) is constructed to solve 3D transient wave equations with specified sound source excitations, which only require the node discretization on the spatial–temporal domain boundaries.

In this paper, a novel spatial–temporal radial Trefftz collocation method is proposed without differential approximation for the temporal derivatives, which may cause the accumulated error to solve the 3D transient wave equations, and the composite multiple reciprocity method is extended from the space domain to the spatial–temporal domain to treat the time-dependent source term. Due to the use of the related spatial–temporal radial Trefftz functions, the proposed STRTCM requires fewer node discretizations to obtain more accurate results. A brief outline of this paper is as follows. In Section 2, the numerical procedure of the spatial–temporal radial Trefftz collocation method for solving 3D transient wave equations with specified sound source excitations is introduced. The efficiency of the proposed method is numerically verified by four benchmark examples in Section 3. In Section 4, several conclusions are drawn based on the present study.

2. Methodology

Considering a transient wave equation in 3D finite domain Ω bounded by Γ , the governing equation of 3D transient wave propagation problem with sound source excitations is stated as follows:

$$\left(\frac{\partial^2}{\partial t^2} - v^2\Delta\right)u(\mathbf{x}, t) = f(\mathbf{x}, t), \quad \mathbf{x} \in \Omega, 0 < t \leq T \tag{1}$$

subjected to the initial conditions

$$u(\mathbf{x}, t)|_{t=0} = u_0, \mathbf{x} \in \Omega \tag{2}$$

$$\frac{\partial u(\mathbf{x}, t)}{\partial t}|_{t=0} = u_1, \mathbf{x} \in \Omega \tag{3}$$

and the Dirichlet boundary condition

$$u(\mathbf{x}, t)|_{\Gamma} = \bar{u}, \quad \mathbf{x} \in \Gamma, 0 < t \leq T. \tag{4}$$

where Δ is the Laplace operator, v denotes the wave speed, T represents the final time instant, u_0, u_1 and \bar{u} are the known functions, and $f(\mathbf{x}, t)$ is the known sound source function.

If the sound source function $f(\mathbf{x}, t) = 0$, then the homogeneous type of Equation (1) is obtained as

$$\left(\frac{\partial^2}{\partial t^2} - v^2\Delta\right)u(\mathbf{x}, t) = 0, \quad \mathbf{x} \in \Omega, 0 < t \leq T. \tag{5}$$

By using the derived spatial-temporal radial Trefftz function [41],

$$G_0(\mathbf{x}, t; \mathbf{s}, \tau) = \left[\cos(v(t - \tau)) + \frac{\sin(v(t - \tau))}{v} \right] \frac{\sin(r(\mathbf{x}, \mathbf{s}))}{r(\mathbf{x}, \mathbf{s})} \tag{6}$$

the approximate solution of Equation (5) by using the spatial-temporal radial Trefftz collocation method can be represented as follows

$$u^0(\mathbf{x}, t) = \sum_{j=1}^{N_S} \alpha_{0j} G_0(\mathbf{x}, t; \mathbf{s}_j, \tau_j) \tag{7}$$

where $r(\mathbf{x}, \mathbf{s}) = \|\mathbf{x} - \mathbf{s}\|_2$ denotes the Euclidean distance between collocation nodes \mathbf{x}_i and source nodes \mathbf{s}_j , t and τ are the time variables corresponding to the collocation nodes \mathbf{x}_i and source nodes \mathbf{s}_j , respectively. $\{\alpha_{0j}\}$ are the unknown coefficients and N_S represents the number of the source node pair $(\mathbf{s}_j, \tau_j) \in \partial(\Omega \times \langle 0, T \rangle)$, in which $\partial(\Omega \times \langle 0, T \rangle) = [\Gamma \times \langle 0, T \rangle] \cup [\Omega \times \{0, T\}]$ stands for the boundaries of the considered spatial-temporal domain $\Omega \times \langle 0, T \rangle$. Substituting expression (7) into the initial conditions (2) (3) and boundary conditions (4), one may have

$$\sum_{j=1}^{N_S} \alpha_{0j} G_0(\mathbf{x}, 0; \mathbf{s}_j, \tau_j) = u_0, \mathbf{x} \in \Omega, t = 0 \tag{8}$$

$$\sum_{j=1}^{N_S} \alpha_{0j} \frac{\partial G_0(\mathbf{x}, 0; \mathbf{s}_j, \tau_j)}{\partial t} = u_1, \mathbf{x} \in \Omega, t = 0 \tag{9}$$

$$\sum_{j=1}^{N_S} \alpha_{0j} G_0(\mathbf{x}, t; \mathbf{s}_j, \tau_j) = \bar{u}, \quad \mathbf{x} \in \Gamma, 0 < t \leq T \tag{10}$$

To determine the unknown coefficient $\{\alpha_{0j}\}$, N collocation node pairs $(x_i, t_i) \in [\Gamma \times \langle 0, T \rangle] \cup [\Omega \times \{0\}]$ are placed on the boundaries of the considered spatial-temporal domain, and then the discretized formulation can be represented as follows

$$\sum_{j=1}^{N_S} \alpha_{0j} G_0(x_i, t_i; \mathbf{s}_j, \tau_j) = u_0, x_i \in \Omega, t_i = 0 \tag{11}$$

$$\sum_{j=1}^{N_S} \alpha_{0j} \frac{\partial G_0(x_i, t_i; \mathbf{s}_j, \tau_j)}{\partial t} = u_1, x_i \in \Omega, t_i = 0 \tag{12}$$

$$\sum_{j=1}^{N_S} \alpha_{0j} G_0(x_i, t_i; \mathbf{s}_j, \tau_j) = \bar{u}, x_i \in \Gamma, 0 < t_i \leq T. \tag{13}$$

which can be also written as the following matrix form

$$\begin{bmatrix} [G_0(x_i, t_i; \mathbf{s}_j, \tau_j)]_{N_i \times N_S} \\ [\frac{\partial G_0(x_i, t_i; \mathbf{s}_j, \tau_j)}{\partial t}]_{N_i \times N_S} \\ [G_0(x_i, t_i; \mathbf{s}_j, \tau_j)]_{N_b N_t \times N_S} \end{bmatrix} [\alpha_{0j}]_{N_S \times 1} = \begin{bmatrix} [u_0]_{N_i \times 1} \\ [u_1]_{N_i \times 1} \\ [\bar{u}]_{N_b N_t \times 1} \end{bmatrix} \tag{14}$$

where $N = 2N_i + N_b N_t$, in which N_i and N_b represent the number of the collocation nodes inside the spatial domain Ω and on the boundary Γ of spatial domain Ω , respectively. The total node number in the spatial domain Ω is $N_{Total} = N_i + N_b$, and N_t represents the number of the collocation nodes along the time axis. If the same set of nodes to the collocation node discretization is used in the source node discretization inside the spatial domain Ω and on the boundary Γ of spatial domain Ω , the resultant matrix in Equation (14) is square due to $N_S = 2N_i + N_b N_t$.

Next, consider 3D transient wave propagation problems (1–4) with the non-zero sound source function $f(x, t)$. The approximate solution can be first divided into two parts, homogeneous solution $u_h(x, t)$ and particular solution $u_p(x, t)$, i.e.,

$$u(x, t) = u_h(x, t) + u_p(x, t) \tag{15}$$

where the particular solution $u_p(x, t)$ is constructed to satisfy the following equation

$$\left(\frac{\partial^2}{\partial t^2} - v^2 \Delta \right) u_p(x, t) = f(x, t) \tag{16}$$

and then the following updated homogeneous problem can be represented by substituting Equations (15) and (16) into the original transient wave propagation problems (1–4),

$$\left\{ \begin{array}{l} \left(\frac{\partial^2}{\partial t^2} - v^2 \Delta \right) u_h(x, t) = 0, x \in \Omega, 0 < t \leq T \\ u_h(x, t) |_{\Gamma} = \bar{u} - u_p \\ u_h(x, t) |_{t=0} = u_0 - u_p \\ \frac{\partial u_h(x)}{\partial t} |_{t=0} = u_1 - \frac{\partial u_p}{\partial t} \end{array} \right. , \tag{17}$$

where the homogeneous solution $u_h(x, t)$ of Equation (17) can be obtained by using the spatial-temporal radial Trefftz collocation method with node discretization on the boundaries of the considered spatial-temporal domain.

To evaluate the particular solution $u_p(x, t)$, the composite multiple reciprocity method (CMRM) is extended from the spatial domain to the spatial-temporal domain. The key issue

is to introduce the different spatial/spatial–temporal differential operators L_1, L_2, \dots, L_M to eliminate the related non-zero sound source function $f(x, t)$ in Equation (16), namely,

$$L_M \cdots L_2 L_1 f(x, t) \cong 0 \tag{18}$$

It should be pointed out that the commonly used differential operators (Laplace, Helmholtz, modified Helmholtz, diffusion equation and wave equation operators) can be chosen as L_1, L_2, \dots, L_M according to the form of $f(x, t)$, which could be the polynomial, exponential and trigonometric functions, or a combination of these functions. For complex functions, e.g., non-smooth functions, a set of discrete measured data or large-gradient functions in the source term $f(x, t)$, we can express the complex functions or a set of discrete measured data by a series representation of polynomial or trigonometric functions, and then Laplace and Helmholtz operators can be chosen as L_1, L_2, \dots, L_M to satisfy Equation (18). In the numerical implementation, the order M is usually finite, or can be determined by a specified truncation error.

Then the particular solution $u_p(x, t)$ can be obtained by solving the following m -order homogeneous equation with $m - 1$ constraint conditions

$$\begin{cases} L_m \cdots L_2 L_1 \Re u_p(x, t) = 0 & (x, t) \in (\Omega \times (0, T]) \\ \vdots \\ L_2 L_1 \Re u_p(x, t) = L_2 L_1 f(x, t) & (x, t) \in \partial(\Omega \times (0, T]) \\ L_1 \Re u_p(x, t) = L_1 f(x, t) & (x, t) \in \partial(\Omega \times (0, T]) \\ \Re u_p(x, t) = f(x, t) & (x, t) \in \partial(\Omega \times (0, T]) \end{cases} \tag{19}$$

where $\Re = (\frac{\partial^2}{\partial t^2} - v^2 \Delta)$ denotes the governing differential operator. Then the particular solution $u_p(x, t)$ can be represented by a linear combination of high-order spatial–temporal radial Trefftz functions $G_1(x, t; \mathbf{s}, \tau), \dots, G_m(x, t; \mathbf{s}, \tau)$, namely,

$$u_p(x, t) = \sum_{k=1}^m \sum_{j=1}^{N_S} \alpha_{kj} G_k(x, t; \mathbf{s}_j, \tau_j) \tag{20}$$

where the high-order spatial–temporal radial Trefftz functions are derived by satisfying the following equations:

$$\begin{cases} L_1 \Re G_1(x, t; \mathbf{s}_j, \tau_j) = 0 \\ \vdots \\ L_m \cdots L_2 L_1 \Re G_m(x, t; \mathbf{s}_j, \tau_j) = 0 \end{cases} \tag{21}$$

Table 1 lists the related radial Trefftz functions for several commonly used spatial/spatial–temporal differential operators.

Table 1. Radial Trefftz functions of some commonly used spatial/spatial–temporal differential operators [41].

L_k	3D
$\Delta + k^2$	$\sin(kr) / (4\pi r)$
$\Delta - k^2$	$\sinh(kr) / (4\pi r)$
$\frac{\partial}{\partial t} - k\Delta$	$\frac{e^{-k(t-\tau)} \sin(r)}{r}$
$\frac{\partial^2}{\partial t^2} - v_k^2 \Delta$	$\left[\cos(v_k(t - \tau)) + \frac{\sin(v_k(t-\tau))}{v_k} \right] \frac{\sin(r)}{r}$

By combining Equations (7), (15) and (20), the approximate solution of 3D transient wave propagation problems (1–4) can be expressed as follows:

$$u(x, t) = \sum_{k=0}^m \sum_{j=1}^{N_s} \alpha_{kj} G_k(x, t; \mathbf{s}_j, \tau_j), \tag{22}$$

By employing Equation (22) to discretize Equations (17) and (19), the unknown coefficients $\{\alpha_{kj}\}_{j=1,2,\dots,N_s}^{k=0,1,\dots,m}$ can be obtained. After that, the numerical solution at any node pair $(x, t) \in [\Omega \times (0, T)]$ can be calculated by using Equation (22).

3. Numerical Results and Discussions

This section presents four benchmark examples of 3D transient wave propagation problems with specified sound source excitations to verify the efficiency of the proposed spatial–temporal radial Trefftz collocation method (STRTCM). To assess the performance of the proposed solver, the following L_2 relative error $Lerr$, relative error $Rerr$ and maximum relative error MRE are adopted as follows:

$$Lerr = \sqrt{\frac{1}{NN} \sum_{n=1}^{NN} \left(\frac{u_{num}(x_n, t) - u_{ana}(x_n, t)}{u_{ana}(x_n, t)} \right)^2} \tag{23}$$

$$Rerr = \left| \frac{u_{num}(x_n, t) - u_{ana}(x_n, t)}{u_{ana}(x_n, t)} \right| \tag{24}$$

$$MRE = \max_{1 \leq n \leq NN} \left| \frac{u_{num}(x_n, t) - u_{ana}(x_n, t)}{u_{ana}(x_n, t)} \right| \tag{25}$$

where $u_{ana}(x_n, t)$ and $u_{num}(x_n, t)$ stand for the analytical solution and the numerical solution on the test nodes $x_n \in \Omega, n = 1, \dots, NN$ at time instant t , respectively. NN denotes the number of test nodes $\{x_n\}$. Unless otherwise specified, the test nodes $\{x_n\}$ are chosen as the same set of the collocation nodes inside 3D spatial domain $\{x_i\} \in \Omega \setminus \Gamma$ and $NN = N_i$ in this study.

Example 1. *Transient wave equation with specified sound source excitation under a unit cube.*

In this example, the efficiency and accuracy of the proposed spatial–temporal radial Trefftz collocation method (STRTCM) in the solution of transient wave equations with the sound source $f(x, t) = -(\sin(x_1) + \cos(x_2) + \sin(x_3)) \cos(\sqrt{2}t)$ under the unit cubic domain $\Omega_1 = \{(x_1, x_2, x_3) | 0 \leq x_1, x_2, x_3 \leq 1\}$ are investigated. The geometry and node distribution are depicted in Figure 1. The governing equation is represented as

$$\left(\frac{\partial^2}{\partial t^2} - v^2 \Delta \right) u(x, t) = -(\sin(x_1) + \cos(x_2) + \sin(x_3)) \cos(\sqrt{2}t), \quad x \in \Omega, \quad 0 < t \leq T, \tag{26}$$

subjected to the initial conditions

$$u(x, t)|_{t=0} = (\sin(x_1) + \cos(x_2) + \sin(x_3)), \quad x \in \Omega, \tag{27}$$

$$\frac{\partial u(x, t)}{\partial t} \Big|_{t=0} = 0, \quad x \in \Omega, \tag{28}$$

and the Dirichlet boundary condition

$$u(x, t) \Big|_{\Gamma} = (\sin(x_1) + \cos(x_2) + \sin(x_3)) \cos(\sqrt{2}t), \quad x \in \Gamma, \quad 0 < t \leq T \tag{29}$$

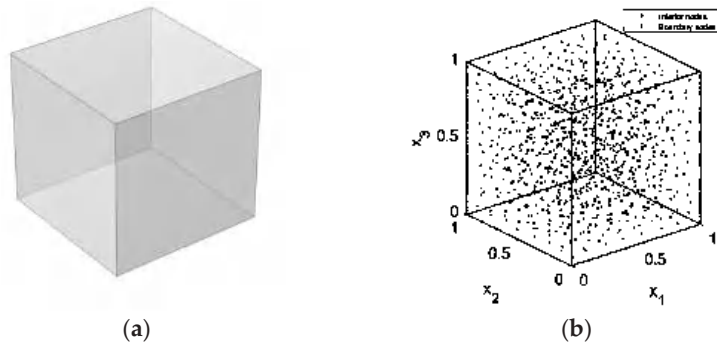


Figure 1. Schematic configurations of the unit cube model. (a) Geometry, (b) Node distribution.

Its analytical solution of Example 1 is

$$u(x, t) = (\sin(x_1) + \cos(x_2) + \sin(x_3)) \cos(\sqrt{2}t) \tag{30}$$

Table 2 presents L_2 relative errors obtained by the proposed STRTCM and COMSOL at different time instants in Example 1. It can be found that under the same node discretization, the proposed STRTCM produces more accurate results with a slight longer computational time than the COMSOL (FEM). Figure 2 shows the numerical errors along with the time evolution by using the proposed STRTCM in Example 1. From Table 2 and Figure 2, it can be observed that the numerical errors may slightly increase with the time evolution. Table 3 presents L_2 relative errors obtained by the proposed STRTCM with different total node numbers, it can be found that with the increasing total node number, the L_2 relative error decreases rapidly and then remains at the same level.

Table 2. Relative errors obtained by the proposed STRTCM and COMSOL at different time instants in Example 1.

	T = 0.1 s	t = 0.5 s	T = 1.0 s	CPU Time
STRTCM	1.92×10^{-7}	6.21×10^{-7}	1.20×10^{-6}	1.76 s
COMSOL	2.14×10^{-3}	2.33×10^{-2}	5.98×10^{-2}	1.00 s

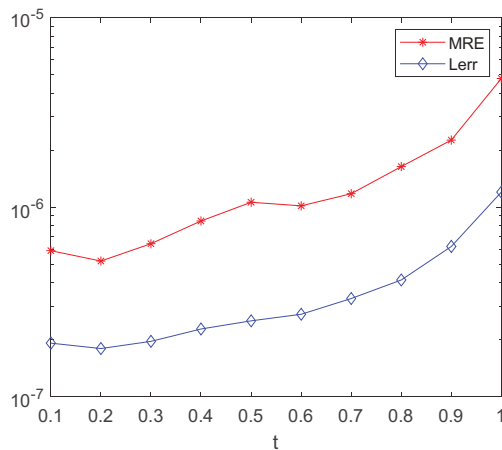


Figure 2. Numerical errors along with the time evolution by using the proposed STRTCM in Example 1.

Table 3. Relative errors obtained by the proposed STRTCM with different total node numbers in Example 1.

N_{Total}	32	81	432	896	1600	4725
L_{err}	1.01×10^{-1}	4.04×10^{-6}	1.30×10^{-6}	1.31×10^{-6}	1.06×10^{-6}	1.34×10^{-6}

For ease of comparison, the same set of discretized nodes are used in both the proposed STRTCM and COMSOL, in which the number of collocation nodes is $N_{Total} = 1023$, the boundary nodes number is $N_b = 374$ and the interior nodes number is $N_i = 649$, and the number of total nodes distributed on the boundaries of spatial–temporal domain is $N = 5421$. It should be mentioned that, based on these collocation nodes, 4892 four-node tetrahedral elements are used in the COMSOL simulation. In addition, some other parameters are set as follows: the wave speed $v = 1.0$ m/s, the final time $T = 1.0$ s, the time interval $dt = 0.1$ s. The annihilation spatial–temporal differential operator $L_1 = \left(\frac{\partial^2}{\partial t^2} - 2\Delta\right)$ is employed to vanish the specified sound source excitation $f(x, t)$ in Equation (26) by using the extended CMRM.

Example 2. Transient wave equation with specified sound source excitation under a circular tube.

This example considers the transient wave equations with the sound source $f(x, t) = -\sin\left(\frac{x_1+x_2+x_3}{\sqrt{3}}\right)\cos(340\sqrt{2}t)$ under the circular tube domain as shown in Figure 3a. The distribution of boundary nodes and interior nodes is depicted in Figure 3b. The governing equation is represented as

$$\left(\frac{\partial^2}{\partial t^2} - v^2\Delta\right)u(x, t) = -\sin\left(\frac{x_1 + x_2 + x_3}{\sqrt{3}}\right)\cos(340\sqrt{2}t), \quad x \in \Omega, \quad 0 < t \leq T, \quad (31)$$

subjected to the initial conditions

$$u(x, t)|_{t=0} = -\sin\left(\frac{x_1 + x_2 + x_3}{\sqrt{3}}\right), \quad x \in \Omega \quad (32)$$

$$\frac{\partial u(x, t)}{\partial t}|_{t=0} = 0, \quad x \in \Omega \quad (33)$$

and the Dirichlet boundary condition

$$u(x, t)|_{\Gamma} = \sin\left(\frac{x_1 + x_2 + x_3}{\sqrt{3}}\right)\cos(340\sqrt{2}t), \quad x \in \Gamma, \quad 0 < t \leq T \quad (34)$$

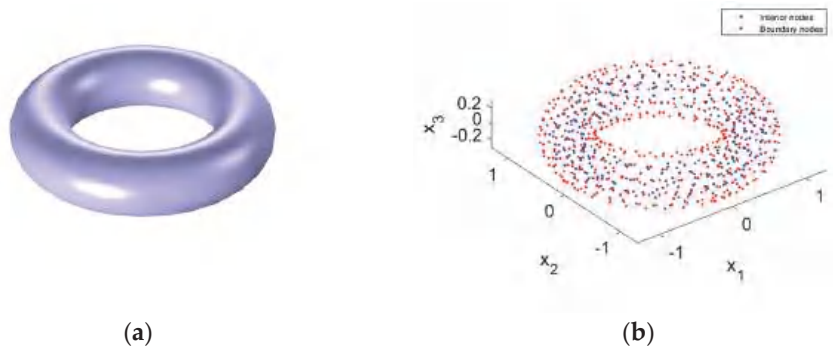


Figure 3. Schematic configurations of the circular tube model. (a) Geometry, (b) Node distribution.

Its analytical solution of Example 2 is

$$u(x, t) = \sin\left(\frac{x_1 + x_2 + x_3}{\sqrt{3}}\right) \cos(340\sqrt{2}t) \tag{35}$$

In the proposed STRTCM implementation, the number of collocation nodes is $N_{Total} = 780$, the boundary nodes number is $N_b = 499$, the interior nodes number is $N_i = 281$, the wave speed is $v = 340$ m/s, the final time instant is $T = 10$ s, and the annihilation spatial-temporal differential operator $L_1 = \left(\frac{\partial^2}{\partial t^2} - 231200\Delta\right)$ is employed to vanish the specified sound source excitation $f(x, t)$ in Equation (31) by using the extended CMRM.

Table 4 presents numerical errors at final time instant $T = 10$ s obtained by using the proposed STRTCM with different time intervals dt in Example 2. From Table 3, it can be found that the proposed STRTCM with different time intervals dt can provide equally accurate results, which reveals that the time interval dt has a slight influence on the numerical accuracy. Figure 4 plots the absolute and relative error distributions at two time instants ($t = 5$ s and 10 s) by using the proposed STRTCM with a large time interval $dt = 5.0$ s. Numerical results given in Figure 4 show that the proposed STRTCM performs very accurate results, even with large time interval $dt = 5.0$ s.

Table 4. Numerical errors at final time instant $T = 10$ s obtained by using the proposed STRTCM with different time intervals dt in Example 2.

dt	0.5 s	1.0 s	2.0 s	2.5 s	5 s	10 s
$Lerr$	1.55×10^{-5}	3.84×10^{-6}	3.76×10^{-6}	2.34×10^{-5}	2.54×10^{-6}	3.23×10^{-5}
MRE	3.14×10^{-5}	9.94×10^{-6}	9.96×10^{-6}	8.98×10^{-5}	9.77×10^{-6}	9.86×10^{-5}

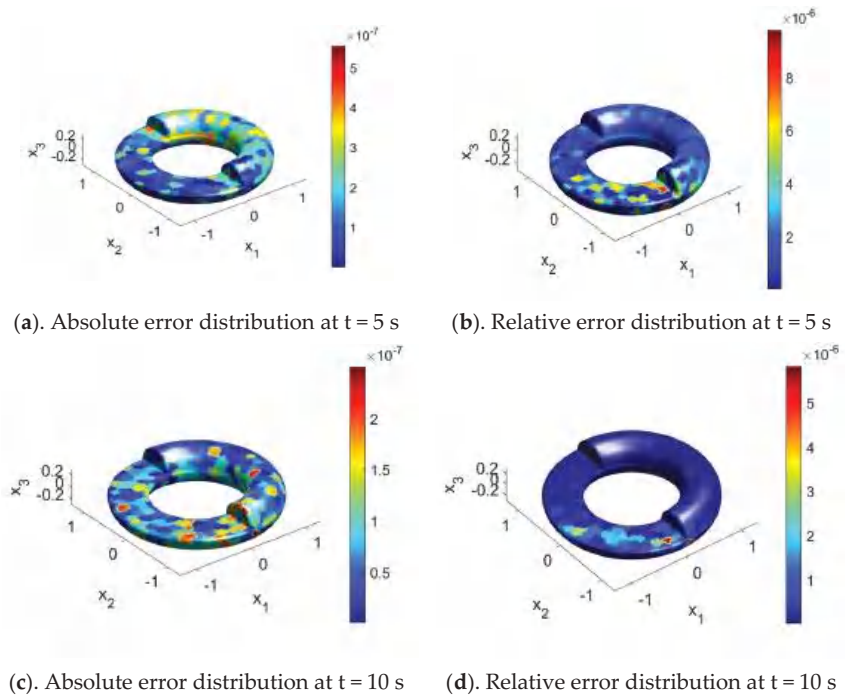


Figure 4. Error distributions at two time instants ($t = 5$ s and 10 s) by using the proposed STRTCM with large time interval $dt = 5.0$ s: (a) absolute error distribution and (b) relative error distribution at $t = 5$ s; (c) absolute error distribution and (d) relative error distribution at $t = 10$ s.

Example 3. Transient wave equation with specified sound source excitation under a room model.

This example considers the transient wave equations with the sound source $f(\mathbf{x}, t) = -(\cos(x_1) + \sin(x_2) + \cos(x_3)) \sin(\sqrt{2}t)$ under the room model [42] with principal dimensions being 5.0 m in length, 4.0 m in width and 3.0 m in height (see Figure 5a). The distributions of boundary nodes and interior nodes are depicted in Figure 5b. The governing equation is represented as

$$\left(\frac{\partial^2}{\partial t^2} - v^2 \Delta\right) u(\mathbf{x}, t) = -(\cos(x_1) + \sin(x_2) + \cos(x_3)) \sin(\sqrt{2}t), \mathbf{x} \in \Omega, 0 < t \leq T \quad (36)$$

subjected to the initial conditions

$$u(\mathbf{x}, t)|_{t=0} = 0, \mathbf{x} \in \Omega \quad (37)$$

$$\frac{\partial u(\mathbf{x}, t)}{\partial t}|_{t=0} = \sqrt{2}(\cos(x_1) + \sin(x_2) + \cos(x_3)) \cos(\sqrt{2}t), \mathbf{x} \in \Omega \quad (38)$$

and the Dirichlet boundary condition

$$u(\mathbf{x}, t)|_{\Gamma} = (\cos(x_1) + \sin(x_2) + \cos(x_3)) \sin(\sqrt{2}t), \mathbf{x} \in \Gamma, 0 < t \leq T \quad (39)$$

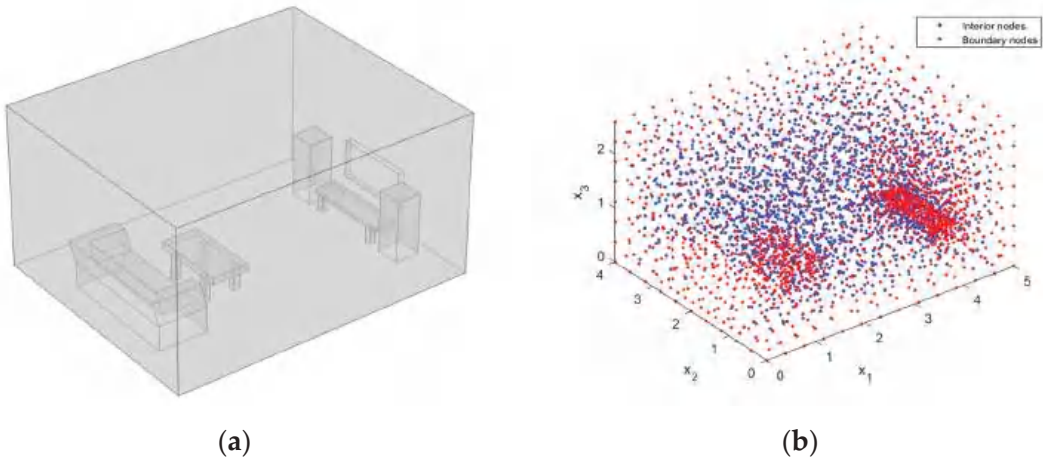


Figure 5. Schematic configurations of the room model. (a) Geometry, (b) Node distribution.

Its analytical solution of Example 3 is

$$u(\mathbf{x}, t) = (\cos(x_1) + \sin(x_2) + \cos(x_3)) \sin(\sqrt{2}t) \quad (40)$$

In the proposed STRTCM implementation, the number of collocation nodes is $N_{Total} = 3588$, the boundary nodes number is $N_b = 1447$, the interior nodes number is $N_i = 2141$, the number of total nodes distributed on the boundaries of the spatial-temporal domain is $N = 17,305$, the wave speed is $v = 1.0$ m/s, the final time instant is $T = 1000$ s, the time interval is $dt = 125$ s, and the annihilation spatial-temporal differential operator $L_1 = \left(\frac{\partial^2}{\partial t^2} - 2\Delta\right)$ is employed to vanish the specified sound source excitation $f(\mathbf{x}, t)$ in Equation (36) by using the extended CMRM.

Figure 6 shows the relative error distributions on the plane $x_3 = 1.5$ at different time instants ($t = 250, 500, 750, 1000$ s) by using the proposed STRTCM with time interval $dt = 125$ s in Example 3. It can be observed that the proposed STRTCM with a large

time interval can still obtain very accurate results in the solution of the transient wave problem under a complicated geometry domain (room model). This is because the semi-analytical spatial-temporal radial Trefftz functions are employed as the basis functions in the proposed STRTCM, which allows the few temporal discretizations to simulate the long-term evolution of the wave propagation.

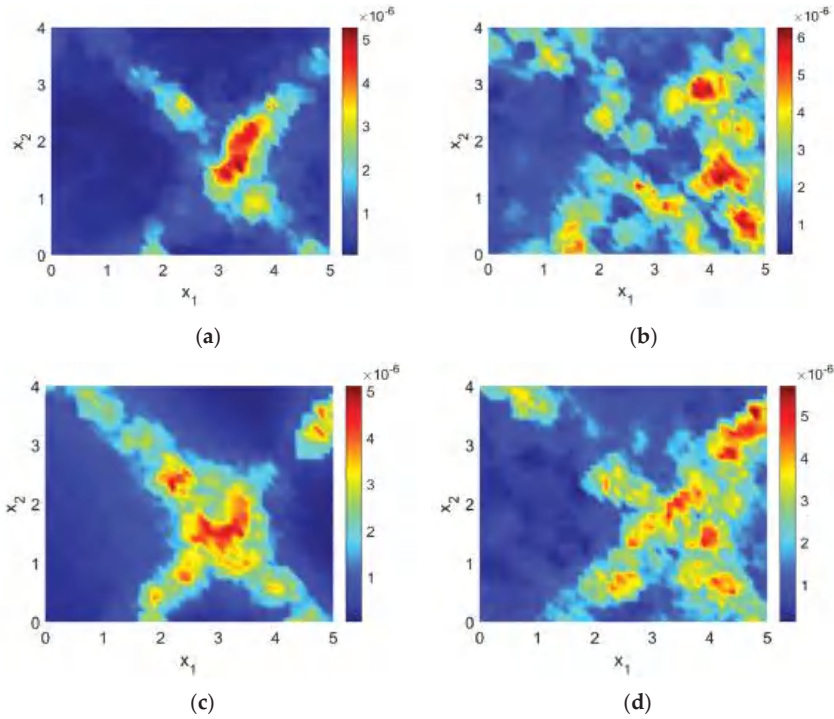


Figure 6. Relative error distributions on the plane $x_3 = 1.5$ at different time instants ((a) $t = 250$, (b) $t = 500$, (c) $t = 750$, (d) $t = 1000$ s) by using the proposed STRTCM with time interval $dt = 125$ s in Example 3.

Example 4. Transient wave equation with specified sound source excitation under a submarine model.

The final example considers the transient wave equations with the sound source $f(x, t) = -(\cos(x_1) + \sin(x_2) + \cos(x_3)) \sin(\sqrt{2}t)$ under the submarine model with the principal dimensions being 15.0 m in length, 4.0 m in width and 6.0 m in height (see Figure 7a). The distribution of boundary nodes and interior nodes are depicted in Figure 7b.

The governing equation is represented as

$$\left(\frac{\partial^2}{\partial t^2} - v^2 \Delta \right) u(x, t) = -(\cos(x_1) + \sin(x_2) + \cos(x_3)) \sin(\sqrt{2}t), \quad x \in \Omega, \quad 0 < t \leq T \quad (41)$$

subjected to the initial conditions

$$u(x, t)|_{t=0} = 0, \quad x \in \Omega \quad (42)$$

$$\frac{\partial u(x, t)}{\partial t} \Big|_{t=0} = \sqrt{2}(\cos(x_1) + \sin(x_2) + \cos(x_3)) \cos(\sqrt{2}t), \quad x \in \Omega \quad (43)$$

and the Dirichlet boundary condition

$$u(\mathbf{x}, t)|_{\Gamma} = (\cos(x_1) + \sin(x_2) + \cos(x_3)) \sin(\sqrt{2}t), \mathbf{x} \in \Gamma, 0 < t \leq T \tag{44}$$

Its analytical solution of Example 4 is

$$u(\mathbf{x}, t) = (\cos(x_1) + \sin(x_2) + \cos(x_3)) \sin(\sqrt{2}t) \tag{45}$$

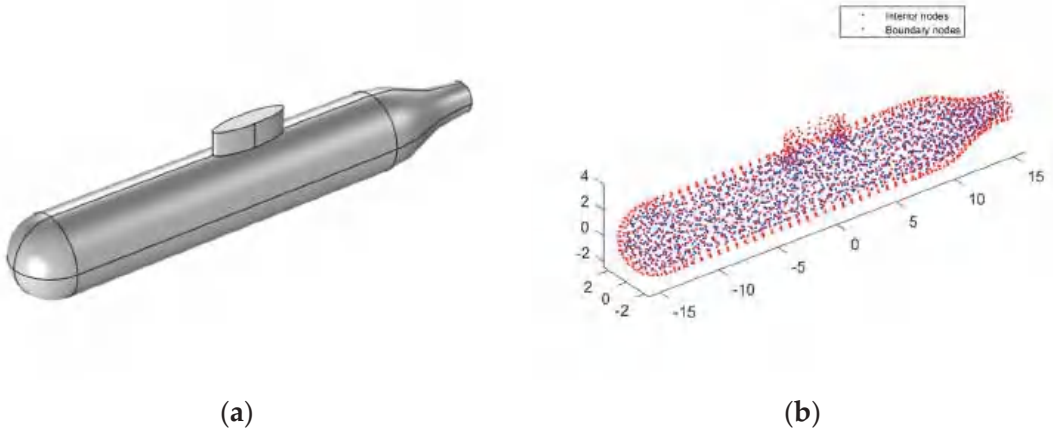


Figure 7. Schematic configurations of the submarine model. (a) Geometry, (b) Node distribution.

In the proposed STRTCM implementation, the number of collocation nodes is $N_{Total} = 2804$, the boundary nodes number is $N_b = 1312$, and the interior nodes number is $N_i = 1492$, the wave speed is $v = 1.0$ m/s, the time interval is $dt = 1$ s, the final time is $T = 10$ s, and the annihilation spatial–temporal differential operator $L_1 = \left(\frac{\partial^2}{\partial t^2} - 2\Delta\right)$ is employed to vanish the specified sound source excitation $f(\mathbf{x}, t)$ in Equation (41) by using the extended CMRM.

By using the proposed STRTCM for Example 4, very accurate results with $Lerr = 4.40 \times 10^{-6}$ can be obtained in 1 min. However, it requires about 9 GB memory storage for getting the results in a large time instant $T = 10$ s. To enhance the ability of the proposed STRTCM for long-time evolution simulation, the entire time interval $[0, 10]$ is divided into NP sub-time intervals $([0, 10/NP], \dots, [10(NP - 1)/NP, 10])$, and the STRTCM is used to solve the problems (41–44) in each sub-time interval in sequence. For each problem in the considered sub-time interval (np) , the initial conditions are updated by using the final solution at the previous sub-time interval $(np - 1)$, $np = 1, \dots, NP$. Table 5 gives the numerical results of Example 4 by using the proposed STRTCM with different numbers of sub-time intervals. It can be found from Table 5 that with the increasing NP , the proposed STRTCM can perform enough accurate results with less computational cost (CPU time and memory storage).

Table 5. Numerical results of Example 4 by using the proposed STRTCM with different numbers of sub-time intervals.

NP	1	2	5	10
CPU time	53.0 s	20.0 s	15.9 s	15.7 s
$Lerr$	4.40×10^{-6}	6.92×10^{-6}	1.39×10^{-5}	5.17×10^{-5}
Memory requirement	9973 MB	5671 MB	4794 MB	4647 MB

4. Conclusions

In this paper, the spatial–temporal radial Trefftz collocation method (STRTCM) is proposed to solve transient wave propagation problems with specified sound source excitations.

To deal with the specified sound source excitations, the extended composite multiple reciprocity method (CMRM) is presented from the spatial domain to the spatial–temporal domain for constructing the high-order homogeneous equation with the related constraint conditions. Then, the particular solution can be obtained by using a linear combination of the related high-order spatial–temporal radial Trefftz functions. Therefore, the proposed STRTCM only requires the node discretization on the boundaries of the spatial–temporal domain in 3D transient wave propagation analysis.

Numerical investigation shows that the proposed STRTCM produces more accurate results with a slight longer computational time than the COMSOL (FEM) under the same node discretization. The time interval dt has a slight influence on the numerical accuracy of the proposed STRTCM. The iterative strategy is feasible to reduce the storage and CPU time. Due to the use of the spatial–temporal radial Trefftz functions, the proposed STRTCM only requires few temporal discretizations to accurately simulate the long-term evolution of the wave propagation.

Overall, it is concluded that the proposed STRTCM could be considered as a competitive alternative for the transient wave problems with specified sound source excitations under 3D complicated structures after further theoretical and numerical investigations. Moreover, it should be mentioned that as the first step, only 3D transient wave propagation with specified sound source excitations is considered in this paper, whose analytical solutions with regular form can be easily derived. The STRTCM for 3D transient wave problems with general sound source excitations is still under our intensive investigation. In addition, the present STRTCM scheme cannot handle the problems with heterogeneous materials because it is a nontrivial task to derive the corresponding semi-analytical basis solutions. For this, combining with the localized collocation scheme [43] and the extended multiple reciprocity method—generalized reciprocity method [44]—may be a good way. These topics are under study and will be reported in a subsequent paper.

Author Contributions: Conceptualization, L.C.; formal analysis, Z.F.; methodology, W.X.; writing—original draft, L.C. All authors contributed equally to writing this article. All authors have read and agreed to the published version of the manuscript.

Funding: This research was funded by the National Natural Science Foundation of China (Grant Nos. 12122205, 11772119), the Six Talent Peaks Project in Jiangsu Province of China (Grant No. 2019-KTHY-009).

Institutional Review Board Statement: Not applicable.

Informed Consent Statement: Not applicable.

Data Availability Statement: Not applicable.

Acknowledgments: The authors thank the anonymous reviewers of this article for their very helpful comments and suggestions to significantly improve the academic quality of this article. The work described in this paper was supported by the National Natural Science Foundation of China (Grant Nos. 12122205, 11772119) and the Six Talent Peaks Project in Jiangsu Province of China (Grant No. 2019-KTHY-009).

Conflicts of Interest: The authors declare no conflict of interest.

Nomenclature

$u(x, t)$	acoustic pressure	$r(x, s)$	distance between source node and colocation node
v	wave speed	$\{\alpha\}$	unknown coefficients
Δ	Laplace operator	N_i	number of interior nodes on spatial domain
$f(x, t)$	spatial-temporal source function	N_b	number of boundary nodes on spatial domain
x	colocation node	N_t	number of colocation nodes along with time axis
s	source node	N_{Total}	number of total nodes on spatial domain
T	final time instant	$G_0(x, t; s, \tau)$	spatial-temporal radial Trefftz function
t	time variable corresponding to colocation node	$u_h(x, t)$	homogeneous solution
τ	time variable corresponding to source node	$u_p(x, t)$	particular solution
u_0, u_1	known functions on boundary	$L_M \cdots L_2 L_1$	differential operators
Ω	computational domain	MRE	maximum absolute error
Γ	boundary of computational domain	$Lerr L_2$	relative error
\mathfrak{R}	partial differential operator matrix	$Rerr$	relative error
N	number of colocation node pairs	NP	numbers of evolution steps
N_S	number of source node pairs		

References

1. Bellis, C.; Lombard, B. Simulating transient wave phenomena in acoustic metamaterials using auxiliary fields. *Wave Motion* **2019**, *86*, 175–194. [CrossRef]
2. Gao, J.; Ma, X.; Zang, J.; Dong, G.; Ma, X.; Zhu, Y.; Zhou, L. Numerical investigation of harbor oscillations induced by focused transient wave groups. *Coast. Eng.* **2020**, *158*, 103670. [CrossRef]
3. Chen, J.; Shou, Y.; Zhou, X. Implementation of the novel perfectly matched layer element for elastodynamic problems in time-domain finite element method. *Soil Dyn. Earthq. Eng.* **2022**, *152*, 107054. [CrossRef]
4. Ghafoor, A.; Haq, S.; Hussain, M.; Kumam, P.; Jan, M.A. Approximate Solutions of Time Fractional Diffusion Wave Models. *Mathematics* **2019**, *7*, 923. [CrossRef]
5. Weng, J.; Liu, X.; Zhou, Y.; Wang, J. A Space-Time Fully Decoupled Wavelet Integral Collocation Method with High-Order Accuracy for a Class of Nonlinear Wave Equations. *Mathematics* **2021**, *9*, 2957. [CrossRef]
6. Qing, H.L.; Gang, Z. Review of PSTD methods for transient electromagnetics. *Int. J. Numer. Model. Electron. Netw. Devices Fields* **2004**, *17*, 299–323. [CrossRef]
7. Fu, Z.J.; Xie, Z.Y.; Ji, S.Y.; Tsai, C.C.; Li, A.L. Meshless generalized finite difference method for water wave interactions with multiple-bottom-seated-cylinder-array structures. *Ocean. Eng.* **2020**, *195*, 106736. [CrossRef]
8. Cohen, G. *Higher-Order Numerical Methods for Transient Wave Equations*; Springer Science & Business Media: Berlin, Germany, 2001.
9. Astley, R.J.; Hamilton, J.A. The stability of infinite element schemes for transient wave problems. *Comput. Methods Appl. Mech. Eng.* **2006**, *195*, 3553–3571. [CrossRef]
10. Chai, Y.; Li, W.; Liu, Z. Analysis of transient wave propagation dynamics using the enriched finite element method with interpolation cover functions. *Appl. Math. Comput.* **2022**, *412*, 126564. [CrossRef]
11. Deckers, E.; Atak, O.; Coox, L.; D'Amico, R.; Devriendt, H.; Jonckheere, S.; Koo, K.; Plumeyers, B.; Vandepitte, D.; Desmet, W. The wave based method: An overview of 15 years of research. *Wave Motion* **2014**, *51*, 550–565. [CrossRef]
12. Chen, D.; Birk, C.; Song, C.; Du, C. A high-order approach for modelling transient wave propagation problems using the scaled boundary finite element method. *Int. J. Numer. Methods Eng.* **2014**, *97*, 937–959. [CrossRef]
13. Demirel, V.; Wang, S. An efficient boundary element method for two-dimensional transient wave propagation problems. *Appl. Math. Model.* **1987**, *11*, 411–416. [CrossRef]
14. Jiang, F.; Chen, L.; Wang, J.; Miao, X.; Chen, H. Topology optimization of multimaterial distribution based on isogeometric boundary element and piecewise constant level set method. *Comput. Methods Appl. Mech. Eng.* **2022**, *390*, 114484. [CrossRef]
15. Jelich, C.; Zhao, W.; Chen, H.; Marburg, S. Fast multipole boundary element method for the acoustic analysis of finite periodic structures. *Comput. Methods Appl. Mech. Eng.* **2022**, *391*, 114528. [CrossRef]
16. Ilati, M.; Dehghan, M. Direct local boundary integral equation method for numerical solution of extended Fisher-Kolmogorov equation. *Eng. Comput.* **2018**, *34*, 203–213. [CrossRef]
17. Li, X.L.; Li, S.L. Meshless boundary node methods for Stokes problems. *Appl. Math. Model.* **2015**, *39*, 1769–1783. [CrossRef]
18. Yan, F.; Jiang, Q.; Bai, G.F.; Li, S.J.; Li, Y.; Qiao, Z.B. Dual reciprocity hybrid boundary node method for nonlinear problems. *Eng. Anal. Bound. Elem.* **2019**, *108*, 385–392. [CrossRef]
19. Zhang, J.M.; Ju, C.M.; Wen, P.H.; Shu, X.M.; Lin, W.C.; Chi, B.T. A dual interpolation boundary face method for 3D elasticity. *Eng. Anal. Bound. Elem.* **2021**, *122*, 102–116. [CrossRef]
20. Chen, J.T.; Kao, S.K.; Hsu, Y.H.; Fan, Y. Scattering problems of the SH Wave by Using the Null-Field Boundary Integral Equation Method. *J. Earthq. Eng.* **2018**, *22*, 1–35. [CrossRef]
21. Ergin, A.A.; Shanker, B.; Michielssen, E. The plane-wave time-domain algorithm for the fast analysis of transient wave phenomena. *IEEE Antennas Propag. Mag.* **1999**, *41*, 39–52. [CrossRef]

22. Geng, L.; Zhang, X.-Z.; Bi, C.-X. Reconstruction of transient vibration and sound radiation of an impacted plate using time domain plane wave superposition method. *J. Sound Vib.* **2015**, *344*, 114–125. [CrossRef]
23. Young, D.L.; Gu, M.H.; Fan, C.M. The time-marching method of fundamental solutions for wave equations. *Eng. Anal. Bound. Elem.* **2009**, *33*, 1411–1425. [CrossRef]
24. Fairweather, G.; Karageorghis, A.; Martin, P.A. The method of fundamental solutions for scattering and radiation problems. *Eng. Anal. Bound. Elem.* **2003**, *27*, 759–769. [CrossRef]
25. Liu, L. Single layer regularized meshless method for three dimensional exterior acoustic problem. *Eng. Anal. Bound. Elem.* **2017**, *77*, 138–144. [CrossRef]
26. Kim, S. An improved boundary distributed source method for two-dimensional Laplace equations. *Eng. Anal. Bound. Elem.* **2013**, *37*, 997–1003. [CrossRef]
27. Chen, W.; Li, J.; Fu, Z.J. Singular boundary method using fund-dependent fundamental solution for scalar wave equations. *Comput. Mech.* **2016**, *58*, 717–730. [CrossRef]
28. Fu, Z.J.; Chen, W.; Wen, P.; Zhang, C. Singular boundary method for wave propagation analysis in periodic structures. *J. Sound Vib.* **2018**, *425*, 170–188. [CrossRef]
29. Fu, Z.J.; Xi, Q.; Li, Y.; Huang, H.; Rabczuk, T. Hybrid FEM–SBM solver for structural vibration induced underwater acoustic radiation in shallow marine environment. *Comput. Methods Appl. Mech. Eng.* **2020**, *369*, 113236. [CrossRef]
30. Qu, W.; Zheng, C.; Zhang, Y.; Gu, Y.; Wang, F. A wideband fast multipole accelerated singular boundary method for three-dimensional acoustic problems. *Comput. Struct.* **2018**, *206*, 82–89. [CrossRef]
31. Fu, Z.-J.; Yang, L.-W.; Xi, Q.; Liu, C.-S. A boundary collocation method for anomalous heat conduction analysis in functionally graded materials. *Comput. Math. Appl.* **2021**, *88*, 91–109. [CrossRef]
32. Li, Z.-C.; Lu, T.-T.; Huang, H.-T.; Cheng, A.H.D. Trefftz, collocation, and other boundary methods—A comparison. *Numer. Methods Partial Differ. Equ.* **2007**, *23*, 93–144. [CrossRef]
33. Liu, C.-S.; Kuo, C.-L. A multiple-direction Trefftz method for solving the multi-dimensional wave equation in an arbitrary spatial domain. *J. Comput. Phys.* **2016**, *321*, 39–54. [CrossRef]
34. Siraj, U.I.; Šarler, B.; Vertnik, R.; Kosec, G. Radial basis function collocation method for the numerical solution of the two-dimensional transient nonlinear coupled Burgers' equations. *Appl. Math. Model.* **2012**, *36*, 1148–1160. [CrossRef]
35. Sun, L.; Wei, X. A frequency domain formulation of the singular boundary method for dynamic analysis of thin elastic plate. *Eng. Anal. Bound. Elem.* **2019**, *98*, 77–87. [CrossRef]
36. Sun, L.; Chen, W.; Cheng, A.H.D. Singular boundary method for 2D dynamic poroelastic problems. *Wave Motion* **2016**, *61*, 40–62. [CrossRef]
37. Huang, Y.; Skandari, M.H.N.; Mohammadzadeh, F.; Tehrani, H.A.; Georgiev, S.G.; Tohidi, E.; Shateyi, S. Space–Time Spectral Collocation Method for Solving Burgers Equations with the Convergence Analysis. *Symmetry* **2019**, *11*, 1439. [CrossRef]
38. Ku, C.-Y.; Hong, L.-D.; Liu, C.-Y. Solving Transient Groundwater Inverse Problems Using Space–Time Collocation Trefftz Method. *Water* **2020**, *12*, 3580. [CrossRef]
39. Rezazadeh, A.; Mahmoudi, M.; Darehmiraki, M. Space–time spectral collocation method for one-dimensional PDE constrained optimisation. *Int. J. Control.* **2020**, *93*, 1231–1241. [CrossRef]
40. Xi, Q.; Fu, Z.-J.; Rabczuk, T. An efficient boundary collocation scheme for transient thermal analysis in large-size-ratio functionally graded materials under heat source load. *Comput. Mech.* **2019**, *64*, 1221–1235. [CrossRef]
41. Chen, W.; Fu, Z.-J.; Chen, C.-S. *Recent Advances in Radial Basis Function Collocation Methods*; Springer: Heidelberg, Germany, 2014.
42. COMSOL. Available online: <https://www.comsol.com/model/full-wave-time-domain-room-acoustics-with-frequency-dependent-impedance-90551> (accessed on 3 March 2022).
43. Xi, Q.; Fu, Z.J.; Wu, W.; Wang, H.; Wang, Y. A novel localized collocation solver based on Trefftz basis for potential-based inverse electromyography. *Appl. Math. Comput.* **2021**, *390*, 125604. [CrossRef]
44. Xi, Q.; Fu, Z.J.; Zhang, C.; Yin, D. An efficient localized Trefftz-based collocation scheme for heat conduction analysis in two kinds of heterogeneous materials under temperature loading. *Comput. Struct.* **2021**, *255*, 106619. [CrossRef]



Article

Localized Boundary Knot Method for Solving Two-Dimensional Inverse Cauchy Problems

Yang Wu¹, Junli Zhang¹, Shuang Ding^{2,3} and Yan-Cheng Liu^{1,*}

¹ School of Civil Engineering and Architecture, Nanchang University, Nanchang 330031, China; wuy_96@outlook.com (Y.W.); zhangjunli_@outlook.com (J.Z.)

² Shanghai Engineering Research Center of Underground Infrastructure Detection and Maintenance Equipment, Shanghai 200092, China; dingshuang525@hotmail.com

³ Shanghai Tongyan Civil Engineering Technology Co., Ltd., Shanghai 200092, China

* Correspondence: yanchengliu1113@gmail.com

Abstract: In this paper, a localized boundary knot method is adopted to solve two-dimensional inverse Cauchy problems, which are controlled by a second-order linear differential equation. The localized boundary knot method is a numerical method based on the local concept of the localization method of the fundamental solution. The approach is formed by combining the classical boundary knot method with the localization method. It has the potential to solve many complex engineering problems. Generally, in an inverse Cauchy problem, there are no boundary conditions in specific boundaries. Additionally, in order to be close to the actual engineering situation, a certain level of noise is added to the known boundary conditions to simulate the measurement error. The localized boundary knot method can be used to solve two-dimensional Cauchy problems more stably and is truly free from mesh and numerical quadrature. In this paper, the stability of the method is verified by using multi-connected domain and simply connected domain examples in Laplace equations.

Keywords: inverse Cauchy problem; Laplace equation; localized boundary knot method; noise; multiply domain

MSC: 65N21

Citation: Wu, Y.; Zhang, J.; Ding, S.; Liu, Y.-C. Localized Boundary Knot Method for Solving Two-Dimensional Inverse Cauchy Problems. *Mathematics* **2022**, *10*, 1324. <https://doi.org/10.3390/math10081324>

Academic Editors: Zhuojia Fu and Yiqian He

Received: 8 March 2022

Accepted: 14 April 2022

Published: 15 April 2022

Publisher's Note: MDPI stays neutral with regard to jurisdictional claims in published maps and institutional affiliations.



Copyright: © 2022 by the authors. Licensee MDPI, Basel, Switzerland. This article is an open access article distributed under the terms and conditions of the Creative Commons Attribution (CC BY) license (<https://creativecommons.org/licenses/by/4.0/>).

1. Introduction

In the engineering field, due to the limitations of engineering measurement technology, some information that is required for engineering calculations can be difficult to obtain. Such problems are called inverse problems. The lack of information about inverse problems can be mainly classified into two modes: the detection of the boundary location and the determination of boundary conditions. Chang, Yei and Shieh (2001) [1] showed that neither the traditional Tikhonov's regularization method, nor the singular value decomposition method can yield an acceptable numerical result for the inverse Cauchy problem of Laplace equations, when the influence matrix is highly ill-posed. In order to obtain sufficiently stable and accurate numerical results for inverse Cauchy problems, different numerical methods have been studied by scholars in previous works.

In order to obtain stable solutions, some mesh-based methods have been widely used to solve inverse problems, including the finite element method (FEM) [2], the finite difference method (FDM) [3] and the boundary element method (BEM) used by Lesnic et al. [4–6]. However, as a mesh-based method, it is still nontrivial of the BEM to generate a well-behaved mesh for complex-shaped surfaces. As a competitor to the mesh-based method, the meshless method has been proposed by researchers to solve inverse Cauchy problems. Similar to the FEM, the domain-type meshless method needs to employ arbitrarily distributed interior and boundary collocations to represent the domain and boundary of the problem. The domain-type meshless methods are the radial basis function method

(RBFCM) and the generalized finite-difference method (GFDM), which are commonly used recently. The RBFCM was proposed by Kansa in 1990 [7,8], after which the selection of its optimal parameters was studied [9–11], and then this method became popular [12]. The GFDM has been applied to inverse problems and is widely used for engineering problems [13–16]. Similar to the BEM, boundary-type methods have the advantages of reducing the calculation dimensions and can easily obtain highly accurate numerical results. Considering their merits, boundary-type methods, including the Trefftz method [17–19], the modified collocation Trefftz method (MCTM) [20,21], the singular boundary method (SBM) [22] and the boundary particle method (BPM) have been widely studied for use in inverse Cauchy problems [23].

It is worth emphasizing that among the boundary-type meshless methods, the method of fundamental solutions (MFS) proposed by Kupradze and Aleksidze in 1964 [24] is the most popular in the application of inverse problems [25,26] due to its high accuracy. Young [27] studied the condition number of MFS in a Cauchy problem, and Fan [28] further extended the scheme to solve a Cauchy problem involving Stokes equations. Despite the popularity of the method, determining the appropriate location of the source nodes is one of the difficulties that the MFS needs to overcome. Therefore, in 2002, Chen and Tanaka [29,30] proposed a boundary-type method with a nonsingular general solution instead of a singular fundamental solution as its basis function, named the boundary knot method (BKM). Since then, the BKM has also been applied to solve different problems [31,32], especially inverse problems [33,34].

In recent years, the concept of localization has been proposed to overcome the problems caused by the full matrix. The localized radial basis function collocation method (LRBFCM) [35–38], the first localized meshless method, was developed from the combination of the localization method and the RBFCM. Then, this method was applied to the study of an inverse Cauchy problem by Chan and Fan in 2013 [39]. After that, in 2019, in order to expand the application of the MFS in large-scale problems, Fan [40] proposed the localized method of fundamental solutions (LMFS) by combining a similar localization concept with MFS. This localized method was used to solve inverse Cauchy problems by Wang [41], who proved its accuracy. In addition, the localized Trefftz method (LTM) and the localized singular boundary method (LSBM) were studied by Liu et al. [42] and Wang et al. [43], respectively. In this paper, the traditional BKM is improved into a localized meshless method, which is called the localized boundary knot method (LBKM). Moreover, large-scale problems that were difficult to solve in the past using the traditional methods can be solved efficiently by the LBKM, and successful tests for solving direct problems can be found in recent works [44,45]. Considering the merits of the LBKM, we take the Laplace equation as the governing equation and discuss the application of the LBKM for the inverse Cauchy problem for the first time.

The structure of this paper can be studied as follows: In the first section, we introduce previous research on the use of numerical methods in inverse problems and discuss their merits and drawbacks. In the second section, we give the details and formulations of the inverse Cauchy problem. In the third section, we illustrate the LBKM calculation process with a specific description. Six numerical examples are shown in the fourth section. Then, the defined errors and numerical results are compared and analyzed. In the last section, the discussion and conclusions about the entire work can be found.

2. Inverse Cauchy Problem

In this paper, we use the localized boundary knot method to solve the two-dimensional Cauchy inverse problem. The core of the problem is that some of the boundary conditions are unknown, so we need to add the overdetermined boundary condition to the known boundary section. The governing equation and boundary conditions are:

$$\nabla^2 U(x, y) = 0, \quad (x, y) \in \Omega, \quad (1)$$

$$U(x, y) = p(x, y), \quad (x, y) \in \Gamma^D, \quad (2)$$

$$U_N = (\nabla U) \cdot \vec{n} = q(x, y), \quad (x, y) \in \Gamma^N, \tag{3}$$

$$U(x, y) = k(x, y), \quad (x, y) \in \Gamma^{os}, \tag{4}$$

$$U_N = (\nabla U) \cdot \vec{n} = d(x, y), \quad (x, y) \in \Gamma^{os}, \tag{5}$$

where $\nabla^2 = \frac{\partial^2}{\partial x^2} + \frac{\partial^2}{\partial y^2}$ is the two-dimensional Laplacian, $U(x, y)$ represents any unknown variable in the field Ω , $\partial\Omega = \Gamma^D \cup \Gamma^N \cup \Gamma^{os} \cup \eta$ is the boundary of the computational domain and we assume that the boundary $\partial\Omega$ consists of two components that are disjointed from each other $\Gamma^{os} \cap \eta = \emptyset$. Γ^D and Γ^N are the Dirichlet boundary condition and the Neumann boundary condition, respectively. Γ^{os} represents the boundary portions with overspecified boundary conditions. η represents the boundary portions without boundary conditions. $\vec{n} = (n_x, n_y)$ is the unit outward normal vector on the boundary. $p(x, y)$ and $q(x, y)$ are the given boundary conditions.

3. Numerical Method

In this study, we used a localized BKM to solve this two-dimensional Cauchy inverse problem, whose governing equation is the Laplace equation. However, the traditional boundary knot method is extended from the method of the fundamental solution, and this study improves the global-type meshless method by changing it into the local type. $N = n_i + n_{b1} + n_{b2}$ is assumed to represent the total number of points to be calculated, where n_i represents the number of internal points, while n_{b1} and n_{b2} represent the points of two kinds of boundary, i.e., Γ^D and Γ^N , respectively. A schematic diagram of the calculation nodes of the localized BKM method is shown in Figure 1a.

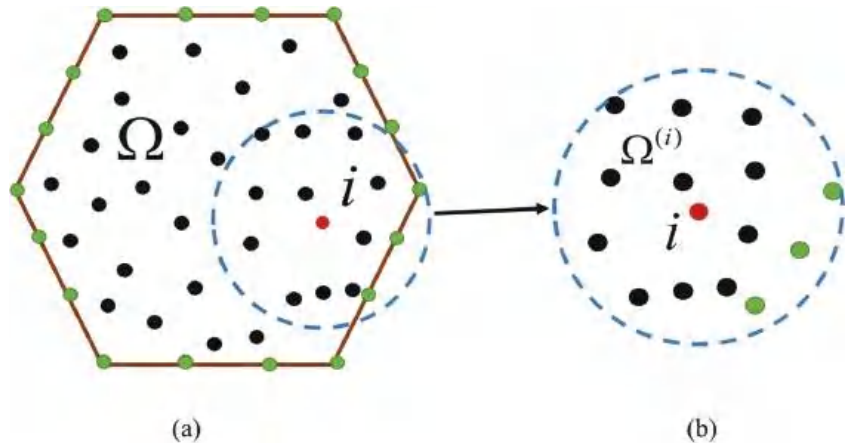


Figure 1. Schematic diagram of the localized boundary knot method. (a) The global domain. (b) The local domain of the i th node.

In the localized BKM method, a subdomain is formed in each node, as shown in Figure 1b. The numerical solution for each subdomain can be approximately expressed as follows:

$$U(x_i, y_i) = \sum_{k=1}^{n_k} \alpha_k G(r_k), \quad x, y \in \Omega, \tag{6}$$

in which α_j stands for the unknown coefficients, and N is the number of adjacent nodes. $G(r_k) = e^{(-c(x^2-y^2))} \cos(2cxy)$ is the BKM basis function, which satisfies the two-dimensional Laplace equation. n_k is the number of nodes in a subdomain. c is the shape parameter. $c = 0.1$ is adopted in the following case. $r = \sqrt{x^2 + y^2}$ ($x = \|x - x_k\|$, $y = \|y - y_k\|$) is the Euclidean distance, where x_k and y_k represent the x and y coordinates of the local node

near the computing node, respectively. The source points are obtained from the nearest computing nodes in the subdomain.

By introducing the spatial coordinates of the nearest nodes into Equation (6), the following system is obtained:

$$U^{(i)} = C\alpha^{(i)}, \tag{7}$$

where $U^{(i)} = [u_1^{(i)} u_2^{(i)} u_3^{(i)} \dots u_N^{(i)}]^T$ is the vector of unknown variables at n_k nodes, and $\alpha^{(i)} = [\alpha_1^{(i)} \alpha_2^{(i)} \alpha_3^{(i)} \dots \alpha_m^{(i)}]^T$ is the vector of the unknown coefficients. C is the coefficient matrix. The unknown coefficients can be expressed by unknown variables:

$$\alpha^{(i)} = C^{-1}U^{(i)}. \tag{8}$$

The inverse matrix C^{-1} is calculated by using the MATLAB command *pinv*, and we set the tolerance to be 10^{-3} – 10^{-4} in this article.

The numerical solution for the i th node can be obtained from introducing the node coordinates of this point into Equation (7). The form is as follows:

$$U_{(i)} = \sum_{k=1}^{n_k} \alpha_k^{(i)} G(r_k) = c^{(i)T} \alpha^{(i)} = c^{(i)T} C^{-1} U^{(i)} = \sum_{k=1}^{n_k} \psi_k^i U_k^i, \tag{9}$$

where $c^{(i)} = [G(r_{i1}) G(r_{i2}) G(r_{i3}) \dots G(r_{in_k})]^T$ is the vector of the fundamental solution at the i th node. $\{\psi_k^{(i)}\}_{k=1}^{n_k}$ represents the weighting coefficients.

In addition, according to Equation (3), we have

$$\left. \frac{\partial U}{\partial x} \right|_i = \sum_{k=1}^{n_k} \alpha_k^{(i)} \left. \frac{\partial}{\partial x} G(r_k) \right|_i = h_x^{(i)T} \alpha^{(i)} = h_x^{(i)T} H^{-1} U^{(i)} = \sum_{k=1}^{n_k} \psi_k^{x(i)} U_k^i, \tag{10}$$

and

$$\left. \frac{\partial U}{\partial y} \right|_i = \sum_{k=1}^{n_k} \alpha_k^{(i)} \left. \frac{\partial}{\partial y} G(r_k) \right|_i = h_y^{(i)T} \alpha^{(i)} = h_y^{(i)T} H^{-1} U^{(i)} = \sum_{k=1}^{n_k} \psi_k^{y(i)} U_k^i, \tag{11}$$

where

$$h_x^{(i)} = \left[\left. \frac{\partial G(r_1)}{\partial x} \right|_i \left. \frac{\partial G(r_2)}{\partial x} \right|_i \left. \frac{\partial G(r_3)}{\partial x} \right|_i \dots \left. \frac{\partial G(r_k)}{\partial x} \right|_i \right]^T, \tag{12}$$

$$h_y^{(i)} = \left[\left. \frac{\partial G(r_1)}{\partial y} \right|_i \left. \frac{\partial G(r_2)}{\partial y} \right|_i \left. \frac{\partial G(r_3)}{\partial y} \right|_i \dots \left. \frac{\partial G(r_k)}{\partial y} \right|_i \right]^T \tag{13}$$

In order to obtain the expression for the Neumann boundary conditions, we can bring Equations (10) and (11) into Equation (3):

$$\frac{\partial U}{\partial n} = \frac{\partial U}{\partial x} n_x + \frac{\partial U}{\partial y} n_y = q(x, y), \quad x, y \in \Gamma^N \tag{14}$$

The linear equations that satisfy the Laplace equation, Dirichlet boundary conditions and Neumann boundary conditions are combined to form sparse linear algebraic equations,

$$\mathbf{A}\mathbf{U} = \mathbf{b}, \tag{15}$$

where $\mathbf{A}_{N \times N}$ is the sparse coefficient matrix that avoids the ill-conditioned matrix, $\mathbf{U} = [U_1 U_2 U_3 \dots U_N]^T$ is the unknown field quantity at every node and \mathbf{b} represents the known conditions. Therefore, \mathbf{U} can be calculated from Equation (15). The localized BKM, which combines BKM with the localization concept of localized MFS, is simple and clear, and the method of determining local points is also novel. In addition, due to the sparse matrix generated in the calculation of linear algebraic equations, it can also be applied to some complex fields.

4. Numerical Results and Comparisons

In this section, we present an analysis and comparison of the results of five cases. These five examples include a simply connected domain and a multi-connected domain. At the same time, different levels of noise are added to the boundary conditions to verify the stability of the localized BKM. For the last case, we carry out the process of forward calculation and then reverse calculation by guessing the analytical solution and relative error of the Laplace equation. In this paper, we compare the analytical solution u_a with the numerical solution U and take the maximum relative error as the index of error analysis.

$$error = \max(|(U - u_a)/u_a|).$$

4.1. Case 1

In the first example, we use a square computing field, as shown in Figure 2. The field is denoted by $\partial\Omega = \Gamma_1 + \Gamma_2 + \Gamma_3 + \Gamma_4$. The boundary corner points are removed, and the internal points and boundary points are evenly distributed throughout the entire calculation domain. The analytical solution of the applied boundary condition is as follows:

$$u_a(x, y) = e^x \cos(y) + e^y \sin(x) + 5, \tag{16}$$

where the Γ_1 boundary is unknown, and the overdetermined boundary conditions (Dirichlet and Neumann) are added to the remaining edges, which are Γ_2, Γ_3 and Γ_4 . Hence, the points on this edge are calculated as interior points. The following parameters are used in this example: $N = 4896, n_b = 272, n_k = 100, c = 0.1$, where N is the number of total nodes, while n_b is the number of boundary nodes.

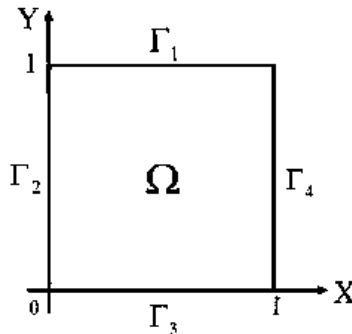


Figure 2. Schematic diagram for case 1.

In order to reflect the real boundary conditions, different levels of noise s are added to the boundary to consider possible errors in advance. Therefore, the boundary conditions take the following forms:

$$u_a = f(x, y)(1 + \frac{s}{100} \times rand), \quad (x, y) \in \Gamma_2 + \Gamma_3 + \Gamma_4, \tag{17}$$

$$\begin{aligned} u_{an} &= [(\nabla u) \cdot \vec{n}](1 + \frac{s}{100} \times rand) = g(x, y)(1 + \frac{s}{100} \times rand) \\ &= [\nabla(u_a(x, y)) \cdot \vec{n}](1 + \frac{s}{100} \times rand), \quad (x, y) \in \Gamma_2 + \Gamma_3 + \Gamma_4 \end{aligned} \tag{18}$$

where s is the percentage of added noise, $rand$ is the random number and the range is $-1 \leq rand \leq 1$. The function $rand$ in MATLAB software is used in this paper to generate the noise.

In order to show the calculation results more clearly, we draw the solution along the boundary Γ_1 , as shown in Figure 3. In this figure, we can see that, although different degrees of noise interference are added, the numerical solution along the boundary Γ_1 is relatively stable, and the line-fitting degree with the analytical solution is relatively high.

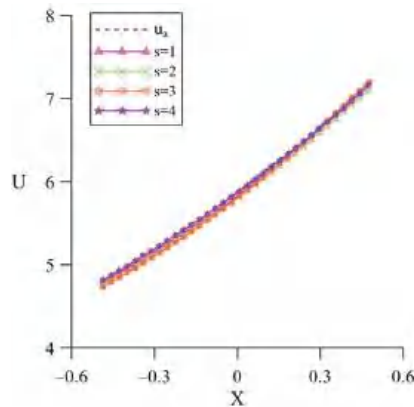


Figure 3. The profiles of numerical solutions along Γ_1 for case 1.

In Figure 4, we use a solid line to represent the internal numerical solution and a dotted line to represent the internal analytical solution. It can be seen from these four pictures that the errors increase with an increase in added noise, but they are all within the acceptable range, and those near the unknown boundary increase significantly. In Table 1, we describe the maximum relative error corresponding to different degrees of disturbance in detail.

Table 1. The maximum relative error obtained by adding different percentages of noise for case 1.

Percentage of Noise	$s = 1$	$s = 2$	$s = 3$	$s = 4$	$s = 5$	$s = 6$	$s = 7$
Maximum relative error	0.00943	0.0136	0.0147	0.0184	0.0189	0.0209	0.0286

4.2. Case 2

In this case, a circle is used as the calculation domain, as shown in Figure 5. The radius of the circle is 1, and half of the boundary is unknown. Γ_1 is an unknown boundary, while Γ_2 is a known boundary. The analytical solution for this example is:

$$u_a = x^2 - y^2 + xy + 5 \tag{19}$$

The following parameters are used in this example: $N = 2809$, $n_b = 200$, $n_k = 100$, $c = 0.1$. The boundary conditions take the following forms:

$$u = f(x, y) \left(1 + \frac{s}{100} \times rand\right) = (x^2 - y^2 + xy + 5) \left(1 + \frac{s}{100} \times rand\right), \quad (x, y) \in \Gamma_2 \tag{20}$$

$$u_{an} = [(\nabla u) \cdot \vec{n}] \left(1 + \frac{s}{100} \times rand\right) = g(x, y) \left(1 + \frac{s}{100} \times rand\right) = [\nabla(x^2 - y^2 + xy + 5) \cdot \vec{n}] \left(1 + \frac{s}{100} \times rand\right), \quad (x, y) \in \Gamma_1 \tag{21}$$

The marked solid lines in Figure 6 represent the numerical results for the unknown boundary Γ_1 under different noise disturbances, and the dotted line represents the analytical solution curve of Γ_1 . Obviously, the numerical solutions are in good agreement with the analytical solution.

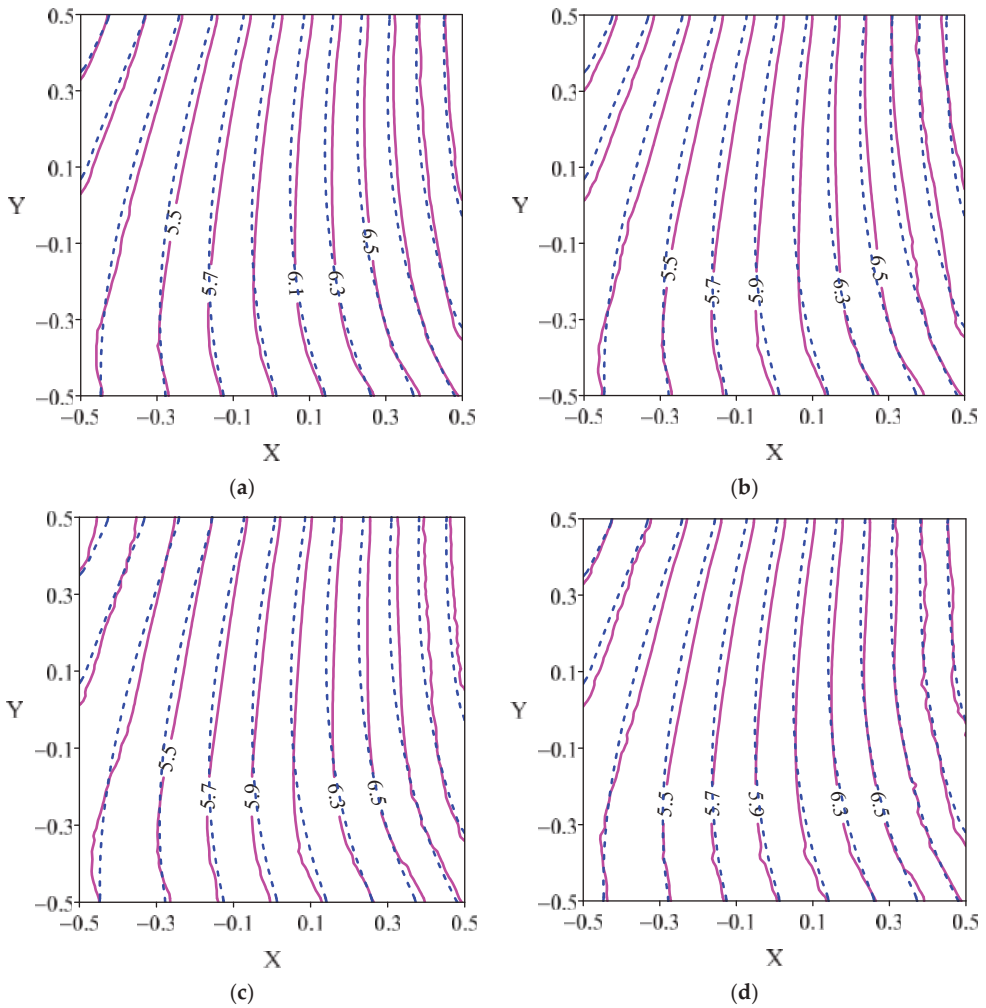


Figure 4. The distributions of numerical (solid lines) and analytical solutions (dashed lines) (a) $s = 1$ (b) $s = 2$ (c) $s = 3$ (d) $s = 4$.

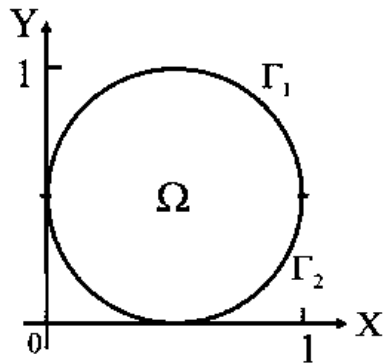


Figure 5. Schematic diagram for case 2.

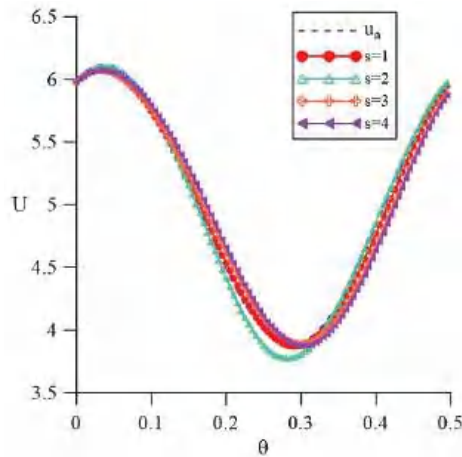


Figure 6. The profiles of numerical solutions along Γ_1 for case 2.

In Table 2, we list the maximum relative error obtained when adding different degrees of noise, and they are all very small. In Figure 7, we draw the internal distributions under different disturbances. The error near the unknown boundary is relatively large but is still within the acceptable range. The analytical solution line and the numerical solution line near the boundary with known boundary conditions fit well.

Table 2. The maximum relative error obtained by adding different percentages of noise for case 2.

Percentage of Noise	s = 1	s = 2	s = 3	s = 4	s = 5	s = 6	s = 7
Maximum relative error	0.0198	0.0272	0.0347	0.0428	0.0504	0.0596	0.0779

4.3. Case 3

For the third inverse problem, we use a doubly connected domain. The computational domain is concentric annular, as shown in Figure 8. The radius of the outer circle is 2, and the radius of the inner circle is 1. The analytical solution for this example is:

$$u_a = \sinh(y) \sin(x) + \cosh(x) \cos(y) + 5. \tag{22}$$

The outer boundary has two kinds of boundary conditions, while the inner boundary has no boundary conditions. The given boundary conditions are obtained by the analytical solution, and the nodes are uniformly distributed in the computational domain and on the boundary. The parameters used in this example are as follows:

$N = 1476$, $n_{b1} = 380$, $n_{b2} = 180$, $n_k = 60$, $c = 0.1$, where n_{b1} and n_{b2} represent the numbers of nodes on the outer and inner boundaries, respectively.

In Table 3, we list the maximum relative errors obtained when adding different degrees of noise, and the errors are also stable. A comparison of the analytical and numerical solutions drawn along the unknown boundary is shown in Figure 9. An internal contour map of different degrees of disturbance is shown in Figure 10. It can be seen from the figures that the numerical solution and the analytical solution are very similar.

Table 3. The maximum relative error obtained by adding different percentages of noise for case 3.

Percentage of Noise	s = 0	s = 1	s = 2	s = 3	s = 4	s = 5	s = 6	s = 7
Maximum relative error	9.45×10^{-5}	0.0056	0.0146	0.0214	0.0274	0.0375	0.0465	0.0654

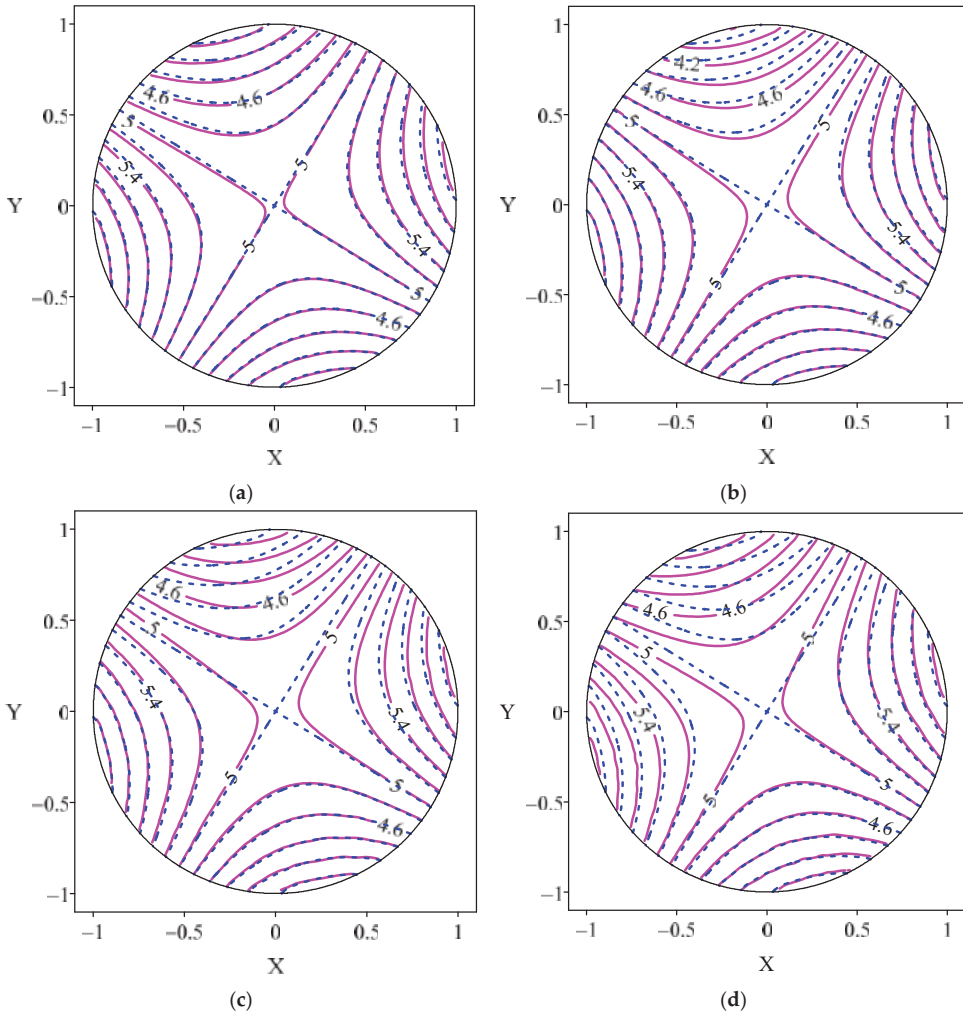


Figure 7. The distributions of numerical (solid lines) and analytical solutions (dashed lines). (a) $s = 1$ (b) $s = 2$ (c) $s = 3$ (d) $s = 4$.

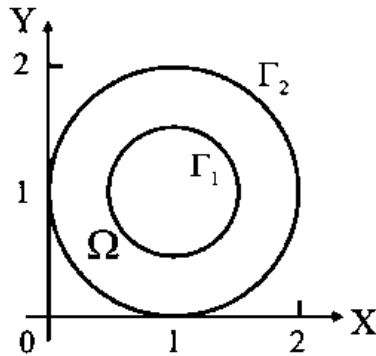


Figure 8. Schematic diagram for case 3.

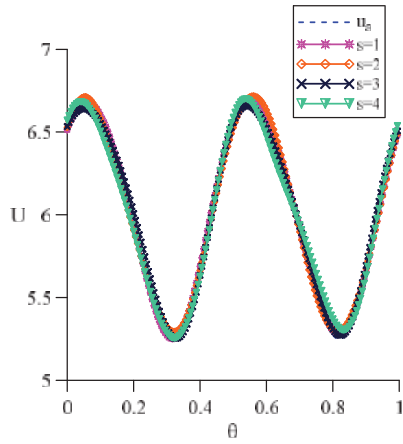


Figure 9. The profiles of numerical solutions along Γ_1 for case 3.

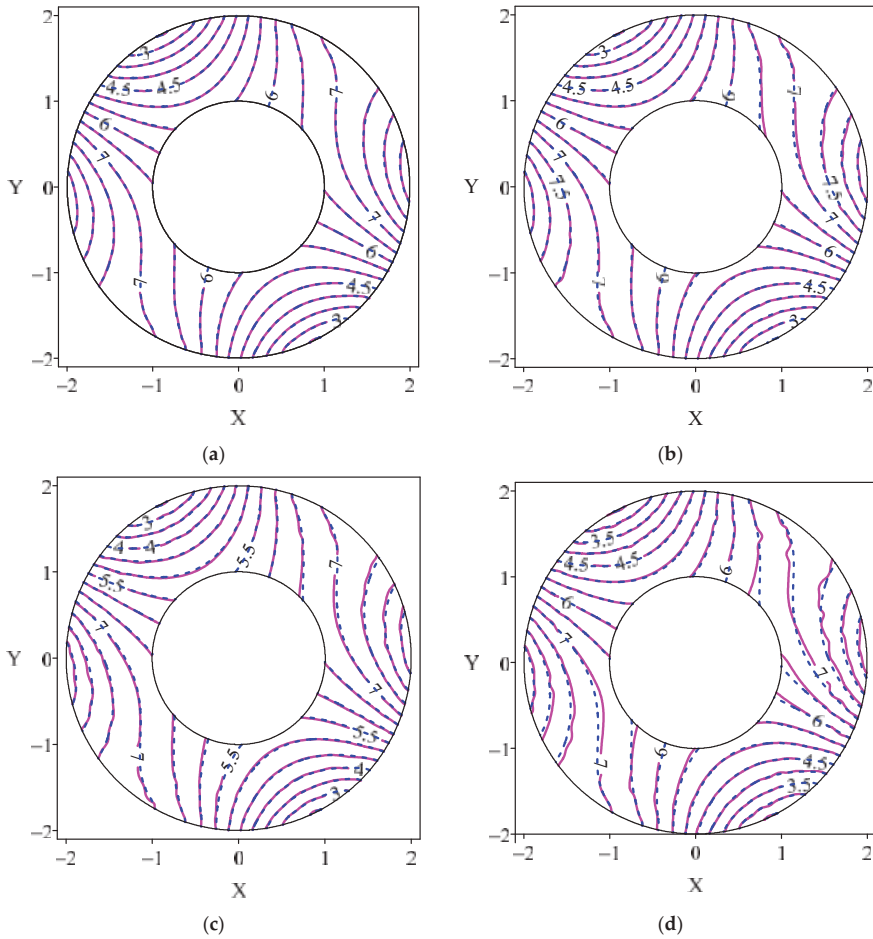


Figure 10. The distributions of numerical (solid lines) and analytical solutions (dashed lines). (a) $s = 1$ (b) $s = 2$ (c) $s = 3$ (d) $s = 4$.

4.4. Case 4

In order to verify the stability of the numerical method, we use the multi-connected domain as the computational domain in this case, as shown in Figure 11. In this case, we take the outer boundary Γ_2 as the unknown boundary and the inner boundary Γ_1 as the known boundary. Therefore, two kinds of boundary conditions are added to the inner boundary. The analytical solution for this example is:

$$u_a = x^2 - y^2 + xy + 5. \tag{23}$$

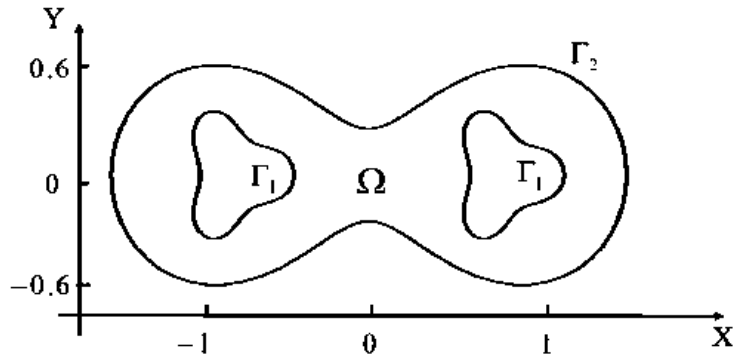


Figure 11. Schematic diagram for case 4.

The boundary of the peanut shape is regarded as an unknown boundary, so the points on the boundary are calculated as internal nodes. Two internal wave elimination blocks are used as known boundaries, and a Dirichlet boundary condition and Neumann boundary condition are added. The parameters used in this example are as follows:

$$N = 3068, n_{b1} = 120, n_{b2} = 102, n_k = 100, c = 0.1.$$

In Table 4, we list the maximum relative errors obtained when adding different degrees of noise, and the errors are also stable. A comparison of the analytical and numerical solutions drawn along the unknown boundary is shown in Figure 12. The data from tables and graphs show that the error is relatively stable and small.

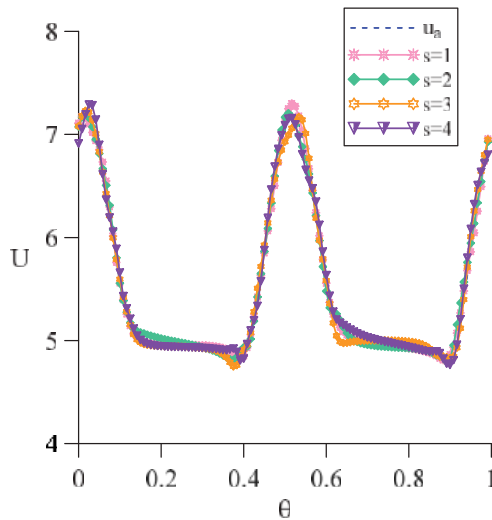


Figure 12. The profiles of numerical solutions along Γ_2 for case 4.

Table 4. The maximum relative error obtained by adding different noise for case 4.

Percentage of Noise	s = 0	s = 1	s = 2	s = 3	s = 4	s = 5	s = 6
Maximum relative error	1.96×10^{-4}	0.0154	0.0196	0.0277	0.0496	0.0590	0.0688

4.5. Case 5

In this example, the geometry of this computational domain is more complex and there are many sharp angles at the boundary; its schematic diagram is shown in Figure 13. The equation for the gear shape is as follows:

$$\partial\Omega = \{ (x, y) | x = \rho(\theta) \cos(\gamma(\theta)), y = \rho(\theta) \sin(\gamma(\theta)) \}, \tag{24}$$

where $\rho(\theta) = 0.2(2 + 0.5 \sin(7\theta))$, $\gamma(\theta) = \theta + 0.5 \sin(\theta)$, $0 \leq \theta \leq 2\pi$.

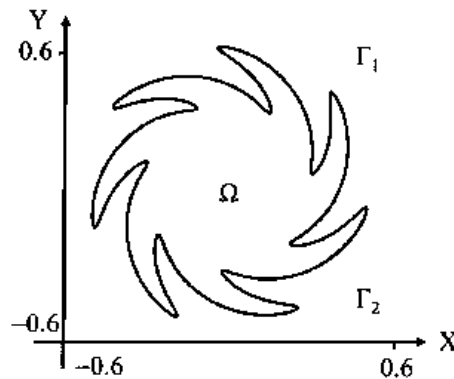


Figure 13. Schematic diagram for case 5.

We set the boundary conditions ($0 < \theta \leq \pi$) of the upper half as unknown and the boundary conditions of the lower half ($\pi < \theta \leq 2\pi$) as given. The Dirichlet boundary condition and the Neumann boundary condition are given by the following analytical solution:

$$u_a = \cos(x)\sinh(y) + x^2 - y^2 + xy + 1 \tag{25}$$

The following parameters are used: $N = 901$, $n_{b1} = 150$, $n_{b2} = 150$, $n_k = 80$, $c = 0.1$.

From Table 5, it can be observed that even the geometry of the boundary is more complex under the setting of different levels of noise, and we can use the localized boundary knot method to solve this inverse Cauchy problem and still maintain a stable level of accuracy. Additionally, Figure 14 clearly shows the error curves obtained by applying different percentages of noise under different numbers of local points. This means that when the number of local points increases, the maximum relative error from the analytical solution approaches a stable state. In Figure 15, we show that (a) $s = 1$, (b) $s = 2$, (c) $s = 3$ and (d) $s = 4$. These four graphs show that there is indeed a certain degree of deviation in the upper half of the lack of boundary information, but the numerical results in the domain are consistent with the analytical solution.

Table 5. The maximum relative error obtained by adding different noise for case 5.

Percentage of Noise	s = 0	s = 1	s = 2	s = 3	s = 4	s = 5	s = 6
Maximum relative error	7.39×10^{-4}	0.0150	0.0265	0.0376	0.0473	0.0582	0.0675

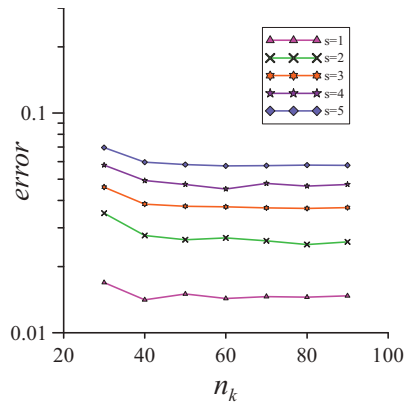


Figure 14. The maximum relative error of the different percentages of noise and local nodes for case 5.

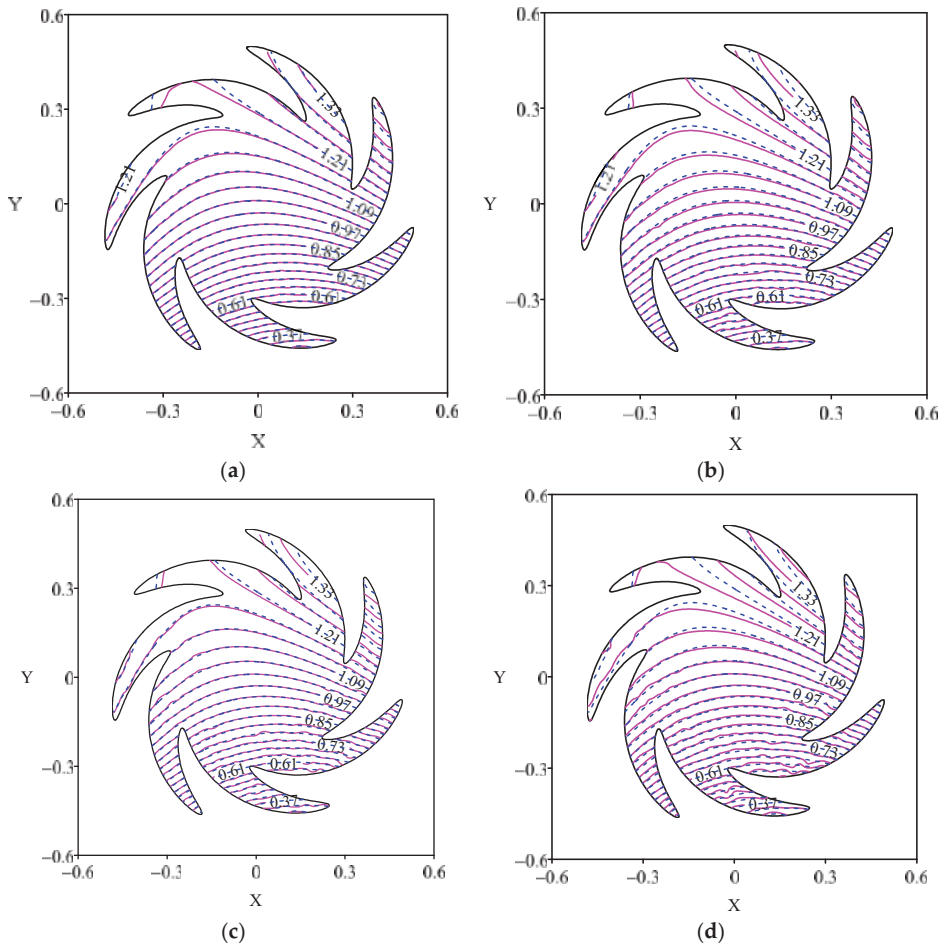


Figure 15. The distributions of numerical (solid lines) and analytical solutions (dashed lines) for Case 6. (a) $s = 1$ (b) $s = 2$ (c) $s = 3$ (d) $s = 4$.

4.6. Case 6

In order to further verify the accuracy of the localized BKM, in the last case, we also use the circle as the calculation domain, where a quarter of the boundary is used as the unknown boundary, namely $\Gamma_2 : (\frac{3}{2}\pi \leq \theta \leq 2\pi)$. We assume that the boundary conditions do not satisfy the analytical solution. This means that the corresponding analytical solution cannot be derived from the governing equations and boundary conditions. The known boundary satisfies the following conditions:

$$u = \left(\sinh\left(\frac{x}{4}\right) + \cosh\left(\frac{x}{4}\right) \right) \cos\left(\frac{y}{4}\right) + 50, \quad x \in \Gamma^D, \tag{26}$$

$$\frac{\partial u(x)}{\partial n} = \frac{1}{10}(x + y), \quad x \in \Gamma^N, \tag{27}$$

In Step 1, the boundary $\Gamma_1 : (0 \leq \theta < \frac{3}{2}\pi)$ is set as the Neumann boundary condition, and the boundary Γ_2 is set as the Dirichlet boundary condition. The numerical solutions $[u]_{\Gamma_1}$ can be solved by LBKM.

In Step 2, Γ_1 is selected as the unknown boundary condition and the numerical solution obtained from the previous solution $[u]_{\Gamma_1}$ and the Neumann boundary condition on the Γ_2 boundary are used. For the first of the step calculation, the total number of nodes is $N = 2949$, the number of boundary nodes is $n_b = 200$, the number of local domain nodes is $n_k = 100$, and the shape parameter is $c = 0.1$, and for the second step of the calculation, the total number of nodes is $N = 4249$, the number of boundary nodes is $n_b = 200$, and the shape parameter is $c = 0.1$. We analyze the maximum relative error of the numerical solutions for Step 1 and Step 2.

To show the stability of the numerical method, we solved this problem by using different numbers of local points, and the maximum relative error is presented in Table 6. The change in maximum relative error corresponding to the change in total points is recorded in Table 7. It can be seen from the test of different total points N and local points n_k that, in the case where the boundary conditions do not use analytical solutions, the maximum relative error can still remain accurate and stable.

Table 6. The maximum relative error obtained with different values of n_k for case 6. ($N = 2949$).

n_k	40	70	100	130	150
Maximum relative error	3.75×10^{-3}	7.22×10^{-4}	1.20×10^{-3}	1.92×10^{-3}	1.72×10^{-3}

Table 7. The maximum relative errors with different values of N for case 6. ($n_k = 100$).

N	3405	4093	5308	6380	8560
Maximum relative error	1.00×10^{-3}	7.89×10^{-4}	9.91×10^{-4}	9.76×10^{-4}	2.14×10^{-3}

The distributions of numerical solutions to the direct and inverse problems are shown in Figure 16. In this figure, it can be seen that numerical solutions to the inverse problem are basically the same as in Step 1, and the maximum relative error is 7.89×10^{-4} .

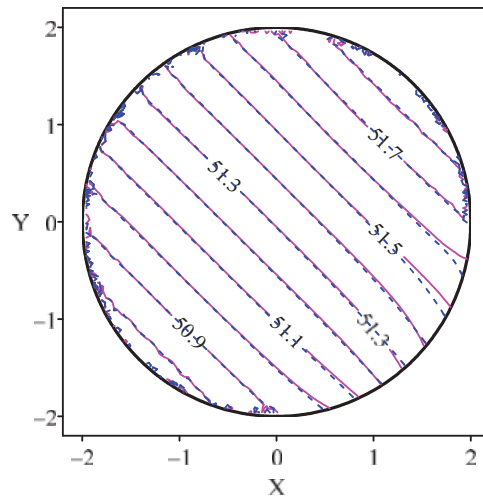


Figure 16. The numerical solution distribution of Step 1 (dashed lines) and Step 2 (solid lines) for case 6. ($N = 4093$, $n_k = 100$).

5. Conclusions

In this paper, the localized BKM was used to solve an inverse Cauchy problem controlled by a two-dimensional Laplace equation. The localized BKM is a method that combines the BKM of the meshless method with the localization concept. This method does not need grid generation and numerical integration, and it eliminates border radius issues with source points. For Cauchy problems, some boundary conditions are not readily available or there are measurement errors, so the numerical simulation is unstable. Therefore, we used the localized BKM to calculate such problems and verify the accuracy of this method.

We presented five examples that illustrate the stability and accuracy of this method for solving inverse problems. With different percentages of noise on the boundaries, the maximum relative error remained stable and within the acceptable range. In particular, in the last case, the direct algorithm was first used to obtain the data with an extra boundary and was then applied to the reverse calculation in the second step. From the results of the error analysis presented in this paper, the localized BKM was shown to be more stable and accurate for solving Cauchy inverse problems.

In the future, the localized BKM will be applied to various mathematical and physical problems as well as more complex problems, for example, moving boundary problems and three-dimensional problems.

Author Contributions: Conceptualization, Y.-C.L.; Data curation, Y.W.; Formal analysis, Y.-C.L. and S.D.; Investigation, J.Z.; Methodology, Y.-C.L.; Software, Y.W. and J.Z.; Supervision, Y.-C.L. and S.D.; Writing—original draft, Y.W. and J.Z.; Writing—review & editing, Y.-C.L. and S.D. All authors have read and agreed to the published version of the manuscript.

Funding: This research received no external funding.

Institutional Review Board Statement: Not applicable.

Informed Consent Statement: Not applicable.

Data Availability Statement: Not applicable.

Conflicts of Interest: The authors declare no conflict of interest.

References

1. Chang, J.R.; Yeih, W.; Shieh, M.H. On the modified Tikhonov's regularization method for the Cauchy problem of the Laplace equation. *J. Mar. Sci. Technol.* **2001**, *9*, 113–121. [CrossRef]
2. Chakib, A.; Nachaoui, A. Convergence analysis for finite element approximation to an inverse Cauchy problem. *Inverse Probl.* **2006**, *22*, 1191–1206. [CrossRef]
3. Vanrumste, B.; Van, H.G.; Van de Walle, R.; D'Havè, M.R.; Lemahieu, I.A.; Boon, P.A. The validation of the finite difference method and reciprocity for solving the inverse problem in EEG dipole source analysis. *Brain Topogr.* **2001**, *14*, 83–92. [CrossRef] [PubMed]
4. Lesnic, D.; Elliott, L.; Ingham, D.B. An iterative boundary element method for solving numerically the Cauchy problem for the Laplace equation. *Eng. Anal. Bound. Elem.* **1997**, *20*, 123–133. [CrossRef]
5. Mera, N.S.; Elliott, L.; Ingham, D.B.; Lesnic, D. An iterative boundary element method for the solution of a Cauchy steady state heat conduction problem. *CMES Comput. Modeling Eng. Sci.* **2000**, *1*, 101–106.
6. Lesnic, D.; Elliott, L.; Ingham, D.B. A alternating boundary element method for solving Cauchy problems for the biharmonic equation. *Inverse Probl. Eng.* **1997**, *5*, 145–168. [CrossRef]
7. Kansa, E.J. Multiquadrics—A scattered data approximation scheme with applications to computational fluid-dynamics—II solutions to parabolic, hyperbolic and elliptic partial differential equations. *Comput. Math. Appl.* **1990**, *19*, 147–161. [CrossRef]
8. Kansa, E.J. Multiquadrics—A scattered data approximation scheme with applications to computational fluid-Dynamics—I surface approximations and partial derivative estimates. *Comput. Math. Appl.* **1990**, *19*, 127–145. [CrossRef]
9. Hardy, R.L. Multiquadric equations of topography and other irregular surfaces. *J. Geophys. Res.* **1971**, *76*, 1905–1915. [CrossRef]
10. Duchon, J. Splines minimizing rotation-invariant semi-norms in Sobolev spaces. In *Constructive Theory of Functions of Several Variables*; Springer: Berlin/Heidelberg, Germany, 1977; pp. 85–100.
11. Franke, R. Scattered data interpolation: Tests of some methods. *Math. Comput.* **1982**, *38*, 181–200.
12. Nam, M.D.; Thanh, T.C. Mesh-free radial basis function network methods with domain decomposition for approximation of functions and numerical solution of Poisson's equations. *Eng. Anal. Bound. Elem.* **2002**, *26*, 133–156.
13. Fan, C.M.; Huang, Y.K.; Li, P.W.; Chiu, C.L. Application of the generalized finite-difference method to inverse biharmonic boundary-value problems. *Numer. Heat Transf. Part B Fundam.* **2014**, *65*, 129–154. [CrossRef]
14. Fan, C.M.; Li, P.W.; Yeih, W. Generalized finite difference method for solving two-dimensional inverse Cauchy problems. *Inverse Probl. Sci. Eng.* **2015**, *23*, 737–759. [CrossRef]
15. Li, P.W.; Fan, C.M.; Grabski, J.K. A meshless generalized finite difference method for solving shallow water equations with the flux limiter technique. *Eng. Anal. Bound. Elem.* **2021**, *131*, 159–173. [CrossRef]
16. Li, P.W. Space–time generalized finite difference nonlinear model for solving unsteady Burgers' equations. *Appl. Math. Lett.* **2021**, *114*, 106896. [CrossRef]
17. Chu, H.F.; Fan, C.M.; Yeih, W.C. Solution of inverse boundary optimization problem by Trefftz method and exponentially convergent scalar homotopy algorithm. *CMC-Comput. Mater. Contin.* **2011**, *24*, 125–142.
18. Liu, C.S.; Atluri, S.N. Numerical solution of the Laplacian Cauchy problem by using a better postconditioning collocation Trefftz method. *Eng. Anal. Bound. Elem.* **2013**, *37*, 74–83. [CrossRef]
19. Kołodziej, J.A.; Grabski, J.K. Many names of the Trefftz method. *Eng. Anal. Bound. Elem.* **2018**, *96*, 169–178. [CrossRef]
20. Liu, C.S. A highly accurate MCTM for direct and inverse problems of biharmonic equation in arbitrary plane domains. *CMES: Comput. Modeling Eng. Sci.* **2008**, *30*, 65–75.
21. Fan, C.M.; Chan, H.F. Modified collocation Trefftz method for the geometry boundary identification problem of heat conduction. *Numer. Heat Transf. Part B Fundam.* **2011**, *59*, 58–75. [CrossRef]
22. Gu, Y.; Chen, W.; Zhang, C.; He, X. A meshless singular boundary method for three-dimensional inverse heat conduction problems in general anisotropic media. *Int. J. Heat Mass Transf.* **2015**, *84*, 91–102. [CrossRef]
23. Fu, Z.; Chen, W.; Zhang, C. Boundary particle method for Cauchy inhomogeneous potential problems. *Inverse Probl. Sci. Eng.* **2012**, *20*, 189–207. [CrossRef]
24. Kupradze, V.D.; Aleksidze, M.A. The method of functional equations for the approximate solution of certain boundary value problems. *USSR Comput. Math. Math. Phys.* **1964**, *4*, 82–126. [CrossRef]
25. Karageorghis, A.; Lesnic, D. Detection of cavities using the method of fundamental solutions. *Inverse Probl. Sci. Eng.* **2009**, *17*, 803–820. [CrossRef]
26. Karageorghis, A.; Lesnic, D.; Marin, L. A survey of applications of the MFS to inverse problems. *Inverse Probl. Sci. Eng.* **2011**, *19*, 309–336. [CrossRef]
27. Young, D.L.; Tsai, C.C.; Chen, C.W.; Fan, C.M. The method of fundamental solutions and condition number analysis for inverse problems of Laplace equation. *Comput. Math. Appl.* **2008**, *55*, 1189–1200. [CrossRef]
28. Fan, C.M.; Li, P.W. Numerical solutions of direct and inverse stokes problems by the method of fundamental solutions and the Laplacian decomposition. *Numer. Heat Transf. Part B Fundam.* **2015**, *68*, 204–223. [CrossRef]
29. Chen, W.; Tanaka, M. A meshless, integration-free, and boundary-only RBF technique. *Comput. Math. Appl.* **2002**, *43*, 379–391. [CrossRef]
30. Chen, W. Symmetric boundary knot method. *Eng. Anal. Bound. Elem.* **2002**, *26*, 489–494. [CrossRef]

31. Jiang, X.; Chen, W.; Chen, C.S. Fast multipole accelerated boundary knot method for inhomogeneous Helmholtz problems. *Eng. Anal. Bound. Elem.* **2013**, *37*, 1239–1243. [CrossRef]
32. Chen, W.; Shen, L.J.; Shen, Z.J.; Yuan, G.W. Boundary knot method for Poisson equations. *Eng. Anal. Bound. Elem.* **2005**, *29*, 756–760. [CrossRef]
33. Jin, B.; Zheng, Y. Boundary knot method for some inverse problems associated with the Helmholtz equation. *Int. J. Numer. Methods Eng.* **2005**, *62*, 1636–1651. [CrossRef]
34. Jin, B.; Zheng, Y. Boundary knot method for the Cauchy problem associated with the inhomogeneous Helmholtz equation. *Eng. Anal. Bound. Elem.* **2005**, *29*, 925–935. [CrossRef]
35. Zheng, H.; Zhang, C.; Wang, Y.; Sladek, J.; Sladek, V. A meshfree local RBF collocation method for anti-plane transverse elastic wave propagation analysis in 2D phononic crystals. *J. Comput. Phys.* **2016**, *305*, 997–1014. [CrossRef]
36. Zheng, H.; Yao, G.; Kuo, L.H.; Li, X. On the selection of a good shape parameter of the localized method of approximated particular solutions. *Adv. Appl. Math. Mech.* **2018**, *10*, 896–911. [CrossRef]
37. Zheng, H.; Yang, Z.; Zhang, C.; Tyrer, M. A local radial basis function collocation method for band structure computation of phononic crystals with scatterers of arbitrary geometry. *Appl. Math. Model.* **2018**, *60*, 447–459. [CrossRef]
38. Zheng, H.; Xiong, J.G.; Yuan, Y.; Wen, P.H. Mixed-mode dynamic stress intensity factors by variation technique with finite block method. *Eng. Anal. Bound. Elem.* **2019**, *106*, 27–33. [CrossRef]
39. Chan, H.F.; Fan, C.M. The local radial basis function collocation method for solving two-dimensional inverse Cauchy problems. *Numer. Heat Transf. Part B Fundam.* **2013**, *63*, 284–303. [CrossRef]
40. Fan, C.M.; Huang, Y.K.; Chen, C.S.; Kuo, S. Localized method of fundamental solutions for solving two-dimensional Laplace and biharmonic equations. *Eng. Anal. Bound. Elem.* **2019**, *101*, 188–197. [CrossRef]
41. Wang, F.; Fan, C.M.; Hua, Q.; Gu, Y. Localized MFS for the inverse Cauchy problems of two-dimensional Laplace and biharmonic equations. *Appl. Math. Comput.* **2020**, *364*, 124658. [CrossRef]
42. Liu, Y.C.; Fan, C.M.; Yeih, W.; Ku, C.Y.; Chu, C.L. Numerical solutions of two-dimensional Laplace and biharmonic equations by the localized Trefftz method. *Comput. Math. Appl.* **2021**, *88*, 120–134. [CrossRef]
43. Wang, F.; Chen, Z.; Li, P.W.; Fan, C.M. Localized singular boundary method for solving Laplace and Helmholtz equations in arbitrary 2D domains. *Eng. Anal. Bound. Elem.* **2021**, *129*, 82–92. [CrossRef]
44. Wang, F.; Gu, Y.; Qu, W.; Zhang, C. Localized boundary knot method and its application to large-scale acoustic problems. *Comput. Methods Appl. Mech. Eng.* **2020**, *361*, 112729. [CrossRef]
45. Xiong, J.; Wen, J.; Liu, Y.C. Localized boundary knot method for solving two-dimensional Laplace and Bi-Harmonic equations. *Mathematics* **2020**, *8*, 1218. [CrossRef]

Article

“Mixed” Meshless Time-Domain Adaptive Algorithm for Solving Elasto-Dynamics Equations

Maoxiong Liao, Tao Zhang * and Jinggu Cao

School of Mechatronical Engineering, Beijing Institute of Technology, Beijing 100081, China; maoxiong.liao@gmail.com (M.L.); 3120190207@bit.edu.cn (J.C.)

* Correspondence: taozhang@bit.edu.cn

Abstract: A time-domain adaptive algorithm was developed for solving elasto-dynamics problems through a mixed meshless local Petrov-Galerkin finite volume method (MLPG5). In this time-adaptive algorithm, each time-dependent variable is interpolated by a time series function of n -order, which is determined by a criterion in each step. The high-order series of expanded variables bring high accuracy in the time domain, especially for the elasto-dynamic equations, which are second-order PDE in the time domain. In the present mixed MLPG5 dynamic formulation, the strains are interpolated independently, as are displacements in the local weak form, which eliminates the expensive differential of the shape function. In the traditional MLPG5, both shape function and its derivative for each node need to be calculated. By taking the Heaviside function as the test function, the local domain integration of stiffness matrix is avoided. Several numerical examples, including the comparison of our method, the MLPG5–Newmark method and FEM (ANSYS) are given to demonstrate the advantages of the presented method: (1) a large time step can be used in solving a elasto-dynamics problem; (2) computational efficiency and accuracy are improved in both space and time; (3) smaller support sizes can be used in the mixed MLPG5.

Keywords: meshless local Petrov-Galerkin approach (MLPG); finite volume methods; mixed methods; adaptive algorithm; time-domain; moving least squares (MLS)

MSC: 74H15

Citation: Liao, M.; Zhang, T.; Cao, J. “Mixed” Meshless Time-Domain Adaptive Algorithm for Solving Elasto-Dynamics Equations. *Mathematics* **2022**, *10*, 1722. <https://doi.org/10.3390/math10101722>

Academic Editors: Zhuojia Fu, Yiqian He and Hui Zheng

Received: 16 March 2022

Accepted: 13 May 2022

Published: 18 May 2022

Publisher’s Note: MDPI stays neutral with regard to jurisdictional claims in published maps and institutional affiliations.



Copyright: © 2022 by the authors. Licensee MDPI, Basel, Switzerland. This article is an open access article distributed under the terms and conditions of the Creative Commons Attribution (CC BY) license (<https://creativecommons.org/licenses/by/4.0/>).

1. Introduction

Structural vibration analysis is an important system dynamics problem in engineering. This dynamics problem is governed by partial differential equations of elasto-dynamics associated with a group of boundary conditions and initial conditions. The elasto-dynamics equation is a second-order PDE in both time and space domains. Exact analyses are usually very difficult, and only few analytical solutions are obtained [1]. Therefore, numerical methods have been developed to solve these complex problems, such as the finite difference method (FDM) [2], the stepwise integration method [3], the Newmark method [4], the Wilson- θ method and the Houbolt method [5] for the time domain; and the FDM [6], the finite element method (FEM) [7], the boundary element method (BEM) [8–11], the differential quadrature method (DQM) [12] and the meshless methods (MMs) [2] for the space domain.

Since the dynamics equation of vibration is a high-order partial differential equation in the time domain, many efforts have been made studying the time-domain methods [13]. Thus, the methods that are commonly used in solving vibration problems can be divided into two categories: mode superposition methods and direct integration methods. In a mode superposition method, the computational cost comes from solving the n -order generalized eigenvalue problem. If the structure vibrates in a short period, this method is less efficient than a direct integration method. In contrast, if the vibration lasts for some time, it is more effective to use the mode superposition method. In the direct integration

method, the dynamics equation is directly solved by integration of, e.g., the FDM [2], the Newmark method [4], the Wilson- θ method or the Houbolt method [5]. In these methods, the computational cost in one time step is proportional to the product of the freedom degrees and the square of the average bandwidth of the matrix. All variables are usually constant or linear in every time step, which may lead to inefficient calculation, incomplete accuracy and even divergent results if the time step is selected improperly [14].

To improve the computing accuracy and reduce the error caused by an improper time step size, the time-domain adaptive algorithm was proposed by Haitian. Y. It is an unconditionally stable direct integration method [15]. Differently from the difference method [16], all the time-dependent variables are expanded into series in discrete time steps, and the expansion coefficients can be obtained by solving the recursive equation. Therefore, the variables in each discrete time step can be more accurately described without any assumptions made for nonlinearity. Since the computing accuracy can be controlled by the truncation error, the time step size can be freely selected in a large range. This means large time steps are allowed in the time domain. This method has been successfully used together with FEM in a large time step and has shown advantages in terms of calculation accuracy [17].

Besides the discretization in the time domain, the elasto-dynamics equations also need to be discretized in the space domain. Although the FEM is the most widely used method for structure vibration analysis in engineering, it still encounters many challenges due to the mesh distortion and remeshing when solving large deformation problems, such as high-speed impact, dynamic crack propagation and strain localization [18]. However, these disadvantages of the FEM can be avoided in MMs, as they do not need elements. Over the past two decades, some efforts were devoted to solving the elasto-dynamics equations with MMs [2].

Speaking of MMs, Atluri proposed the meshless local Petrov-Galerkin Method (MLPG) to avoid the background mesh [19]. In this method, the idea of eliminating residuals in the subdomain was firstly proposed. When combined with the moving least squares (MLS) approximation, a true meshless method is realized which does not need interpolation mesh or integral mesh [20]. Since the MLPG method establishes a residual equation on each subdomain separately, the equations from different subdomains are relatively independent, so different weighted residual methods can be easily mixed and used. Additionally, it provides a good platform for the coupling of various methods [21]. Nowadays, the MLPG is a general term for a series of methods (MLPG1–MLPG6) [22]. Nevertheless, MLPG has the problem of low efficiency. An effective way to overcome this shortcoming is to eliminate or simplify the domain integral in the stiffness matrix. In the above six methods, MLPG2, MLPG4 and MLPG5 have no domain integrals. However, MLPG2 relies too much on the configuration of nodes, and MLPG4 has singular integrals. Only MLPG5 includes neither domain integration in the stiffness matrix nor singularity integration, along with only local boundary integrals. Therefore, the MLPG5 is an attractive method that has high computational efficiency [23]. In this paper, MLPG5 is developed for solving elasto-dynamics equations through a “mixed” approach. Independent meshless approximations are used for both strains and displacements. The strain-displacement compatibility is enforced at nodal points by using the collocation method; thus, the independent nodal strains are expressed in terms of nodal displacements. The “mixed” approach eliminates the expensive process of differentiating the shape function, which greatly increases the computational efficiency.

In this paper, attention is devoted to the meshless time-domain adaptive method for structural vibration analyses of two-dimensional solids. Local weak forms are developed using the weighted residual method from the elasto-dynamics equations. In Section 2, the MLS approximation is introduced to establish shape functions for a set of regularly or randomly distributed nodes, and the Heaviside function is used as a test function. In Section 3, all the time related-variables are expanded in every time step, and then the spatiotemporally coupled dynamics equations are converted into a series of recursively

solved spatial problems. In Section 4, the validity and accuracy of the proposed method are verified by several numerical examples.

2. Moving Least Square (MLS) Approximation

The moving least square (MLS) interpolation is generally considered to be one of the best schemes with which to interpolate random data with a reasonable accuracy, because of its completeness, robustness and continuity [24]. In this section, a briefing of MLS approximation is given. Consider a local sub-domain Ω_s , which is the neighborhood of a point $\mathbf{X} = [x, y]$. The distribution of a function u can be approximated, over a number of scattered local points $\{x_i\}$, ($i = 1, 2, \dots, n$), as

$$u(\mathbf{X}) \approx u^h(\mathbf{X}) = \sum_{j=1}^m p_j(\mathbf{X})a_j(\mathbf{X}) = \mathbf{p}^T(\mathbf{X})\mathbf{a}(\mathbf{X}) \tag{1}$$

where $\mathbf{p}(\mathbf{X})$ is a monomial basis function of order m . In two dimensions, it is given by

$$\mathbf{p}^T(\mathbf{X}) = [1, x, y, x^2, xy, y^2, \dots] \tag{2}$$

The vector $\mathbf{a}(\mathbf{X})$ containing coefficients are functions of the global Cartesian coordinates, depending on the monomial basis. They are determined by minimizing a weighted discrete L_2 norm, defined as:

$$J = \sum_{i=1}^n \hat{W}(\mathbf{X} - \mathbf{X}_i) [\mathbf{p}^T(\mathbf{X}_i)\mathbf{a}(\mathbf{X}) - u_i]^2 \tag{3}$$

where \hat{W} are the weight functions and u_i are the fictitious nodal values.

The stationarity of J in Equation (3) with respect to $\mathbf{a}(\mathbf{X})$ leads to the following relationship:

$$\mathbf{a}(\mathbf{X}) = \mathbf{A}^{-1}(\mathbf{X})\mathbf{B}(\mathbf{X})\mathbf{U}_s \tag{4}$$

Substituting $\mathbf{a}(\mathbf{X})$ into Equation (1), we have

$$u^h(\mathbf{X}) = \sum_{i=1}^n \phi_i(\mathbf{X})u_i \tag{5}$$

where the MLS shape function $\phi_i(\mathbf{X})$ can be defined as:

$$\phi_i(\mathbf{X}) = \sum_{j=1}^m p_j(\mathbf{X})\left(\mathbf{A}^{-1}(\mathbf{X})\mathbf{B}(\mathbf{X})\right)_{ji} = \mathbf{p}^T(\mathbf{X})\left(\mathbf{A}^{-1}\mathbf{B}\right)_i \tag{6}$$

where $\mathbf{A}(\mathbf{x})$ and $\mathbf{B}(\mathbf{x})$ are defined by

$$\mathbf{A}(\mathbf{X}) = \sum_{i=1}^n \hat{W}(\mathbf{X} - \mathbf{X}_i)p(\mathbf{X}_i)\mathbf{p}(\mathbf{X})\mathbf{p}^T(\mathbf{X}_i) = \sum_{i=1}^n \hat{W}(\mathbf{X} - \mathbf{X}_i) \begin{bmatrix} 1 & x_i & y_i \\ x_i & x_i^2 & x_i y_i \\ y_i & x_i y_i & y_i^2 \end{bmatrix} \tag{7}$$

$$\mathbf{B}(\mathbf{X}) = [W_1(\mathbf{X})\mathbf{p}(\mathbf{X}_1), W_2(\mathbf{X})\mathbf{p}(\mathbf{X}_2), \dots, W_n(\mathbf{X})\mathbf{p}(\mathbf{X}_n)] \tag{8}$$

The weight function is very important for the MLS interpolation, because the smoothness of the shape function and its derivatives depends on the order of the weight function. In two-dimensional problems, discontinuities in derivatives can be produced if the order of the spline is not sufficient, and unwanted oscillations in nodal shape functions are produced when a high order of spline function is used. It has been found that the best nodal shape

function and its first derivative come from 4th order spline function [25]. Thus, in this paper, the following 4-order spline function is used:

$$\hat{W}_i(\mathbf{X}) = \begin{cases} 1 - 6\left(\frac{d_i}{r_w}\right)^2 + 8\left(\frac{d_i}{r_w}\right)^3 - 3\left(\frac{d_i}{r_w}\right)^4 & 0 \leq d_i \leq r_w \\ 0 & d_i > r_w \end{cases} \quad (9)$$

where $d_i = |x_Q - x_i|$ is the distance from node x_i to the sampling point x_Q , and r_w is the support size for the weight function.

3. Recursive Governing Equations

3.1. Recursive Elasto-Dynamics Equations

Consider a linear elastic body in a 2D domain Ω , with a boundary Γ , shown in Figure 1. The solid is assumed to undergo infinitesimal deformations. The governing differential equation for small displacement elasto-dynamics can be written as:

$$\sigma_{ij,j} + b_i - \rho \ddot{u}_i - c \dot{u}_i = 0; \quad \sigma_{ij} = \sigma_{ji} \quad (10)$$

where σ_{ij} is the stress tensor, which corresponds to the displacement field u_i ; b_i is the body force; ρ is the mass density; c is the damping coefficient; $\dot{u}_i = \frac{\partial u_i}{\partial t}$ is the velocity; $\ddot{u}_i = \frac{\partial^2 u_i}{\partial t^2}$ is the acceleration.

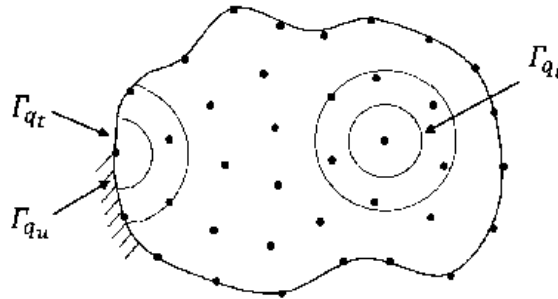


Figure 1. Local domains and boundaries of MLPG.

The boundary conditions are given as follows,

$$u_i = \bar{u}_i \quad \text{on } \Gamma_u \quad (11)$$

$$t_i \equiv n_j \sigma_{ij} = \bar{p}_i \quad \text{on } \Gamma_t \quad (12)$$

where \bar{u}_i and \bar{t}_i are the prescribed displacements and tractions, respectively, on the displacement boundary Γ_u and on the traction boundary Γ_t ; and n_i is the unit outward normal to the boundary Γ . The initial conditions are defined by

$$\mathbf{u}(\mathbf{X}, t_0) = \mathbf{u}_{in}(\mathbf{X}) \quad \mathbf{X} \in \Omega \quad (13)$$

$$\dot{\mathbf{u}}(\mathbf{X}, t_0) = \mathbf{v}_{in}(\mathbf{X}) \quad \mathbf{X} \in \Omega \quad (14)$$

With \mathbf{u}_{in} and \mathbf{v}_{in} being the initial displacements and velocities at the initial time t_0 , respectively.

To improve the computing accuracy, exploiting a discretized expanding technique is of interest. At each discretized time subdomain, all variables can be described as

$$\sigma = \sum_{m=0} \sigma_m s^m \quad (15)$$

$$\varepsilon = \sum_{m=0} \varepsilon_m s^m \tag{16}$$

$$c = \sum_{m=0} c_m s^m \tag{17}$$

$$b = \sum_{m=0} b_m s^m \tag{18}$$

$$u = \sum_{m=0} u_m s^m \tag{19}$$

$$\tilde{u} = \sum_{m=0} \tilde{u}_m s^m \tag{20}$$

$$\tilde{p} = \sum_{m=0} \tilde{p}_m s^m \tag{21}$$

$$s = \frac{t - t_{k-1}}{T_k} \tag{22}$$

where t_{k-1} and T_k represent the beginning time and size of time step, respectively; \tilde{u} and \tilde{p} represent the prescribed displacement and traction on the boundary, respectively; and $\sigma_m, \varepsilon_m, c_m, b_m, u_m, \tilde{u}_m, p_m$ and \tilde{p}_m are the expanding coefficients of $\sigma, \varepsilon, c, b, u, \tilde{u}, p$ and \tilde{p} , respectively.

The derivative with respect to t can be written in the form

$$\frac{d}{dt} = \frac{1}{T_k} \frac{d}{ds} \tag{23}$$

Substitute Equations (15), (18) and (19) into Equation (10), and obtain

$$\sum_{m=0} \sigma_{mij,j} s^m + \sum_{m=0} b_{mi} s^m - \rho \sum_{m=0} \frac{(m+2)(m+1)}{T_k^2} u_{m+2i} s^m - c \sum_{m=0} \frac{m+1}{T_k} u_{m+1i} s^m = 0 \tag{24}$$

Equate every power of $s^m, m = 1, 2, 3, \dots$, and obtain

$$\sigma_{mij,j} + b_{mi} - \rho \frac{(m+2)(m+1)}{T_k^2} u_{m+2i} - c \frac{m+1}{T_k} u_{m+1i} = 0 \tag{25}$$

Equation (25) is the recursive governing equation by the time-domain adaptive method.

In the first time step, u_0 and u_1 are the initial conditions of displacement u and velocity \dot{u} , which can be described as:

$$u_0 = u(X, 0) \tag{26}$$

$$u_1 = \dot{u}(X, 0) T_k \tag{27}$$

Then, u_m can be obtained by solving Equation (37) iteratively. In the $(m + 1)$ th time step, the displacement and velocity can be obtained by:

$$u_{n+1} = \sum_{m=0}^n u_{m_k} \tag{28}$$

$$\dot{u}_{n+1} = \frac{1}{T_k} \sum_{m=0}^n m u_{m_k} \tag{29}$$

In each time step, the expanded order m could be obtained adaptively from the following criteria:

$$\frac{\|u_m s^m\|_2}{\|\sum_{0}^{m-1} u_m s^m\|_2} \leq \beta \tag{30}$$

where β is an error bound (for example $\beta = 10^{-6}$); $\|\cdot\|_2$ represents the 2-norm of the matrix.

3.2. Numerical Implementation of MLPG5

In the MLPG approaches, one may write a weak form over a local sub-domain Ω_s , which can be: (1) a circle, (2) an ellipse, (3) a rectangle or any other regular or irregular shape. A generalized local weak form of the differential Equation (25) over a local sub-domain Ω_s can be written as:

$$\int_{\Omega_q} W_I(\sigma_{mij,j} + b_{mi} - \rho \frac{(m+2)(m+1)}{T_k^2} u_{m+2i} - c \frac{m+1}{T_k} u_{m+1i}) d\Omega = 0 \quad (31)$$

where W_I is the test function. In mixed MLPG5, the Heaviside function is used as the test function in the local weak form. It is defined as:

$$W_I = \begin{cases} 1 & \text{inside } \Omega_q \\ 0 & \text{outside } \Omega_q \end{cases} \quad (32)$$

By substituting Equation (32) into Equation (31) and applying the divergence theorem, Equation (31) may be rewritten in a symmetric weak form as:

$$\int_{\Omega_q} \left(\rho \frac{(m+2)(m+1)}{T_k^2} u_{m+2i} + c \frac{m+1}{T_k} u_{m+1i} \right) d\Omega - \int_{\Gamma_{qi}} \sigma_{mij} n_j d\Gamma - \int_{\Gamma_{qu}} \sigma_{mij} n_j d\Gamma = \int_{\Gamma_{qt}} \sigma_{mij} n_j d\Gamma + \int_{\Omega_q} b_{mi} d\Omega \quad (33)$$

where Γ_{qi} is a part of the local boundary, which is inside the solution domain; Γ_{qu} is the intersection between the local boundary and the global displacement boundary; and Γ_{qt} is a part of the boundary over which the natural boundary conditions are specified, as shown in Figure 1.

In this paper, it is assumed that the body force is zero. By substituting the Equation (12) into Equation (33), we have:

$$\int_{\Omega_q} \left(\rho \frac{(m+2)(m+1)}{T_k^2} u_{m+2i} + c \frac{m+1}{T_k} u_{m+1i} \right) d\Omega - \int_{\Gamma_{qi}} t_{m_i} d\Gamma - \int_{\Gamma_{qu}} t_{m_i} d\Gamma = \int_{\Gamma_{qt}} \tilde{p}_{m_i} d\Gamma \quad (34)$$

with the constitutive relations of an isotropic linear elastic homogeneous solid, the tractions in Equation (34) can be written in terms of the strains:

$$t_{m_i} = n \sigma_m = n D \epsilon_m \quad (35)$$

$$\epsilon_m = L u_m \quad (36)$$

where

$$n = \begin{bmatrix} n_x & 0 & n_y \\ 0 & n_y & n_x \end{bmatrix} \quad (37)$$

$$D = \frac{E}{1-\nu^2} \begin{bmatrix} 1 & \nu & 0 \\ \nu & 1 & 0 \\ 0 & 0 & \frac{1-\nu}{2} \end{bmatrix} \text{ for plane stress} \quad (38)$$

In the mixed MLPG5 method, the interpolation of nodal displacements u_{m_i} and strains ϵ_{m_i} can be accomplished by using the shape function mentioned in Section 2, as

$$u_m^h(X) = \sum_{k=1}^n \phi_k(X) u_{m_k} = \Phi U_m \quad (39)$$

$$\epsilon_m^h(X) = \sum_{k=1}^n \phi_k(X) \epsilon_{m_k} = \Phi \epsilon_m \quad (40)$$

where Φ is the shape function matrix; and U_m and ϵ_m are the vector of virtual nodal displacement and strain, respectively.

With Equations (35)–(40), one may discretize the local symmetric weak-form of Equation (34), as:

$$\frac{(m+2)(m+1)}{T_k^2} \int_{\Omega_q} \rho \Phi d\Omega U_{m+2} + \frac{m+1}{T_k} \int_{\Omega_q} c \Phi d\Omega U_{m+1} - \int_{\Gamma_{qi}} n D \Phi d\Gamma(L\Phi U_m) - \int_{\Gamma_{qu}} n D \Phi d\Gamma(L\Phi U_m) = \int_{\Gamma_{qt}} \tilde{p}_m d\Gamma \tag{41}$$

Obviously, it can be found that no derivatives of the shape functions are involved in the local integrals. While both shape function and its derivative at each point need to be calculated in the traditional MLPG, which greatly increases the computing cost. The final system equation can be rewritten in a matrix form:

$$\frac{(m+2)(m+1)}{T_k^2} M U_{m+2} + \frac{m+1}{T_k} C U_{m+1} - K U_m = F \tag{42}$$

where M , C , K and F are the matrixes of mass, damping and stiffness, and the vector of force, respectively. They are defined as follows.

$$M = \rho \int_{\Omega_q} \Phi d\Omega = \rho S \tag{43}$$

$$C = c \int_{\Omega_q} \Phi d\Omega = c S \tag{44}$$

$$F = \int_{\Gamma_{qt}} \tilde{p}_m d\Gamma \tag{45}$$

$$K = \int_{\Gamma_{qi}} n D \Phi d\Gamma(L\Phi) + \int_{\Gamma_{qu}} n D \Phi d\Gamma(L\Phi) \tag{46}$$

Once nonlinear damping is introduced, the system equation can be rewritten in another form:

$$\frac{(m+2)(m+1)}{T_k^2} M U_{m+2} + \frac{c_0(m+1)}{T_k} S U_{m+1} + \left(\frac{c_1 m}{T_k} S - K \right) U_m = F \tag{47}$$

where c_0 and c_1 represent the expanding coefficients of damping coefficient c .

In the present study, the Gauss quadrature is used for the subdomain integration in Equations (43)–(46).

3.3. Natural Frequency Solved by Mixed MLPG5

The natural frequencies and corresponding mode shapes are often referred to as the dynamic characteristics of the structure. While the mass matrix M and the stiffness matrix K in the vibration system are obtained from Equation (42), the elasto-dynamics equation of the undamped system can be written as a typical eigenvalue equation as follows:

$$\lambda = eig(M^{-1}K) \tag{48}$$

where λ is the vector of eigenvalues. Finally, the natural frequency can be solved by:

$$f_i = \frac{\sqrt{\lambda_i}}{2\pi} \tag{49}$$

4. Numerical Examples

4.1. Free Vibration Analysis

Example 1: A Variable-Cross-Section Beam

In this example, the presented method is used in free vibration analysis of a cantilever beam with a variable cross-section, as shown in Figure 2. The problem is solved for the plane stress case with the following parameters: the length $L = 10$ m, the height $H1 = 5$ m,

$H2 = 3$ m, the density $\rho = 1 \text{ kg/m}^3$, the Young's modulus $E = 3 \times 10^7$ Pa and the Poisson ratio $\nu = 0.3$.

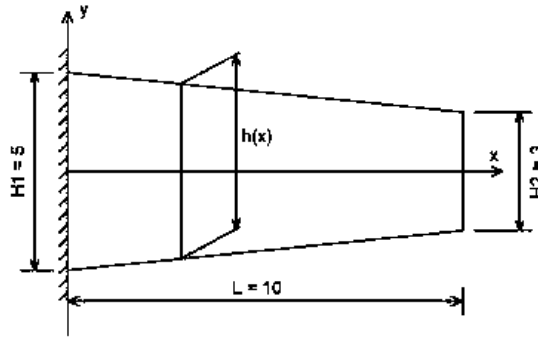


Figure 2. A cantilever beam with a variable cross-section.

Regular and irregular nodal configurations were used, as shown in Figure 3. For comparison, the problem was also analyzed by FEM software ANSYS (Mechanical). Additionally, the number of nodes used in ANSYS was 3978, which is 13 times more that used in the presented method.

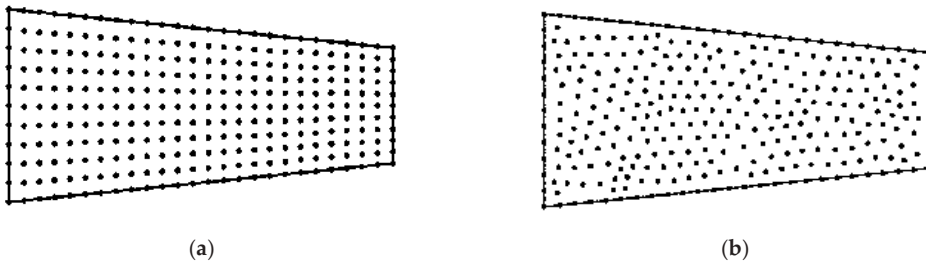


Figure 3. Nodal configuration for a variable-cross-section beam. (a) regular nodal distribution; (b) irregular nodal distribution.

The natural frequencies of the first five modes were calculated by the presented mixed MLPG5 method and the FEM software, as listed in Table 1. It can be seen that the natural frequencies obtained by the presented method are in good agreement with that of ANSYS, whether a regular or random node distribution is used.

Table 1. Comparison of the natural frequencies of the variable-cross-section beam obtained by the meshless algorithm and ANSYS (FEM).

Mode	Mixed MLPG5 Regular		Mixed MLPG5 Random		ANSYS (FEM) (Hz)
	Frequency (Hz)	Relative Error (%)	Frequency (Hz)	Relative Error (%)	
1	42.65	2.45	42.37	1.78	41.63
2	145.57	0.36	147.43	0.92	146.09
3	153.44	1.27	153.88	1.56	151.51
4	293.04	0.64	293.52	0.48	294.94
5	412.59	0.30	414.02	0.64	411.37

The first four eigenmodes obtained with the present mixed MLPG5 method are plotted in Figure 4. Compared with the FEM results obtained by ANSYS, the results are identical. As fewer nodes are used, the presented method has higher computational efficiency.

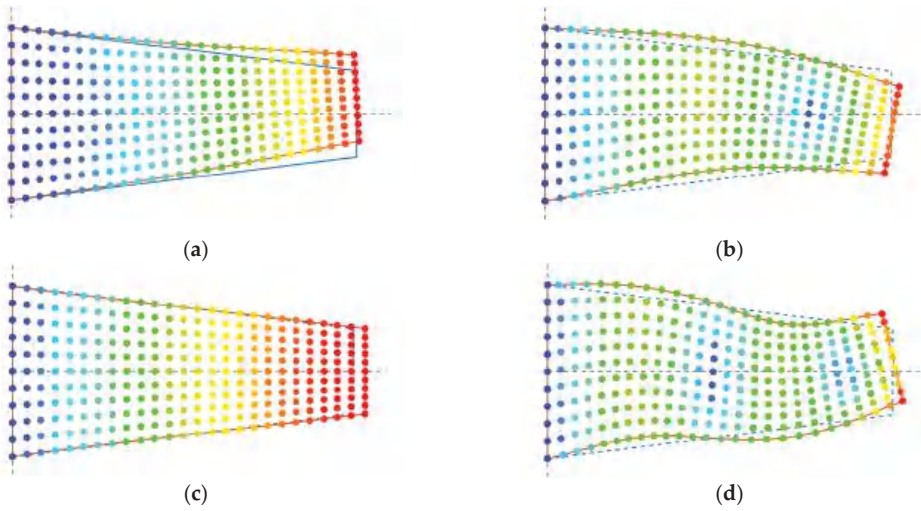


Figure 4. Eigenmodes for the variable-cross-section beam by the mixed MLPG5 method. (a) Mode 1; (b) mode 2; (c) mode 3; (d) mode 4.

4.2. Forced Vibration Analysis

Example 2: A cantilever beam with horizontal traction.

In the second example, the forced vibration analysis of a 2D cantilever beam is considered, as shown in Figure 5. The parameters are taken as, length $L = 20$ m, width $D = 4$ m, Young’s modulus $E = 1 \times 10^5$ Pa, Poisson ratio $\nu = 0.3$, density $\rho = 1$ kg/m³ and damping coefficient $c = 1$ Ns/m. The initial conditions are defined as:

$$u_0 = u_{in}(X, 0) = 0 \tag{50}$$

$$u_1 = \dot{u}_{in}(X, 0) = 0 \tag{51}$$

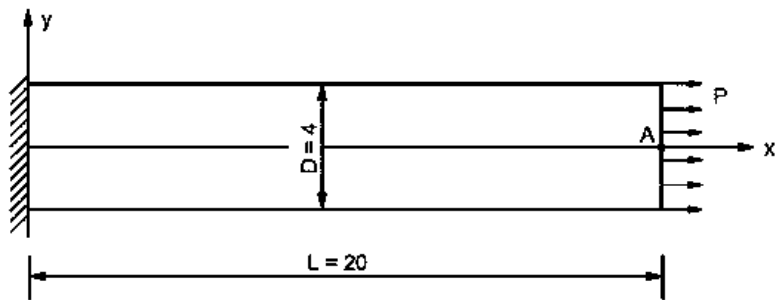


Figure 5. A cantilever beam subjected to horizontal traction.

The transient response of the beam subjected to a suddenly loaded traction $P = 300$ Pa is considered. A regular uniform nodal configuration is used with nodal distances $d = 1$ m, as shown in Figure 6.

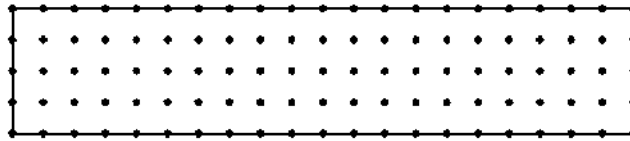


Figure 6. The nodal distribution for a cantilever beam.

The presented method was used to obtain the transient response. The Newmark method and the present time-adaptive method were utilized in this analysis. The results of time steps $\Delta t = 0.001, 0.002, 0.005, 0.01, 0.02$ s were obtained. For comparison, solutions for this problem were also obtained using the FEM software ANSYS (Mechanical).

The horizontal displacement u_x at point A of different time steps by the Newmark method is plotted in Figure 7. Additionally, the parameters $\beta = 0.3$ and $\gamma = 0.6$ were used. One can observe that for $\Delta t = 0.001$ s, the results are in good agreement with FEM. However, it should be noted that the computational error would increase with the increase in time step in the Newmark method due to the dissipation and dispersion errors. When the time step is too large (e.g., $\Delta t = 0.02$ s), the accuracy would become unacceptable. Thus, a straightforward way of reducing the dispersion and dissipation error in Newmark method is to use a smaller time step size.

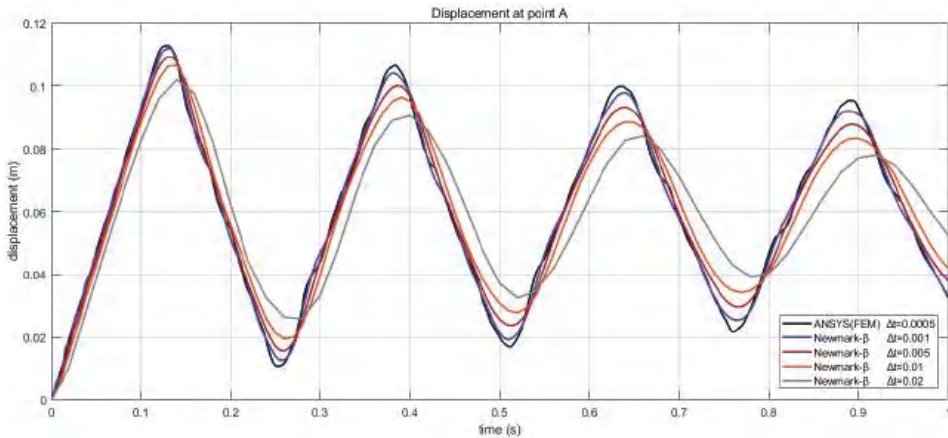


Figure 7. Displacements u_x at point A using Newmark method with different time steps. ($\alpha = 0.3, \beta = 0.6, 105$ nodes with nodal distance $d = 1.0$ m).

The horizontal displacement u_x at point A for different time steps via the time-adaptive method is plotted in Figure 8. As the results are quite close to the reference solution when the time steps are 0.001, 0.002 and 0.005 s, it is hard to distinguish them on the figure. Only the results of the time steps $\Delta t = 0.01, 0.02, 0.04$ s are plotted in Figure 8. It can be found that all the results obtained by time-adaptive methods are in good agreement with FEM, even if the time step is very large and the peak of displacement cannot be accurately obtained. Since high-order expansion in each time step is adopted in a time-domain adaptive method, a high precision result can be obtained by this time-adaptive method.

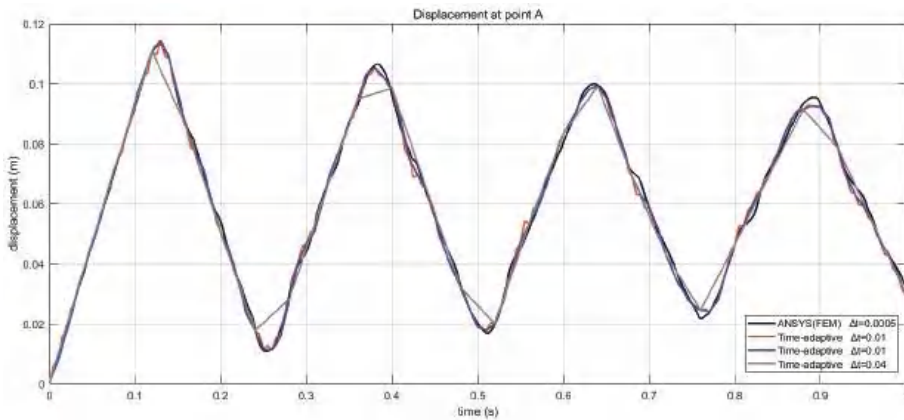


Figure 8. Displacements u_x at point A using a time-adaptive method with different time steps (105 nodes with nodal distance $d = 1.0$ m).

The calculation time and relative error at point A obtained by the two methods at different time steps are shown in Table 2. One can observe that the computing time of the Newmark method is less than that of our method, which shows that efficiency of Newmark method is higher at any sized time step. Although not as fast as the Newmark method, our method has higher accuracy when a large time step is used. Only when $\Delta t = 0.001$, were the efficiency and accuracy of Newmark method higher than those of our method. However, in engineering, it is difficult to predict the “best time step size.” As shown in Table 2, the expansion order would increase with the increase in time step while the relative error would remain unchanged. This is very useful for the forced vibration analysis in engineering applications, especially in long-time response analysis, as a large time step is preferred.

Table 2. The computing time, the order of expanding and the mean relative error at point A for two time-discretization methods.

Method	DeltaT (s)	Computing Time (s)	Order of Expanding	Relative Error at Point A (%)
Newmark	0.001	0.283		3.30
	0.002	0.164		3.99
	0.005	0.072		7.45
	0.01	0.042	/	14.40
	0.02	0.026		27.87
	0.04	0.018		52.91
Adaptive	0.001	1.183	7	3.47
	0.002	0.693	9	3.42
	0.005	0.419	15	3.72
	0.01	0.314	24	3.17
	0.02	0.259	42	3.29
	0.04	0.227	79	3.13

The test-domain size S_t and the support size S_s (or the size of the influence domain) are the key components for the mixed MLPG5 method. Both of them affect the computational efficiency and the accuracy. In the present study, the test domain size and the support size were chosen to be proportional to the nodal distance d .

In practice, the test-domain size is chosen to be less than $1.0 d$ to ensure that the local sub-domains of the internal nodes are entirely within the solution domain, without being intersected by the global boundary. In the present study, five test-domain sizes were used,

0.4, 0.5, 0.6, 0.7 and 0.8 d. Additionally, the support size was fixed as 1.5 d and the nodal distance was fixed as 1 m. The displacements u_x at point A (shown in Figure 5) were used to examine the effects of the different test-domain size, as shown Figure 9. It can be seen that accuracy is excellent when the test-domain size is less than 0.7 d. It is noticeable that the accuracy would become unacceptable when the test-domain size is larger than 0.8 d, as the sub-domains are obviously over-lapping. Our study has found that the test size $S_t = 0.4 - 0.7$ works for most of forced vibration problems. Additionally, $S_t = 0.6$ was used in the following calculations.

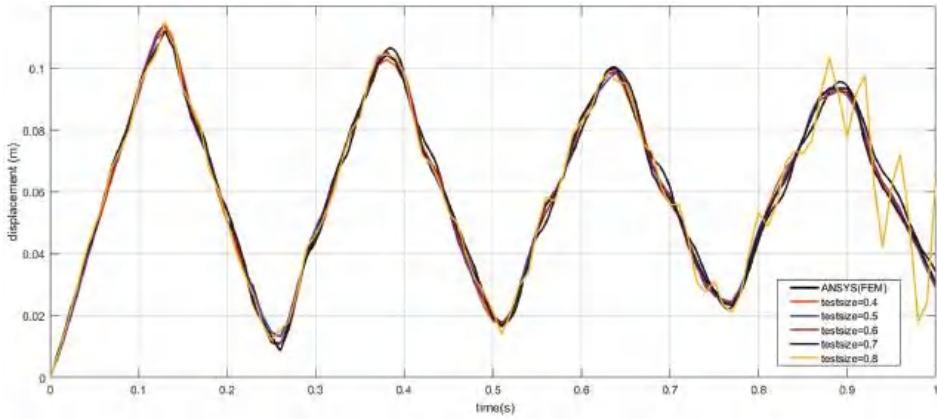


Figure 9. Influence of the test domain size in a cantilever beam under an end load (105 nodes with nodal distance $d = 1.0$ m, at point A).

For a small support size, the meshless approximation algorithms may be singular, and the shape function cannot be constructed because of too few nodes. In the present study, four support sizes (1.2, 1.5, 1.8 and 2.1 d) were used for the MLPG5 mixed approach. The nodal distance was fixed as 1 m. The displacements u_x at point A (shown in Figure 5) were also used to examine the effects of the support-domain size, as shown in Figure 10.

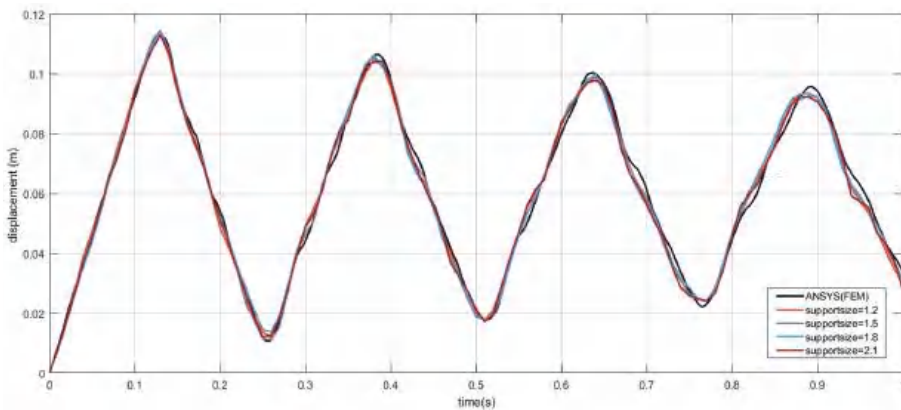


Figure 10. Influence of the support size in a cantilever beam under an end load (105 nodes with nodal distance $d = 1.0$ m, at point A).

It can be seen that good accuracy is obtained when the support sizes are 1.5 d and 1.8 d. However, the result becomes more unstable when the support size is 2.1 d, as the continuous shape function leads to smoother results but lower accuracy. Our study has

found that support sizes of $S_s = 1.2 - 1.8$ work for most of forced vibration problems. Additionally, $S_s = 1.5$ was used in the following calculations.

Example 3: A cantilever beam with vertical traction.

In this example, our method is used to analyze the forced vibration of a cantilever beam subjected to a vertical traction with different damping coefficient, as shown in Figure 11. The problem is solved for the plane stress case with: length $L = 48$ m, width $D = 12$ m, Young’s modulus $E = 3 \times 10^7$ Pa, Poisson ratio $\nu = 0.3$ and density $\rho = 1$ kg/m³. A regular set of 85 scattered nodes with nodal distances $d = 3$ m is employed here, as shown in Figure 12. The same initial conditions are defined as:

$$u_0 = u_{initial}(X, 0) = 0 \tag{52}$$

$$u_1 = \dot{u}_{initial}(X, 0) = 0 \tag{53}$$

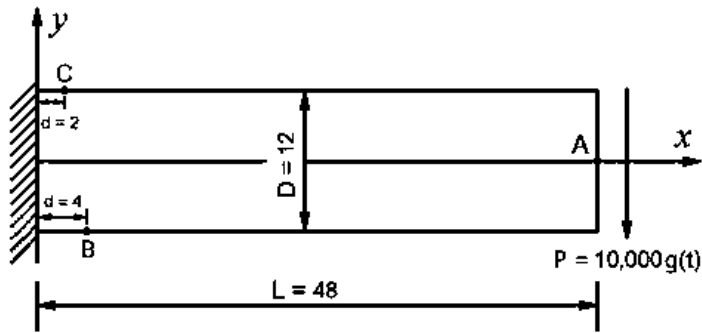


Figure 11. A cantilever beam subjected to a vertical traction.

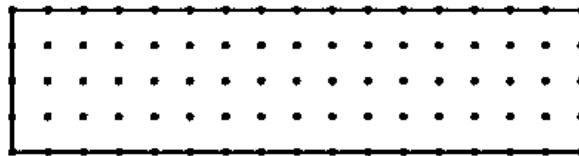


Figure 12. The nodal distribution for a cantilever beam.

Three kinds of traction at the free end of the beam while using $P(x, t) = 10,000 g(t)$ N/m are considered in this example: one is a Heaviside step loading, another is a transient loading with a finite decreasing time and the last is a transient loading with a finite increasing time, as shown in Figure 13. Additionally, the $g(t)$ is the time-dependent function. The vertical displacement at point A, and the normal stress at points B and C (shown in Figure 11) were computed. To verify the accuracy of the present algorithm, the problem was also analyzed by FEM software ANSYS (Mechanical), where 2425 nodes (27 times more than our method) were adopted.

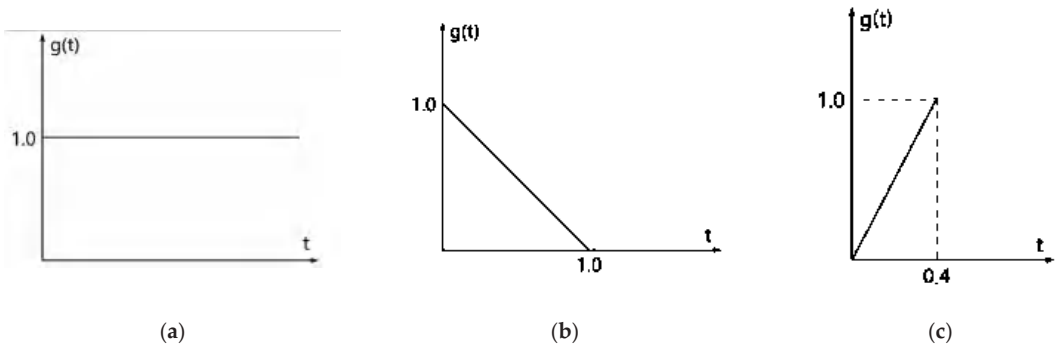


Figure 13. Schematic diagram of dynamic loadings. (a) Heaviside step loading with an infinite duration; (b) transient loading with a finite decreasing time; (c) transient loading with a finite increasing time.

a. Heaviside step loading with an infinite duration

The transient response of the beam subjected to Heaviside step loading with an infinite duration is considered. The loading function is determined by

$$g(t) = 1.0 \tag{54}$$

as shown in Figure 13a. This type of dynamics analysis under impact loading is usually defined as dynamic relaxation [26]. The mixed MLPG5 method was combined with the time-adaptive method and used to obtain the transient response. The displacements u_y of point A with damping coefficients $c = 1, 10$ and 20 Ns/m are plotted in Figures 14–16, respectively. It is evident that the response converges to the static deformation ($u_y = 10.682$ m, obtained by ANSYS) once a damping is introduced, and the deformation declines fast with an increase in damping coefficient. All of them are in good agreement with the ANSYS results.

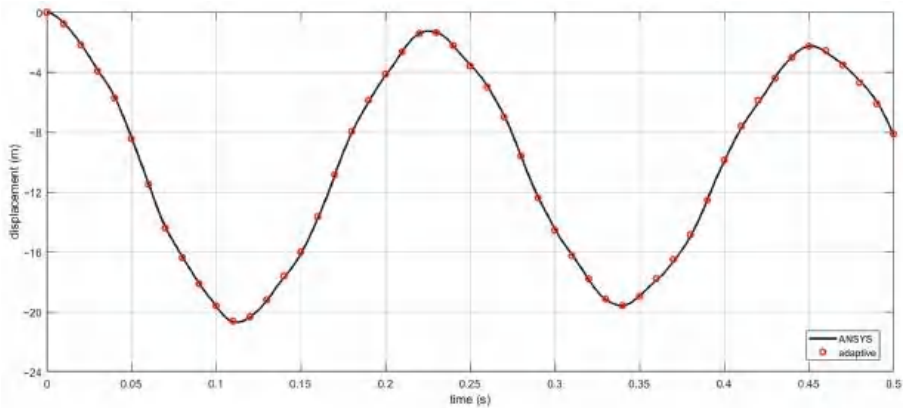


Figure 14. The transient vertical displacement at point A with damping ($c = 1$ Ns/m), $\Delta t = 0.005$ s, under Heaviside step loading with an infinite duration.

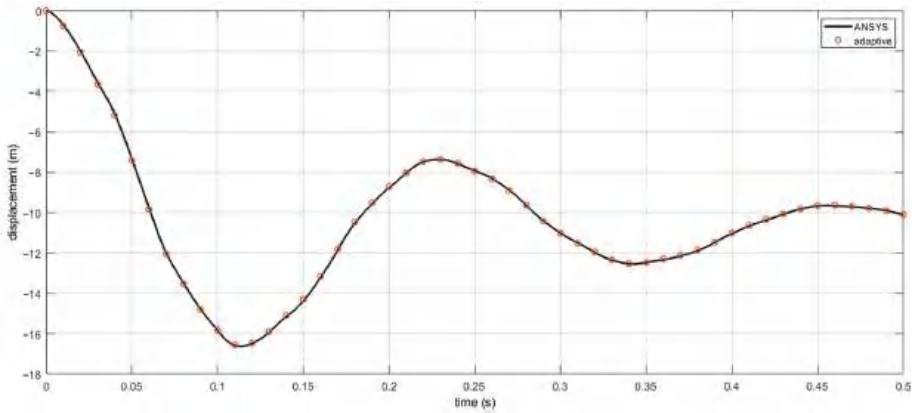


Figure 15. The transient vertical displacement at point A with damping ($c = 10 \text{ Ns/m}$), $\Delta t = 0.005 \text{ s}$, under Heaviside step loading with an infinite duration.

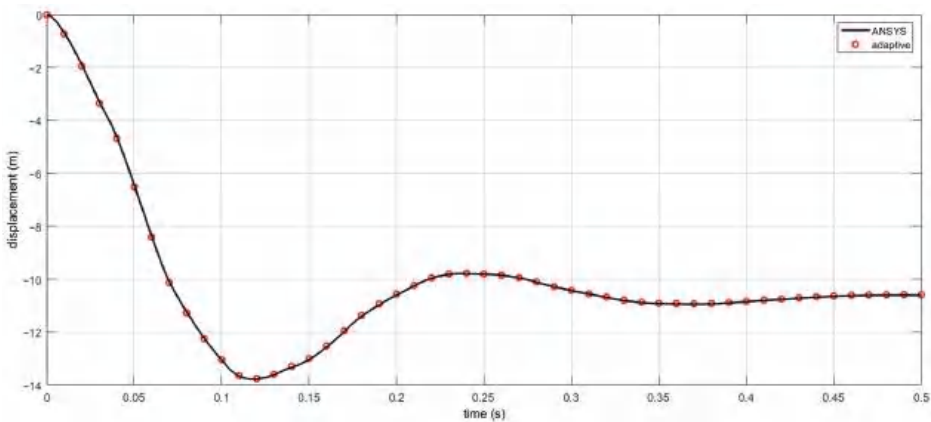


Figure 16. The transient vertical displacement at point A with damping ($c = 20 \text{ Ns/m}$), $\Delta t = 0.005 \text{ s}$, under Heaviside step loading with an infinite duration.

In addition, the vertical displacement fields of the deformed cantilever beam at different time steps ($t = 0.005, 0.01, \text{ and } 0.02 \text{ s}$) are shown in Figures 17–19. One can observe that with time, the stress wave propagates from the free end towards the fixed end. Thus, the displacement distribution in elasto-dynamics is quite different from that in static analysis.

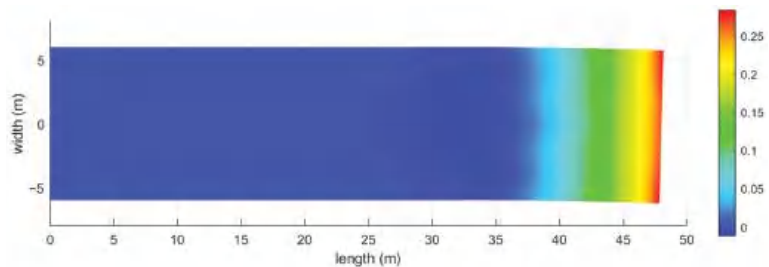


Figure 17. Vertical displacement field of the cantilever beam ($c = 1 \text{ Ns/m}$, $t = 0.005 \text{ s}$), under Heaviside step loading with an infinite duration.

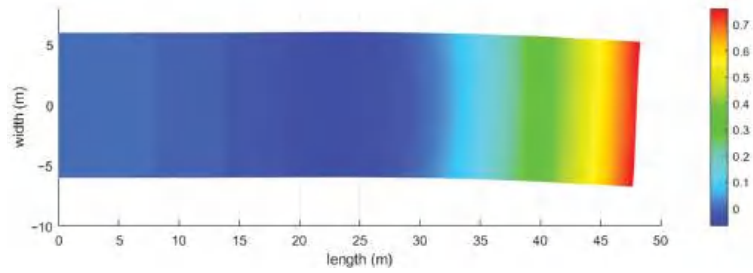


Figure 18. Vertical displacement field of the cantilever beam ($c = 1 \text{ Ns/m}$, $t = 0.010 \text{ s}$), under Heaviside step loading with an infinite duration.

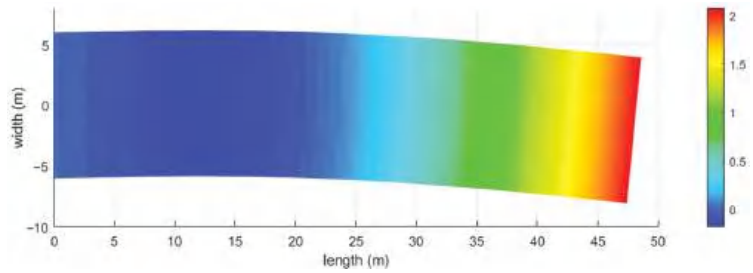


Figure 19. Vertical displacement field of the cantilever beam ($c = 1 \text{ Ns/m}$, $t = 0.020 \text{ s}$), under Heaviside step loading with an infinite duration.

The normal stress σ_{xx} at point B is shown in Figure 20. The damping coefficient is $c = 1 \text{ Ns/m}$. It can be seen that the results obtained by Newmark method have larger errors due to the numerical dissipation and dispersion, and the results obtained by our time-adaptive method are in good agreement with those of the reference solution. Thus, our method works very well, and it is more accurate than the Newmark method for the forced vibration analysis.

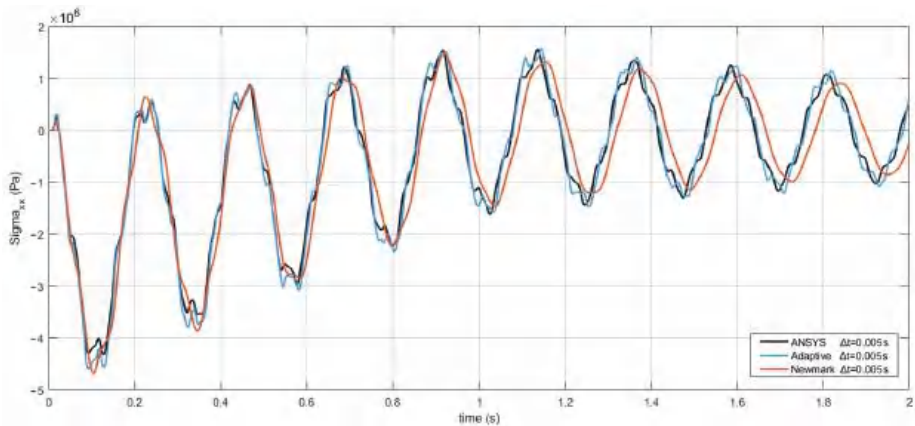


Figure 20. The normal stress σ_{xx} at point B with damping coefficient $c = 1 \text{ Ns/m}$ and $\Delta t = 0.005 \text{ s}$ under Heaviside step loading with an infinite duration.

b. Transient loading with finite decreasing time

The transient response of the beam subjected to a transient loading with a finite decreasing time is considered. The loading function is defined as

$$g(t) = \begin{cases} 1 - t & 0 < t < 1 \\ 0 & t > 1 \end{cases}, \tag{55}$$

as shown in Figure 13b.

The displacements u_y of point A with different damping coefficients are plotted in Figures 21–23. It can be seen that as the damping coefficient increases, the amplitudes decay faster and the duration of vibration is shorter. Very stable results with different damping coefficients were obtained by our method, and they are in good agreement with the results obtained by ANSYS. The computing time with the mixed MLPG5 time-domain adaptive method and ANSYS (FEM) are included in Table 3, for different nodal numbers. Additionally, the time step was fixed to 0.001 s. It also can be seen that our method is more efficient than ANSYS (FEM). From these results, our method shows good approximations to the transient responses of different damps with high efficiency.

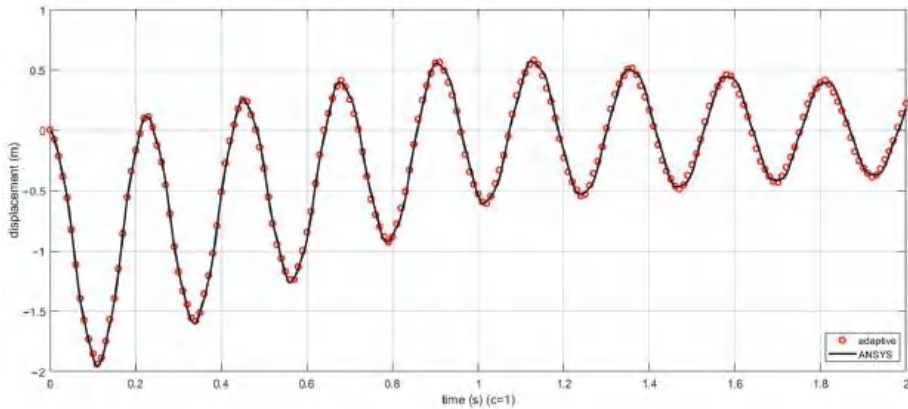


Figure 21. The transient vertical displacement at point A with damping ($c = 1$ Ns/m) and $\Delta t = 0.001$ s under transient loading with finite decreasing time.

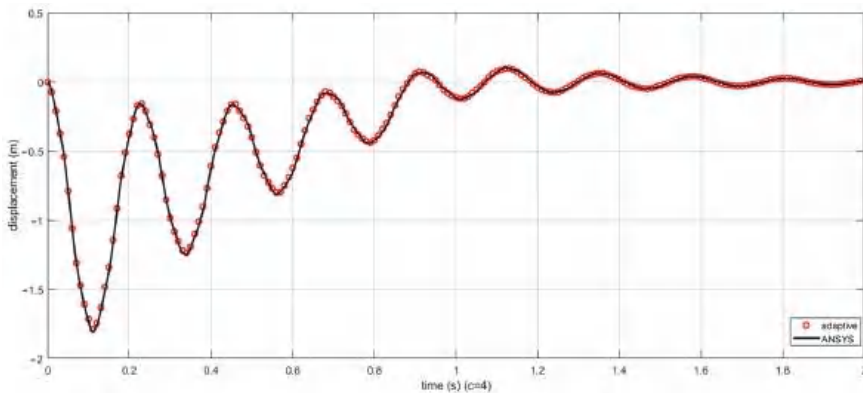


Figure 22. The transient vertical displacement at point A with damping ($c = 4$ Ns/m) and $\Delta t = 0.001$ s under transient loading with finite decreasing time.

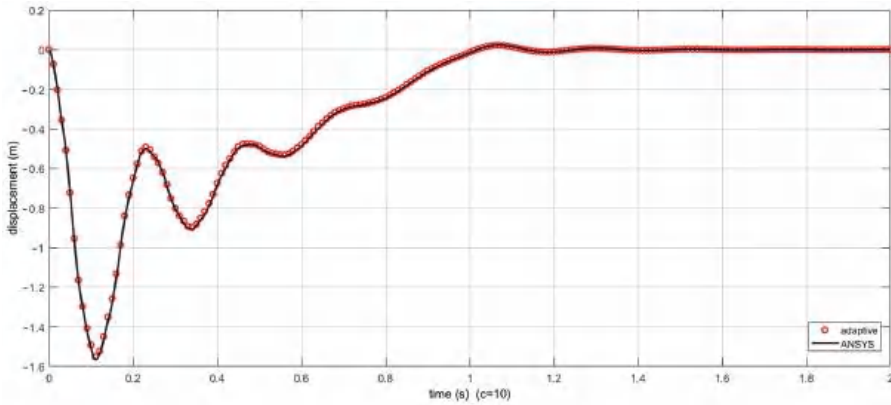


Figure 23. The transient vertical displacement at point A with damping ($c = 10$ Ns/m) and $\Delta t = 0.001$ s under transient loading with finite decreasing time.

Table 3. Computing time of two algorithms.

Numerical Methods	Number of Nodes	Step Size (s)	Computing Time (s)
Mixed MLPG5 time	85 (17×5)	0.001	3.3257
Adaptive Method	175 (25×7)		10.105
ANSYS(FEM)	85(17×5)		10.484
	175 (25×7)		21.828

c. Time-dependent damping

In this example, the transient response of the beam subjected to a time dependent loading (shown in Figure 13c) and nonlinear damping is considered. The loading function and the damping coefficient are defined as follows:

$$g(t) = \begin{cases} 2.5t & 0 < t < 0.4 \\ 0 & t > 0.4 \end{cases} \tag{56}$$

$$c = 1 + t \tag{57}$$

The example was solved by our method using different time step sizes. It can be seen in Figure 24 that the normal stress levels σ_{xx} at point C with different time step sizes are quite close to each other. For comparison, the normal stress levels σ_{xx} at point C solved by the Newmark method are plotted in Figure 25. It can be seen that the Newmark method still has large errors due to the numerical dissipation and dispersion. It also cannot accurately capture the stress peaks when a larger time step ($\Delta t = 0.006$ s) is adopted.

In addition, the shear stress levels τ_{xy} at different times solved by our method are shown in Figures 26–28. It can be clearly seen in Figures 27 and 28 that the stress concentrated on the center of the beam, as a result of the diffraction and reflection of elastic stress waves. This shows that the stress distribution in the dynamic problem is very different from that in a static problem. The results demonstrate that our method works well for the nonlinear forced vibration analysis.

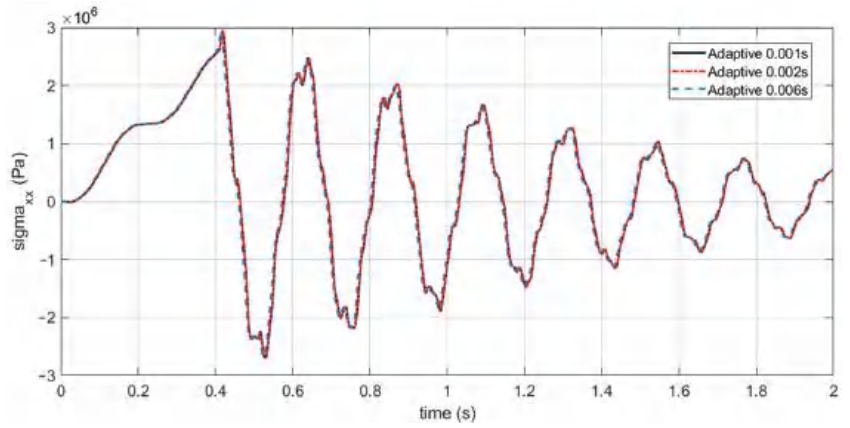


Figure 24. The normal stress σ_{xx} at point C with different time steps (nonlinear damping $c = 1 + t$ Ns/m).

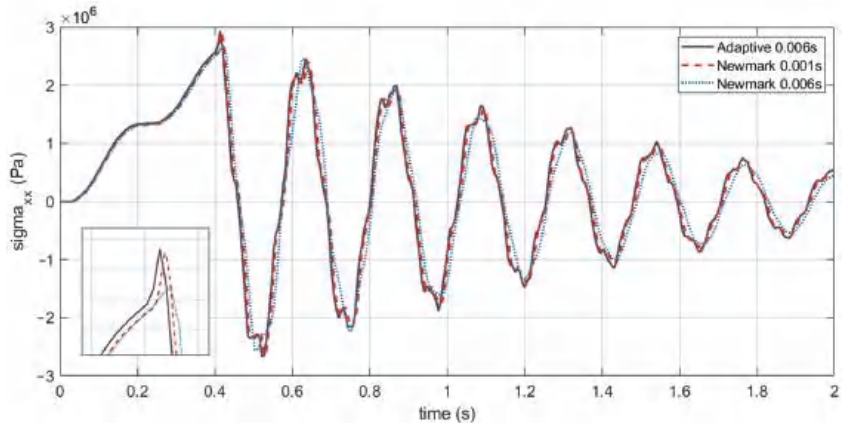


Figure 25. The normal stress σ_{xx} at point C using time-adaptive method and the Newmark method (nonlinear damping $c = 1 + t$ Ns/m).

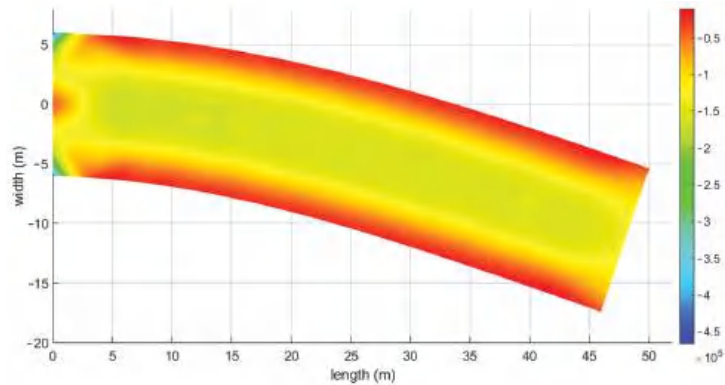


Figure 26. Shear stress τ_{xy} of the cantilever beam ($t = 0.4$ s), with time-dependent damping.

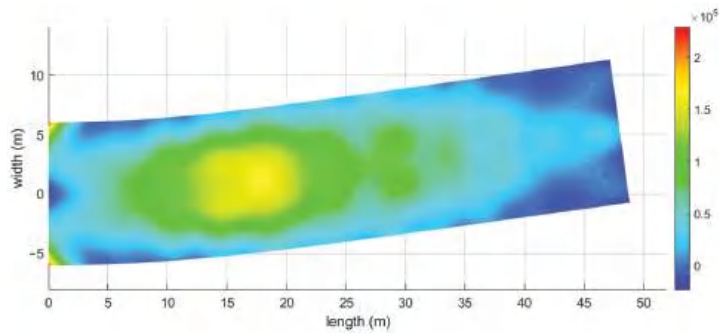


Figure 27. Shear stress τ_{xy} of the cantilever beam ($t = 0.48$ s), with time-dependent damping.

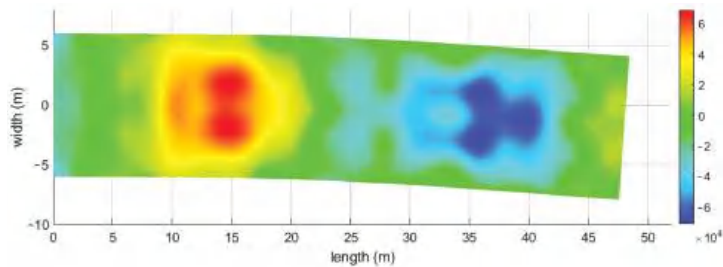


Figure 28. Shear stress τ_{xy} of the cantilever beam ($t = 0.58$ s), with time-dependent damping.

Example 4: A Perforated Tension Strip

The last example is a perforated strip under axial tension, as shown in Figure 29. This problem has been studied by Kontoni and Beskos, using the dual reciprocity BEM [27]. The strip was subjected to a Heaviside tension step load with initial value $P = 20$ Pa. The material properties of the strip were taken as: length $L = 1.6$ m, width $D = 1.0$ m, Young's modulus $E = 2 \times 10^3$ Pa, Poisson ratio $\nu = 0.3$, density $\rho = 1$ kg/m³ and damping coefficient $c = 1$ Ns/m. The initial conditions were defined as:

$$u_0 = u_{in}(X, 0) = 0 \tag{58}$$

$$u_1 = \dot{u}_{in}(X, 0) = 0 \tag{59}$$

Symmetry conditions were imposed on the left and right edges, and the inner boundary of the hole had no traction. Regular uniform nodal configurations with nodal distances $d = 0.03$ m were used in this example, as shown in Figure 30. The time step used in the time-adaptive method was $\Delta t = 0.001$ s. The horizontal displacement of point A (0.00, 0.05) and vertical displacement of point B (0.05, 0.00) are plotted in Figures 31 and 32, respectively. For comparison, solutions for this problem were also obtained using the finite element software ANSYS (Mechanical). It is evident that the results obtained by our method are in very good agreement with those obtained by ANSYS.

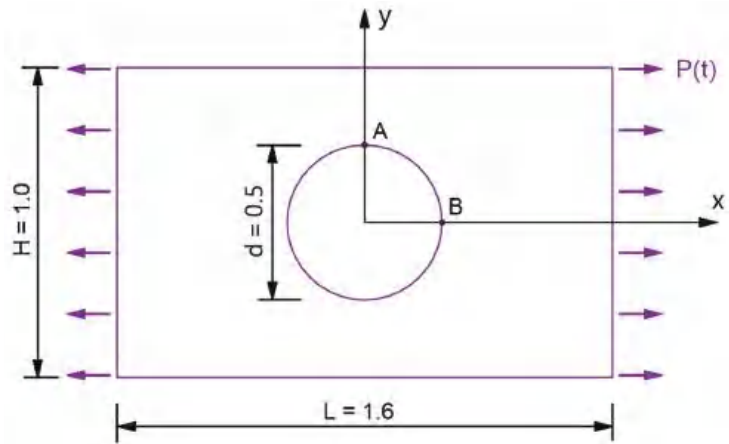


Figure 29. A perforated tension strip subjected to a Heaviside tension step loading.

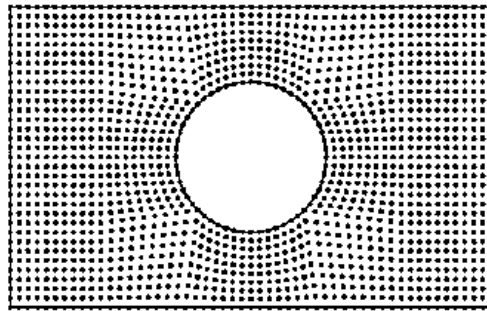


Figure 30. Nodal configurations for a perforated tension strip.

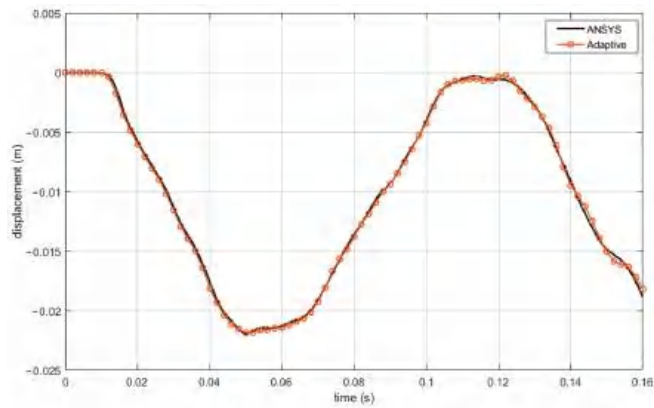


Figure 31. The transient vertical displacement at point A, $\Delta t = 0.001$ s and $c = 1$ Ns/m for the Heaviside tension step loading.

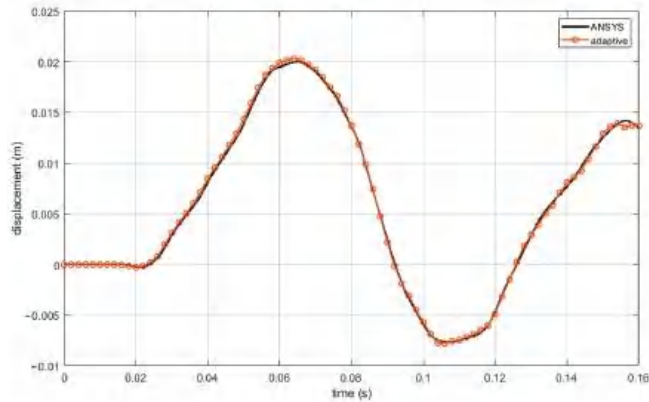


Figure 32. The transient vertical displacement at point B, $\Delta t = 0.001$ s and $c = 1$ Ns/m for the Heaviside tension step loading.

It can be observed that the maximum displacement level for point A and point B occurs at $t = 0.065$ s, and the maximum displacement of point A in the reverse direction occurs at $t = 0.105$ s. The displacement fields of this perforated tension strip at $t = 0.065$ s and $t = 0.105$ s are shown in Figures 33 and 34. The results prove the efficiency and accuracy of the developed meshless time-adaptive method for forced vibration analysis in multiple connected domains.

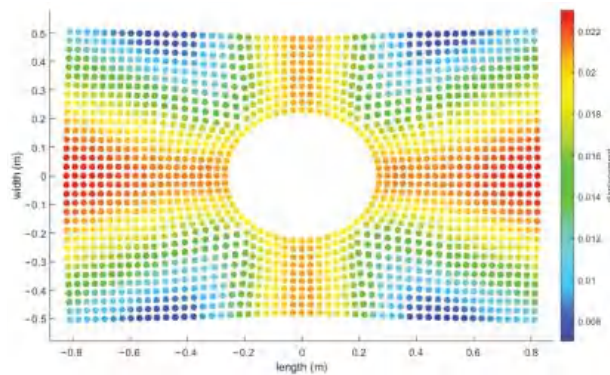


Figure 33. The displacement field of this perforated tension strip at $t = 0.065$ s.

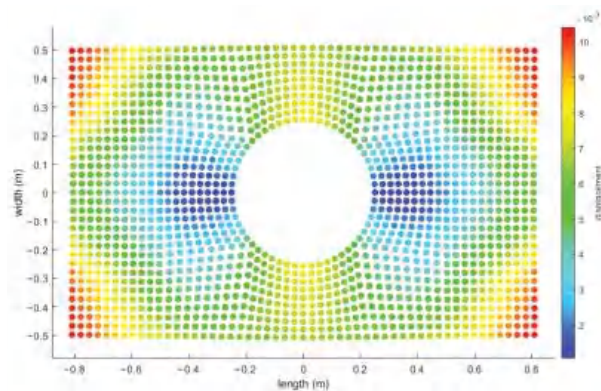


Figure 34. The displacement field of this perforated tension strip at $t = 0.105$ s.

5. Conclusions

In this paper, a new meshless time-domain adaptive method was presented for vibration analysis through mixed MLPG-FVM (MLPG5). In this method, each variable is interpolated by time series of variable order in the time domain. Thus, more accurate stress and displacement can be obtained, and larger time steps can be used in vibration analysis compared with the Newmark method (when the time step is 0.04, the calculation error of this method is only 1/17 of that of the Newmark method). Furthermore, through the independent interpolation of strain and displacement, the differentiation of the shape function is eliminated and the lower-order polynomial basis can be used in the MLS interpolations. Thus, smaller support sizes ($S_s = 0.4 - 0.7$, and the test sizes S_t were 1.2–1.8) can be used in the MLPG approach. By using the Heaviside function as the weighted function, the domain integral of stiffness matrix is removed and the calculation efficiency is improved. All the numerical results show that the time-domain adaptive method can cooperate well with the meshless method, and the calculation accuracy of the present method is satisfactory with various time step sizes. This high-accuracy time-domain scheme is very attractive for second-order PDE in time as elasto-dynamics equations. Put simply, this method provides a high efficiency and accuracy solution for solving free and forced vibration problems in both simply and multiply-connected domains under large time step sizes without any type of mesh.

Author Contributions: Conceptualization, T.Z. and M.L.; methodology, T.Z. and M.L.; software, M.L. and J.C.; investigation, T.Z. and M.L.; data curation, M.L. and J.C.; writing—original draft preparation, M.L. and J.C.; writing—review and editing, T.Z. and M.L.; visualization, M.L. and J.C.; supervision, T.Z.; project administration, T.Z. All authors have read and agreed to the published version of the manuscript.

Funding: This research received no external funding.

Institutional Review Board Statement: Not applicable.

Informed Consent Statement: Not applicable.

Data Availability Statement: Data sharing not applicable to this article, as no datasets were generated or analyzed during the current study.

Conflicts of Interest: The authors declare no conflict of interest.

References

1. Meirovitch, L. Computational methods in structural dynamics. *J. Vib. Acoust.* **1982**, *49*, 259–260. [CrossRef]
2. Gu, Y.; Liu, G.R. A meshless local Petrov-Galerkin (MLPG) method for free and forced vibration analyses for solids. *Comput. Mech.* **2001**, *27*, 188–198. [CrossRef]
3. Mohebpour, S.R.; Malekzadeh, P.; Ahmadzadeh, A.A. Dynamic analysis of laminated composite plates subjected to a moving oscillator by FEM. *Compos. Struct.* **2011**, *93*, 1574–1583. [CrossRef]
4. Ghafoori, E.; Asghari, M. Dynamic analysis of laminated composite plates traversed by a moving mass based on a first-order theory. *Compos. Struct.* **2010**, *92*, 1865–1876. [CrossRef]
5. Yang, Y.; Lam, C.C.; Kou, K.P. Forced vibration analysis of functionally graded beams by the meshfree boundary-domain integral equation method. *Eng. Anal. Bound. Elem.* **2016**, *72*, 100–110. [CrossRef]
6. Thankane, K.S. Finite Difference Method for Beam Equation with Free Ends Using Mathematica. *S. Afr. J. Pure Appl. Math.* **2009**, *4*, 61–78.
7. Chakravorty, D.; Sinha, P.K.; Bandyopadhyay, J.N. Applications of fem on free and forced vibration of laminated shells. *J. Eng. Mech.* **1998**, *124*, 1–8. [CrossRef]
8. Ahmad, S.; Banerjee, P.K. Free vibration analysis by BEM using particular integrals. *J. Eng. Mech.* **1986**, *112*, 682–695. [CrossRef]
9. Schanz, M. Application of 3d time domain boundary element formulation to wave propagation in poroelastic solids. *Eng. Anal. Bound. Elem.* **2001**, *25*, 363–376. [CrossRef]
10. Israil, A.; Banerjee, P.K. Advanced development of time-domain bem for two-dimensional scalar wave propagation. *Int. J. Numer. Methods Eng.* **2010**, *29*, 1003–1020. [CrossRef]
11. Guoyou, Y.; Mansur, W.J.; Carrer, J.A.M.; Gong, L. Stability of Galerkin and collocation time domain boundary element methods as applied to the scalar wave equation. *Comput. Struct.* **2000**, *74*, 495–506.

12. Malekzadeh, P.; Haghghi, M.R.G.; Gholami, M. Dynamic response of thick laminated annular sector plates subjected to moving load. *Compos. Struct.* **2010**, *92*, 155–163. [CrossRef]
13. Schenk, C.A.; Bergman, L.A.; Asce, M. Response of continuous system with stochastically varying surface roughness to moving load. *J. Eng. Mech.* **2003**, *129*, 759–768. [CrossRef]
14. Ikuno, S.; Fujita, Y.; Hirokawa, Y. Large-Scale Simulation of Electromagnetic Wave Propagation Using Meshless Time-domain Method with Parallel Processing. *IEEE Trans. Magn.* **2013**, *49*, 1613–1616. [CrossRef]
15. Haitian, Y. A new approach of time stepping for solving transfer problems. *Int. J. Numer. Methods Biomed. Eng.* **1999**, *15*, 325–334. [CrossRef]
16. Liu, Q.; Zhang, J.; Yan, L. A numerical method of calculating first and second derivatives of dynamic response based on gauss precise time step integration method. *Eur. J. Mech.* **2010**, *29*, 370–377. [CrossRef]
17. Yang, H.T.; Liu, Y.; Wu, R.F. Solving 2-D nonlinear coupled heat and moisture transfer problems via a self-adaptive precise algorithm in time-domain. *Appl. Math. Mech.* **2005**, *26*, 848–854.
18. Taylor, R.L.; Papadopoulos, P. On a finite element method for dynamic contact/impact problems. *Int. J. Numer. Methods Eng.* **1993**, *36*, 2123–2140. [CrossRef]
19. Atluri, S.N.; Zhu, T. A new meshless local Petrov-Galerkin (MLPG) approach in computational mechanics. *Comput. Mech.* **1998**, *22*, 117–127. [CrossRef]
20. Atluri, S.N.; Zhu, T. The meshless local Petrov-Galerkin (MLPG) approach for solving problems in elasto-statics. *Comput. Mech.* **2000**, *25*, 169–179. [CrossRef]
21. Atluri, S.N.; Han, Z.; Shen, S. Meshless Local Petrov-Galerkin (MLPG) approaches for weakly singular traction & displacement boundary integral equations. *Comput. Model. Eng. Sci.* **2003**, *4*, 507–517.
22. Shen, S.; Atluri, S.N. Multiscale Simulation Based on The Meshless Local Petrov-Galerkin (MLPG) Method. *Comput. Model. Eng. Sci.* **2004**, *5*, 235–255.
23. Shen, S.; Atluri, S.N. The Meshless Local Petrov-Galerkin (MLPG) Method: A Simple & Less-costly Alternative to the Finite Element and Boundary Element Methods. *Comput. Model. Eng. Sci.* **2002**, *3*, 11–51.
24. Atluri, S.N.; Han, Z.D.; Rajendran, A.M. A New Implementation of the Meshless Finite Volume Method, through the MLPG “Mixed” Approach. *Comput. Model. Eng. Sci.* **2004**, *6*, 491–513.
25. Atluri, S.N.; Shen, S. *The Meshless Local Petrov-Galerkin (MLPG) Method*; Tech Science Press: Encino, CA, USA, 2002.
26. Gu, Y.T.; Liu, G.R. A meshfree weak-strong (mws) form method for time dependent problems. *Comput. Mech.* **2005**, *35*, 134–145. [CrossRef]
27. Kontoni, D.P.N.; Beskos, D.E. Transient dynamic elastoplastic analysis by the dual reciprocity BEM. *Eng. Anal. Bound. Elem.* **1993**, *12*, 1–16. [CrossRef]

Article

A Multi-View Ensemble Width-Depth Neural Network for Short-Term Wind Power Forecasting

Jing Wan ^{1,†}, Jiehui Huang ^{2,†}, Zhiyuan Liao ^{2,†}, Chunquan Li ^{2,*} and Peter X. Liu ^{2,3}¹ The School of Qianhu, Nanchang University, Nanchang 330031, China; 6112119016@email.ncu.edu.cn² The School of Information Engineering, Nanchang University, Nanchang 330031, China; 7803018161@email.ncu.edu.cn (J.H.); 6105118084@email.ncu.edu.cn (Z.L.); xpliu@sce.carleton.ca (P.X.L.)³ The Department of Systems and Computer Engineering, Carleton University, Ottawa, ON K1S 5B7, Canada

* Correspondence: lichunquan@ncu.edu.cn

† These authors contributed equally to this work.

Abstract: Short-term wind power forecasting (SWPF) is essential for managing wind power systems management. However, most existing forecasting methods fail to fully consider how to rationally integrate multi-view learning technologies with attention mechanisms. In this case, some potential features cannot be fully extracted, degenerating the predictive accuracy and robustness in SWPF. To solve this problem, this paper proposes a multi-view ensemble width-depth neural network (MVEW-DNN) for SWPF. Specifically, MVEW-DNN consists of local and global view learning subnetworks, which can effectively achieve more potential global and local view features of the original wind power data. In MVEW-DNN, the local view learning subnetwork is developed by introducing the deep belief network (DBN) model, which can efficiently extract the local view features. On the other hand, by introducing the attention mechanism, a new deep encoder based learning system (deBLS) is developed as the global view learning subnetwork, which provides more comprehensive global information. Therefore, by rationally learning the effective local and global view features, MVEW-DNN can achieve competitive predictive performance in SWPF. MVEW-DNN is compared with the state-of-the-art models in SWPF. The experiment results indicate that MVEW-DNN can provide competitive predictive accuracy and robustness.

Keywords: renewable energy; wind power forecasting; hybrid model; machine learning**MSC:** 65-04

Citation: Wan, J.; Huang, J.; Liao, Z.; Li, C.; Liu, P.X. A Multi-View Ensemble Width-Depth Neural Network for Short-Term Wind Power Forecasting. *Mathematics* **2022**, *10*, 1824. <https://doi.org/10.3390/math10111824>

Academic Editors: Zhuojia Fu, Yiqian He and Hui Zheng

Received: 23 March 2022

Accepted: 17 May 2022

Published: 25 May 2022

Publisher's Note: MDPI stays neutral with regard to jurisdictional claims in published maps and institutional affiliations.



Copyright: © 2022 by the authors. Licensee MDPI, Basel, Switzerland. This article is an open access article distributed under the terms and conditions of the Creative Commons Attribution (CC BY) license (<https://creativecommons.org/licenses/by/4.0/>).

1. Introduction

Since wind power has clean and pollution-free features compared with traditional energy sources, it has become an important part of modern power systems [1–3]. In fact, accurate wind power forecasting (WPF) is becoming increasingly important because it can optimize the generation schedules and units, as well as improve the profitability and stability of the power system [4,5]. However, it is still a challenging task to obtain accurate and robust WPF due to the uncertainty, volatility, and intermittency of wind speed [6].

To improve the predictive accuracy and robustness in SWPF, various forecasting methods have been developed. These systems can be divided into physical methods, statistical methods, and machine learning methods [7]. Physical methods mainly rely on numerical weather prediction (NWP) information such as atmospheric pressure, temperature, and relative humidity [8]. For example, Zjavka et al. [9] designed a wind power forecasting system by polynomial decomposition of the general differential equation. Jacondino et al. [10] proposed a weather and research forecasting (WRF) system for forecasting wind power from two different wind farms.

Statistical methods involve the application of autoregressive dynamic adaptive (ARDA) models [11], Bayesian models [12], autoregressive moving average (ARMA) models [13], Gaussian mixture models [14,15], and the quantile regression neural network (QRNN) models [16]. In ultra-short wind power forecasting (UWPF), wind power data are almost linear. Since statistical and physical methods can be easily formulated into linear predictive models, they provide promising predictive results for UWPF [17]. However, different from UWPF, short-term wind power forecasting (SWPF) has higher volatility and more uncertain power load data. Therefore, statistical and physical methods cannot handle such nonlinear characteristics information in SWPF [18].

To obtain better predictive performance in SWPF, various machine learning models have been developed. Because machine learning effectively constructs the nonlinear mapping relationship between the input and output of wind power data, it can effectively learn and mine the nonlinear characteristics from wind power data [19]. The commonly used machine learning models are support vector machines (SVRs) [20], deep belief networks (DBNs) [21], echo state networks (ESNs) [22], extreme learning machines (ELMs) [23], and broad learning systems (BLSs) [24].

For example, as a promising deep learning network, DBN is composed of multiple restricted Boltzmann machines, which provides powerful nonlinear data processing capability. However, DBN can produce high-dimensional features because of multiple BPNN layers. This may limit the prediction performance [25]. BLS is a new single-layer incremental neural network. Its advantages lie in fast computing speed, low computing resource consumption, easy online incremental learning, and easy expansion. However, BLS needs to perform the random nodes selection and pseudo-inverse calculation, so that its predictive accuracy is often inferior to deep-learning networks in the face of large-scale data. Furthermore, a single BLS model may have problems such as over-training, poor generalization ability, or limited prediction accuracy [26].

Wind power can be significantly influenced by many natural factors such as geographical location, weather conditions, and seasonal effects [27]. To overcome the instability and intermittent nature of the time series in SWPF, the combination of the decomposition-based method and the machine learning model has been proven to be an effective solution [28]. Chen et al. [29] used the discrete wavelet transform to decompose PV output power. The decomposed subsequences were then fed into an adaptive neuro-fuzzy inference system (ANFIS) to predict the short-term PV output power. Wang et al. [30] developed the VMD-CISSA-LSSVM model, consisting of the variational modal decomposition (VMD) data preprocessing method, the sparrow search algorithm (SSA), and the least squares support vector machine (LSSVM) model, which has high prediction accuracy and stable prediction results. Devi et al. [31] rationally combined ensemble empirical mode decomposition (EEMD), cuckoo search optimization algorithm, and an improved LSTM to improve forecasting accuracy. Zhang et al. [15] integrated CEEMDAN to Gaussian process regression, which can also obtain promising prediction performance.

Furthermore, to further improve the prediction ability of a single machine learning model, hybrid models are also considered effective solutions. This because the hybrid models can compensate for the disadvantage of each method. For example, Zhao et al. [32] used CNN and attention mechanisms to provide more reliable multitask learning accuracy. In [33], the attention mechanism is combined with the gated recurrent unit (GRU) network, obtaining robust prediction performance. In [34], a novel genetic long short-term memory (GLSTM) framework was developed to provide accurate, reliable, and robust performance in SWPF. The genetic technology is used to automatically optimize LSTM parameters according to different wind power data. Khan et al. [35] combined autoencoder (AE) and bidirectional long short-term memory (BiLSTM) to form a novel hybrid model. Duan et al. [36] proposed a novel hybrid model consisting of VMD, LSTM, and PSO-DBN. Wu et al. [37] used the charged system search (CSS) algorithm to construct a hybrid model, which consists of least-squares-support vector machines (LS-SVM), a modified artificial neural network (ANN), and an adaptive network-based fuzzy inference system (ANFIS)

model. Ogliari et al. [38] built a hybrid model by combining the physical and ANN-developed models, which can give some knowledge about the wind turbine characteristics to the ANN model. Hong et al. [39] effectively combined CNN with a radial basis function neural network (RBFNN). Here, RBFNN is built for dealing with uncertain characteristics, and CNN is built for extracting wind power characteristics, so that it also has outstanding prediction performance. Ribeiro et al. [40] proposed an ensemble learning model by introducing bagging and stacking, which integrated the samples through the arithmetic and weighted average values.

Note that some multi-view hybrid models have recently also gained outstanding prediction performance. For example, Lai et al. [41] proposed a multi-view neural network by rationally combining LSTM model with RBFNN model for short- and mid-term load forecast, which has higher generalization ability. Nguyen et al. [42] decomposed time series data into a closely related time series group and a loosely related group, which are fed into a multitask learning model and a multi-view learning part, respectively. Zhong et al. [43] devised a multi-view deep forecast model for solar irradiance forecast, which uses multiple related data sets to feed into the RBFNN model and one hybrid model (MvDF).

Although the existing methods have achieved great success, there are still some problems that need to be further solved as follows:

1. For the SWPF task, the existing machine learning methods rarely consider the compromise between prediction accuracy and computation cost. Although BLS [24] has attracted considerable attention for its fast training speed and incremental learning algorithm, the prediction performance of BLS is also limited. Because BLS has problems such as the randomness of its parameter settings [26] and its sensitivity to the number of enhanced nodes, vulnerability to noise, and lack of uncertainty expression ability. Furthermore, although various deep learning models can achieve promising performance, computation costs are high.
2. Most hybrid machine learning methods rarely consider how to establish a multi-view learning mechanism, which may degenerate the predictive accuracy. Although researchers [15,30,31] have introduced decomposition in single models, the models cannot comprehensively learn original data characteristics, so that the robustness of the models is limited.
3. The attention mechanism is integrated into CNN [32] and GRU [33] for obtaining stable performance and providing feature selection, respectively. However, this technology is rarely considered for adjusting network structures while applying to different regression tasks, which may limit the improvement of model performance on other data sets.
4. Most existing models seldom consider how to effectively and stably connect two distinctly different models. For instance, a fully connected neural network is used to connect two different models in [35], which may cause gradient disappearing or exploding while connecting two much different models.

From the above analysis, our investigation mainly considers how to effectively integrate a decomposition mechanism and a multi-view learning mechanism into machine learning for efficient and stable SWPF. Considering the above motivation, this paper proposes a multi-view ensemble width-depth neural network (MVEW-DNN), which involves a local view learning subnetwork (CEEMDAN-DBN), a global view learning subnetwork (deBLS), and a feature dynamic decisionmaker (FDDM). The local view learning subnetwork covers CEEMDAN and a deep belief network (DBN), which can effectively extract part features of wind power load data. On the other hand, the global view learning subnetwork is an encoder board learning system (deBLS), which can provide more comprehensive features. In addition, the effective feature dynamic decisionmaker (FDDM) is developed to effectively fuse the local view learning subnetwork and the global view learning subnetwork.

The main contributions are as follows:

1. A novel width-depth integration model with a global view and a local view is introduced for short-term wind power forecasting. Different from other multi-view models, our model focuses on improving model performance and reducing the computational cost of the global view learning subnetwork (deBLS) as much as possible.
2. The deBLS model is developed by rationally replacing the feature nodes with the multiple encoder nodes, which can improve the learning ability of BLS. Furthermore, the deBLS introduced an attention mechanism of adjusting the enhancement nodes to achieve higher prediction accuracy.
3. An effective feature fusion model FDDM is proposed for rationally combining the deBLS and CEEMDAN-DBN, which can promise optimal predictive performance.

The rest of this paper is arranged as follows. The framework of the model and related theoretical knowledge are introduced in Section 2. Section 3 analyses the test data and details the concrete case analysis. Section 4 is the conclusion of this paper.

2. The Proposed MVEW-DNN

As shown in Figure 1, the proposed MVEW-DNN is divided into global view and local view learning subnetworks. In the local view learning subnetwork (CEEMDAN-DBN), CEEMDAN decomposes the original wind power data into multiple local view components. Then, the DBN network is used to extract the features of the local view components. In the global view learning subnetwork (deBLS), the original wind power data are regarded as the global view data. The deBLS model is developed to learn the features of the global view data. Finally, the FDDM method is developed to fuse CEEMDAN-DBN and deBLS by dynamically adjusting the fusion parameters. The FDDM method can monitor the performance of deBLS and CEEMDAN-DBN in the training phase, which can obtain the best model fusion performance.

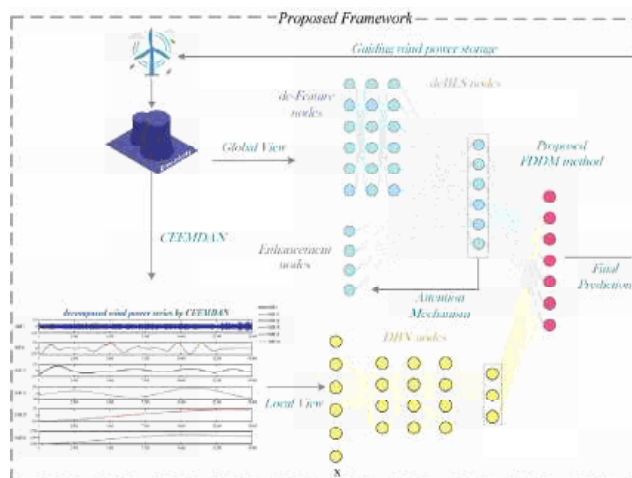


Figure 1. MVEW-DNN consists of the CEEMDAN-DBN, deBLS, and FDDM. deBLS is established for the global view. CEEMDAN-DBN is established for the local view.

2.1. Local View Subnetwork

Wind power data have high uncertainty and volatility, degenerating the predictive accuracy. To address these problems, CEEMDAN is applied to decompose the original wind power data into multiple smooth local view components called eigen-modes [44], and DBN is used to effectively capture more local view characteristics of wind power data.

2.1.1. Empirical Mode Decomposition with Adaptive Noise (CEEMDAN)

In contrast with EMD and EEMD, CEEMDAN overcomes the modal aliasing of EMD and the inefficiency of EEMD on some closely spaced spectral signals. Furthermore, CEEMDAN adds white noise to each decomposition stage so that the noise of the original data and the added white noise are superimposed and cancel each other. Therefore, CEEMDAN gradually eliminates the reconstruction error in the iterative process, which ensures the accuracy of the decomposition and greatly improves the influence of the modal aliasing. The details of CEEMDAN are given as follows:

Assumption 1. $y_0(t)$ is defined as the original signal. $n^m(t)$ is defined as a Gaussian white noise signal with a standard normal distribution, and $m \in [1, M]$. β is defined as the noise coefficient of $n^m(t)$. $E[\ast]$ is defined as the EMD decomposition. $\overline{IMF}_k(t)$ is defined as the k th intrinsic mode function obtained by the CEEMDAN.

- Step 1 Add Gaussian white noise to $y_0(t)$ to get a new signal $y_0(t) + (-1)^q \beta_0 n^m(t)$, $q = 1, 2$. Perform EMD on the new signal to get the $IMF_1^m(t)$:

$$E(y_0(t) + (-1)^q \beta_0 n^m(t)) = IMF_1^m(t) + r^m \tag{1}$$

- Step 2 Average $IMF_1^m(t)$ to get $\overline{IMF}_1(t)$, as show in Formula (2). Then, calculate the residual $r_1(t)$ after removing $\overline{IMF}_1(t)$:

$$\overline{IMF}_1(t) = \frac{1}{M} \sum_{m=1}^M IMF_1^m(t) \tag{2}$$

$$r_1(t) = y_0(t) - \overline{IMF}_1(t) \tag{3}$$

- Step 3 Add Gaussian white noise to $r_1(t)$ to get a new signal and perform EMD on the new signal to get the $IMF_2^m(t)$. Then, $\overline{IMF}_2(t)$ and residual $r_2(t)$ can be obtained:

$$\overline{IMF}_2(t) = \frac{1}{M} \sum_{m=1}^M IMF_2^m(t) \tag{4}$$

$$r_2(t) = r_1(t) - \overline{IMF}_2(t) \tag{5}$$

- Step 4 The above steps are repeated until the obtained residual signal is a monotonic function and the decomposition signal cannot be continued. At this time, the number of intrinsic mode function is K . Finally, the original signal $y_0(t)$ is decomposed into

$$y_0(t) = \sum_{k=1}^K \overline{IMF}_k(t) + r_K(t) \tag{6}$$

2.1.2. Deep Belief Network (DBN)

DBN is a probability map model that includes multiple restricted Boltzmann machines (RBM). Here, it is used to effectively extract effective local multiple view features from the decomposed smooth signals of CEEMDAN. The training process of DBN can be divided into two phases, namely pretraining and fine-tuning. In the pretraining phase, RBM is trained in an unsupervised manner. In the fine-tuning phase, DBN is treated as a backward propagation neural network for supervised learning that can fine-tune the model parameters.

2.2. Global View

Although decomposition methods such as CEEMDAN can decompose the original wind power load data into multiple smooth local view components, it may lead to the loss of the original wind data during the entire decomposed process. To compensate for the information loss from the above decomposed view components, we develop a deep encoder board learning system (deBLS) to extract global view information from original wind power data.

In the traditional BLS, its feature node generation method is feature mapping, and its number of enhancement nodes is preset. Different from the traditional BLS, deBLS has improvements in how it generates both feature nodes and enhancement nodes. Specifically, the deBLS method of generating feature nodes contains not only feature mapping but also a sparse encoder. Its number of enhanced nodes can also be automatically adjusted via an attention mechanism. The details of deBLS are given as follows:

Definition 1. X and \hat{Y} are defined as the input and output of deBLS, respectively. J_i is defined as the feature nodes, $i = 1, 2, \dots, n$. $J^n = [J_1, J_2, \dots, J_n]$ is defined as the combination of all feature nodes; δ_e , and δ_h are defined as bias matrices; and the four matrices are fine-tuned by a sparse encoder.

Step 1 By feature mapping, the original data X is mapped into n nodes K_i , as shown in Formula (7). Here, $\eta(\cdot)$ is a linear transform. Then, by increasing the depth, a three-layer sparse encoder is used to perform feature extraction on nodes K_i to obtain J^n .

$$K_i = \eta(XW_{e_i} + \delta_{e_i}), i = 1, 2, \dots, n \tag{7}$$

Step 2 By enhancing and transforming with J^n , the enhancement nodes E_k can be obtained as

$$E_k = \tanh(J^n W_{h_k} + \delta_{h_k}), k = 1, 2, \dots, m \tag{8}$$

Note that the number of enhancement nodes has an impact on the prediction performance. To obtain a suitable number of enhancement nodes, we introduce the attention mechanism to deBLS, which can automatically adjust the number of nodes of deBLS to the most suitable number in the training phase. Here, a detailed pseudo-code for the attention mechanism algorithm is given in Algorithm 1. When the number of enhancement nodes is determined, E^m and B can be obtained.

Algorithm 1: Attention Mechanism Algorithm.

// Our attention mechanism Algorithm is located on lines 11 to 13

Original data X is divided into training set and testing set. The training set consists of train-x and train-y, the testing set consists of test-x and test-y.

Input: train-x, train-y, test-x

Output: W

Process:

while 1

```

1:  if the training error threshold is not satisfied do
2:       $k = k + 1, m = m + 1$ ;
3:      Random  $W_{h_k}, \delta_{h_k}$ ;
4:      Calculate  $E_m = [\xi(J^n W_{h_k} + \delta_{h_k})]$ ;
5:      Set  $E^m = [E_1, E_2, \dots, E_m], B = [J^n | E^m]$ ;
6:       $r$  is the number of rows of matrix  $B'$ ;
7:       $I$  is a  $r \times r$  unit matrix;
8:      Set parameter  $C$  as  $2^{-30}$ ;
9:      Calculate  $W^m$  by  $\frac{B' \times \text{train-y}}{(B' \times B + I \times C)}$ ;
10:     Calculate  $Y$  by  $B \times W^m$ ;
11:     Calculate the cosine similarity between train-y and  $Y$  as  $\delta$ ;
12:      $W^m = W^m + \delta \times \omega$ ,  $\omega$  is a parameter  $\in [0, 1]$ ;
13:     Update  $Y$  by  $Y = B \times W^m$ ;
14:     Calculate the training error between  $Y$  and train-y;
15:  else
16:      break;
17:  end
18: end

```

Step 3 Calculate the weight matrix W . The predictive result \hat{Y} can be expressed as $\hat{Y} = BW$. Furthermore, during the training phase, the actual value Y is known, and therefore,

the weight matrix W can be calculated as shown in Formula (9), where B^+ is the pseudo-inverse of B :

$$W = B^+Y \tag{9}$$

To obtain a suitable W , the ridge regression is used to transform the above problem into $\operatorname{argmin}_W \left(\|\hat{Y} - Y\|_2^2 + \lambda \|W\|_2^2 \right)$. Here, λ is the regularization parameter; when $\lambda \rightarrow 0$, $W = (\lambda I + BB^T)^{-1}B^TY$ where I is the identity matrix. Thus, B^+ can be obtained as

$$B^+ = \lim_{\lambda \rightarrow 0} ((\lambda I + BB^T)^{-1}B^T). \tag{10}$$

2.3. FDDM

FDDM was developed to reasonably allocate the fusion weights of deBLS and CEEMDAN-DBN on the training stage and the test stage by dynamically adjusting the fusion parameters. This can achieve the optimal prediction performance of the proposed hybrid MVEW-DNN model (Algorithm 2).

Algorithm 2: FDDM Algorithm.

\mathcal{M} : Cross-validation fold

\mathcal{N} : The length of the test set (the number of output nodes)

\mathcal{W}_B : Fusion weight of deBLS

$V_B(\hat{V}_B)$: Prediction validation data (Real validation data) of deBLS

T_B : Prediction test data of deBLS

\mathcal{W}_D : Fusion weight of DBN

$V_D(\hat{V}_D)$: Prediction validation data (Real validation data) of DBN

T_D : Prediction test data of DBN

ρ : Correlation test threshold

Error of each node : $\varepsilon(x, y) = \frac{|x_i - y_i|}{\|x - y\|_2}, i \in [1, \mathcal{N}]$ (11)

Correlation value : $\lambda(x, y) = \frac{|\sum_{i=1}^n (x_i - \bar{x})(y_i - \bar{y})|}{\sqrt{\sum_{i=1}^n (x_i - \bar{x})^2 \sum_{i=1}^n (y_i - \bar{y})^2}}$ (12)

Process:

- 1: $\mathcal{W}_B = \mathcal{W}_D = \text{zero}[\mathcal{M}, \mathcal{N}]$;
 - 2: $\rho = 2; \mathcal{M} = 4$;
 - 3: **for** $m = 1; m \leq \mathcal{M}$ **do**
 - 4: Obtain V_B^m and \hat{V}_B^m from V_B and \hat{V}_B , respectively.
 - 5: Obtain V_D^m and \hat{V}_D^m from V_D and \hat{V}_D , respectively.
 - 6: **for** $n = 1; n \leq \mathcal{N}$ **do**
 - 7: Calculate error ε_B between V_B^m and \hat{V}_B^m by Formula (11).
 - 8: Calculate error ε_D between V_D^m and \hat{V}_D^m by Formula (11).
 - 9: **if** $\varepsilon_B^n > \varepsilon_D^n$ **then**
 - 10: $\mathcal{W}_B(m, n) = 1$; // Give deBLS a higher fusion weight.
 - 11: **else** $\mathcal{W}_D(m, n) = 1$;
 - 12: **end**
 - 13: **end**
 - 14: **for** $m = 1; m \leq \mathcal{M}$ **do**
 - 15: Calculate λ between $\mathcal{W}_B(m, :)$ and $\mathcal{W}_D(m, :)$ by Formula (12).
 - 16: **if** $\lambda < \rho$ **then**
 - 17: $\mathcal{W}_B(m, :) = \mathcal{W}_D(m, :) = []$; // Clear $\mathcal{W}_B(m, :)$ and $\mathcal{W}_D(m, :)$.
 - 18: **end**
- end**
-

Here, the original data are divided into training data set, validation data set, and the test data set, whose proportion is set as 6:2:2. The cross-validation fold parameter \mathcal{M} is set as 4, which keeps the same weight length of validation data set and test data set. Therefore, the final prediction data can be defined as $P = \mathcal{W}_B * T_B + \mathcal{W}_D * T_D$. Additionally, the

parameter ρ is set as 2, which is determined by our experimental tests [45]. In general, MVEW-DNN can effectively provide the prediction of SWPF by rationally combining deBLS and CEEMDAN-DBN.

2.4. Evaluation Criteria

To test the performance of the proposed MVEW-DNN, we use three evaluation indicators: Normalized Root Mean Square Error (NRMSE), Normalized Mean Absolute Error (NMAE), and Theil’s inequality coefficient (TIC), as shown in Formulas (13)–(15). NRMSE and NMAE are utilized to measure the deviation between the actual value and the predictive value. TIC is applied to characterize the predictive performance of predictive models. The smaller the NRMSE and NMAE are, the stronger the non-linear approximation capability is. The closer to 0 the TIC is, the stronger the spatial learning ability is:

$$NRMSE = \frac{\sqrt{\frac{1}{N} \sum_{i=1}^N (y_i - \hat{y}_i)^2}}{\hat{y}_{max} - \hat{y}_{min}} \tag{13}$$

$$NMAE = \frac{\frac{1}{N} \sum_{i=1}^N |\hat{y}_i - y_i|}{\hat{y}_{max} - \hat{y}_{min}} \tag{14}$$

$$TIC = \frac{\sqrt{\frac{1}{N} \sum_{i=1}^N (y_i - \hat{y}_i)^2}}{\sqrt{\frac{1}{N} \sum_{i=1}^N y_i^2} + \sqrt{\frac{1}{N} \sum_{i=1}^N \hat{y}_i^2}} \tag{15}$$

where \hat{y}_i and y_i are the predictive and actual values at the time i , N is the observation size.

3. Results and Discussion

3.1. Data Description and Experiment Settings

3.1.1. Data Description

The real wind power data from the Wind Forecasting track of the Global Energy Forecasting Competition 2021 (GEF-Com2021) are used to test the predictive performance of MVEW-DNN [46]. This data set contains the wind power measurement values and wind speed data from seven wind farms (WF1–WF7). The time resolution of the data is one hour. In [46], the data set was normalized. The data set contains data from 1 a.m. on 1 July 2009 to 12 a.m. on 26 June 2012. The entire data set contains 18,757 samples. In experiments, we consider the forecasts for the next 24 h. To effectively test the predictive models, the data from the last 24 h of the data set is first excluded. Then, the data set is divided into training set (75%) and testing set (25%).

Wind power data form a random, seasonal, nonlinear time series. Figure 2 displays the wind power data characteristics of the seven wind farms (wp1–wp7) in a box diagram. By analyzing the data characteristics of the seven wind farms, we find that there are inevitably abnormal data points in the data set. The abnormal data points are mainly caused by uncontrollable factors such as breakdown and operation planning [47].

Figure 3 shows some data points that correspond to high wind speeds and zero power generation. These abnormal data points are mainly caused by the shutdown of the turbine [48]. Therefore, prediction systems are required to provide high prediction accuracy and robustness when performing SWPF tasks.

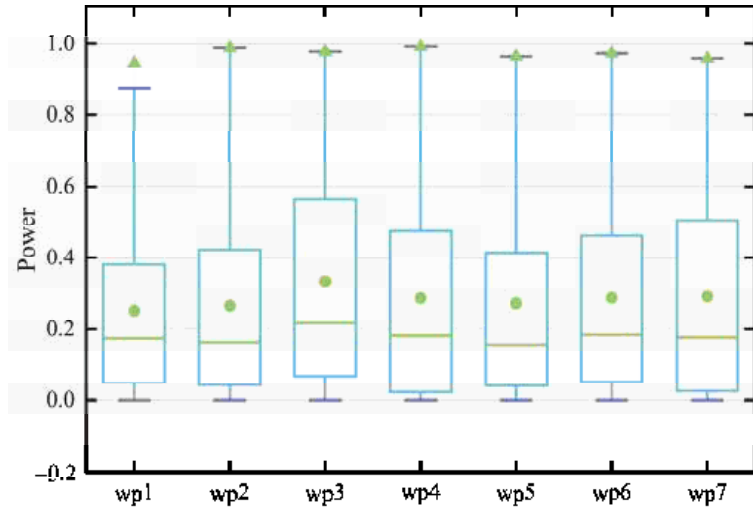


Figure 2. The wind power data characteristics of 7 wind farms. The green triangles and circles represent the outliers and the average values of the data set respectively. The short purple lines on the upper side represent the maximum values, while those on the lower side represent the minimum values. And the short green lines represent the median values.

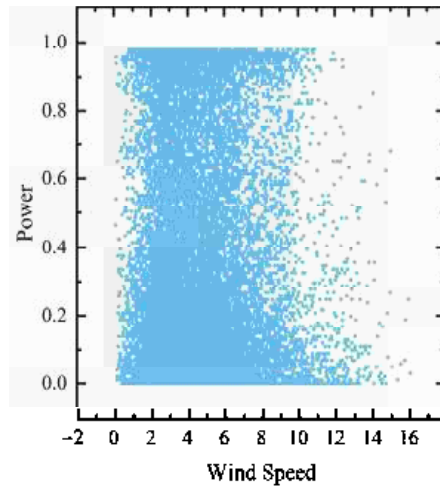


Figure 3. Wind power curve of WF3 under 1-h sampling rate. The blue points refer to the sampling moments. The vertical coordinates of the blue points indicate the wind power measurement values at the sampling moments, and the horizontal coordinates of the points are the corresponding wind speed data.

3.1.2. Experiment Settings

The parameter settings of the proposed MVEW-DNN model are given as follows. MVEW-DNN mainly consists of the local learner (DBN) and the global learner (deBLS). First, when the original data are decomposed by the CEEMDN algorithm, the signal-to-noise ratio of CEEMDN (N_{std}) is set as 0.01. The number of noise additions is set to 6. The maximum number of iterations is 2000. Then, the sub-models (IMFs) are split into training set (train-x, train-y) and testing set (test-x, test-y) in a ratio of 8 to 2. The training data set is used as input data, and the input layer of the local learner (DBN) has 20 input layer nodes. We adopt three hidden layers of 100 nodes in each layer. Each sigmoid activation function is optimized.

For the global learner, we directly use the original normalized wind power measurement values for the training task. We set the number of mapped features to 73 and the dimension of the mapped features is 6. The mapped features are mapped to the enhancement nodes. Every enhancement node group has 4 enhancement nodes. All experiments are implemented using MATLAB on a laptop equipped with Intel-i7 1.8 GHz CPU.

3.2. Models

To verify the predictive performance of the MVEW-DNN model, we compare it with some state-of-the-art and conventional predictive models in the SWPF task. These models are described as follows:

1. Autoregressive Integrated Moving Average (ARIMA) [49] is a seasonal model expressed as $ARIMA(p, d, q)(P, D, Q)_m$. Here, m refers to the number of periods in each season, and $P, D,$ and Q refer to autoregressive, differencing, and moving average terms for the seasonal part of the ARIMA model, respectively.
2. Random Vector Functional Link (RVFL) Network [50] is a multilayer perceptron (MLP). Its input and output are directly linked; only the output weights are selected as adaptive parameters. However, the remaining parameters are set to random values that are independently preselected. RVFL can also obtain promising prediction performance on SWPF tasks.
3. MOGWO-ELM [51] can provide promising SWPF by integrating the variational mode decomposition (VMD), the extreme learning machine model, the error factor, and a nonlinear ensemble method.
4. IVMD-SE-MCC-LSTM [52] is composed of the improved variational mode decomposition (IVMD), sample entropy (SE), the maximum correntropy criterion (MCC), and long short-term memory (LSTM) neural network. Here, the parameter K of the IVMD is determined by the MCC; the decomposed subseries is reconstructed by SE to improve the prediction efficiency. Then, the MCC is also utilized to replace the mean square error in the classic LSTM network.
5. Multi-view Neural Network Ensemble [41] is an ensemble of Radial Basis Function Neural Networks (RBFNN). In this ensemble neural network, a long short-term memory network (LSTM) and a multi-resolution wavelet transform are first used to extract the features for training. Then, the extracted feature data is input into multiple RBFNN networks for prediction. The output layer of the Multi-view Neural Network Ensemble is a local generalization error model, which assigns the corresponding weights to the output of multiple RBFNN networks. Finally, these output results of RBFNN are weighted and summed to provide the final predictive results.

3.3. Results

The NRMSE, NMAE, and TIC metrics are used to evaluate the predictive performance of the above six models on wind farm validation data (WF1–WF7). Interestingly, Table 1 shows that the proposed MVEW-DNN model provides lower NRMSR, NMAE, and TIC values than those of ARIMA, RVFL, MOGWO-ELM, IVMD-SE-MCC-LSTM, and Multi-view Neural Network Ensemble on WF1-WF7. For instance, the predictive results given by IVMD-SE-MCC-LSTM for NRMSE, NMAE, and TIC on WF1 are 0.2547, 0.2058, and 0.4131, respectively. On the other hand, the proposed MVEW-DNN gives 0.2103, 0.1603, and 0.3381 from NRMSE, NMAE, and TIC, respectively. Furthermore, we also provide a clear visual prediction display of the above six predictive models on WF3 in Figure 4. An interesting observation is that the proposed MVEW-DNN model has the best predictive performance among all compared models. Table 1 and Figure 4 indicate that our model can provide the best nonlinear approximation capability, robustness, and spatial learning ability among all six models.

Table 1. The NRMSE, NMAE, and TIC assessment results of the 6 models.

Data Set	Metrics	ARIMA	RVFL	MOGWO-ELM	IVMD-SE-MCC-LSTM	Multi-View Neural Network Ensemble	MVEW-DNN
WF1	NRMSE	0.4477	0.3417	0.2534	0.2547	0.2758	0.2103
	NMAE	0.3285	0.2505	0.2042	0.2058	0.1916	0.1603
	TIC	0.5878	0.651	0.4118	0.4131	0.6618	0.3381
WF2	NRMSE	0.4744	0.3494	0.2761	0.2766	0.2944	0.2236
	NMAE	0.3458	0.2575	0.2306	0.2275	0.241	0.173
	TIC	0.571	0.6543	0.4219	0.4253	0.4145	0.3281
WF3	NRMSE	0.5442	0.4566	0.3188	0.3119	0.2839	0.2378
	NMAE	0.4178	0.3373	0.2744	0.268	0.2386	0.1879
	TIC	0.5503	0.7596	0.398	0.3865	0.3714	0.2784
WF4	NRMSE	0.5008	0.4023	0.2992	0.2925	0.2664	0.2264
	NMAE	0.3686	0.2935	0.2505	0.2465	0.1859	0.1784
	TIC	0.5586	0.7166	0.4217	0.4035	0.6372	0.2954
WF5	NRMSE	0.4978	0.425	0.3208	0.3221	0.3863	0.2502
	NMAE	0.36	0.308	0.2591	0.2603	0.2738	0.1988
	TIC	0.5838	0.7119	0.453	0.4535	0.7101	0.3113
WF6	NRMSE	0.4804	0.4057	0.2915	0.2882	0.302	0.2328
	NMAE	0.356	0.2936	0.2414	0.2349	0.208	0.1821
	TIC	0.5504	0.7219	0.4078	0.4092	0.6483	0.2977
WF7	NRMSE	0.5041	0.4058	0.3025	0.2973	0.3872	0.5041
	NMAE	0.368	0.2953	0.2599	0.2541	0.2367	0.368
	TIC	0.5492	0.7502	0.4218	0.4108	0.6439	0.5492

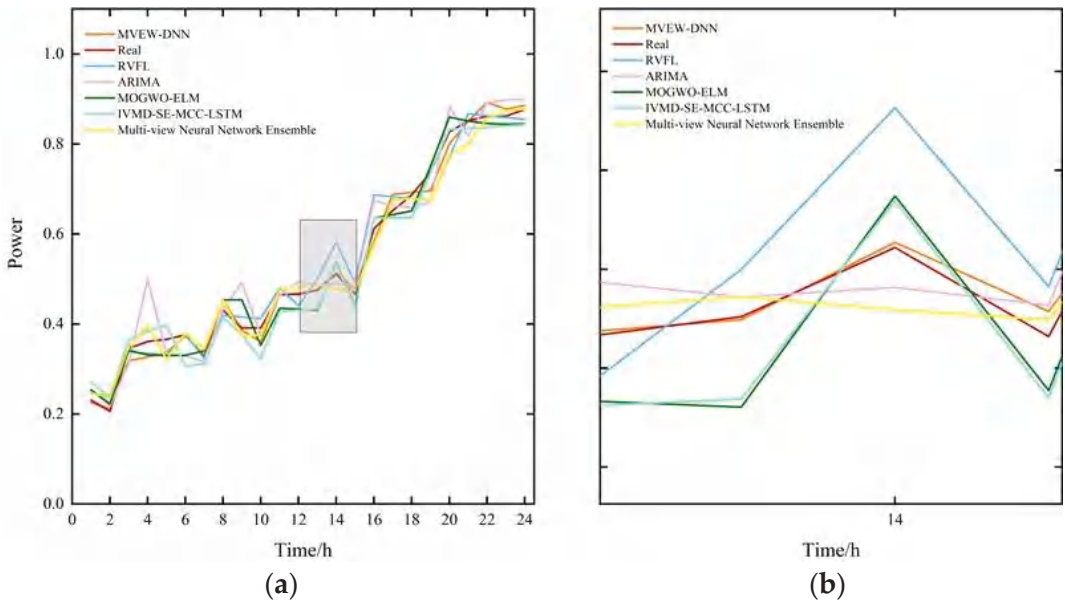
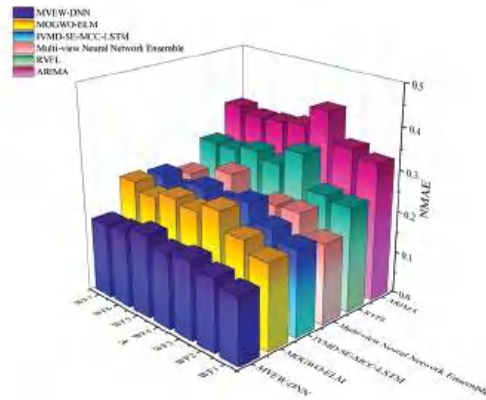


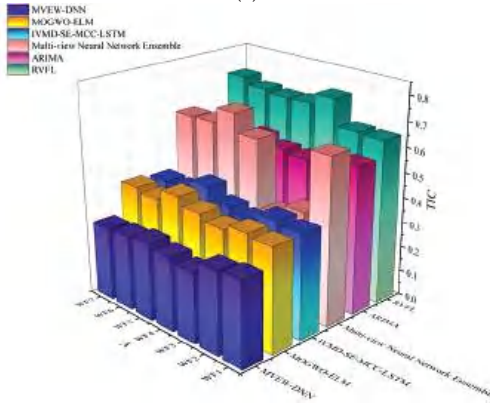
Figure 4. The prediction results are executed by the above models with the data set from WF3. (a) Prediction results from 6 models for WF3 wind power data forecasted 24-h in advance. (b) Partial enlargement of the 6 model predictions.

Figure 5 shows the NRMSE, NMAE, and TIC results for the six predictive models on WF1-WF7. We can clearly see that the proposed MVEW-DNN model achieves the

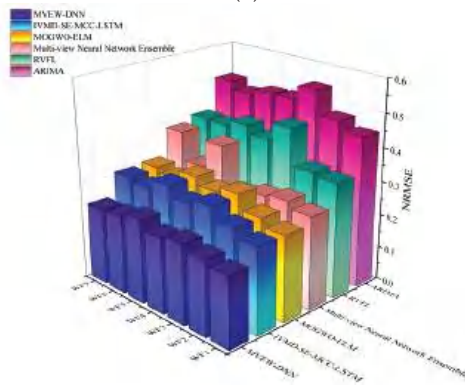
best predictive performance. This further indicates that our model has the best nonlinear approximation capability, robustness, and spatial learning ability among all six models.



(a)



(b)



(c)

Figure 5. The NRMSE, NMAE, and TIC assessment results: (a) comparison of prediction results from 6 models on NMAE; (b) comparison of prediction results from 6 models on TIC; (c) comparison of prediction results from 6 models on NRMSE.

3.4. Ablation Investigations of MVEW-DNN

Note that the proposed MVEW-DNN model covers the local view learning subnetwork (CEEMDAN-DBN), the global view learning subnetwork (deBLS), and FDDM. To evaluate the effectiveness of the local view learning subnetwork (CEEMDAN-DBN), the global view learning subnetwork (deBLS), and FDDM, ablation investigations are performed.

3.4.1. Effect of the Local View Learning Subnetwork

The local view learning subnetwork covers CEEMDAN and DBN. To evaluate the performance of the local view learning subnetwork (CEEMDAN-DBN), it is compared with DBN. The experimental results are listed in Table 2, where we can observe that CEEMDAN-DBN has better results for NRMSE, NMAE, and TIC on WF1–WF7 than DBN. For instance, CEEMDAN-DBN can provide NRMSE = 0.2555 on WF4, whereas DBN provides NRMSE = 0.3024 on WF4. CEEMDAN-DBN can provide NMAE = 0.2054 on WF4, but DBN provides NMAE = 0.2583 on WF4. These findings indicate that CEEMDAN-DBN has better nonlinear approximation capability than the single DBN. Furthermore, CEEMDAN-DBN can provide TIC = 0.3364 on WF4, whereas the single DBN achieves TIC = 0.4077. This implies that CEEMDAN-DBN has better spatial learning ability than the single DBN. From the above analyses, CEEMDAN-DBN can provide promising predictive performance on WF1–WF7.

Table 2. The assessments results of DBN and CEEMDAN-DBN on three metrics.

Data Set	Metrics	CEEMDAN-DBN	DBN
WF1	NRMSE	0.2519	0.2702
	NMAE	0.1925	0.2172
	TIC	0.3388	0.4146
WF2	NRMSE	0.2454	0.2778
	NMAE	0.1979	0.2338
	TIC	0.3595	0.4141
WF3	NRMSE	0.2845	0.3278
	NMAE	0.2346	0.2798
	TIC	0.3275	0.4021
WF4	NRMSE	0.2555	0.3024
	NMAE	0.2054	0.2583
	TIC	0.3364	0.4077
WF5	NRMSE	0.2736	0.3327
	NMAE	0.2204	0.2678
	TIC	0.3592	0.4561
WF6	NRMSE	0.2533	0.3002
	NMAE	0.2124	0.2506
	TIC	0.3155	0.4049
WF7	NRMSE	0.2512	0.3178
	NMAE	0.2102	0.2745
	TIC	0.3296	0.4195

3.4.2. Effect of the Global Network

The proposed global view learning subnetwork is called deBLS, which is composed of the attention mechanism, the additional enhancement nodes, and BLS. To assess the performance of deBLS, it is compared with BLS, BLS with the additional enhancement nodes (BLS-AEN), and BLS with the attention mechanism (BLS-A). The experimental results are presented in Table 3. It can be seen that deBLS has better results than BLS, BLS-AEN, and BLS-A on the NRMSE, NMAE, and TIC indicators of WF1–WF7. For example, deBLS can provide NRMSE = 0.2956 on WF4, whereas BLS, BLS-AEN, and BLS-A provide NRMSE = 0.3074, NRMSE = 0.3028, and NRMSE = 0.2999 on WF4, respectively. The NMAE for deBLS is 0.245 on WF4, versus 0.2521, 0.2531, and 0.251 for BLS, BLS-AEN, and BLS-A, respectively. These suggest that deBLS has better non-linear approximation capability than either BLS, BLS-AEN, and BLS-A. Furthermore, deBLS provides TIC = 0.4053 on WF4, ver-

sus TIC = 0.4174, TIC = 0.4215, and TIC = 0.4206 for BLS, BLS-AEN, and BLS-A, respectively. This implies that deBLS has better spatial learning ability. Based on the above analyses, deBLS has competitive predictive performance on WF1–WF7.

Table 3. The assessment results of BLS, BLS-AEN, BLS-A, and deBLS.

Data Set	Metrics	BLS	BLS-AEN	BLS-A	deBLS
WF1	NRMSE	0.2776	0.2713	0.2628	0.2548
	NMAE	0.2223	0.2184	0.213	0.209
	TIC	0.4082	0.4128	0.3998	0.3783
WF2	NRMSE	0.2817	0.2783	0.2759	0.2757
	NMAE	0.2329	0.2313	0.2255	0.2241
	TIC	0.418	0.4219	0.4257	0.4362
WF3	NRMSE	0.3238	0.3199	0.3127	0.3126
	NMAE	0.2731	0.2742	0.2669	0.2628
	TIC	0.3863	0.3975	0.3791	0.3879
WF4	NRMSE	0.3074	0.3028	0.2999	0.2956
	NMAE	0.2521	0.2531	0.251	0.245
	TIC	0.4174	0.4215	0.4206	0.4053
WF5	NRMSE	0.339	0.3321	0.3205	0.3179
	NMAE	0.2727	0.2683	0.2597	0.2543
	TIC	0.4451	0.4526	0.4508	0.4443
WF6	NRMSE	0.3052	0.2944	0.2925	0.2892
	NMAE	0.2462	0.2428	0.2424	0.2376
	TIC	0.408	0.4117	0.4071	0.3917
WF7	NRMSE	0.3203	0.3054	0.3023	0.2997
	NMAE	0.2652	0.2608	0.2576	0.2521
	TIC	0.4181	0.4247	0.4016	0.4085

3.4.3. Effect of FDDM

Our MVEW-DNN consists of CEEMDAN-DBN, deBLS, and FDDM. To better assess the performance of MVEW-DNN, it is compared with CEEMDAN-DBN and deBLS. The experimental results are displayed in Table 4. We can see that the proposed MVEW-DNN model has better NRMSE, NMAE, and TIC results on WF1–WF7 than either CEEMDAN-DBN or deBLS. For example, the proposed MVEW-DNN model can provide NRMSE = 0.2264 and NMAE = 0.1784 on WF4, versus either NRMSE = 0.2555 and NMAE = 0.2054 for CEEMDAN-DBN or NRMSE = 0.2956 and NMAE = 0.245 for deBLS. This indicates that the proposed MVEW-DNN has better nonlinear approximation capability than CEEMDAN-DBN and deBLS. Furthermore, the proposed MVEW-DNN model can provide TIC = 0.2954 on WF4, versus TIC = 0.3364 and TIC = 0.4053 for CEEMDAN-DBN and deBLS, respectively. This means that the proposed MVEW-DNN model has better spatial learning ability. Moreover, the above analyses also imply that FDDM can effectively integrate CEEMDAN-DBN and deBLS to improve the predictive performance of MVEW-DNN.

To highlight the prediction performance difference, we visualize the data from Tables 2–4 with the radar charts in Figure 6. Interestingly, we can see that CEEMDAN-DBN outperforms DBN in predicting wind power generation on WF1–WF7. It strongly clarifies the effectiveness of CEEMDAN. Moreover, both BLS-AEN and BLS-A have better prediction performance than that of BLS, validating the effectiveness of the attention mechanism and the additional enhancement nodes. The proposed deBLS outperforms BLS-A and BLS-AEN, further suggesting that the combination of the attention mechanism and the additional enhancement nodes can improve the prediction performance of deBLS. MVEW-DNN outperforms CEEMDAN-DBN and deBLS, indicating that FDDM can provide effective combination between CEEMDAN-DBN and deBLS.

Table 4. The results of CEEMDAN-DBN, deBLS, and the proposed MVEW-DNN model.

Data Set	Metrics	CEEMDAN-DBN	deBLS	MVEW-DNN
WF1	NRMSE	0.2519	0.2548	0.2103
	NMAE	0.1925	0.209	0.1603
	TIC	0.3388	0.3783	0.3381
WF2	NRMSE	0.2454	0.2757	0.2236
	NMAE	0.1979	0.2241	0.173
	TIC	0.3595	0.4362	0.3281
WF3	NRMSE	0.2845	0.3126	0.2378
	NMAE	0.2346	0.2628	0.1879
	TIC	0.3275	0.3879	0.2784
WF4	NRMSE	0.2555	0.2956	0.2264
	NMAE	0.2054	0.245	0.1784
	TIC	0.3364	0.4053	0.2954
WF5	NRMSE	0.2736	0.3179	0.2502
	NMAE	0.2204	0.2543	0.1988
	TIC	0.3592	0.4443	0.3113
WF6	NRMSE	0.2533	0.2892	0.2328
	NMAE	0.2124	0.2376	0.1821
	TIC	0.3155	0.3917	0.2977
WF7	NRMSE	0.2512	0.2997	0.2271
	NMAE	0.2102	0.2521	0.1782
	TIC	0.3296	0.4085	0.2926

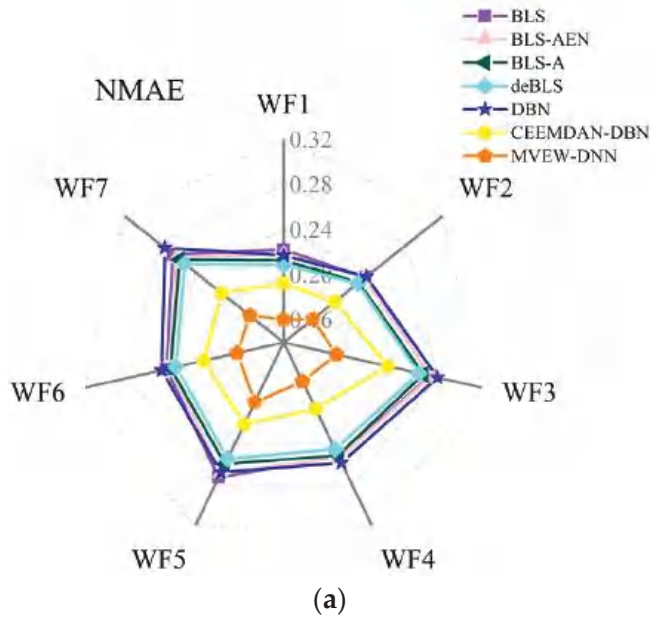


Figure 6. Cont.

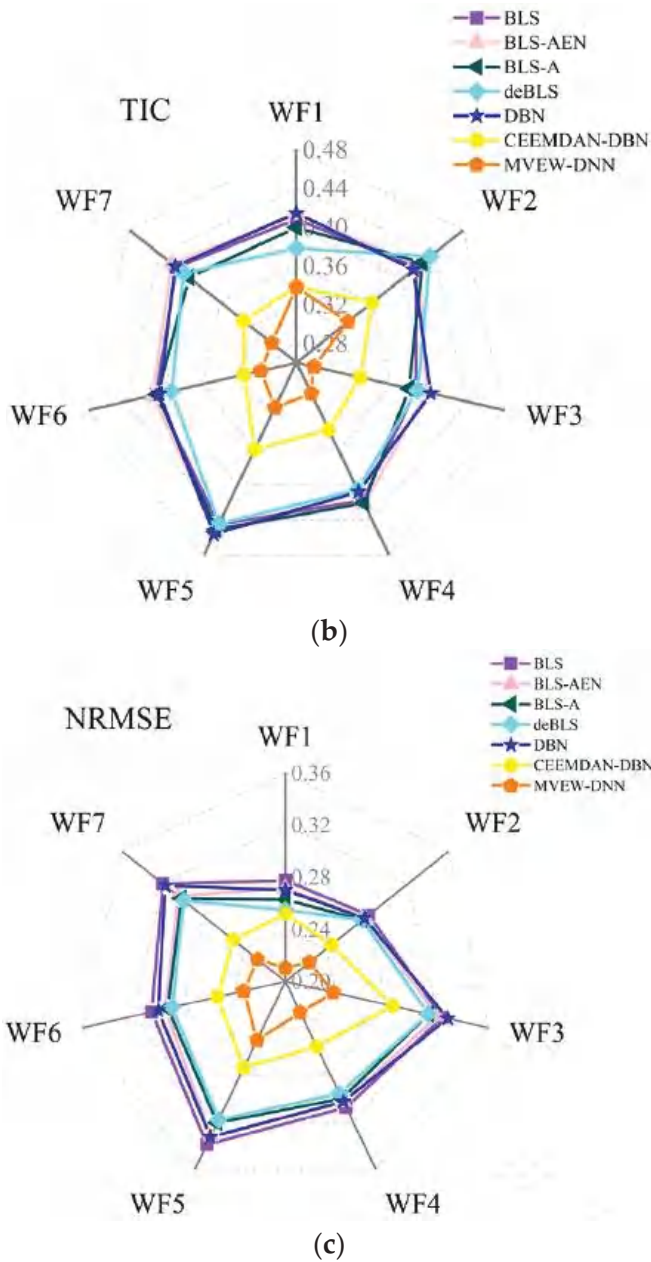


Figure 6. Ablation experiments on NMAE, TIC, and NRMSE evaluation indicators for 7 wind power data sets: (a) results of ablation experiments on NMAE evaluation indicators for 7 wind power data sets; (b) results of ablation experiments on TIC evaluation indicator for 7 wind power data sets; (c) results of ablation experiments on NRMSE evaluation indicator for 7 wind power data sets.

3.5. Parameter Selection Experiments

Our proposed model involves only one key parameter, ω , which is used for the attention mechanism. It serves to adjust the output layer weights W^m (see Algorithm 1). The different values of ω inevitably lead to discrepancies in the global learner predictions.

We apply different values of ω to optimize the global learner on different sub-data sets. Some representative results are listed in Table 5. It can be seen that the different values of ω provide similar results for NRMSE, NMAE, and TIC on WF3. This indicates that MVEW-DNN is insensitive to ω . This further implies that MVEW-DNN has promising robustness in predictive performance.

Table 5. Effect of adjusting parameter ω with the data from WF3.

ω	NRMSE	NMAE	TIC
0.5	0.3275	0.2794	0.3881
0.6	0.3268	0.2692	0.3857
0.7	0.3263	0.2792	0.3835
0.8	0.3257	0.2891	0.3814

3.6. Discussion

Based on the above experiments, our proposed MVEW-DNN has outstanding predictive performance in the SWPF field, mainly for the following reasons:

First, MVEW-DNN provides global and local view learning subnetworks, which can effectively learn more potential feature information to enhance the prediction accuracy.

Second, in MVEW-DNN, deBLS can provide higher predictive accuracy by rationally integrating the attention mechanism and the additional enhancement nodes.

Third, FDDM can provide effective feature fusion between the global and local view learning subnetworks to perfectly complement each other.

Fourth, the local view learning subnetwork provides the combination of CEEMDAN and DBN to achieve more potential local view feature data in SWPF, effectively reducing the impact of data volatility and avoiding the model confounding problem on model prediction results.

4. Conclusions

In this paper, the developed MVEW-DNN model is a new width-depth integrated predictor that consists of a global view learning subnetwork and a local view learning subnetwork. The global view learning subnetwork effectively integrates the attention mechanism and the additional enhancement nodes, which gives it the advantages of low computational cost and high prediction accuracy. The local view learning subnetwork rationally combines CEEMDAN and DBN, which can achieve better potential local view features, enhancing the predictive accuracy and robustness. FDDM can provide an effective feature fusion between the global and local view learning subnetworks, further enhancing the predictive accuracy and robustness. Therefore, the proposed MVEW-DNN provides better predictive performance, e.g., nonlinear approximation capability and spatial learning ability, than that of the state-of-the-art and conventional predictive models on the SWPF task. MVEW-DNN can effectively and significantly improve the wind power schedule and production program, which relieves the pressure on the power system for peak and frequency regulation, to greatly improve the wind energy utilization. Table 6 shows that the high time-computation costs of our model are mainly due to the local view learning subnetwork (CEEMDAN-DBN). Therefore, in the future, we will consider how to effectively reduce the computational costs of the proposed MVEW-DNN.

Table 6. The time computation costs of deBLS, CEEMDAN-DBN, FDDM, and the proposed MVEW-DNN.

Wind Farm	deBLS (s)	CEEMDAN-DBN (s)	FDDM (s)	MVEW-DNN (s)
WF1	0.654	142.582	0.984	144.22
WF2	0.833	135.888	0.994	137.715
WF3	0.438	149.442	0.643	150.523
WF4	0.394	160.626	0.717	161.737
WF5	0.423	188.86	0.815	190.098
WF6	0.417	163.324	0.893	164.634
WF7	0.433	172.055	0.927	173.415

Author Contributions: Conceptualization, J.H., J.W. and Z.L.; methodology, J.H., J.W. and Z.L.; software, J.W., J.H. and Z.L.; validation, J.W.; formal analysis, J.H., J.W. and Z.L.; investigation, J.W.; resources, J.W.; data curation, J.W.; writing—original draft preparation, J.H., J.W. and Z.L.; writing—review and editing, C.L., J.H. and Z.L.; visualization, J.W.; supervision, C.L. and P.X.L.; project administration, C.L. and J.H.; funding acquisition, C.L. All authors have read and agreed to the published version of the manuscript.

Funding: This work was supported in part by the National Natural Science Foundation of China under grants 61863028, 62173176, 81660299, and 61503177, and in part by the Science and Technology Department of Jiangxi Province of China under grants 20204ABC03A39, 20161ACB21007, 20171BBE50071, and 20171BAB202033.

Institutional Review Board Statement: The study did not involve humans or animals.

Informed Consent Statement: The study did not involve humans.

Data Availability Statement: Publicly available data sets were analyzed in this study. These data can be found here: [<https://www.kaggle.com/c/GEF2012-wind-forecasting/data>] (accessed on 14 October 2021).

Conflicts of Interest: The authors declare no conflict of interest.

Abbreviations

SWPF	Short-term wind power forecasting
CEEMDAN	Complete ensemble empirical mode decomposition with adaptive noise
BLS-AEN	BLS network with Addition Enhancement Nodes
BLS-A	The BLS network with Attention Mechanism
deBLS	Deep encoder based learning system
MVEW-DNN	Multi-view ensemble-based width-depth neural network

Variables

$X(t)$	The original wind power data
$IMF_k(t)$	The k th decomposition in CEEMDAN
W_{e_i}	The randomly generated weight matrix
δ_{e_i}	The randomly generated bias matrix
J_n	The feature nodes
J^n	The feature nodes group
E_m	The enhancement nodes
E^m	The enhancement nodes group
B	The combination matrix of J^n and E^m
P	The output of our proposed model
W_B	The fusion weight of deBLS
W_D	The fusion weight of DBN

Indices

k	The IMF index
n	The index of the feature nodes
m	The index of the enhancement nodes
N_{std}	The signal-to-noise ratio
ω	The adjusting weights in attention mechanism algorithm
C	The regularization parameter for sparse regularization
S	The shrinkage parameter in deBLS
ρ	The correlation test threshold

References

- Hong, T.; Pinson, P.; Wang, Y.; Weron, R.; Yang, D.; Zareipour, H. Energy forecasting: A review and outlook. *IEEE Open Access J. Power Energy* **2020**, *7*, 376–388. [CrossRef]
- Singh, U.; Rizwan, M. A Systematic Review on Selected Applications and Approaches of Wind Energy Forecasting and Integration. *J. Inst. Eng. Ser. B* **2021**, *102*, 1061–1078. [CrossRef]
- Kerem, A.; Saygin, A.; Rahmani, R. A green energy research: Forecasting of wind power for a cleaner environment using robust hybrid metaheuristic model. *Environ. Sci. Pollut. Res.* **2021**. [CrossRef]

4. Liu, H.; Li, Y.; Duan, Z.; Chen, C. A review on multi-objective optimization framework in wind energy forecasting techniques and applications. *Energy Convers. Manag.* **2020**, *224*, 113324. [CrossRef]
5. Maciejowska, K.; Nitka, W.; Weron, T. Enhancing load, wind and solar generation for day-ahead forecasting of electricity prices. *Energy Econ.* **2021**, *99*, 105273. [CrossRef]
6. Rodriguez, H.; Flores, J.J.; Morales, L.A.; Lara, C.; Guerra, A.; Manjarrez, G. Forecasting from incomplete and chaotic wind speed data. *Soft Comput.* **2019**, *23*, 10119–10127. [CrossRef]
7. Yang, B.; Zhong, L.; Wang, J.; Shu, H.; Zhang, X.; Yu, T.; Sun, L. State-of-the-art one-stop handbook on wind forecasting technologies: An overview of classifications, methodologies, and analysis. *J. Clean. Prod.* **2021**, *283*, 124628. [CrossRef]
8. Foley, A.M.; Leahy, P.G.; Marvuglia, A.; McKeogh, E.J. Current methods and advances in forecasting of wind power generation. *Renew. Energy* **2012**, *37*, 1–8. [CrossRef]
9. Zjavka, L.; Mišák, S. Direct wind power forecasting using a polynomial decomposition of the general differential equation. *IEEE Trans. Sustain. Energy* **2018**, *9*, 1529–1539. [CrossRef]
10. Jacondino, W.D.; da Silva Nascimento, A.L.; Calvetti, L.; Fisch, G.; Beneti, C.A.; da Paz, S.R. Hourly day-ahead wind power forecasting at two wind farms in northeast Brazil using WRF model. *Energy* **2021**, *230*, 120841. [CrossRef]
11. Zhang, F.; Li, P.C.; Gao, L.; Liu, Y.Q.; Ren, X.Y. Application of autoregressive dynamic adaptive (ARDA) model in real-time wind power forecasting. *Renew. Energy* **2021**, *169*, 129–143. [CrossRef]
12. Xie, W.; Zhang, P.; Chen, R.; Zhou, Z. A nonparametric Bayesian framework for short-term wind power probabilistic forecast. *IEEE Trans. Power Syst.* **2018**, *34*, 371–379. [CrossRef]
13. Zhang, J.; Wang, C. Application of ARMA model in ultra-short term prediction of wind power. In Proceedings of the 2013 International Conference on Computer Sciences and Applications IEEE, Washington, DC, USA, 14–15 December 2013; pp. 361–364.
14. Jia, M.; Shen, C.; Wang, Z. A distributed incremental update scheme for probability distribution of wind power forecast error. *Int. J. Electr. Power Energy Syst.* **2020**, *121*, 106151. [CrossRef]
15. Zhang, C.; Peng, T.; Nazir, M.S. A novel hybrid approach based on variational heteroscedastic Gaussian process regression for multi-step ahead wind speed forecasting. *Int. J. Electr. Power Energy Syst.* **2022**, *136*, 107717. [CrossRef]
16. He, Y.; Zhang, W. Probability density forecasting of wind power based on multi-core parallel quantile regression neural network. *Knowl.-Based Syst.* **2020**, *209*, 106431. [CrossRef]
17. Pearre, N.S.; Swan, L.G. Statistical approach for improved wind speed forecasting for wind power production. *Sustain. Energy Technol. Assess.* **2018**, *27*, 180–191.
18. Hu, T.; Wu, W.; Guo, Q.; Sun, H.; Shi, L.; Shen, X. Very short-term spatial and temporal wind power forecasting: A deep learning approach. *CSEE J. Power Energy Syst.* **2019**, *6*, 434–443.
19. Zendejboudi, A.; Baseer, M.A.; Saidur, R. Application of support vector machine models for forecasting solar and wind energy resources: A review. *J. Clean. Prod.* **2018**, *199*, 272–285. [CrossRef]
20. Li, R.; Ke, Y.Q.; Zhang, X.Q. Wind power forecasting based on time series and SVM. *Electr. Power* **2012**, *45*, 64–68.
21. Sun, W.; Wang, Y. Short-term wind speed forecasting based on fast ensemble empirical mode decomposition, phase space reconstruction, sample entropy and improved back-propagation neural network. *Energy Convers. Manag.* **2018**, *157*, 1–12. [CrossRef]
22. Hu, H.; Wang, L.; Lv, S.X. Forecasting energy consumption and wind power generation using deep echo state network. *Renew. Energy* **2020**, *154*, 598–613. [CrossRef]
23. Shetty, R.P.; Sathyabhama, A.; Pai, P.S. An efficient online sequential extreme learning machine model based on feature selection and parameter optimization using cuckoo search algorithm for multi-step wind speed forecasting. *Soft Comput.* **2021**, *25*, 1277–1295. [CrossRef]
24. Chen, C.P.; Liu, Z. Broad learning system: An effective and efficient incremental learning system without the need for deep architecture. *IEEE Trans. Neural Netw. Learn. Syst.* **2017**, *29*, 10–24. [CrossRef] [PubMed]
25. Hu, Q.; Zhang, R.; Zhou, Y. Transfer learning for short-term wind speed prediction with deep neural networks. *Renew Energy* **2016**, *85*, 83–95. [CrossRef]
26. Xu, L.; Chen, C.P.; Han, R. Sparse Bayesian broad learning system for probabilistic estimation of prediction. *IEEE Access* **2020**, *8*, 56267–56280. [CrossRef]
27. Yan, J.; Liu, Y.; Han, S.; Wang, Y.; Feng, S. Reviews on uncertainty analysis of wind power forecasting. *Renew. Sustain. Energy Rev.* **2015**, *52*, 1322–1330. [CrossRef]
28. Jiajun, H.; Chuanjin, Y.; Yongle, L.; Huoyue, X. Ultra-short term wind prediction with wavelet transform, deep belief network and ensemble learning. *Energy Convers. Manag.* **2020**, *205*, 112418. [CrossRef]
29. Chen, C.R.; Ouedraogo, F.B.; Chang, Y.M.; Larasati, D.A.; Tan, S.W. Hour-Ahead Photovoltaic Output Forecasting Using Wavelet-ANFIS. *Mathematics* **2021**, *9*, 2438. [CrossRef]
30. Wang, G.; Wang, X.; Wang, Z.; Ma, C.; Song, Z. A VMD-CISSA-LSSVM Based Electricity Load Forecasting Model. *Mathematics* **2022**, *10*, 28.
31. Devi, A.S.; Maragatham, G.; Boopathi, K.; Rangaraj, A.G. Hourly day-ahead wind power forecasting with the EEMD-CSO-LSTM-EFG deep learning technique. *Soft Comput.* **2020**, *24*, 12391–12411. [CrossRef]

32. Zhao, X.; Bai, M.; Yang, X.; Liu, J.; Yu, D.; Chang, J. Short-term probabilistic predictions of wind multi-parameter based on one-dimensional convolutional neural network with attention mechanism and multivariate copula distribution estimation. *Energy* **2021**, *234*, 121306. [CrossRef]
33. Niu, Z.; Yu, Z.; Tang, W.; Wu, Q.; Reformat, M. Wind power forecasting using attention-based gated recurrent unit network. *Energy* **2020**, *196*, 117081. [CrossRef]
34. Shahid, F.; Zameer, A.; Muneeb, M. A novel genetic LSTM model for wind power forecast. *Energy* **2021**, *223*, 120069. [CrossRef]
35. Khan, N.; Ullah, F.U.M.; Haq, I.U.; Khan, S.U.; Lee, M.Y.; Baik, S.W. AB-Net: A Novel Deep Learning Assisted Framework for Renewable Energy Generation Forecasting. *Mathematics* **2021**, *9*, 2456. [CrossRef]
36. Duan, J.; Wang, P.; Ma, W.; Fang, S.; Hou, Z. A novel hybrid model based on nonlinear weighted combination for short-term wind power forecasting. *Int. J. Electr. Power Energy Syst.* **2022**, *134*, 107452. [CrossRef]
37. Wu, Y.K.; Su, P.E.; Hong, J.S. Stratification-based wind power forecasting in a high-penetration wind power system using a hybrid model. *IEEE Trans. Ind. Appl.* **2016**, *52*, 2016–2030. [CrossRef]
38. Ogliari, E.; Guilizzoni, M.; Giglio, A.; Pretto, S. Wind power 24-h ahead forecast by an artificial neural network and an hybrid model: Comparison of the predictive performance. *Renew. Energy* **2021**, *178*, 1466–1474. [CrossRef]
39. Hong, Y.Y.; Rioflorido, C.L.P.P. A hybrid deep learning-based neural network for 24-h ahead wind power forecasting. *Appl. Energy* **2019**, *250*, 530–539. [CrossRef]
40. Ribeiro, M.H.D.M.; da Silva, R.G.; Moreno, S.R.; Mariani, V.C.; dos Santos Coelho, L. Efficient bootstrap stacking ensemble learning model applied to wind power generation forecasting. *Int. J. Electr. Power Energy Syst.* **2022**, *136*, 107712. [CrossRef]
41. Lai, C.S.; Yang, Y.; Pan, K.; Zhang, J.; Yuan, H.; Ng, W.W.; Gao, Y.; Zhao, Z.; Wang, T.; Shahidehpour, M.; et al. Multi-view neural network ensemble for short and mid-term load forecasting. *IEEE Trans. Power Syst.* **2020**, *36*, 2992–3003. [CrossRef]
42. Nguyen, L.H.; Pan, Z.; Openiyi, O.; Abu-gellban, H.; Moghadasi, M.; Jin, F. Self-boosted time-series forecasting with multi-task and multi-view learning. *arXiv* **2019**, arXiv:1909.08181.
43. Zhong, C.; Lai, C.S.; Ng, W.W.; Tao, Y.; Wang, T.; Lai, L.L. Multi-view deep forecasting for hourly solar irradiance with error correction. *Sol. Energy* **2021**, *228*, 308–316. [CrossRef]
44. Torres, M.E.; Colominas, M.A.; Schlotthauer, G.; Flandrin, P. A Complete Ensemble Empirical Mode Decomposition with Adaptive Noise. In Proceedings of the 2011 IEEE International Conference on Acoustics, Speech and Signal Processing (ICASSP), Prague, Czech Republic, 22–27 May 2011; pp. 4144–4147.
45. Flores, J.H.F.; Engel, P.M.; Pinto, R.C. Autocorrelation and Partial Autocorrelation Functions to Improve Neural Networks Models on Univariate Time Series Forecasting. In Proceedings of the The 2012 International Joint Conference on Neural Networks (IJCNN) IEEE, San Diego, CA, USA, 10–15 June 2012; pp. 1–8.
46. Global Energy Forecasting Competition 2012—Wind Forecasting. Available online: <https://www.kaggle.com/c/GEF2012-wind-forecasting/data> (accessed on 14 October 2021).
47. Kisvari, A.; Lin, Z.; Liu, X. Wind power forecasting—A data-driven method along with gated recurrent neural network. *Renew. Energy* **2021**, *163*, 1895–1909. [CrossRef]
48. Zhu, Y.; Zhu, C.; Song, C.; Li, Y.; Chen, X.; Yong, B. Improvement of reliability and wind power generation based on wind turbine real-time condition assessment. *Int. J. Electr. Power Energy Syst.* **2019**, *113*, 344–354. [CrossRef]
49. Putz, D.; Gumhalter, M.; Auer, H. A novel approach to multi-horizon wind power forecasting based on deep neural architecture. *Renew. Energy* **2021**, *178*, 494–505. [CrossRef]
50. Ren, Y.; Suganthan, P.N.; Srikanth, N.; Amaratunga, G. Random vector functional link network for short-term electricity load demand forecasting. *Inf. Sci.* **2016**, *367*, 1078–1093. [CrossRef]
51. Hao, Y.; Tian, C. A novel two-stage forecasting model based on error factor and ensemble method for multi-step wind power forecasting. *Appl. Energy* **2019**, *238*, 368–383. [CrossRef]
52. Duan, J.; Wang, P.; Ma, W. Short-term wind power forecasting using the hybrid model of improved variational mode decomposition and Correntropy Long Short-term memory neural network. *Energy* **2021**, *214*, 118980. [CrossRef]

Article

Study on Failure Characteristics and Control Technology of Roadway Surrounding Rock under Repeated Mining in Close-Distance Coal Seam

Yuqi Shang ¹, Dezhong Kong ^{1,2,*}, Shijiang Pu ³, Yu Xiong ¹, Qiang Li ¹ and Zhanbo Cheng ^{4,*}

¹ College of Mining, Guizhou University, Guiyang 550025, China; gs.yqshang20@gzu.edu.cn (Y.S.); gs.xiongy19@gzu.edu.cn (Y.X.); gs.liq19@gzu.edu.cn (Q.L.)

² State Key Laboratory of Public Big Data, Guizhou University, Guiyang 550025, China

³ Faculty of Land and Resources Engineering, Kunming University of Science and Technology, Kunming 650093, China; pu_shijiang@163.com

⁴ School of Engineering, University of Warwick, Coventry CV4 7AL, UK

* Correspondence: dzkong@gzu.edu.cn (D.K.); z.cheng.4@warwick.ac.uk (Z.C.)

Abstract: In this study, taking the Sheng'an coal mine as an engineering background, the failure characteristics of the surrounding rock of a roadway under repeated mining in a close-distance coal seam is comprehensively illustrated through field measurements (e.g., drilling imaging), theory analysis and numerical simulation (finite difference method (FDM)). The results show that although the return airway 10905 remains intact, the apparent failure of the roadway's roof and the coal pillar can be observed. In addition, the expression of floor failure depth caused by upper coal seam mining is obtained through elastic-plastic theory. Meanwhile, the deformation of the surrounding rock of the roadway increases with the increase of repeated mining times, especially for the horizontal displacement of the roadway on the coal pillar side. Moreover, the cracks' evolution of surrounding rock in the roadway can be observed as asymmetric characteristics. Finally, the stability control technology of "asymmetric anchor net cable + I-steel" is proposed to prevent potential mining disasters, and the feasibility of this support scheme is verified by numerical simulation and field practices. It can meet the requirement of safe mining and provide guidelines to effectively solve the failure of a roadway in close-distance coal seam mining.

Keywords: failure characteristics; surrounding rock of roadway; repeated mining; close-distance coal seam; stability control technology

MSC: 86-08; 86-10; 65E05

Citation: Shang, Y.; Kong, D.; Pu, S.; Xiong, Y.; Li, Q.; Cheng, Z. Study on Failure Characteristics and Control Technology of Roadway Surrounding Rock under Repeated Mining in Close-Distance Coal Seam.

Mathematics **2022**, *10*, 2166. <https://doi.org/10.3390/math10132166>

Academic Editors: Zhuojia Fu, Yiqian He and Hui Zheng

Received: 19 May 2022

Accepted: 20 June 2022

Published: 21 June 2022

Publisher's Note: MDPI stays neutral with regard to jurisdictional claims in published maps and institutional affiliations.



Copyright: © 2022 by the authors. Licensee MDPI, Basel, Switzerland. This article is an open access article distributed under the terms and conditions of the Creative Commons Attribution (CC BY) license (<https://creativecommons.org/licenses/by/4.0/>).

1. Introduction

In the process of coal formation, it will experience many crustal movements, and the coal measure strata are hosted in sedimentary rocks. Therefore, multiple coal seams will appear in the same coal measure strata with a small distance between the adjacent multi-coal seams. Different from the mining of a single coal seam, the mining activities of a close coal seam group can be influenced by each other's coal seams with the characteristics of mutual disturbance, stress concentration and severe damage to the mining roadway [1–4]. The roadway in the lower coal seam is significantly affected by the caving gangue generated after upper coal seam mining and the dynamic pressure due to the mining activities of the adjacent working face. Therefore, the roof management of the working face under repeated mining should be paid more attention in order to prevent the occurrence of mining disasters. In the process of coal formation, it will experience many crustal movements, and the coal measure strata are hosted in sedimentary rocks. Therefore, multiple coal seams will appear in the same coal measure strata with a small distance between the adjacent multi-coal seams. Different from the mining of a single coal seam, the mining activities of a close coal

seam group can be influenced by each other's coal seams with the characteristics of mutual disturbance, stress concentration and severe damage to the mining roadway [5–10]. The roadway in the lower coal seam is significantly affected by the caving gangue generated after upper coal seam mining and the dynamic pressure due to the mining activities of the adjacent working face.

Currently, the support theory and control technology of the surrounding rock of a roadway under repeated mining in a close-distance coal seam is comprehensively illustrated. Refs. studied the dynamic stress evolution law of floor in the process of repeated mining and discussed the distribution characteristics of surrounding rock stress and the displacement of floor roadway. Meanwhile, the grouting bolt to strengthen shallow broken surrounding rock and hollow grouting anchor cable to strengthen deep cracks combined with double anchor mesh shotcrete support were proposed to fully mobilize the self-supporting ability of the surrounding rock. In addition, Xiong et al. [11] illustrated the stress distribution of the floor under the repeated mining and the staggered arrangement of the roadway in the lower coal seam. Zhang et al. [12] illustrated that the lower coal mining roadway was prone to instability under the action of the low support strength of the roadway, the over-speed mining and the vertical arrangement of the upper coal seam roadway. Liu et al. [13] proposed the segmented support design technology to control different types of roofs, which can significantly improve the stress state of the surrounding rock. Using numerical simulation, Han et al. [14] conducted the roadway stability under a reinforcement support scheme. The results showed that the instability mechanism of the roadway met the requirements of an extremely close coal seam, and the section shrinkage rate remained at 5.29%. Cheng et al. [15] proposed three schemes of lengthening an anchor bolt combined support to solve the problem of significant roof subsidence in the roadway of the lower coal seam. Geng et al. [16] analyzed the plastic failure characteristics, stress distribution and displacement variation of the roadway under the influence of the superimposed stress after the upper coal seam mining. Then the comprehensive roof control technology of 'broken roof hole + pressure relief hole + high pre-stressed anchor cable + single hydraulic prop' was proposed.

Throughout the literature review, the current research mainly focused on the stress distribution law of a floor under a coal pillar in the close-distance coal seam group mining and the layout offset of a roadway in the lower coal seam. However, there are few studies proposing the stability control technology to support the surrounding rock of a roadway in the lower coal seam while considering the action of the caving gangue generated in the upper coal seam and the dynamic pressure due to the mining activities of the adjacent working face. There may be no residual coal pillar after the upper coal seam mining when the close-distance coal seam group adopts the downward mining method. In addition, the stress and displacement of the surrounding rock of the roadway under the repeated mining in the close-distance coal seam group should be explored in detail. Therefore, taking the Sheng'an coal mine in Guizhou Province (China) as an engineering background, this study aims to illustrate the failure characteristics and instability law of the surrounding rock of the roadway in the lower coal seam and the damage depth of the floor caused by the upper coal seam mining [17,18]. Most importantly, the corresponding support techniques are proposed and applied in engineering practices, which provide the guideline to control the stability of the surrounding rock of the roadway in similar mining conditions.

2. Engineering Background

2.1. Geological Conditions

The Sheng'an coal mine has two main coal seams, named #6 and #9, respectively. The coal seam #9 is buried with a depth of 191 m and an average thickness of 1.81 m. Moreover, its roof is silty mudstone, argillaceous siltstone and mudstone, and its floor is mudstone, silty mudstone and argillaceous siltstone. On the other hand, the coal seam #6 with an average thickness of 1.26 m is away from coal seam #9 by 4.14–7.01 m, which is a typical close-distance coal seam group.

The working face 10905 is arranged in coal seam #9 without leaving the coal pillar, located in the south of working face 10903, as shown in Figures 1 and 2. Moreover, the return airway of working face 10905 and the transportation roadway of working face 10903 are separated by coal pillars of 13 m. Therefore, significant roof subsidence and horizontal displacement of the return airway in working face 10905 during the excavation process can be observed due to the influence of upper coal seam #6 mining and the adjacent working face 10903 mining. Notably, various disasters (e.g., roof leakage and roof caving) can be observed, which greatly affect the safe and efficient production of the mine in working face 10905.

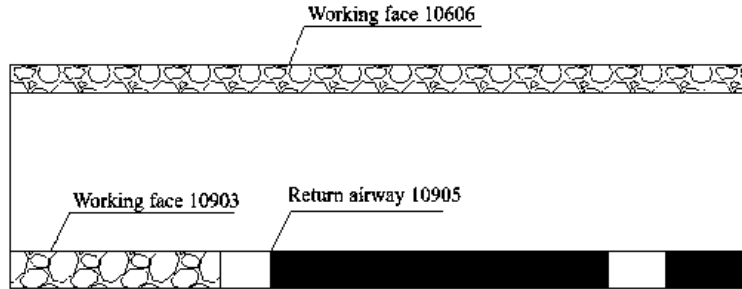


Figure 1. Arrangement of multi-working faces.

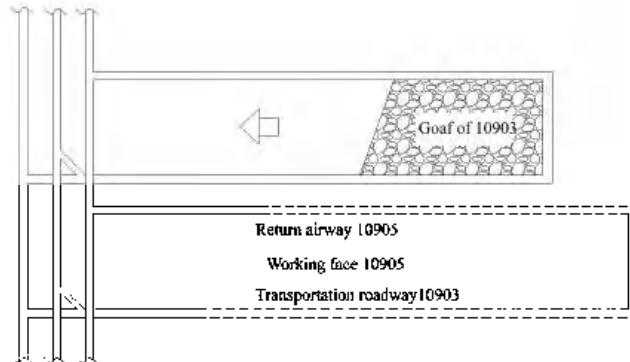


Figure 2. Arrangement of working face 10905.

2.2. Roof Failure Characteristics of Return Airway in Working Face 10905

The working face 10905 mined coal seam #9 is arranged below the 10606 working face of coal seam #6. Originally, the bolt + I-steel combined symmetric support scheme was adopted as shown in Figure 3. The row spacing between the bolts is 0.8×0.8 m, and the spacing between the sheds and frames is 0.8 m. However, the sidewall of the return airway is not fully supported, and the I-steel is only used to maintain the stability of the roadway. Due to the neglect of the asymmetry of the stress and deformation of the roadway sidewall, severe sidewall heave and roof subsidence deformation can still be observed in the process of roadway excavation, as shown in Figure 4.

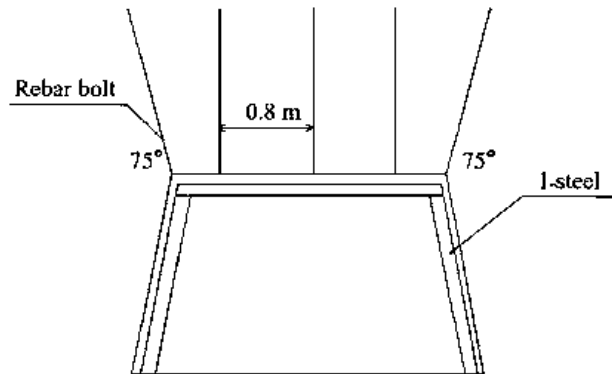


Figure 3. Previous support scheme of return airway of working face 10905.



Figure 4. Deformation of surrounding rock during roadway excavation.

Based on the results of drilling images, Figure 5 illustrates that there are few cracks in the upper part of the roadway roof from 2.5 to 3.0 m, while the surrounding rock of the borehole is relatively complete. In addition, an obvious transverse fracture in the upper roof 3.5 m can be observed, which is similar to the annular interval fracture zone. Moreover, the loose fracture of the surrounding rock in the borehole is observed at the upper roof of 4 m, and zoning fracture exists in shallow and deep parts of the roadway roof. On the other hand, the integrity of the surrounding rock in the borehole is good when the borehole depth on the coal pillar side of the roadway reaches 1.5–2 m as shown in Figure 6. When the drilling depth reaches 2.5 m, the coal body begins in a broken state. Meanwhile, the number of cracks is small, and there are few longitudinal cracks when the depth of the borehole on the side of the roadway increases to 1.5 m, as shown in Figure 7. With the increase of drilling depth, the shape of longitudinal fractures decreases, and the integrity of the surrounding rock is good at the drilling depth of 2.5–3 m. The comprehensive analysis shows that the roadway roof of working face 10905 is not fully broken, while the overall bearing capacity is weak. However, the roof and coal pillar side of the roadway are obviously broken in different areas. It is possible that a large deformation in the future working face mining may appear.

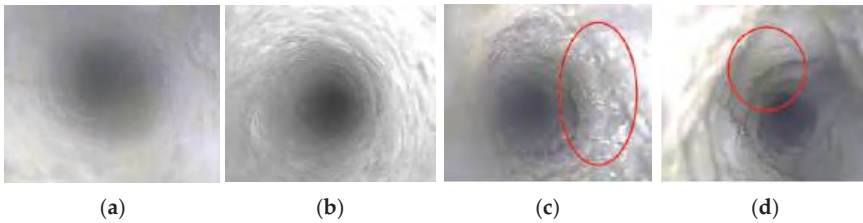


Figure 5. Drilling images of a borehole at different distances from roadway roof. (a) 2.5 m. (b) 3.0 m. (c) 3.5 m. (d) 4.0 m.

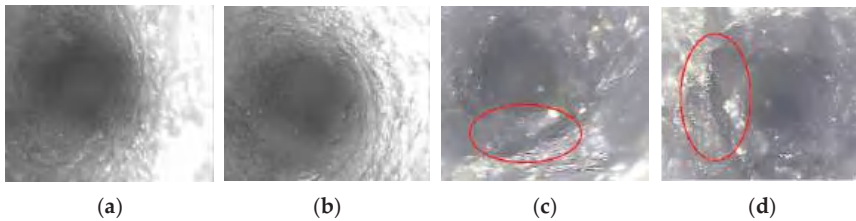


Figure 6. Drilling images of a borehole at different distances from coal pillar side of roadway. (a) 1.5 m. (b) 2.0 m. (c) 2.5 m. (d) 3.0 m.

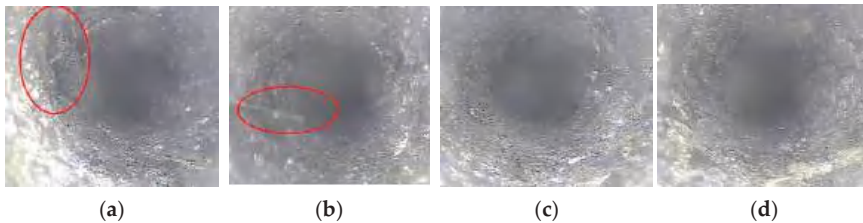


Figure 7. Drilling images of a borehole at different distances from working face side. (a) 1.5 m. (b) 2.0 m. (c) 2.5 m. (d) 3.0 m.

2.3. Instability Factors of Roadway

After coal seam #6 was mined, the floor strata were damaged to influence the mining of lower coal seam #9. Moreover, the coal seam #6 above the working face 10905 was mined without leaving the coal pillar. In addition, the rock strata activity of adjacent working face 10903 has not reached a stable state. The surrounding rock of the roadway in working face 10905 is again experiencing severe deformation and failure, especially in the coal pillar side of the roadway. Most importantly, the support method of the return airway in working face 10905 is unreasonable. Therefore, the roof subsidence of the roadway in working face 10905 is significant, and two sides of the roadway are seriously moved during the excavation process.

3. Calculation of Floor Damage Depth after Coal Seam #6 Mining

A rectangular goaf is generally formed in the rear after the working face is mined, and the ratio of the height of the mined coal seam to the width of the working face is minimal [19–22]. Therefore, the mechanical model of the longwall working face can be simplified, as shown in Figure 8.

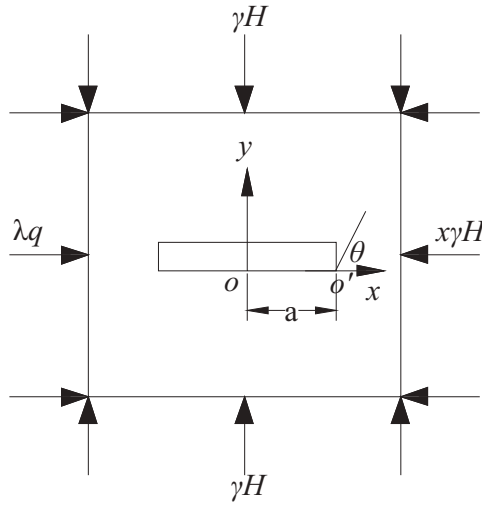


Figure 8. Mechanical model based on elastic-plastic theory.

According to the elastic-plastic theory and using the coordinate system as shown in Figure 9, the vertical stress and shear stress of the surrounding rock can be expressed as follows.

$$\begin{cases} \sigma_x = \gamma H \sqrt{\frac{L}{2r}} \cos \frac{\theta}{2} (1 - \sin \frac{\theta}{2} \sin \frac{3\theta}{2}) - (1 - x) \gamma H \\ \sigma_y = \gamma H \sqrt{\frac{L}{2r}} \cos \frac{\theta}{2} (1 + \sin \frac{\theta}{2} \sin \frac{3\theta}{2}) \\ \tau_{xy} = \gamma H \sqrt{\frac{L}{2r}} \cos \frac{\theta}{2} \sin \frac{\theta}{2} \cos \frac{3\theta}{2} \end{cases} \quad (1)$$

where L and H are the length and buried depth of the working face, γ is the bulk density of rock mass, x is lateral stress ratio, r is the limit failure distance ahead of the working face, θ is the angle between the edge line and the horizontal direction at the maximum yield depth h .

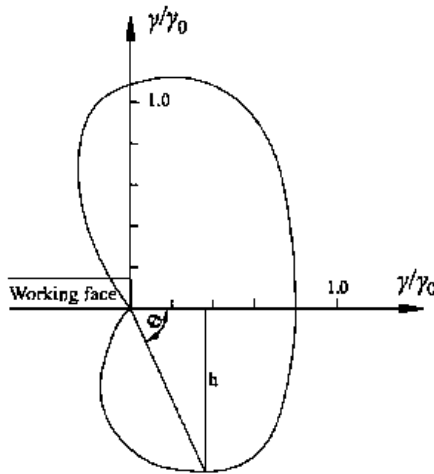


Figure 9. Surrounding rock yield failure of working face.

According to the actual mining situation of the Sheng'an coal mine, the lateral pressure coefficient is 1, and then the principal stress expression of the stope edge can be deduced as follows.

$$\begin{cases} \sigma_1 = \frac{\gamma H}{2} \sqrt{\frac{L}{r}} \cos \frac{\theta}{2} (1 + \sin \frac{\theta}{2}) \\ \sigma_2 = \frac{\gamma H}{2} \sqrt{\frac{L}{r}} \cos \frac{\theta}{2} (1 - \sin \frac{\theta}{2}) \\ \sigma_3 = \mu \gamma H \sqrt{\frac{L}{r}} \cos \frac{\theta}{2} \end{cases} \quad (2)$$

where μ is the Poisson's ratio of surrounding rock.

Assuming that the failure of surrounding rock obeys the Mohr-Coulomb criterion, the following expression can be obtained.

$$\sigma_1 - \zeta \sigma_3 = R_c \quad (3)$$

$$\zeta = \frac{1 + \sin \phi}{1 - \sin \phi} \quad (4)$$

where R_c is the uniaxial compressive strength of surrounding rock, and ϕ is the internal friction angle of the surrounding rock.

Therefore, the yield failure depth (h) of floor rock caused by stress concentration in coal seam mining can be obtained as follows.

$$h = \frac{\gamma^2 H^2 L}{4R_c^2} \cos^2 \frac{\theta}{2} (1 + \sin \frac{\theta}{2})^2 \sin \theta \quad (5)$$

The maximum failure depth of floor strata under the plane stress state is expressed as follows.

$$h_{\max} = \frac{1.57 \gamma^2 H^2 L}{4R_c^2} \quad (6)$$

It can be observed that the damage depth of floor rock increases linearly with the square of inclined length and the buried depth of the working face, and decreases linearly with the square of the compressive strength of floor rock.

On the other hand, the failure zone near the stope edge (r') can be expressed as follows.

$$r' = \frac{\gamma^2 H^2 L}{4R_c^2} \cos^2 \frac{\theta}{2} (1 + \sin \frac{\theta}{2} - 2\varepsilon \mu)^2 \quad (7)$$

where ε is the strain of the rock element in the plane strain state.

Therefore, the horizontal failure range of stope edge r'_0 at $\theta = 0^\circ$ is shown as follows.

$$r'_0 = \frac{\gamma^2 H^2 L (1 - 2\varepsilon \mu)^2}{4R_c^2} \quad (8)$$

The failure depth of floor strata in lower coal seam (h') can be calculated according to the geometric relationship under the plane strain state as follows.

$$h' = r' \sin \theta = \frac{\gamma^2 H^2 L}{4R^2} \cos^2 \frac{\theta}{2} (1 + \sin \frac{\theta}{2} - 2\zeta \mu)^2 \sin \theta \quad (9)$$

According to the comparison of the failure depth of floor strata under the plane stress and strain states, it can be seen that the failure range obtained under the plane stress state is larger than that under the plane strain state. Therefore, when the elastic-plastic theory is used to calculate the failure depth of floor strata, the calculation results in plane stress state are used to measure the failure depth of floor strata in coal mining. The influence of the

joint fissures of the floor strata on the failure depth is then comprehensively considered, and Equation (6) is transformed as follows.

$$h_{\max} = 1.57\gamma^2 H^2 L / (4R_c^2 \bullet \delta^2) \quad (10)$$

where δ is the influence coefficient of joint fissure in floor strata.

The average mining height and buried depth of coal seam #6 in Sheng'an Coal Mine is 1.35 m and 185 m, respectively. The length of the working face 10606 is 150 m. According to the experimental test results, the internal friction angle of cohesion of coal body #6 are 25.2° and 1.18 MPa, respectively. In addition, the friction coefficient of the contact surface between coal seam 5# and the floor is 0.32, and the influence coefficient of the joint fracture is 0.39. Moreover, the uniaxial compressive strength of floor strata is 14.9 MPa, and the bulk density of floor strata is 2300 kN/m³. The maximum stress concentration coefficient is 3.5. Inserting these geological parameters into Equation (10), the failure depth of floor strata caused by the upper coal seam #6 is 4.63 m, as follows.

$$h_{\max} = 1.57\gamma^2 H^2 L / (4R_c^2 \bullet \delta^2) = \frac{1.57 \times 23^2 \times 185^2 \times 150}{0.6084 \times 31,900^2} \approx 4.63 \text{ m}$$

4. Numerical Simulation of Roadway Instability under Repeated Mining

4.1. Numerical Model Establishment and Parameter Determination

In order to explore the influence of repeated mining on the instability law of the roadway, FLAC3D is used to illustrate the stress distribution law and the development of the plastic zone in the stope when the upper and lower coal seams are mined [23–25]. The numerical calculation model adopts the Mohr-Coulomb constitutive model because it is a nonlinear model and is widely used in the calculation of the actual bearing capacity and failure load of rock mass in underground space engineering. FLAC 3D can simulate the mechanical properties and plastic flow analysis of three-dimensional structures of soil, rock and other materials by adjusting the polyhedral units. Based on the finite difference method, the computational region is divided into several tetrahedral elements, each of which follows the Mohr-Coulomb constitutive model under given boundary conditions.

According to the occurrence conditions of the coal seam in the Sheng'an coal mine, the numerical simulation model is established with the length, width and height of 250 m, 120 m and 108 m, respectively, as shown in Figure 10. The bottom boundary of the model is fixed, and the displacement in the X, Y and Z directions of the bottom boundary is set as zero. In addition, the top of the model is a free boundary. The upper rock layer is applied to the equivalent load, and the self-balancing treatment is carried out before the excavation of the model.

The average buried depth of coal seam #6 is about 185 m, and the uniform load is applied according to the buried depth. The average density of rock strata is 2500 kg/m³, and the lateral stress coefficient is 1. In addition, according to the experimental tests of rock specimens collected from the Sheng'an coal mine and then conducted in the laboratory of Guizhou University, various physical and mechanical parameters (e.g., volumetric weight, compressive strength, tensile strength, Poisson's ratio, cohesion and internal friction angle) of coal seam and rock mass are obtained and used in the numerical model as listed in Table 1.

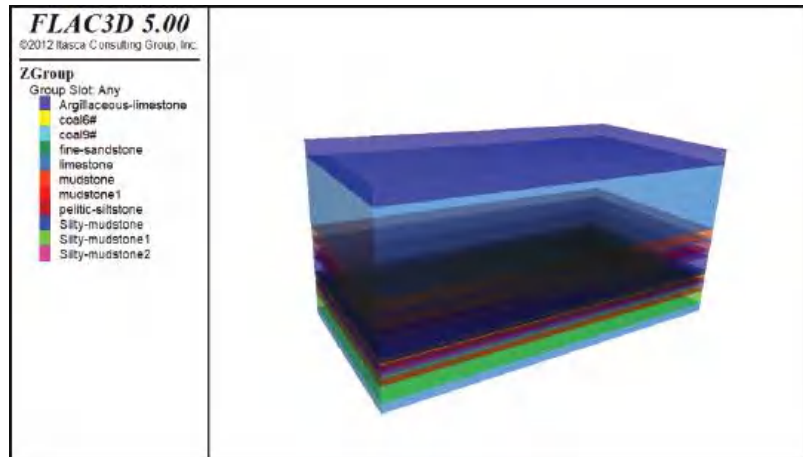


Figure 10. Numerical simulation model.

Table 1. Physical and mechanical properties of coal and rock mass.

Rock Name	Volumetric Weight g/cm ³	Compressive Strength/MPa	Tensile Strength/MPa	Poisson's Ratio	Cohesion/MPa	Internal Friction Angle/°
Coal #6	1.29	13.25	0.33	0.32	1.18	25.16
Mudstone-1	2.13	38.90	0.88	0.31	1.78	23.40
Argillaceous Sandstone	2.32	79.65	1.57	0.28	3.80	34.00
Silty Mudstone	2.44	62.18	1.23	0.21	3.30	30.05
Coal #9	1.30	11.89	0.26	0.36	1.42	24.50
Mudstone-2	2.00	38.20	0.82	0.29	1.80	24.00

4.2. Stress and Displacement Characteristics of Surrounding Rock in Lower Coal Seam

4.2.1. Stress Evolution Law

Figure 11 illustrates the stress distribution of surrounding rock in lower coal seam mining #9 with the working face advancing of 20 m, 40 m, 60 m and 80 m. Specifically, the stress concentration coefficient at the coal wall of the working face on the open-off cut is significantly reduced with the working face advancing of 20 m under the pressure relief effect of coal seam #6 mining. With the working face advancing increasing to 40 m, the small stress value of the roof and floor of coal seam #9 has been extended to an extensive range, and a small range of the stress concentration area appears in front of the coal wall of the working face. Subsequently, part of the pressure relief is reduced to connect into slices, and the force is redistributed again when the advance of the working face is 60 m. With the continuous increase of working face advancing, the pressure relief range of the connected slices increases periodically, while the increased effect of the pressure relief range is not apparent in the upper and lower ranges. It indicates that the rock entirely collapses, the rear of the working face is compacted, and the pressure relief range reaches stability.

4.2.2. Evolution Law of Plastic Zone

Figure 12 illustrates the distribution of plastic zone during the lower coal seam mining. It can be seen that there is a large range of plastic area at the cutting hole, while the plastic range at the coal wall is less under the working face advancing 20 m. Subsequently, the plastic range in the front of the working face and floor strata increase with the advance of working face increasing to 40 m, and the roof of the goaf is still in the elastic area. Moreover,

the plastic zones of overlying and floor strata increase significantly at the working face advancing 60 and 80 m.

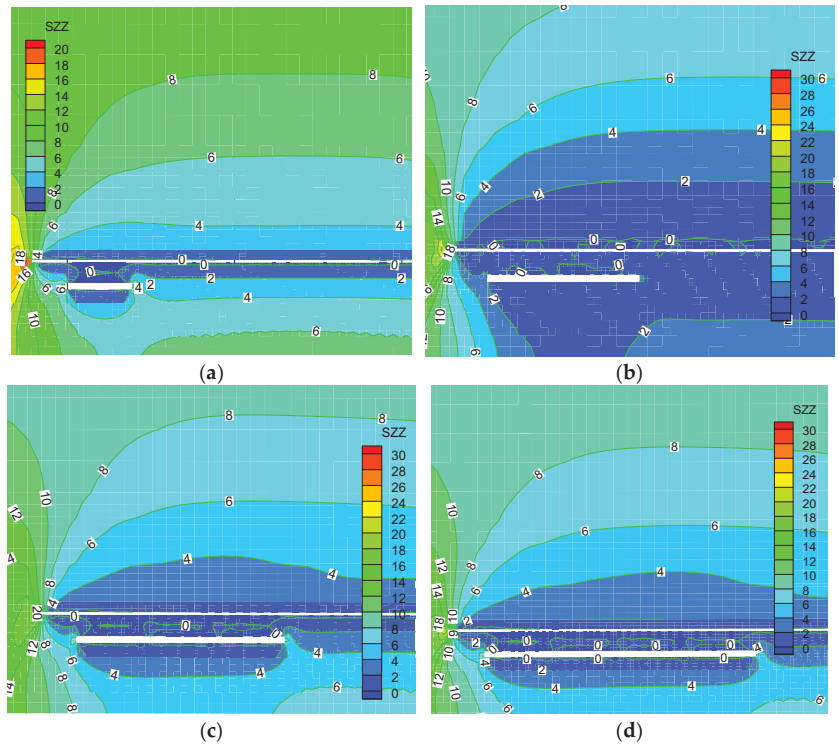


Figure 11. Vertical stress distribution of surrounding rock in lower coal seam #9. (a) Advancing 20 m. (b) Advancing 40 m. (c) Advancing 60 m. (d) Advancing 80 m.

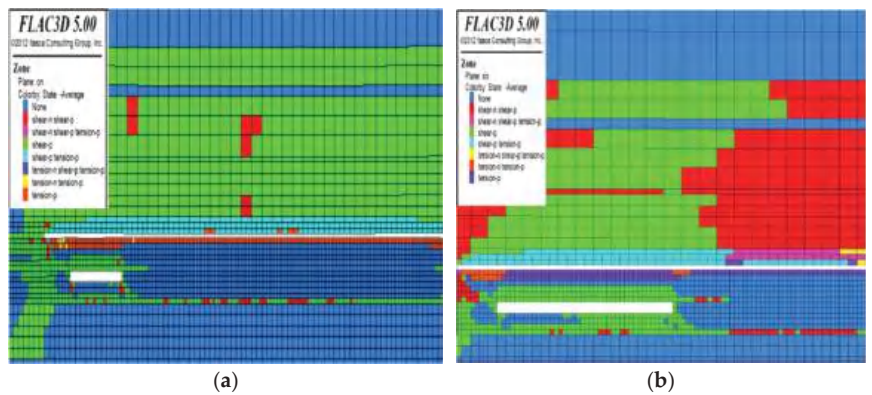


Figure 12. Cont.

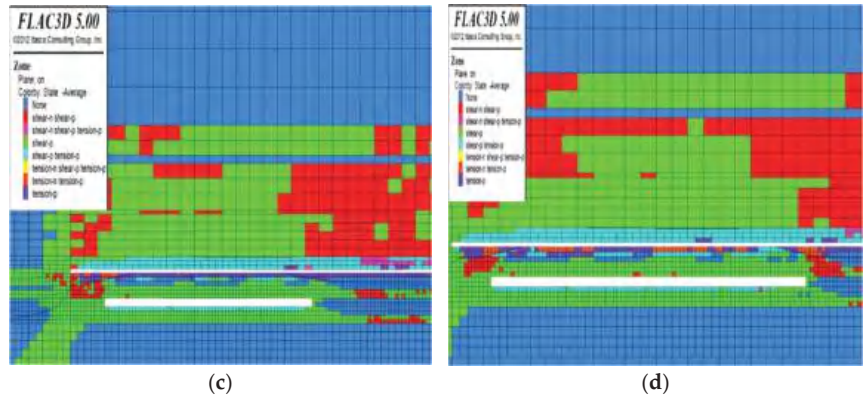


Figure 12. Plastic zone of coal seam #9 with different advancing distances. (a) Advancing 20 m. (b) Advancing 40 m. (c) Advancing 60 m. (d) Advancing 80 m.

4.3. Stress and Deformation Evolution Law of Surrounding Rock under Repeated Mining

Figure 13 illustrates the model excavation scheme to fully mine the upper coal seam and excavate the adjacent roadway of 30 m. Moreover, the gob-side entry retaining technology without the coal pillar is used in the mining of upper coal seam #6.

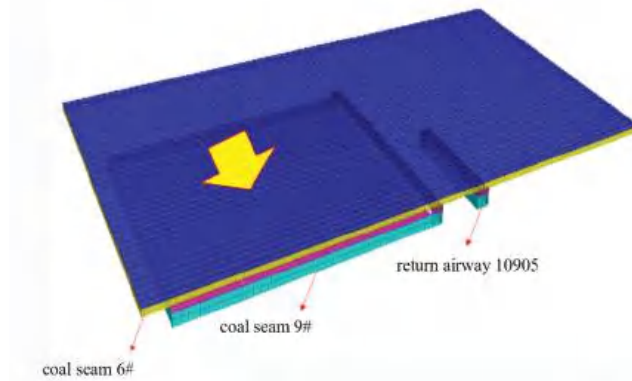


Figure 13. Model excavation scheme.

Figure 14 shows the vertical stress distribution at the position of the reserved roadway and the roof of the coal pillar in the upper coal seam mining. The pressure relief effect at the position of reserved roadway and coal pillar is good with the low stress value due to the small space between the two coal seams. Moreover, the stress value at the position of reserved roadway strike 30 m and 90 m is slightly higher with the average value of about 0.3 MPa due to the influence of the coal pillar boundary in the goaf, and the direction of vertical stress is downward. On the other hand, the direction of vertical stress at the position of the reserved roadway strike 40 m, 50 m, 70 m and 80 m is upward because the lower strata of the goaf is changed from original extrusion pressure into tensile stress and the cracks also begin to be expanded after the upper coal seam mining. Meanwhile, the location of a roadway strike at 60 m may be the first weighing site, and the overlying strata is collapsed and compacted resulting in the downward direction of vertical stress.

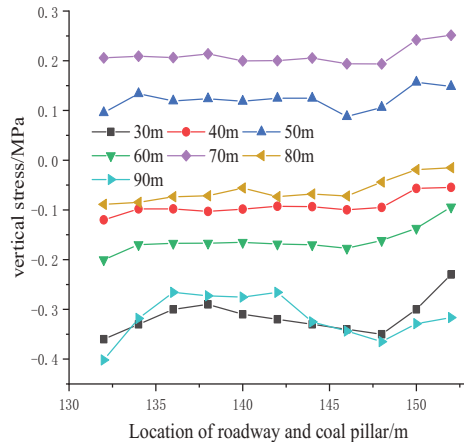


Figure 14. Influence of excavation disturbance on upper coal seam.

Figure 15 illustrates that there exists a certain of lateral pressure concentration because of the adjacent roadway excavation to cause the vertical stress of the reserved roadway and the roof of the coal pillar increasing firstly and then decreasing from near to far. Figure 16 illustrates that the vertical stress distribution at the position of 40 m and 50 m along the roadway has limited change, while the vertical stress distribution is greatly changeable at the position of 30 m and 60 m along the roadway behind the working face. Meanwhile, the stress in the roof of the roadway is large. In summary, the excavation of the upper coal seam has a significant effect on the stress value and distribution of the reserved roadway and coal pillar because of the low rock strength and the small interlay space of two coal seams, while the stress value and range is limited changed under the influence of the excavation of adjacent roadway and local roadway.

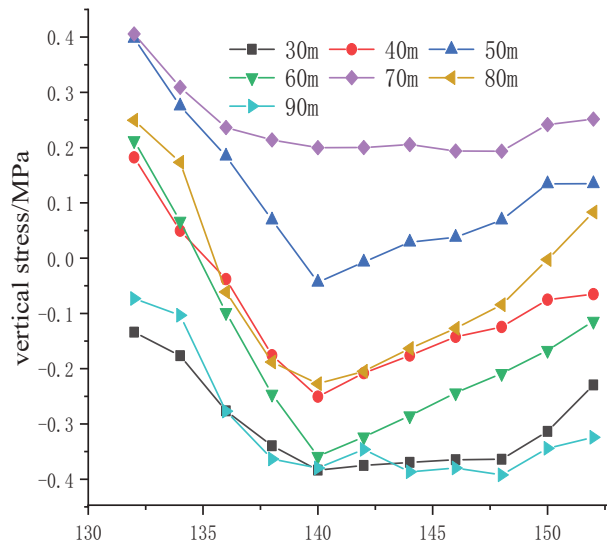


Figure 15. Influence of adjacent roadway excavation disturbance.

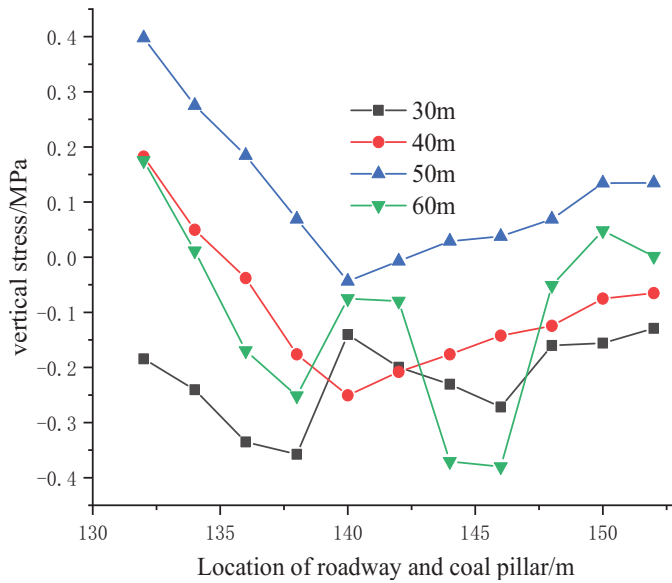


Figure 16. Influence of excavation disturbance on this roadway.

Figure 17 illustrates the variation of horizontal displacement of the roadway along with the strike position. Under the repeated mining, the deformation of surrounding rock in the roadway increases with the increase of mining times, especially for the coal pillar side. The deformation variables of the two sides are prone to have asymmetric situations during the mining process, and the stability maintenance of the coal pillar side needs to be emphasized.

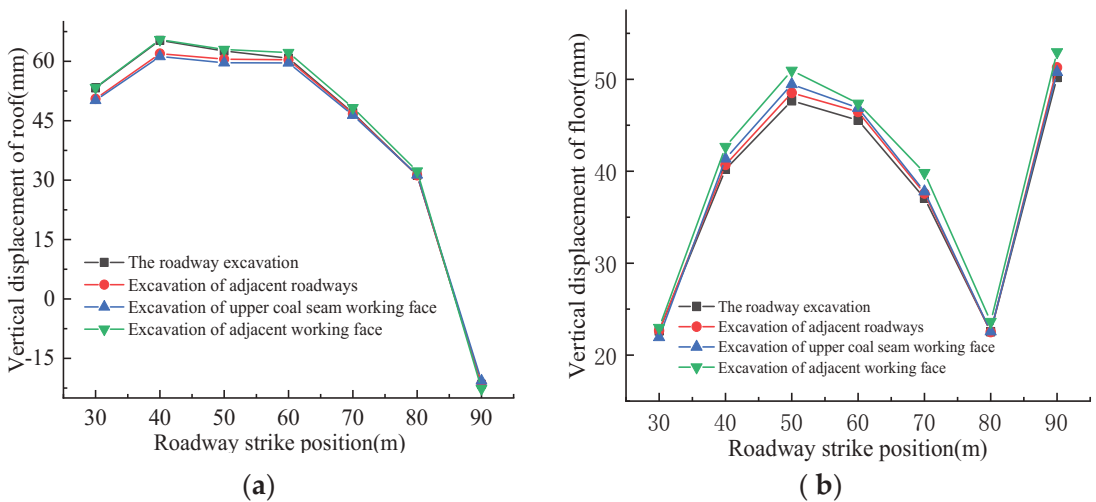


Figure 17. Cont.

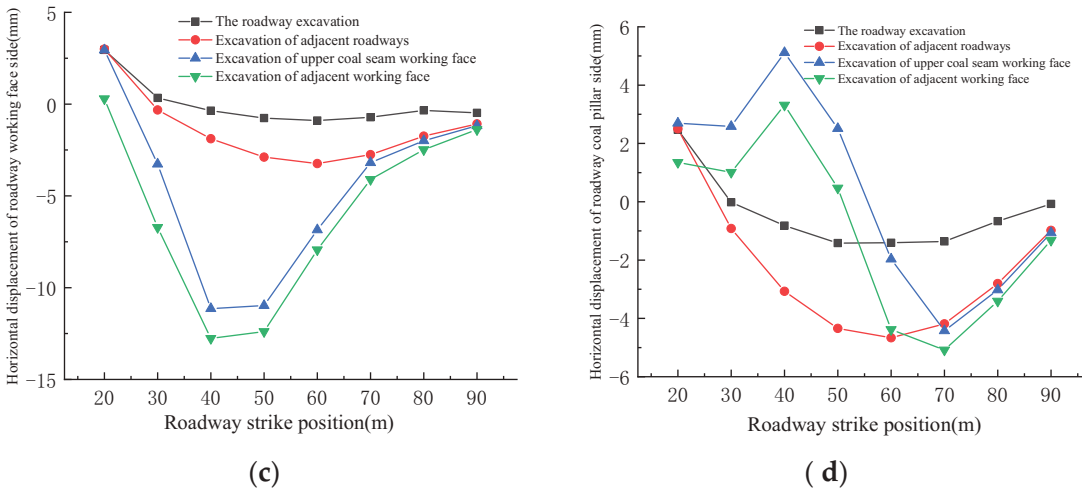


Figure 17. Displacement of roadway. (a) Displacement of roadway roof. (b) Displacement of roadway floor. (c) Displacement of roadway in working face side. (d) Displacement of roadway in coal pillar side.

5. Support Measurements Numerical Simulation Analysis

5.1. Influence of Fracture Angle on Unconfined Compressive Strength

Considering the repeated disturbance of the adjacent working face of the roadway, the asymmetric anchor cable + I-steel support scheme is proposed to effectively prevent the deformation and fracture of the roadway roof as shown in Figure 18. Specifically, five left-handed helical steel bolts ($\Phi 20 \times 2200$ mm), four left spiral steel anchors ($\Phi 20 \times 2400$ mm), and three reinforced fiber glass bolts ($\Phi 20 \times 2200$ mm) are installed in the roof strata of the roadway, the first side of the coal pillar and the first side of the working face with the row spacing of 800×800 mm and connected with W-shaped steel strip, respectively. Meanwhile, a high strength drum anchor plate ($150 \times 150 \times 10$ mm) is also used. In addition, the anchor cables of $\Phi 22 \times 4300$ mm are arranged in the roof strata of the roadway with the spacing of 1400×2400 mm, and three anchor cables are installed in each row. Similarly, the anchor cables are arranged in the side of the coal pillar and working face with the row spacing of 1600×2400 mm, and 2 anchor cables are installed in each row [26–28].

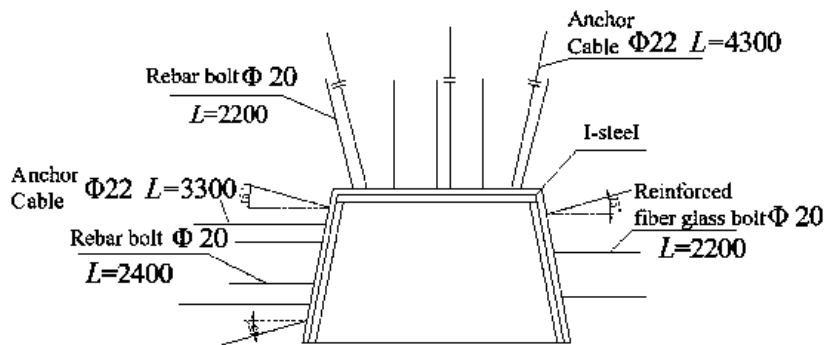


Figure 18. Roadway section support scheme.

5.2. Comparative Analysis of Supporting Effect in Numerical Simulation

Numerical simulation is performed to analyze the feasibility of the surrounding rock control scheme through comparison of the deformation, plastic zone and stress field

distribution of surrounding rock in the roadway of the lower coal seam by using the original support scheme and the proposed optimized support scheme (asymmetric anchor cable + I-steel).

As shown in Figure 19a, the surrounding rock of the roadway is mainly shear failure and the plastic zone decreases when the bolt is used in time after the excavation of the roadway, while there is still a large area of the plastic zones in the roof and the two sides by using the original support scheme. In addition, the surrounding rock is unstable again if the support stillness of the roadway is insufficient in the later period of coal seam mining. However, the timely support of the bolt and anchor cable plays a controlling role in the surrounding rock of the roadway, and the plastic zones of surrounding rock are less by using the proposed optimized support scheme as shown in Figure 19c. Meanwhile, the bearing capacity of surrounding rock can also gradually increase from 0–2 MPa to 2–4 MPa. Overall, the asymmetric anchor cable + I-steel can basically realize the temporary support demand to meet the deformation requirement of surrounding rock in the later mining.

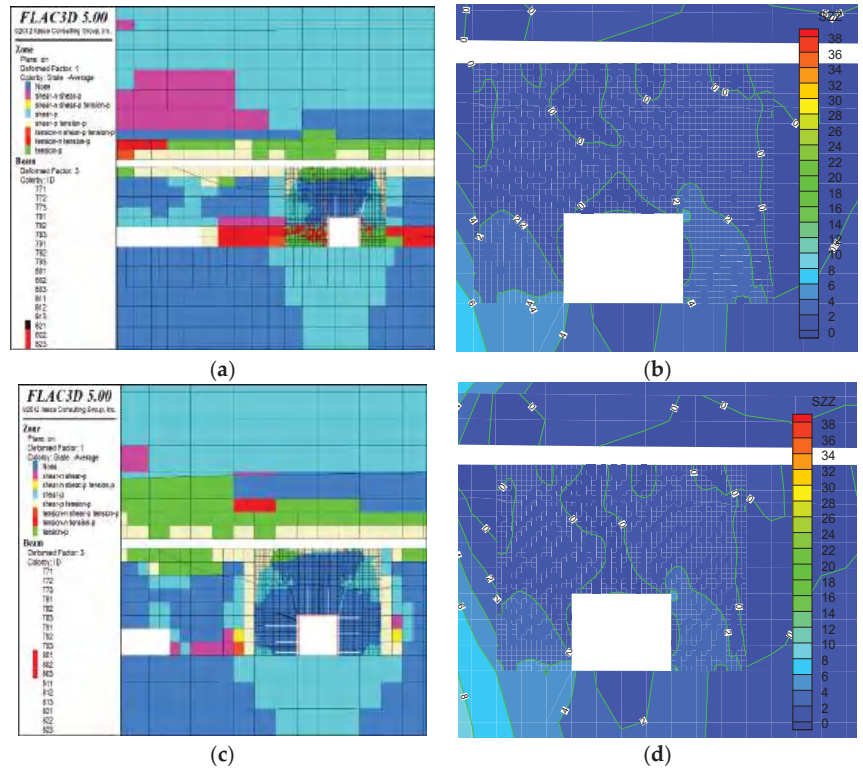


Figure 19. Plastic zone and stress diagram of surrounding rock in two support schemes. (a) Plastic zone of original support scheme. (b) Vertical stress of original support scheme. (c) Plastic zone of proposed support scheme. (d) Vertical stress of proposed support scheme.

5.3. Engineering Practices

As shown in Figure 20, 20 monitoring points are arranged to measure the deformation of surrounding rock in the roadway with the distance of each point being 10 m, and Figure 21 illustrates the typical displacement curve of the surrounding rock of roadway in working face 10905. The results show that the maximum displacement of the roadway roof, coal pillar side and working face side is 326 mm, 225 mm and 201 mm, respectively. Moreover, the deformation on both sides of the roadway is asymmetric distribution and its deformation rate is the largest in the range of +20 m to −40 m from the working face. In

addition, the displacement of the roadway increases with the advancement of the working face 10903, and the displacement of the roadway far from the working face is small. The overall displacement of the roadway is within the controllable range, and the roadway support effect is shown in Figure 22.

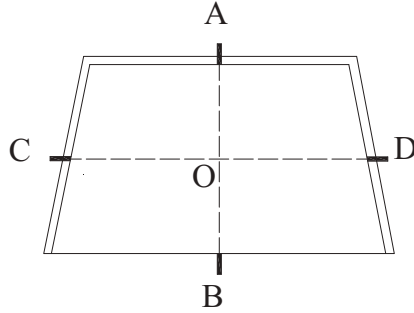


Figure 20. Layout of monitoring points.

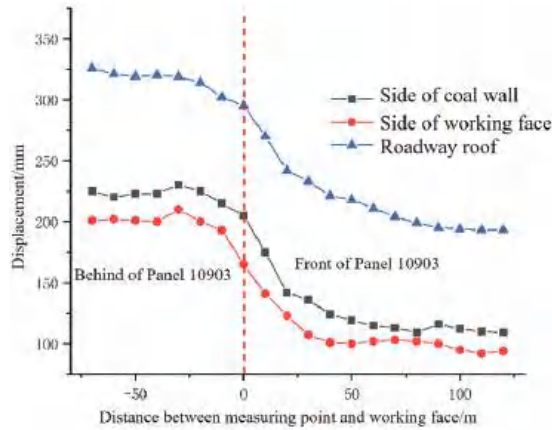


Figure 21. Displacement curve of the surrounding rock of the roadway.



(a)



(b)

Figure 22. Support effect of return airway in working face 10905. (a) Return airway after support. (b) test section.

6. Conclusions

In this study, comprehensive research methods (e.g., field test, theory analysis and numerical simulation) are adopted to illustrate the failure characteristics of surrounding rock of a roadway in a lower coal seam under repeated mining in close-distance coal seam considering the caving gangue in the upper coal seam and the mining activities of the adjacent working face. Meanwhile, the corresponding support scheme is also proposed. The main conclusions can be drawn as follows.

- (1) Through field investigation and data observation, the surrounding rock of the roadway presents the asymmetric evolution characteristics of cracks. The expression of floor failure depth caused by upper coal seam mining is obtained through the elastic-plastic theory. Combined with the geological conditions of coal seam #6, the floor failure depth caused by coal seam #6 is 4.63 m.
- (2) According to the results of numerical simulation, the stress concentration in working face 10905 and roadway without a residual coal pillar is in a low stress environment. After repeated mining, the deformation of the overall surrounding rock of the roadway increases with the increase of mining times. In particular, the horizontal displacement of the roadway coal pillar side changes greatly, and the actual damage degree is the largest. The deformation variables of the two sides are prone to asymmetric situations during mining, and the stability maintenance of the coal pillar side needs to be emphasized.
- (3) The asymmetric anchor cable + I-steel support scheme is proposed to effectively prevent the deformation and fracture of the roadway roof in this study. And the bolt-cable timely support plays a controlling role on the surrounding rock of the roadway. In addition, the plastic zone of the surrounding rock of the roadway is the least, and the bearing capacity of surrounding rock in the roadway increases from 0–2 MPa to 2–4 MPa.
- (4) Through the field observation of the surrounding rock deformation of the roadway in the test section, the maximum displacement of the roadway roof, coal pillar side and working face side is 326 mm, 225 mm and 201 mm, respectively. Moreover, the deformation on both sides of the roadway is asymmetric in distribution, and its deformation rate is the largest in the range of +20 m to −40 m from the working face. The overall displacement of the roadway is within the controllable range as a result of using the optimized support scheme.

The finite difference method in numerical simulation has a certain limitation to simulate the practice situations of background engineering. In addition, further research should also consider the influence of temperature and humidity on the strength of rock mass, especially for the coal seam under a large buried depth.

Author Contributions: Y.S.: Formal analysis, Numerical simulation, Experimental test, Writing—Original draft; D.K.: Data curation, Methodology, Writing—Original draft, Numerical Simulation, Experimental test, Funding acquisition; S.P.: Formal analysis, Investigation; Y.X.: Numerical simulation, Experimental test; Q.L.: Data curation, Numerical simulation, Experimental test; Z.C.: Formal analysis, Methodology, Validation, Writing—Review and editing. All authors have read and agreed to the published version of the manuscript.

Funding: This research was funded by the National Natural Science Foundation of China (No. 52164002, 52164005, 52064005 and 51904082); And this Supported by Guizhou Provincial Science and Technology Projects (Qianke Science Support [2021] General 399). The authors would also like to thank the editors and anonymous reviewers for their valuable time and suggestions.

Institutional Review Board Statement: Not applicable.

Informed Consent Statement: Not applicable.

Data Availability Statement: All data used during the study appear in the submitted article.

Conflicts of Interest: The authors declare no conflict to interest.

References

- Kong, D.; Cheng, Z.; Zheng, S. Study on the failure mechanism and stability control measures in a large-cutting-height coal mining face with a deep-buried seam. *Bull. Eng. Geol. Environ.* **2019**, *78*, 6143–6157. [CrossRef]
- Xiong, Y.; Kong, D.; Cheng, Z.; Wu, G.; Zhang, Q. The Comprehensive Identification of Roof Risk in a Fully Mechanized Working Face Using the Cloud Model. *Mathematics* **2021**, *9*, 2072. [CrossRef]
- Liu, F.; Guo, Z.; Lv, H.; Cheng, Z. Test and analysis of blast wave in mortar test block. *Int. J. Rock Mech. Min. Sci.* **2018**, *108*, 80–85. [CrossRef]
- Klemetti, T.M.; Van Dyke, M.A.; Evaneck, N.; Compton, C.C.; Tulu, I.B. Insights into the Relationships Among the Roof, Rib, Floor, and Pillars of Underground Coal Mines. *Min. Met. Explor.* **2021**, *38*, 531–538. [CrossRef]
- Maleki, H. Coal pillar mechanics of violent failure in U.S. Mines. *Int. J. Min. Sci. Technol.* **2017**, *27*, 387–392. [CrossRef]
- Xue, Y.; Liu, J.; Ranjith, P.G.; Zhang, Z.; Gao, F.; Wang, S. Experimental investigation on the nonlinear characteristics of energy evolution and failure characteristics of coal under different gas pressures. *Bull. Eng. Geol. Environ.* **2022**, *81*, 38. [CrossRef]
- Xie, J.; Xu, J.; Wang, F.; Guo, J.; Liu, D. Deformation effect of lateral roof roadway in close coal seams after repeated mining. *Int. J. Min. Sci. Technol.* **2014**, *24*, 597–601. [CrossRef]
- Kong, D.; Xiong, Y.; Cheng, Z.; Wang, N.; Wu, G.; Liu, Y. Stability analysis of coal face based on coal face-support-roof system in steeply inclined coal seam. *Geomech. Eng.* **2021**, *25*, 233–243. [CrossRef]
- Lv, H.; Cheng, Z.; Dong, Y.; Zhang, J.; Ma, Y. Numerical simulation on the crack initiation and propagation of coal with combined defects. *Struct. Eng. Mech.* **2021**, *79*, 237–245. [CrossRef]
- Xue, Y.; Liu, J.; Liang, X.; Wang, S. Ecological risk assessment of soil and water loss by thermal enhanced methane recovery: Numerical study using two-phase flow simulation. *J. Clean. Prod.* **2022**, *334*, 130183. [CrossRef]
- Xiong, Y.; Kong, D.; Cheng, Z.; Wen, Z.; Ma, Z.; Wu, G.; Liu, Y. Instability Control of Roadway Surrounding Rock in Close-Distance Coal Seam Groups under Repeated Mining. *Energies* **2021**, *14*, 5193. [CrossRef]
- Zhang, Y.; Cheng, Z.; Lv, H. Study on failure and subsidence law of frozen soil layer in coal mine influenced by physical conditions. *Geomech. Eng.* **2019**, *18*, 97–109. [CrossRef]
- Liu, X.; Cheng, Z. Changes in subsidence-field surface movement in shallow-seam coal mining. *J. S. Afr. Inst. Min. Metal.* **2019**, *119*, 201–206. [CrossRef]
- Singh, S.K.; Agrawal, H.; Singh, A.P. Rib stability: A way forward for safe coal extraction in India. *Int. J. Min. Sci. Technol.* **2017**, *27*, 1087–1091. [CrossRef]
- Lv, H.; Cheng, Z.; Liu, F. Study on the mechanism of a new fully mechanical mining method for extremely thick coal seam. *Int. J. Rock Mech. Min. Sci.* **2021**, *142*, 104788. [CrossRef]
- Cheng, Z.; Geng, X. Soil consistency and interparticle characteristics of various biopolymer types stabilization of clay. *Geomech. Eng.* **2021**, *27*, 103–113. [CrossRef]
- Liu, X.; Ning, J.; Tan, Y.; Xu, Q.; Fan, D. Coordinated supporting method of gob-side entry retaining in coal mines and a case study with hard roof. *Geomech. Eng.* **2018**, *15*, 1173–1182. [CrossRef]
- Yu, J.; Liu, G.; Cai, Y.; Zhou, J.; Liu, S.; Tu, B. Time-Dependent Deformation Mechanism for Swelling Soft-Rock Tunnels in Coal Mines and Its Mathematical Deduction. *Int. J. Geomech.* **2020**, *20*, 04019186. [CrossRef]
- Lv, H.; Tang, Y.; Zhang, L.; Cheng, Z.; Zhang, Y. Analysis for mechanical characteristics and failure models of coal specimens with non-penetrating single crack. *Geomech. Eng.* **2019**, *17*, 355–365. [CrossRef]
- Cheng, Z.; Li, L.; Zhang, Y. Laboratory investigation of the mechanical properties of coal–rock combined body. *Bull. Eng. Geol. Environ.* **2020**, *79*, 1947–1958. [CrossRef]
- Cheng, Z.; Pan, W.; Li, X.; Sun, W. Numerical simulation on strata behaviours of TCCWF influenced by coal-rock combined body. *Geomech. Eng.* **2019**, *19*, 269–282. [CrossRef]
- Cheng, Z.; Yang, S.; Li, L.; Zhang, L. Support working resistance determined on top-coal caving face based on coal-rock combined body. *Geomech. Eng.* **2019**, *19*, 255–268. [CrossRef]
- Wang, D.; Barakos, G.; Cheng, Z.; Mischo, H.; Zhao, J. Numerical simulation of pressure profile of mining backfill fly-ash slurry in an L-shaped pipe using a validated Herschel-Bulkley model. *J. Sustain. Cem. Based* **2021**, 1–15. [CrossRef]
- Wang, Y.; Wu, G.; Liu, Y.; Cheng, Z. Study on Overlying Strata Movement and Surface Subsidence of Coal Workfaces with Karst Aquifer Water. *Mathematics* **2022**, *10*, 169. [CrossRef]
- Yang, S.; Chen, M.; Jing, H.; Chen, K.; Meng, B. A case study on large deformation failure mechanism of deep soft rock roadway in Xin'An coal mine, China. *Eng. Geol.* **2017**, *217*, 89–101. [CrossRef]
- Lv, H.; Wang, D.; Cheng, Z.; Zhang, Y.; Zhou, T. Study on mechanical characteristics and failure modes of coal-mudstone combined body with prefabricated crack. *Mathematics* **2022**, *10*, 177. [CrossRef]
- Wang, D.; Cheng, Z.; Shi, Q.; Zhao, J.; Mischo, H. Simulation Study of the Velocity Profile and Deflection Rate of Non-Newtonian Fluids in the Bend Part of the Pipe. *Geofluids* **2022**, *2022*, 7885556. [CrossRef]
- Xu, C.; Xia, C. A new large strain approach for predicting tunnel deformation in strain-softening rock mass based on the generalized Zhang-Zhu strength criterion. *Int. J. Rock Mech. Min.* **2021**, *143*, 104786. [CrossRef]

Article

A Stacking Learning Model Based on Multiple Similar Days for Short-Term Load Forecasting

Qi Jiang ^{1,†}, Yuxin Cheng ^{1,†}, Haozhe Le ¹, Chunquan Li ^{1,*} and Peter X. Liu ^{1,2}

¹ School of Information Engineering, Nanchang University, Nanchang 330031, China; 6104119104@email.ncu.edu.cn (Q.J.); 6108118061@email.ncu.edu.cn (Y.C.); 6108118076@email.ncu.edu.cn (H.L.); xpliu@sce.carleton.ca (P.X.L.)

² Department of Systems and Computer Engineering, Carleton University, Ottawa, ON K1S 5B7, Canada

* Correspondence: lichunquan@ncu.edu.cn

† These authors contributed equally to this work.

Abstract: It is challenging to obtain accurate and efficient predictions in short-term load forecasting (STLF) systems due to the complexity and nonlinearity of the electric load signals. To address these problems, we propose a hybrid predictive model that includes a sliding-window algorithm, a stacking ensemble neural network, and a similar-days predictive method. First, we leverage a sliding-window algorithm to process the time-series electric load data with high nonlinearity and non-stationarity. Second, we propose an ensemble learning scheme of stacking neural networks to improve forecasting performance. Specifically, the stacking neural networks contain two types of networks: the base-layer and the meta-layer networks. During the pre-training process, the base-layer network integrates a radial basis function (RBF), random vector functional link (RVFL), and backpropagation neural network (BPNN) to provide a robust predictive model. The meta-layer network utilizes a deep belief network (DBN) and the improved broad learning system (BLS) to enhance predictive accuracy. Finally, the similar-days prediction method is developed to extract the relationship of electric load data in different time dimensions, further enhancing the robustness and accuracy of the model. To demonstrate the effectiveness of our model, it is evaluated using real data from five regions of the United States in three consecutive years. We compare our method with several state-of-the-art and conventional neural-network-based models. Our proposed algorithm improves the prediction accuracy by 16.08%, 16.83%, and 22.64% compared to DWT-EMD-RVFL, SWT-LSTM, and EMD-BLS, respectively. Empirical results demonstrate that our model achieves better accuracy and robustness compared with the baselines.

Keywords: short-term load forecasting (STLF); stacking ensemble learning; similar-days forecasting; sliding window; broad learning system–backpropagation (BLS–BP)

MSC: 68T07

Citation: Jiang, Q.; Cheng, Y.; Le, H.; Li, C.; Liu, P.X. A Stacking Learning Model Based on Multiple Similar Days for Short-Term Load Forecasting. *Mathematics* **2022**, *10*, 2446. <https://doi.org/10.3390/math10142446>

Academic Editors: Zhuojia Fu, Yiqian He and Hui Zheng

Received: 30 May 2022

Accepted: 5 July 2022

Published: 13 July 2022

Publisher's Note: MDPI stays neutral with regard to jurisdictional claims in published maps and institutional affiliations.



Copyright: © 2022 by the authors. Licensee MDPI, Basel, Switzerland. This article is an open access article distributed under the terms and conditions of the Creative Commons Attribution (CC BY) license (<https://creativecommons.org/licenses/by/4.0/>).

1. Introduction

Power load forecasting is essential to power system planning [1]. Since it is challenging to store electric energy, an accurate load forecasting algorithm is critical for efficient power consumption and the security of the power grid [2]. The load forecasting task can be classified as long-term, medium-term, or short-term based on the time span of the load forecasting. For medium-term and long-term load forecasting, they are mainly used to develop long-term power generation plans. Due to the short interval of STLF, it can be used to adjust the operation mode of the power grid and promote the stable operation of the power system.

In past decades, various forecasting methods have been proposed to tackle STFL. They can be classified into two categories: One includes statistical models such as autoregressive moving average (ARMA) [3,4] and linear regression (LR) [5]. The other includes machine

learning methods including support-vector regression (SVR) [6], backpropagation neural networks (BPNNs), deep neural networks (DBNs) [7], broad learning systems (BLSs) [8], random vector functional link (RVFL) [9], and long short-term memory (LSTM) [10]. Due to the nonlinear and non-stationary characteristics of short-term power load data, statistical methods cannot effectively process such characteristic information. Therefore, machine learning has gradually become the mainstream STLF method, which can effectively extract features from nonlinear time series and provide an effective connection between input and output.

Recently, machine learning has achieved remarkable results in load forecasting [11]. Artificial neural networks (ANNs) are one of the most popular methods [12], which can simulate human brain behavior by training and learning ways to obtain the relationship between input and output. Deep learning methods such as LSTM and DBN have powerful nonlinear data processing capabilities, and are also very popular methods [7,10]. However, a deep neural network requires a lot of computational costs, as it depends on a large amount of training data. To save computational costs, a new single-layer incremental neural network BLS is gradually obtained.

More recently, various hybrid models have been developed to effectively improve the predictive accuracy of STFL. This is because the hybrid models can integrate the advantages of each model to solve the limitations of each mode by weighted combination. Chen et al. [13] presented a new combination model to enhance power load forecasting. In [14,15], multiple artificial neural network models are integrated to improve predictive performance. In [16], artificial neural networks are integrated to improve the accuracy of STLF with a new evolutionary method. In [17], support-vector machines with ant colony optimization are combined to improve the performance of power load forecasting.

To tackle the complexity and nonlinearity of electric signals, various hybrid predictive frameworks have been developed by combining decomposition methods with neural networks. Nengling et al. [18] proposed dividing the load data into different resolutions by wavelet transform and applying different combination forecasting methods based on statistical models to each scale. Ghayekhloo et al. [19] and Ghofrani et al. [20] both used wavelet transform to convert the load data into multiple frequency components. Subsequently, they trained multiple artificial neural networks on the data by linking the weighted outputs of the trained networks in the STLF task. Qiu et al. [7] introduced integrated deep learning based on empirical mode decomposition for load-demand time-series forecasting. Laouafi et al. [21] combined traditional methods and intelligent methods for STLF.

The above hybrid predictive models achieve promising prediction results, as in [22,23]; however, they still cannot solve the following problems:

1. The existing popular empirical mode decomposition [24] often has the problem of modal aliasing. Furthermore, the difficulty of wavelet decomposition [25] lies in how to effectively select the wavelet basis and decomposition scale. In addition, the decomposition methods may introduce some redundant decomposition information to the predictive models, degenerating the predictive computational cost.
2. Each machine learning method—such as LSTM, DBN, and BLS—has its own specific limitations, which may influence its predictive performance in STLF.
3. The selection of the dataset is also a challenging problem. Generally, continuous time series are used, and are divided into training and test sets. This approach can lead to ineffective extraction of correlations between continuous time series and, therefore, may result in lower accuracy of model predictions.

To address the above problems, we propose an improved hybrid predictive model, which includes a sliding-window algorithm, a stacking ensemble neural network model, and a similar-days predictive method. Specifically, a sliding-window algorithm [26] is first introduced to directly process the nonlinearity and non-stationarity of the time-series electric load data. This method effectively mines spatiotemporal features of the time series. Furthermore, a stacking ensemble neural network model is proposed to improve the

forecasting performance. The stacking neural networks contain two types of networks: the base-layer network and the meta-layer network. During the pre-training process, the base-layer networks integrate radial basis function (RBF), random vector functional link (RVFL), and backpropagation neural network (BPNN) to provide a robust predictive model; the meta-layer networks utilize a deep belief network (DBN) and the improved broad learning system (BLS) to improve predictive accuracy; the predictive results of RBF, RVFL, BPNN, DBN, and BLS are rationally weighted to obtain the final prediction result. Finally, the similar-days prediction method is developed to extract the relationship of electric load data in different time dimensions, further enhancing the robustness and accuracy of the model. This paper selects the load data of five regions in the United States for three consecutive years to conduct a large number of experiments, proving that the framework has high prediction accuracy and strong robustness.

The main contributions of this paper are as follows:

1. The sliding-window algorithm is an effective method for extracting the spatiotemporal characteristics of load data, which are used to reduce computational costs and improve prediction accuracy.
2. The stacking neural network is proposed to greatly improve the prediction accuracy.
3. The similar-days predictive method is developed to extract the relationship of electric load data in different time dimensions, further enhancing the robustness and accuracy of the model.

The rest of this paper is organized as follows: Section 2 introduces the framework of the proposed model and the theoretical knowledge of interest; Section 3 shows the data analysis; Section 4 introduces the details of the case analysis; Section 5 concludes the paper.

2. Methodology

2.1. Model Framework

We show the overall framework of our proposed method in Figure 1. It contains four parts: (A) data preprocessing, (B) base learners, (C) data processing, and (D) meta-learners. And the detailed pseudo-code of the stacking algorithm is given in Algorithm 1. The proposed model can be described as follows:

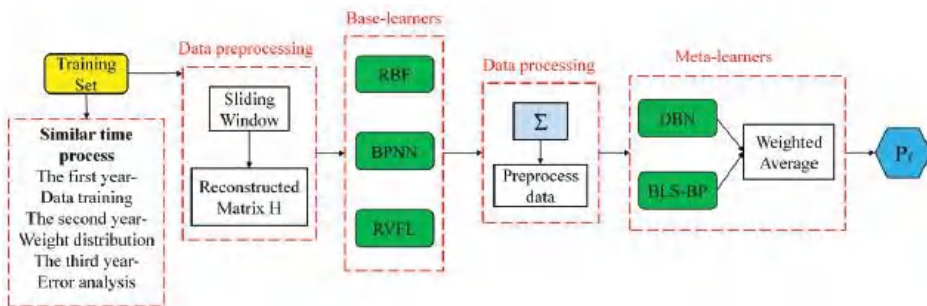


Figure 1. Framework of the proposed model.

Part A: The collected power load data are divided into three parts: (1) the training set, which is used as training data; (2) the validation set, which is used for weight adjustment between meta-learners; and (3) the test set, which is used for evaluation and error analysis. The time series in each of the three parts are input into the sliding-window algorithm to obtain the reconstructed multidimensional matrix H as the data input matrix for the base learner (refer to Section 2.2 for more details).

Part B: The base-layer learning system consists of RBF, BPNN, and RVFL networks for preliminary training (refer to Section 2.3 for more details).

Part C: During data processing, the prediction data of the base-layer learner are recombined as the input of the meta-layer learner (refer to Section 2.3 for more details).

Part D: The meta-layer learning system involves two neural networks: DBN and BLS–BP. BLS–BP is an improved network that is first used in load forecasting (refer to Section 2.3 for more details).

Algorithm 1: Stacking: Based on sliding window

- 1: **Input:** training data

$$D = \{a_i, b_i\}_{i=1}^m (x_i \in R^n, y_i \in Y)$$
- 2: Step 1: analysis with sliding window
- 3: Reconstruct D to H
- 4: **end for**
- 5: Step 2: learn base-layer learners
- 6: **for** n : 1 to N **do**
- 7: Learn a base learner S_n based on H
- 8: **end for**
- 9: Step 3: construct new datasets from H
- 10: **for** i : 1 to m **do**
- 11: Construct a new dataset that contains

$$H_s = \{x_i^1, y_i\},$$
- 12: **end for**
- 13: Step 4: learn meta-layer learners
- 14: **for** t : 1 to T **do**
- 15: Learn a meta-learner S_t based on H_s
- 16: **end for**
- 17: Return $S(x) = s^1\{s_1(x), s_2(x), \dots, s_N(x)\}$
- 18: **Output:** ensemble learner S

2.2. Sliding-Window Algorithm

The principle of the sliding-window algorithm is to reconstruct the original power load data into a multidimensional matrix H by sliding the window. When training and validating the model, the reconstruction matrix H includes both the input and output data (also known as training data and label data, respectively). In the evaluation step, only training data are in the reconstruction matrix H . Figures 2 and 3 illustrate the reconstruction process. In each window slot, three components are included, namely, input data X , output data Y , and delay time T . The window is slid to remove the data at the beginning of the previous window, and then the same amount of new data is added at the end of the window to ensure that the window size is constant. The sliding window will go through the entire dataset until all of the data are covered.

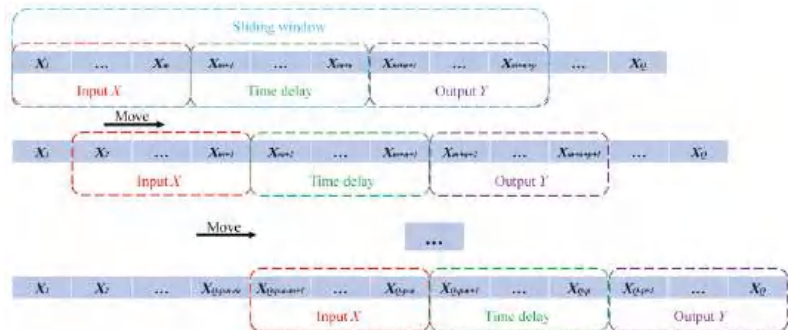


Figure 2. Flowchart of the sliding window.

Input X	Output Y
$X_1, X_2, \dots, X_{m-1}, X_m$	$X_{m+n+1}, X_{m+n+2}, \dots, X_{m+n+p-1}, X_{m+n+p}$
$X_2, X_3, \dots, X_m, X_{m+1}$	$X_{m+n+2}, X_{m+n+3}, \dots, X_{m+n+p}, X_{m+n+p+1}$
...	...
$X_{Q-p-n-m+1}, X_{Q-p-n-m+2}, \dots, X_{Q-p-n-1}, X_{Q-p-n}$	$X_{Q-p+1}, X_{Q-p+2}, \dots, X_{Q-1}, X_Q$

Figure 3. The reconstructed matrix.

2.3. Stacking Algorithm

2.3.1. Algorithm Structure

Figures 4 and 5 show the framework structure of the stacking algorithm; the specific process is as follows:

1. First, we leverage the sliding-window method to perform data preprocessing on the original data and obtain a new training set, validation set, and test set. The training set is divided into n parts: $\{\text{Train}(i) \mid i = 1, 2, \dots, n\}$, where n is the number of folds in cross-validation (see Section 3.3 for details).
2. Model training: We choose RBF, BPNN, and RVFL as the base-layer learners. After each model is pre-trained, we train the base learners with $\{\text{Train}(i) \mid i = 1, 2, \dots, n\}$, in turn. We make the base learners well-trained with the i -folder cross-validation method, as shown in Figure 5. We generate an intermediate dataset A by vertically merging the n predictions of the base learners. Specifically, we name the datasets generated by RBF, BPNN, and RVFL as $A(1)$, $A(2)$, and $A(3)$, respectively, and merge these three datasets horizontally to obtain $A(x)$. We use DBN and BLS-BP as our meta-learners and train the meta-learners on $A(x)$. We repeat the above process for the validation set and the test set using the well-trained base learners to generate two intermediate datasets $B(x)$ and $C(x)$, where $x \in \{1, 2, 3\}$.
3. Weight adjustment between meta-learners: We obtain a new dataset $B(x)$ from the predictions of the base learners on the validation set, and utilize $B(x)$ to adjust the weights between the meta-learners. The weights between the two meta-learners are updated according to the error between the predictions and the labels.
4. Model Evaluation: We forward the test set to the well-trained base learners to obtain $C(x)$, and forward $C(x)$ to the well-trained meta-learners to make predictions. Finally, the optimal weights are used to obtain a weighted average of the predicted values of the two meta-learners to obtain the final prediction results. The model is evaluated by the error between the final prediction result and the actual value.

2.3.2. Base-Layer Network

The base-layer network consists of a radial basis function (RBF), random vector functional link (RVFL), and backpropagation neural network (BPNN), to provide a robust predictive model for STLFL.

The RBF [27] is composed of three layers: The first layer is the input layer, which takes the signal source as input. The second layer is the hidden layer, whose transformation function is the radial basis function. The non-negative transformation function is linear, symmetric, and attenuated. The third layer is the output layer, which responds to the input mode. The output layer leverages a linear optimization strategy to fine-tune the linear weight between the hidden layer and the output layer.

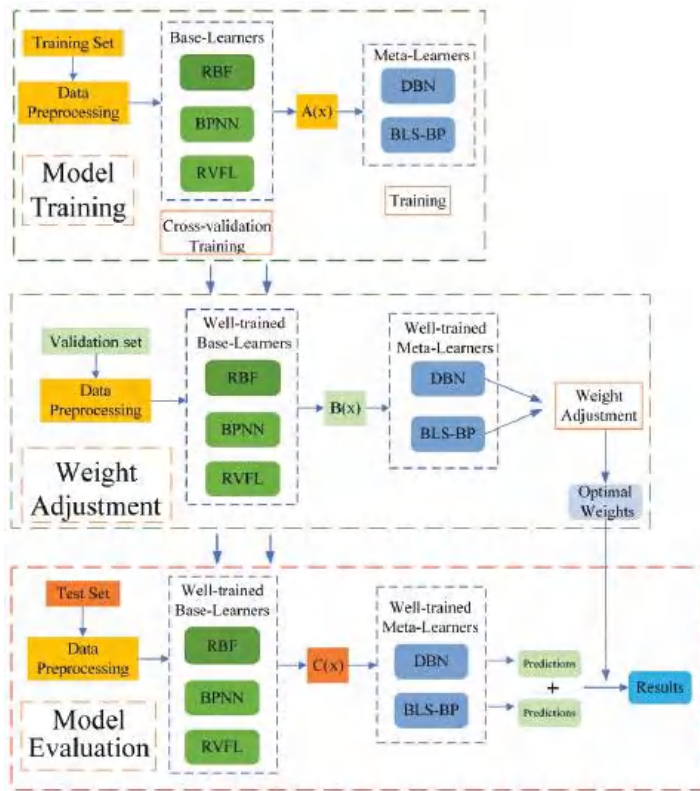


Figure 4. Algorithm structure.



Figure 5. Cross-validation in the training process of the base learners.

RVFL [9] is a neural network based on the learning paradigm. RVFL is more efficient than the conventional iterative learning neural network. This feedforward structure can be regarded as a linear combination of a fixed number of nonlinear expansions of the original inputs. RVFL contains three layers: the input layer, enhanced node layer, and output layer. The principle of RVFL is to use the augmented nonlinear kernel raw data learned at the implicit layer to improve the generalization ability. The neural network has a direct connection from the input layer to the output layer, which is helpful to map the relationship between input and output. It is very suitable for the characteristics of our selected basic learner.

The BPNN [28] is the most basic supervised learning neural network. Its output is rendered by the forward propagation, and the errors are carried out in one-way propagation. The BPNN contains three layers: the input layer, the hidden layer, and the output layer. Specifically, the input of the hidden layer is the output of the input layer. Then, the hidden layer applies an activation function to the hidden features, and the output of the hidden layer is forwarded to the output layer to generate the output results.

The partial derivative gradient descent method is used to obtain the minimum value of the cost function so that the error between the expected value and the output is reduced as much as possible.

2.3.3. Meta-Layer Network

The meta-layer network applies a deep belief network (DBN) and the improved broad learning system (BLS) to improve predictive accuracy.

The DBN [7] is a deep neural network model composed of a stacked RBM and a layer of BP network, and it is also a current mainstream neural network. The structure is shown in Figure 6. The training process of the DBN includes two steps:

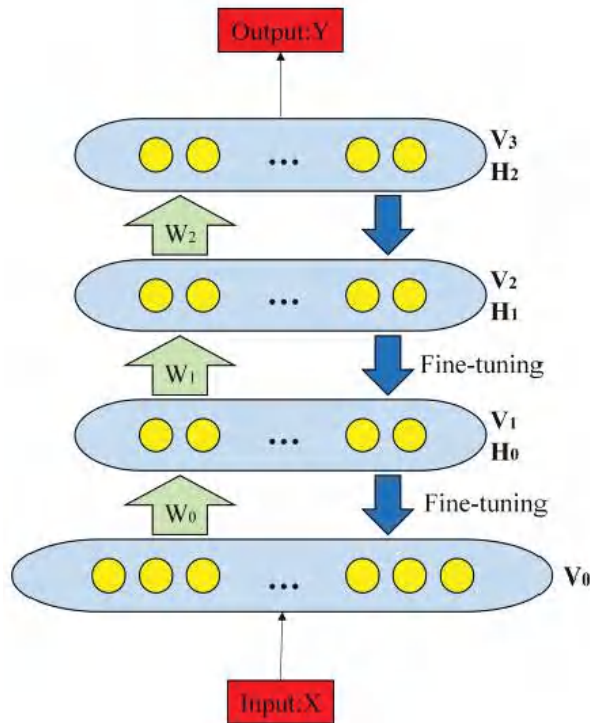


Figure 6. Frame structure of the DBN.

Step 1: Pre-training. The pre-training process involves training each layer of the RBM network in an unsupervised manner. The aim is to keep sufficient feature information when the features are mapped to different feature spaces. The overall training process includes three steps: (1) train the first RBM until convergence; (2) freeze the weight and bias of the well-trained RBM and take the state of its hidden layer as the input of the second RBM; and (3) stack the two RBM models after the second RBM is converged. We repeat the above three steps until the whole network is converged.

Step 2: Fine-tuning. In the fine-tuning step, we set up a supervised network in the last layer of a DBN model. The model takes the output of the RBM as input, and trains the entity relationship in a supervised manner. In addition, the backpropagation process propagates the error information to each RBM model, and fine-tunes the parameters in the DBN network.

As shown in Figure 7, the BLS [8] consists of four parts: input, feature node, enhancement node, and output. In fact, the network performance of the BLS after two training steps is insufficient. We establish the links between the output and input of the network, and fine-tune it by backpropagation. Based on this idea, this paper designs an improved BLS variant, namely, BLS-BP.

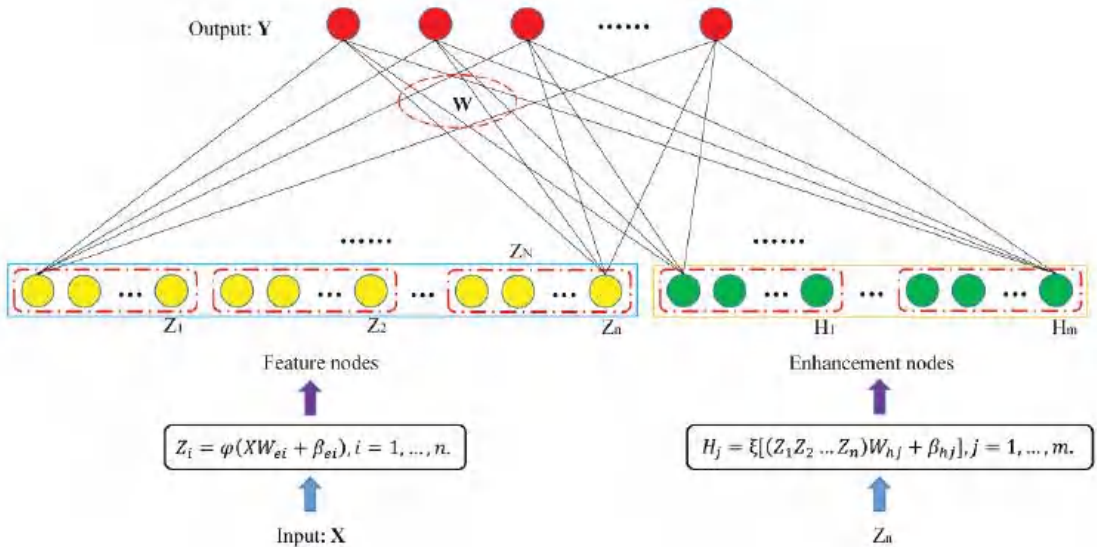


Figure 7. Frame structure of the BLS.

After the load data are trained by the BLS, the error in the output layer is propagated to the input layer for fine-tuning by backpropagation. Then, we calculate the gradient based on the error, and leverage the gradient to update the weights and biases. The training step is stopped if certain conditions are met. We can set the maximum number of iterations or calculate the prediction accuracy of the training set on the network, and stop training after reaching a certain threshold. The training process of the BLS can be viewed as the weight initialization of a BP network, which can help the network get rid of the local optima and shorten the training time. Here, a detailed pseudo-code for the BLS-BP is given in Algorithm 2.

Algorithm 2: Broad Learning: Increment of the backpropagation neural network

Input: training samples X ;
Output: the weight matrix between feature nodes, W ;
Parameter setting: Z_n (the feature mapping group); H_m (the enhancement nodes group); W (the output weight of the BLS); E (the condition for stopping iteration);

- 1: **for** $i = 0; i \leq n$ **do**
- 2: **Random** W_{e_i}, β_{e_i} ;
- 3: Calculate $Z_i = [\varphi(UW_{e_i} + \beta_{e_i})]$;
- 4: **end**
- 5: Set $Z_n = [Z_1, \dots, Z_n]$;
- 6: **for** $j = 1; j \leq m$ **do**
- 7: **Random** W_{h_j}, β_{h_j} ;
- 8: Calculate $H_i = [\xi_j(PW_{h_j} + \beta_{h_j})]$;
- 9: **end**
- 10: Set $H_m = [H_1, H_2, \dots, H_m]$;
- 11: Set $Y = [Z_1, Z_2, \dots, Z_n | H_1, H_2, \dots, H_m]$; $W = [P|H_m]W$;
- 12: Calculate $E_p = f'(Y_p) \cdot (d_p - Y_p)$;
- 13: **while** $E_p > E$ **do**
- 14: Return W
- 15: Calculate $W_{(n)} = W + \cdot E_p \cdot Y_p$;
- 16: Update $Y_{(n)} = [Z_1, Z_2, \dots, Z_n | H_1, H_2, \dots, H_m]$; $W_n = [P|H_m]W_{(n)}$;
- 17: $W = W_{(n)}$;
- 18: $n = n + 1$;
- 19: **end**
- 20: Repeat steps 12–19
- 21: **Export** W

3. Numerical Analysis

3.1. Datasets

To demonstrate the effectiveness and robustness of our model, we conducted experiments on five datasets collected in the United States between 2017 and 2019. All datasets were from five regions in the US, and were called CAPITL, CENTRL, DUNWOD, GENESE, and HUDVL. The dataset sampling interval was 30 min, meaning that one day covers 48 load data samples. Figure 8 shows the load data in March to demo the training mode of similar-days [29] prediction in this paper. We selected the similar-days period data of different years to divide the training set, validation set, and test set. Before starting the experiment, we normalized the sample data to the range [0, 1] to eliminate the dominant effect of those data with large values.

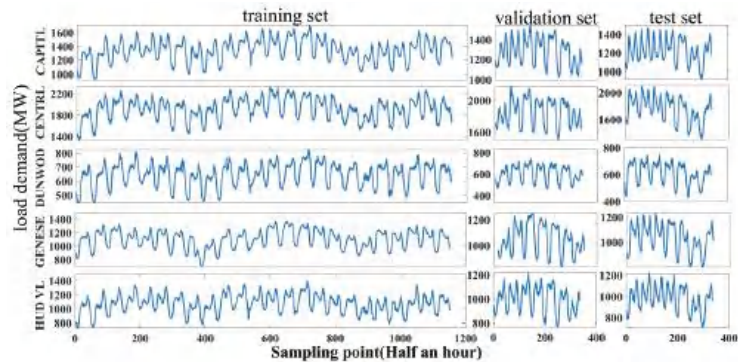


Figure 8. Dataset for March.

The normalization formula was as follows:

$$\hat{y}_m = \frac{y_{max} - y_m}{y_{max} - y_{min}} \tag{1}$$

where \hat{y}_m is the normalized value, y_m represents the actual load data, y_{max} is the maximum value of the load data, and y_{min} is the minimum value of the load data.

3.2. Evaluation Criterion

To effectively evaluate the predictive performance of our proposed model in STLF, we used the following two evaluation criteria: the root-mean-square error (RMSE) [30] and the mean absolute percentage error (MAPE) [31]. They are defined as follows:

$$RMSE = \sqrt{\frac{1}{M} \sum_{m=1}^M (\hat{y}_m - y_m)^2} \tag{2}$$

$$MAPE = \frac{100\%}{M} \sum_{m=1}^M \left| \frac{\hat{y}_m - y_m}{y_m} \right| \tag{3}$$

where \hat{y}_m represents the prediction data, y_m represents the actual load data, and M is the size of the dataset. For both of the evaluation criteria, a smaller value indicates better performance of the models.

3.3. Parameter Settings

We performed hyperparameter exploration before we started our formal experiment. In our data pre-processing, the window size of the sliding-window algorithm was critical to the final performance. To ensure the optimal window size, we applied the controlled variable method, and adopted RMSE and MAPE as the evaluation metrics. According to the test results in Figure 9, we can see that our model has the smallest RMSE and MAPE when the sliding window takes the value of 96, indicating that the model has the best prediction performance. Since there are 48 samples of load data in a day, and the size of the window needs to be an integer number of days, we need to consider the practical significance of the window size representing a specific time interval. Therefore, we determined the optimal window size for the sliding window to be 96.

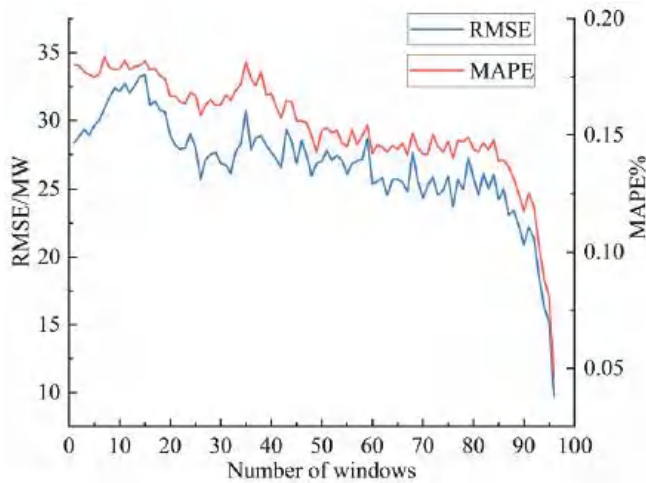


Figure 9. The corresponding error of window size.

In the cross-validation (CV) module [32], an error experiment was carried out to filter out the number of CV folds with the smallest error. We utilized MAPE as the evaluation metric, and plotted the figure of error lines with regard to the power load in the spring for CAPITL. As shown in Figure 10, when the CV is too small, the empirical error is large and the model is not robust. When the CV is too large, the experimental error is not reduced, although the computational effort increases greatly. We set CV to 12 as a compromise of the computational effort and the model prediction performance. Table 1 shows the optimal parameter settings of the machine learning methods used for comparison after many experiments.

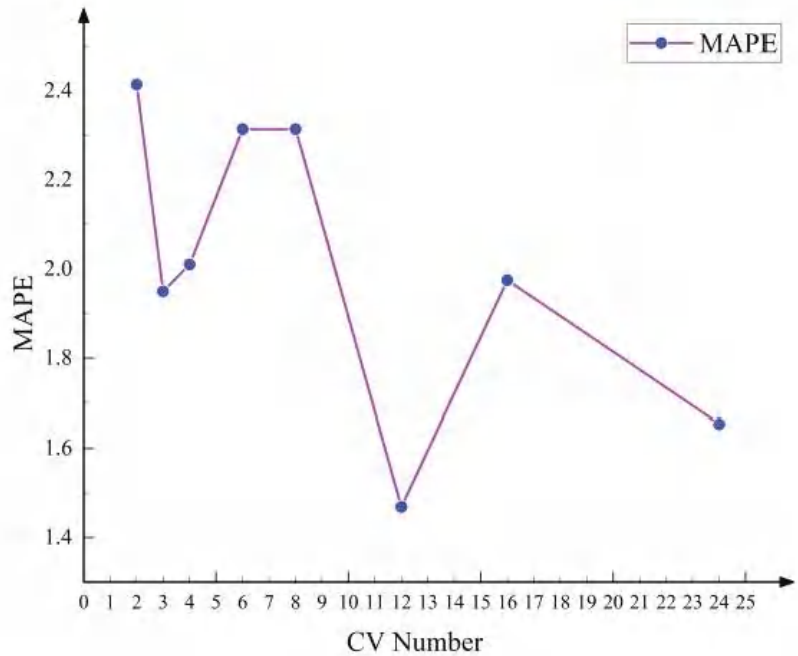


Figure 10. Corresponding error of CV folding number.

Table 1. Comparison of method parameter settings.

Model	Optimal Parameters
BPNN	$n_h = 200, m_i = 10, a_f = Sigmoid$
DBN	$n_h = 10, eta = 0.001, a_f = Sigmoid, r_b = 1, v_m = 0.01, m_i = 20$
RBFNN	$f_{RBF} = Gaussian, s_{RBF} = 50$
RVFL	$n_e = 10000, a_f = Sigmoid, DL = true, r_m = Gaussian$
EMD-BLS	$n_f = 24, n_e = 15$
SWT-LSTM	$n_h = 200, eta = 0.01$
DWT-EMD-RVFL	$n_e = 10000, a_f = Sigmoid, DL = true, r_m = Gaussian$
EMD-EDBN	$n_h = [100, 100], eta = 0.001, a_f = Sigmoid, r_b = 2, v_m = 0.01, m_i = 500$

n_h —the number of hidden nodes; n_h —the maximum number of iterations; a_f —activation function; eta —learning rate; r_b —the random batch size of each time; v_m —momentum value; f_{RBF} —radial basis functions; s_{RBF} —the spread of radial basis functions; n_e —the number of enhancement nodes; DL —whether to have the direct link between the input layer and output layer; r_m —randomization methods; n_f —the number of feature nodes.

4. Case Study

To demonstrate the effectiveness and robustness of our model, we extensively compared the performance of the proposed model with several baselines. Among the baselines,

five approaches are single components of our stacking model: RBFNN, BPNN, RVFL, DBN, BLS-BP, and four models are state-of-the-art in STLF: DWT-EMD-RVFL [9], SWT-LSTM [33], EMD-BLS [8], and EMD-EDBN [7]. We conducted four sets of experiments to show the superiority of our model against the baselines. Our experiments were implemented in MATLAB R2021b (which is produced by US based MathWorks, Inc., Natick, MA, USA) on a laptop equipped with Intel(R) Core (TM) i7-9750H CPU @ 2.60 GHz 2.59 GHz.

1. **Ablation study:** In this experiment, we compared our stacking model with the five components of our model, and verified that the proposed model can outperform all the baselines (see Section 4.1).
2. **Compare to other ensemble models:** In this experiment, we demonstrated the effectiveness of the stacked meta-learners in our model against the baseline models with a single meta-learner. We adopted the same base-layer learners in our model and the baseline models (see Section 4.2).
3. **Compare to state-of-the-art models:** We compared our model with other state-of-the-art models, and demonstrated that our model outperforms other baseline models (see Section 4.3).
4. **Comparison of computation times between models:** We compared the computation times required for each case based on the spring load data in HUDVL (see Section 4.4).
5. **Heavy load test:** In this experiment, we repeated the above three experiments on the data collected on a special holiday. The high demand for electricity on the holiday leads to a heavy power load, and increases the uncertainty of the power load (see Section 4.5).

4.1. Ablation Experiment between Single Models and Hybrid Models

In this experiment, we took five single machine learning methods as baselines, and the results are shown in Table 2. We emphasize the prediction results of our model using the grey background. We can observe that our model outperforms the baselines in each sub-dataset. Specifically, our model can achieve an outstanding performance even when the power load time series is nonlinear and non-stationary (see CAPITL and CENTRL for example). Although DBN can already make good predictions, the improved BLS proposed in this article even has a prediction error less than that of the DBN in many cases. The results demonstrate that the regression-based BLS has an effective predictive ability. In addition, our model significantly outperforms other baseline models. In Figure 11, we can also observe that the proposed method has the lowest MAPE, demonstrating the effectiveness and robustness of our model. The proposed method achieves the best performance in all datasets and forecasting steps. The forecast curves of the various methods on Christmas Day are shown in Section 4.5.

Table 2. The error of comparison with separate neural network models.

Area	Season	Spring		Summer		Autumn		Winter	
	Model	RMSE	MAPE	RMSE	MAPE	RMSE	MAPE	RMSE	MAPE
CAPITL	OURS	21.97	1.47	27.73	1.24	24.72	1.54	25.70	1.47
	RBFNN	60.05	3.93	55.50	2.55	70.27	4.80	38.59	2.34
	BPNN	39.75	2.52	35.70	1.71	37.66	2.59	35.04	2.09
	RVFL	31.13	2.00	38.74	1.77	33.95	2.17	31.29	1.82
	DBN	31.74	2.09	39.39	1.82	33.99	2.17	29.68	1.73
	BLS-BP	37.71	2.38	35.57	1.61	41.29	2.55	26.77	1.48
CENTRL	OURS	41.60	1.95	41.04	1.61	36.20	1.75	38.02	1.74
	RBFNN	79.29	3.69	51.33	1.93	61.56	3.06	66.51	3.03
	BPNN	63.32	2.99	60.29	2.42	46.15	2.28	58.08	2.52
	RVFL	60.14	2.96	44.13	1.74	38.99	1.80	41.17	1.83
	DBN	46.39	2.23	56.13	2.26	37.88	1.78	40.00	1.74
	BLS-BP	50.04	2.37	46.96	1.97	46.45	2.10	42.54	1.88

Table 2. Cont.

Area	Season	Spring		Summer		Autumn		Winter	
	Model	RMSE	MAPE	RMSE	MAPE	RMSE	MAPE	RMSE	MAPE
DUNWOD	OURS	14.20	1.86	22.82	1.82	17.87	2.28	16.42	2.09
	RBFNN	28.05	3.68	34.47	2.92	28.59	3.82	25.46	3.28
	BPNN	25.80	3.40	24.32	2.13	32.09	4.52	18.22	2.43
	RVFL	21.17	2.89	27.93	2.08	19.21	2.38	18.09	2.32
	DBN	16.86	2.17	32.22	2.76	18.61	2.48	17.12	2.16
	BLS-BP	18.29	2.37	24.20	1.89	18.59	2.38	16.29	2.10
GENESE	OURS	18.48	1.44	18.88	1.16	15.55	1.16	16.59	1.18
	RBFNN	29.90	2.38	22.10	1.34	23.71	1.84	24.29	1.78
	BPNN	28.51	2.38	38.84	2.61	16.30	1.19	20.93	1.57
	RVFL	32.36	2.67	28.89	1.69	21.28	1.62	23.06	1.66
	DBN	23.23	1.91	35.34	2.04	21.95	1.71	24.21	1.88
	BLS-BP	29.20	2.23	26.79	1.60	21.69	1.68	24.15	1.69
HUDVL	OURS	24.05	1.99	28.19	2.11	47.49	4.08	28.08	2.07
	RBFNN	48.70	4.12	36.44	1.92	64.84	5.31	41.37	3.10
	BPNN	36.69	3.08	47.62	2.78	50.98	4.17	31.40	2.25
	RVFL	37.67	3.11	39.81	2.10	59.71	5.19	31.51	2.40
	DBN	24.69	1.99	44.47	2.43	56.60	4.83	31.25	2.41
	BLS-BP	32.54	2.73	34.97	1.91	51.98	4.27	32.47	2.46

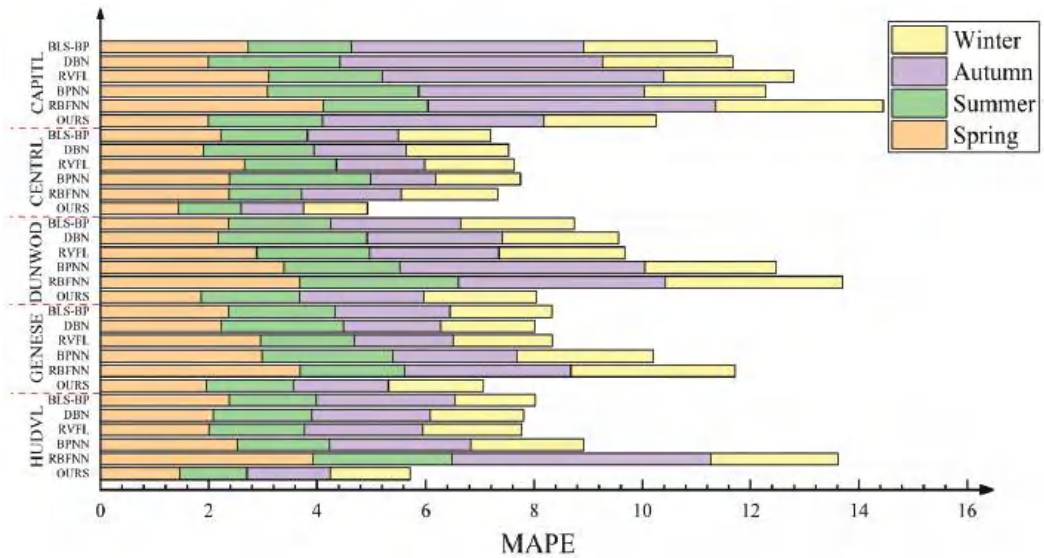


Figure 11. Stacked evaluation indicators of each model.

4.2. Comparison with Other Ensemble Models

Based on the base learners, we utilized DBN and BLS networks as our meta-learners. We further applied the backpropagation algorithm in the BLS network. We renamed the DBN and improved BLS as S-DBN and S-BLS, respectively. The error results are shown in Table 3. From the table, we can observe that the accuracy and stability of the stacked model outperform those of a single model. However, the performance is still insufficient compared to the algorithm proposed in this article, which shows the feasibility of our proposed algorithm. The forecast curves of various methods on Christmas Day are shown in Section 4.5.

Table 3. The error of comparison with other ensemble models.

Area	Season	Spring		Summer		Autumn		Winter	
	Model	RMSE	MAPE	RMSE	MAPE	RMSE	MAPE	RMSE	MAPE
CAPITL	OURS	21.97	1.47	27.73	1.24	24.72	1.54	25.70	1.47
	S-DBN	34.52	2.39	52.53	2.40	34.35	2.26	27.23	1.57
	S-BLS	30.33	1.93	35.28	1.57	31.60	2.01	26.96	1.61
CENTRL	OURS	41.60	1.95	41.04	1.61	36.20	1.75	38.02	1.74
	S-DBN	55.57	2.71	49.04	1.95	36.67	1.79	40.88	1.80
	S-BLS	51.69	2.40	54.28	2.09	58.70	2.77	40.51	1.78
DUNWOD	OURS	14.20	1.86	22.82	1.82	17.87	2.28	16.42	2.09
	S-DBN	15.43	2.06	27.70	2.26	18.00	2.36	16.68	2.14
	S-BLS	15.37	2.05	24.58	1.92	18.98	2.47	20.02	2.52
GENESE	OURS	18.48	1.44	18.88	1.16	15.55	1.16	16.59	1.18
	S-DBN	19.79	1.58	28.20	1.50	17.96	1.34	16.65	1.22
	S-BLS	23.86	1.91	20.77	1.20	17.16	1.26	18.48	1.40
HUDVL	OURS	24.05	1.99	28.19	2.11	47.49	4.08	28.08	2.07
	S-DBN	29.77	2.51	37.57	2.01	60.14	5.39	29.12	2.18
	S-BLS	24.59	2.02	30.12	1.63	48.67	4.08	29.47	2.24

4.3. Comparison with Other Hybrid Models

To date, a variety of hybrid models have been proposed for short-term load forecasting. We took four models as the baselines for our model: DWT-EMD-RVFL [9], SWT-LSTM [33], EMD-BLS [8], and EMD-EDBN [7]. The empirical results show a similar trend with previous experimental results: the proposed model outperforms the hybrid models for each dataset in all forecasting horizons. The respective error experiments are shown in Table 4. We can observe that the EMD-EDBN model has the worst results for all datasets in all forecasting horizons. Figure 12 shows that our method has the smallest errors on each sub-dataset, demonstrating the effectiveness and robustness of our model. The forecast curves of various methods on Christmas Day are shown in Section 4.5.

Table 4. The error of comparison with other hybrid models.

Area	Season	Spring		Summer		Autumn		Winter	
	Model	RMSE	MAPE	RMSE	MAPE	RMSE	MAPE	RMSE	MAPE
CAPITL	OURS	21.97	1.47	27.73	1.24	24.72	1.54	25.70	1.47
	DWT-EMD-RVFL	29.38	1.95	43.22	1.93	27.12	1.75	29.54	1.66
	SWT-LSTM	29.56	1.90	42.37	1.97	25.71	1.60	43.56	2.70
	EMD-BLS	23.28	1.51	30.83	1.43	39.42	3.05	30.93	1.61
	EMD-EDBN	36.00	2.26	74.20	3.64	47.37	3.20	30.93	1.61
CENTRL	OURS	41.60	1.95	41.04	1.61	36.20	1.75	38.02	1.74
	DWT-EMD-RVFL	43.72	2.08	48.46	1.93	39.66	1.86	39.75	1.77
	SWT-LSTM	35.52	1.65	44.14	1.85	37.58	1.79	38.83	1.73
	EMD-BLS	52.07	2.55	47.50	1.92	39.86	1.83	45.50	2.00
	EMD-EDBN	42.34	1.98	88.28	3.64	50.78	2.51	79.92	3.76
DUNWOD	OURS	14.20	1.86	22.82	1.82	17.87	2.28	16.42	2.09
	DWT-EMD-RVFL	16.14	2.20	28.01	2.28	17.94	2.38	17.49	2.16
	SWT-LSTM	15.64	2.06	26.41	1.98	18.70	2.17	18.96	2.45
	EMD-BLS	19.76	2.69	34.56	3.45	30.28	4.71	23.21	3.25
	EMD-EDBN	29.76	4.00	95.57	7.39	45.02	5.93	30.02	4.37

Table 4. Cont.

Area	Season	Spring		Summer		Autumn		Winter	
	Model	RMSE	MAPE	RMSE	MAPE	RMSE	MAPE	RMSE	MAPE
GENESE	OURS	18.48	1.44	18.88	1.16	15.55	1.16	16.59	1.18
	DWT-EMD-RVFL	22.53	1.77	28.59	1.65	19.49	1.42	20.94	1.43
	SWT-LSTM	23.75	1.93	27.46	1.70	23.73	1.87	23.01	1.75
	EMD-BLS	26.34	2.08	26.23	1.42	42.30	3.04	30.54	2.22
	EMD-EDBN	46.70	3.89	153.69	9.01	39.91	3.02	77.17	6.00
HUDVL	OURS	24.05	1.99	28.19	2.11	47.49	4.08	28.08	2.07
	DWT-EMD-RVFL	28.93	2.35	40.06	2.09	48.32	4.14	32.67	2.44
	SWT-LSTM	34.30	2.73	30.61	1.70	59.02	5.21	28.20	2.04
	EMD-BLS	34.64	2.93	40.73	2.41	47.95	4.29	33.41	2.46
	EMD-EDBN	64.31	5.85	82.02	4.61	97.17	8.74	50.54	3.60

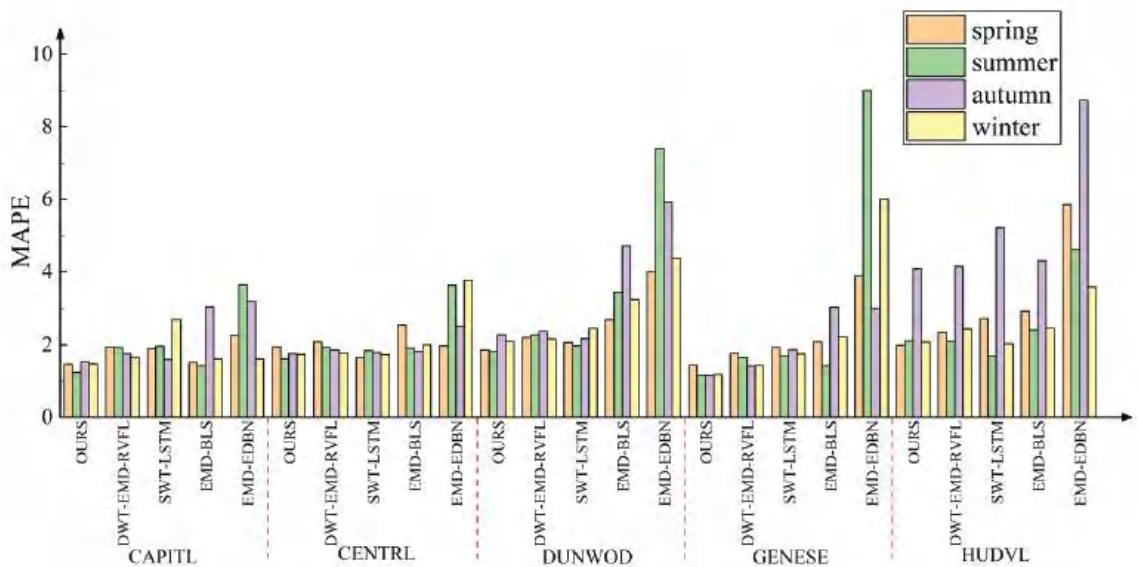


Figure 12. MAPEs of the hybrid models.

4.4. Comparison of Computation Times between Models

Considering that the computational effort should be considered for the prediction performance evaluation of the models, the computation times required for each case are discussed in this section. We selected the computation times of each model in the case of predicting the spring load data in HUDVL, and the computation times for each model are shown in Table 5. As shown in Table 5, the proposed model has a computation time of 83.928 s. Although the proposed model has a longer computation time than most of the individual comparative models, it significantly outperforms the other comparative models in terms of prediction performance, and the time cost of implementation is within acceptable limits. In addition, the experimental results show that the proposed model has a shorter computation time and better prediction performance than a single complex SWT-LSTM model.

Table 5. The computation times required for each case.

Area	Season	Spring
	Model	Time/Second
HUDVL	OURS	83.928
	RBFNN	13.214
	BPNN	15.893
	RVFL	12.039
	DBN	12.901
	BLS-BP	11.574
	S-DBN	81.259
	S-BLS	66.374
	DWT-EMD-RVFL	13.333
	SWT-LSTM	107.791
	EMD-BLS	12.618
	EMD-EDBN	28.211

4.5. Model Performance Analysis on a Heavy Load Test

This section selects a special day in the United States—Christmas—to analyze the performance of the model. Figure 13a–c show the prediction curves of three groups of comparative experiments on Christmas Day. The figures show that although other models can effectively predict the load in some regions where the original electric load increases and decreases steeply, there are still large errors in the prediction results in the regions where the original electric load curve fluctuates widely at the peaks and valleys. In contrast, the load prediction curve of the hybrid network proposed in this paper can fit the original power load curve well. It can predict well even in some areas with large fluctuations of the original power load curve, as well as peaks and troughs. This shows that the method proposed in this paper has strong robustness.

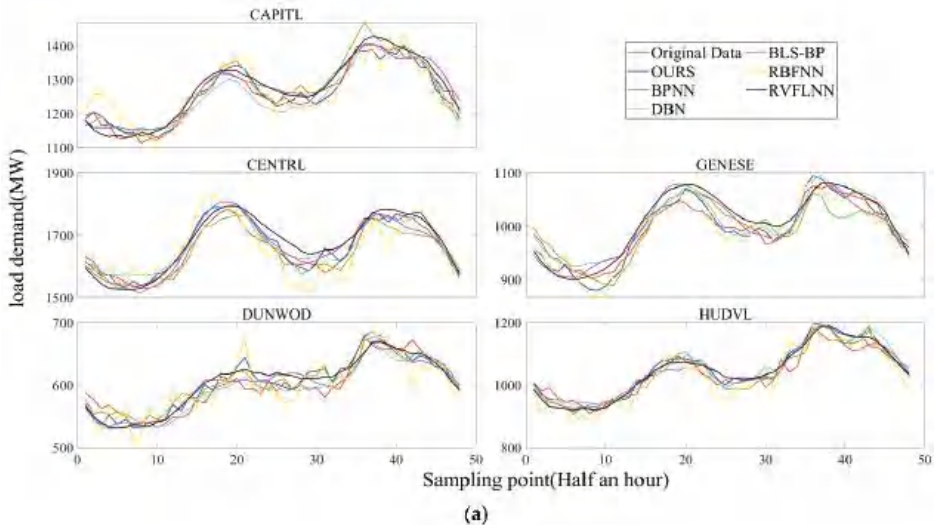


Figure 13. Cont.

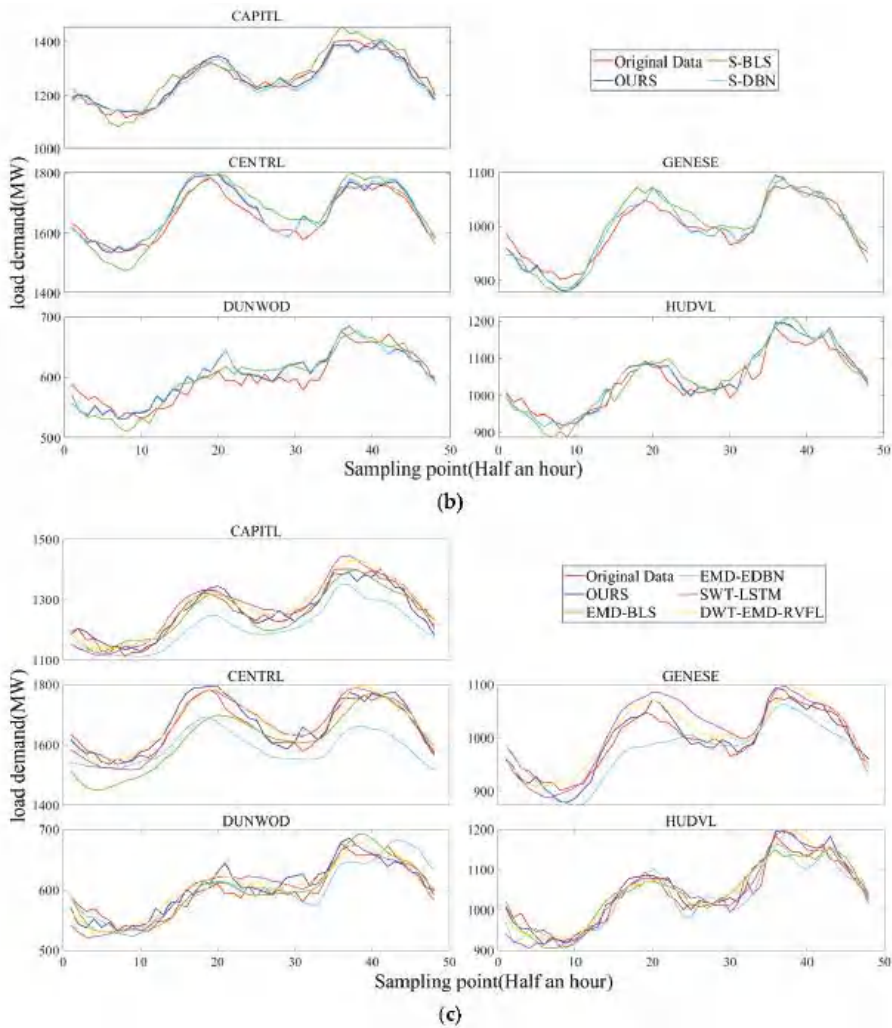


Figure 13. (a) The prediction curve of the comparison with separate neural network models; (b) the prediction curve of the comparison with other ensemble models; (c) the prediction curve of the comparison with other hybrid models.

4.6. Discussion

The empirical results demonstrate that our model can achieve promising performance, and that our model is more robust than the baseline models for the STLTF task. The high-level intuition is that the sliding-window algorithm can smooth the nonlinearity and non-stationarity of the power load data series. In addition, the proposed stacking method can effectively combine multiple neural networks to improve the prediction performance of this method. The forecasting accuracy is further improved by the improved BLS. In addition, the similar-days prediction method is developed for extracting the relationship of electric load data in different time dimensions, proving the robustness of the model.

5. Conclusions

This paper proposes a novel ensemble learning framework for short-term load forecasting. The proposed forecasting framework employs the sliding-window technique to deal

with the time-series electric load data. After that, the data are processed in a similar-time prediction method after the training of ensemble learning. Finally, the proposed model is compared with individual neural network models, other ensemble models, and hybrid models. Error analysis is obtained based on MAPE and RMSE evaluation criteria.

In conclusion, the proposed model has advantages in robustness and effectiveness. (i) Robustness: The regression-based broad learning system can achieve outstanding performance when tackling the noise and outliers. The proposed model stacks sub-models to obtain a stacking ensemble model. Our empirical results show that our proposed stacking method can outperform its sub-component, demonstrating the robustness of our model. (ii) Effectiveness: The proposed model can outperform the four existing hybrid baseline models and the sub-component model. The experimental results show that our model can achieve significantly better results than the baseline models because it has a rational framework and design.

However, there are still some limitations to the proposed work. For example, our proposed stacking model has a higher computational cost compared to other individual prediction models. In the future, we plan to explore better model selection for the base- and meta-learners in the stacking approach to tackle this issue, and we intend to use optimization methods to tune the hyperparameters of the prediction models to obtain better prediction accuracy. In addition, we are also interested in investigating electricity load forecasting for individual household customers with higher volatility to validate the robustness and accuracy of our proposed model.

Author Contributions: Conceptualization, Q.J., Y.C. and C.L.; methodology, Y.C.; software, Y.C. and H.L.; validation, Q.J., Y.C. and H.L.; formal analysis, H.L.; investigation, Y.C.; resources, C.L. and P.X.L.; data curation, Y.C.; writing—original draft preparation, Q.J. and Y.C.; writing—review and editing, Q.J. and C.L.; visualization, Q.J. and Y.C.; supervision, C.L. and P.X.L.; project administration, C.L. and P.X.L.; funding acquisition, C.L. All authors have read and agreed to the published version of the manuscript.

Funding: This work was supported in part by the National Natural Science Foundation of China under grants 61863028, 62173176, 81660299, and 61503177, and in part by the Science and Technology Department of Jiangxi Province of China under grants 20204ABC03A39, 20161ACB21007, 20171BBE50071, and 20171BAB202033.

Institutional Review Board Statement: This study did not involve humans or animals.

Informed Consent Statement: This study did not involve humans.

Data Availability Statement: Not applicable.

Conflicts of Interest: The authors declare no conflict of interest.

Abbreviations

ANN	Artificial neural network
ARMA	Autoregressive moving average
BLS	Broad learning system
BLS–BP	Broad learning system–backpropagation
BPNN	Backpropagation neural network
CV	Cross-validation
DBN	Deep belief network
DWT	Discrete wavelet transform
EMD	Empirical mode decomposition
EDBN	Ensemble DBN
LR	Linear regression
LSTM	Long short-term memory
MAPE	Mean absolute percentage error
RBF	Radial basis function
RBM	Restricted Boltzmann machine

RVFL	Random vector functional link
RMSE	Root-mean-square error
S-BLS	Selected BLS
S-DBN	Selected DBN
STLF	Short-term load forecasting
SVR	Support-vector regression
SWT	Stationary wavelet transform

References

1. Simoglou, C.K.; Biskas, P.N. Assessment of the impact of the National Energy and Climate Plan on the Greek power system resource adequacy and operation. *Electr. Power Syst. Res.* **2021**, *194*, 107113. [CrossRef]
2. Li, X.; Jiang, T.; Liu, G.; Bai, L.; Cui, H.; Li, F. Bootstrap-based confidence interval estimation for thermal security region of bulk power grid. *Int. J. Electr. Power Energy Syst.* **2020**, *115*, 105498. [CrossRef]
3. Moon, J.; Hossain, M.B.; Chon, K.H. AR and ARMA model order selection for time-series modeling with ImageNet classification. *Signal Process.* **2021**, *183*, 108026. [CrossRef]
4. Dosiek, L. The Effects of Forced Oscillation Frequency Estimation Error on the LS-ARMA+S Mode Meter. *IEEE Trans. Power Syst.* **2020**, *35*, 1650–1652. [CrossRef]
5. Prion, S.K.; Haerling, K.A. Making Sense of Methods and Measurements: Simple Linear Regression. *Clin. Simul. Nurs.* **2020**, *48*, 94–95. [CrossRef]
6. Alamdar, F.; Mohammadi, F.S.; Amiri, A. Twin Bounded Weighted Relaxed Support Vector Machines. *IEEE Access* **2019**, *7*, 22260–22275. [CrossRef]
7. Qiu, X.; Ren, Y.; Suganthan, P.N.; Amaratunga, G.A.J. Empirical Mode Decomposition based ensemble deep learning for load demand time series forecasting. *Appl. Soft Comput.* **2017**, *54*, 246–255. [CrossRef]
8. Zhu, L.; Lian, C. Wind Speed Forecasting Based on a Hybrid EMD-BLS Method. In Proceedings of the Chinese Automation Congress (CAC), Hangzhou, China, 22–24 November 2019; IEEE: Piscataway, NJ, USA, 2019; pp. 2191–2195.
9. Qiu, X.; Suganthan, P.N.; Amaratunga, A.J.G. Ensemble Incremental Random Vector Functional Link Network for Short-term Crude Oil Price Forecasting. In Proceedings of the IEEE Symposium Series on Computational Intelligence (SSCI), Bangalore, India, 18–21 November 2018; IEEE: Piscataway, NJ, USA, 2018; pp. 1758–1763.
10. Shahid, F.; Zameer, A.; Muneeb, M. A novel genetic LSTM model for wind power forecast. *Energy* **2021**, *223*, 120069. [CrossRef]
11. Potočnik, P.; Škerl, P.; Govekar, E. Machine-learning-based multi-step heat demand forecasting in a district heating system. *Energy Build.* **2021**, *233*, 110673. [CrossRef]
12. Xu, C.; Gordan, B.; Koopialipoor, M.; Armaghani, D.J.; Tahir, M.M.; Zhang, X. Improving Performance of Retaining Walls under Dynamic Conditions Developing an Optimized ANN Based on Ant Colony Optimization Technique. *IEEE Access* **2019**, *7*, 94692–94700. [CrossRef]
13. Chen, G.J.; Li, K.K.; Chung, T.S.; Sun, H.B.; Tang, G.Q. Application of an innovative combined forecasting method in power system load forecasting. *Electr. Power Syst. Res.* **2001**, *59*, 131–137. [CrossRef]
14. Chen, Y.; Luh, P.B.; Guan, C.; Zhao, Y.; Michel, L.D.; Coolbeth, M.A.; Friedland, P.B.; Rourke, S.J. Short-Term Load Forecasting: Similar Day-Based Wavelet Neural Networks. *IEEE Trans. Power Syst.* **2010**, *25*, 322–330. [CrossRef]
15. Matrenin, P.V.; Manusov, V.Z.; Khalyasmaa, A.I.; Antonenkov, D.V.; Eroshenko, S.A.; Butusov, D.N. Improving Accuracy and Generalization Performance of Small-Size Recurrent Neural Networks Applied to Short-Term Load Forecasting. *Mathematics* **2020**, *8*, 2169. [CrossRef]
16. Singh, P.; Dwivedi, P. Integration of new evolutionary approach with artificial neural network for solving short term load forecast problem. *Appl. Energy* **2018**, *217*, 537–549. [CrossRef]
17. Niu, D.; Wang, Y.; Wu, D.D. Power load forecasting using support vector machine and ant colony optimization. *Expert Syst. Appl.* **2010**, *37*, 2531–2539. [CrossRef]
18. Nengling, T.; Stenzel, J.; Hongxiao, W. Techniques of applying wavelet transform into combined model for short-term load forecasting. *Electr. Power Syst. Res.* **2006**, *76*, 525–533. [CrossRef]
19. Ghayekhloo, M.; Menhaj, M.B.; Ghofrani, M. A hybrid short-term load forecasting with a new data preprocessing framework. *Electr. Power Syst. Res.* **2015**, *119*, 138–148. [CrossRef]
20. Ghofrani, M.; Ghayekhloo, M.; Arabali, A.; Ghayekhloo, A. A hybrid short-term load forecasting with a new input selection framework. *Energy* **2015**, *81*, 777–786. [CrossRef]
21. Laouafi, A.; Mordjaoui, M.; Haddad, S.; Boukelia, T.E.; Ganouche, A. Online electricity demand forecasting based on an effective forecast combination methodology. *Electr. Power Syst. Res.* **2017**, *148*, 35–47. [CrossRef]
22. Wang, G.; Wang, X.; Wang, Z.; Ma, C.; Song, Z. A VMD-CISSA-LSSVM Based Electricity Load Forecasting Model. *Mathematics* **2022**, *10*, 28. [CrossRef]
23. Che, J.; Wang, J. Short-term load forecasting using a kernel-based support vector regression combination model. *Appl. Energy* **2014**, *132*, 602–609. [CrossRef]
24. Zhang, T.; Zhang, Y.; Sun, H.; Shan, H. Parkinson disease detection using energy direction features based on EMD from voice signal. *Biocybern. Biomed. Eng.* **2021**, *41*, 127–141. [CrossRef]

25. Hu, M.; Wang, G.; Ma, K.; Cao, Z.; Yang, S. Bearing performance degradation assessment based on optimized EWT and CNN. *Measurement* **2021**, *172*, 108868. [CrossRef]
26. Cheng, Y.; Le, H.; Li, C. A Decomposition-Based Improved Broad Learning System Model for Short-Term Load Forecasting. *J. Electr. Eng. Technol.* **2022**. [CrossRef]
27. Liang, L.; Guo, W.; Zhang, Y.; Zhang, W.; Li, L.; Xing, X. Radial Basis Function Neural Network for prediction of medium-frequency sound absorption coefficient of composite structure open-cell aluminum foam. *Appl. Acoust.* **2020**, *170*, 107505. [CrossRef]
28. Hu, Y.; Li, J.; Hong, M.; Ren, J.; Lin, R.; Liu, Y.; Liu, M.; Man, Y. Short term electric load forecasting model and its verification for process industrial enterprises based on hybrid GA-PSO-BPNN algorithm—A case study of papermaking process. *Energy* **2019**, *170*, 1215–1227. [CrossRef]
29. Sun, G.; Jiang, C.; Cheng, P.; Liu, Y.; Wang, X.; Fu, Y.; He, Y. Short-term wind power forecasts by a synthetical similar time series data mining method. *Renew. Energy* **2018**, *115*, 575–584. [CrossRef]
30. Mentaschi, L.; Besio, G.; Cassola, F.; Mazzino, A. Problems in RMSE-based wave model validations. *Ocean. Model.* **2013**, *72*, 53–58. [CrossRef]
31. Jahan, S.; Riley, I.; Walter, C.; Gamble, R.F.; Pasco, M.; McKinley, P.K.; Cheng, B.H.C. MAPE-K/MAPE-SAC: An interaction framework for adaptive systems with security assurance cases. *Future Gener. Comput. Syst.* **2020**, *109*, 197–209. [CrossRef]
32. Hirano, K.; Wright, J.H. Analyzing cross-validation for forecasting with structural instability. *J. Econ.* **2021**, *226*, 139–154. [CrossRef]
33. Yan, K.; Li, W.; Ji, Z.; Qi, M.; Du, Y. A Hybrid LSTM Neural Network for Energy Consumption Forecasting of Individual Households. *IEEE Access* **2019**, *7*, 157633–157642. [CrossRef]

Article

Fluid–Structure Interaction Modeling of Structural Loads and Fatigue Life Analysis of Tidal Stream Turbine

Yuquan Zhang ^{1,2}, Zhiqiang Liu ¹, Chengyi Li ^{2,*}, Xuemei Wang ³, Yuan Zheng ¹, Zhi Zhang ², Emmanuel Fernandez-Rodriguez ⁴ and Rabea Jamil Mahfoud ²

¹ College of Energy and Electrical Engineering, Hohai University, Nanjing 210098, China

² College of Water Conservancy and Hydropower Engineering, Hohai University, Nanjing 210098, China

³ Chongqing Jiangjin Shipbuilding Industry Co., Ltd., Chongqing 402263, China

⁴ Technological Institute of Merida, Technological Avenue, Merida 97118, Mexico

* Correspondence: lichengyi@hhu.edu.cn

Abstract: Developing reliable tidal-energy turbines of a large size and capacity links to preservation of the structural safety and stability of the blades. In this study, a bidirectional fluid–structure coupling method was applied to analyze the hydrodynamic performance and structural characteristics of the blade of a tidal-stream turbine. Analyses were conducted on the transient and stable structural stresses, fatigue, and deformations under the influence of water depth and turbine rotational speed. The performance predictions with and without fluid–structure coupling are similar to measurements. The water-depth change has little effect on the stress and deformation change of the blade, while the turbine-speed change has the most significant effect on it. When the turbine just starts, the blade will be subject to a sudden change load. This is due to the increase in turbine speed, resulting in the sudden load. Similar to the trend of blade stress, the blade safety factor is lower near the root of the blade, and the turbine-speed change has a more significant impact on the blade structure’s safety. However, the number of stress cycles in the blade at different rotational speeds is within the safety range.

Keywords: tidal stream turbine; CFD; fatigue life; fluid–structure interaction; blade safety factor

MSC: 76E07

Citation: Zhang, Y.; Liu, Z.; Li, C.; Wang, X.; Zheng, Y.; Zhang, Z.; Fernandez-Rodriguez, E.; Mahfoud, R.J. Fluid–Structure Interaction Modeling of Structural Loads and Fatigue Life Analysis of Tidal Stream Turbine. *Mathematics* **2022**, *10*, 3674. <https://doi.org/10.3390/math10193674>

Academic Editors: Zhuojia Fu, Yiqian He and Hui Zheng

Received: 30 August 2022

Accepted: 29 September 2022

Published: 7 October 2022

Publisher’s Note: MDPI stays neutral with regard to jurisdictional claims in published maps and institutional affiliations.



Copyright: © 2022 by the authors. Licensee MDPI, Basel, Switzerland. This article is an open access article distributed under the terms and conditions of the Creative Commons Attribution (CC BY) license (<https://creativecommons.org/licenses/by/4.0/>).

1. Introduction

Environmentalists emphasize the imminent animal- and human-habitat disruption from the rising climate temperatures due to the large-scale implementation and burning of fossil fuels. Attempts to reverse the ecological damage are without economical side effects and comprise the carbon residues’ elimination and the minimization and eventual substitution of fossil-based systems into renewable power systems. However, the strategy carries obstacles, such as overcoming renewable discontinuous power output, equalizing cost disparities, and improving reception among users. More recently, supporters have stressed the importance of combining renewable resources, named hybrid systems, to achieve economy of scale and solve the cost-inefficient energy accumulators. Tidal-stream energy fits into this concept. It is a high-density, unrenowned, and foreseeable source, and it could supplement wind offshore systems, once viable. The popular mode for current kinetic energy conversion is through rotary machines (three-bladed turbines) stationed in the sea bottom and coupled to electrical generators. Due to its parallelism to offshore wind, the blade profile can be selected to achieve power efficiencies of 48% but may be more in bounded conditions; this is presumed from the multi-member concept and relatively large sweep to incident channel area.

Relevant inquiries, nevertheless, are whether the underwater devices can survive the corrosivity and unexpected sea environments, as well as where they can live up to

investors' expectations to deliver large low-cost energy over a reasonable time. Since direct field testing is difficult, scientific strategies involve the artificial flow replication, to comprehend the alone and multi-turbine operation, and possible interference in the aquatic life. However, as sites diverge in bathymetry and geographical position, caution in regard to the measured properties must be applied; the current may prompt turbine blockage effects due to shallow depth and mix with omni-directional waves, and the turbulence intensity (TI) can be small (0.1) or critical (0.4), whilst the shear may or not exemplify power laws.

Contrary to uniform flows, the turbine's fluctuating performance is intricate, and thus, the association is unclear between the dynamic blade effects and the main properties of the turbulence and with waves. Tidal-energy turbines are generally arranged in complex marine environments with high flow velocities [1,2]. So, the research methods for tidal-energy turbines are mainly model tests and numerical simulations [3–7]. Allmark et al. [8] conducted model tests of a tidal-energy turbine with a model scale of 1:20 in a recirculating water tank. They found that by using the upstream region of the turbine to achieve acceleration, the turbine could achieve higher power, and the control scheme used had a significant effect on power and load fluctuations. Myers et al. [9] conducted model experiments in a circulating water tank with a turbine diameter of 0.4 m and a ratio of 1:30 and found that, as the inlet flow rate increases, it increases the turbulence around the runner and the change in water-surface height. Zhang et al. [10] evaluated the wake characteristics of a turbine under wave action and showed that the presence of waves has an effect on the intensity of vorticity and turbulence in the near wake field. Gaurier et al. [5] studied load fluctuations in a tank for a turbine model with a scale of 1:20 and showed that fluctuations in turbine load respond directly to fluctuations in low-frequency velocities and are influenced by turbulence shedding from the turbine. This provides substantial suggestions for conducting further fatigue analyses for turbine conditions with high Reynolds-number flow.

Numerical simulations have gradually become a convenient and credible research method through the continuous validation of model experiments conducted by researchers [11]. Tian et al. [12] used available experimental data to verify the reliability of the adopted calculation method, and based on this, the effects of the yaw angle and turbulence-intensity drops on the performance of a horizontal axis tidal energy turbine with a diameter of 3 m were calculated. The results showed that the effects of different turbulence intensities on power coefficient (C_p) and thrust coefficient (C_t) are small, but the effects on wake are large. Ahmadi et al. [13] and others studied the evolution of the wake characteristics of horizontal-axis tidal-energy turbines experimentally, followed by numerical simulations of the flow field, using a combination of Large Eddy Simulation (LES) and Augmented Lagrangian Method (ALM) to partition the turbine wake into different regions, suggesting that to study the characteristics of the turbine wake, it is necessary to understand the variation of flow characteristics in the transition zone.

With the development of tidal-energy turbines to large capacity and large size, their structural safety and stability have received more and more attention [14–17]. On the one hand, the horizontal-axis tidal turbine will produce hydroelastic deformation under the action of water flow, and the deformation produced by the blades will also act on the water flow to produce a certain impact on the flow field; on the other hand, compared with the wind turbine, the tidal turbine will be subject to greater thrust due to the density of seawater [18]. Therefore, the study of fluid–structure coupling for tidal-energy turbines has also attracted the attention of experts and scholars. At present, many scholars have started to conduct fluid–structure coupling analysis on tidal turbines, mainly focusing on their structural reliability, and then achieved the purpose of optimizing the blades.

Some researchers have analyzed the structural performance of tidal turbine blades under different conditions by using the unidirectional fluid–structure coupling method [19]. Hafeez et al. [20] investigated the effect of the velocity shear on the performance and structure of the tidal turbine, comparing the blade deformation in uniform flow and

shear flow, and found that the blade deformation of the turbine under velocity shear flow changed significantly. Liu et al. [21] analyzed the structural performance of blades made of stainless steel and structural steel at different rotational speeds, and the results showed that the output power of the turbine was lower at low rotational speeds, but the energy gain efficiency was higher, and the blades of both materials met the structural safety requirements. Ullah et al. [22], on the other hand, performed a fatigue-life analysis and modal analysis of the hydraulic turbine. Some scholars have also used a bidirectional fluid–structure coupling approach in order to obtain the transient structural response of the blades [23–25]. Nicholls-Lee et al. [26] developed an adaptive composite blade design tool and performed a bidirectional fluid–structure coupling analysis on a series of composite bending–torsion coupled blades, and the results showed that practical design of a properly designed blade can achieve a 12% reduction in thrust coefficient and an effective 5% increase in power coefficient. Badshah et al. [27] showed that the difference between CFD calculation results and fluid–structure coupling calculation results is less than 10%, and the two calculation conditions differ in the results of the blade-surface pressure difference. Tatum et al. [28] recognized that wave action would cause the hydraulic turbine’s asymmetric loading, so the turbine characteristics were calculated for uncoupled CFD and bidirectional fluid–structure coupling conditions, and the comparison revealed no significant difference between the two calculations; this is a matter of blade-material selection. Khalid et al. [24] simulated the transient structural response of a vertical axis tidal-energy turbine runner, using the fluid–structure coupling method; the blade deformation at each time step was considered in the calculation, and a new calculation method was proposed: transferring the file in ANSYS-APDL to obtain the solution results.

Clearly, an implication of turbine (performance curve and number of blades) and flow operation (turbulence profile) and design (vertical vs horizontal), along with the model differences, raises important questions about the generalizability of the above numerical findings. Therefore, in this study, the hydrodynamic performance and structural characteristics of the turbine were numerically simulated and analyzed based on the bidirectional fluid–structure coupling calculation, and the accuracy of the calculation results was verified by model tests. The prototype is a standard three-bladed horizontal-axis concept, operating in a flow with a turbulence intensity of 7%, and depth variation resembling the logarithmic power law. The fatigue life of the blade was also predicted by considering the influence of the turbine speed and water-depth-variation factors. Our work provides a reference for the design and material application of the blade of the tidal-energy turbine. In our view, these results represent an excellent initial step toward the wider use of the Coupled Fluid Structure model due to high computational accuracy and resource efficiency, as well as further testing in more complex situations, such as incoming waves and currents, and floating turbine systems.

2. Basic Theory

The fluid–structure coupling models the complex interaction between the turbine and water by first treating separately and then coupling the behavior of the incompressible fluid (water) and deformable structure. The strategy has been used to contemplate complex physical phenomena, such as smoking, and can benefit by the use of advanced backed-up separate solvers, applicable to the matter and operating state. Parameters in the method’s stability, resource and time requirement, and preciseness comprise the mode and mechanisms of fluid–structure data (interface) communication. If the governing equations of the fluid and structure both satisfy, per time-step calculation, the coupling is said to be strong. The integrated equation is as follows:

$$\begin{bmatrix} A_{FF} & A_{FS} \\ A_{SF} & A_{SS} \end{bmatrix} \begin{bmatrix} \Delta X_F^K \\ \Delta X_S^K \end{bmatrix} = \begin{bmatrix} B_F \\ B_S \end{bmatrix} \quad (1)$$

where A_{FF} is the fluid domain coefficient matrix, ΔX_F^K is the physical solvable quantity, B_F is the external force, and K is the number of time iteration steps; the subscripts F and S

refer to the fluid and solid domain, respectively whilst A_{SF} and A_{FS} are both fluid–structure coupling matrices.

Theoretically, the strong coupling lacks time lag, and the solution’s stability, visualization, and accuracy are high. However, the iterative process in the interface becomes time and resource exhaustive, especially for three-dimensional natural-phenomena problems. An alternative to maximize resource efficiency is to satisfy the interface’s governing equations, only once per time step, called weak coupling; however, it carries well-known defects: instabilities in strong added-mass circumstances and in solutions, confining the time-step calculation. Additionally, the data transfer between the fluid and the solid modules can be unidirectional, reducing complexity, or reciprocal by assuming the solid deformations alter the surrounding flow, as in the blade against the incident current. The structural dynamics equations of the two-way coupling is as follows:

$$[M]\{x''\} + [C]\{x'\} + [K]\{x\} = \{F(t)\} \tag{2}$$

where the matrix, $[M]$, is the mass; $[C]$ is the damping; and $[K]$ is the stiffness. Moreover, the vector of displacement is $\{x\}$, that of force is $\{F(t)\}$, that of velocity is $\{x'\}$, and that of acceleration is $\{x''\}$.

The following conditions are satisfied for data exchange at the relevant fluid–structure coupled intersection:

$$\begin{cases} u_{s,f} = u_{f,s} \\ v_{s,f} = v_{f,s} \end{cases} \tag{3}$$

where u is the normal-phase displacement component, and v is the normal-phase velocity component.

3. Computational Model

3.1. Numerical Calculation Model

A bidirectional weak coupling fluid–structure model, the ANSYS Workbench platform Fluent, Transient Structural and System Coupling, simulates the turbine transient responses due to incident turbulent current. The CFD-based model is divided into two domains: the blade domain of radius 0.15 m ($D/2$), and a rectangular prism comprising the outflow field. The width of the prism is set to $4D$, consistent with the channel’s width, whilst the water depth is set to $h = [1.6D, 2D, 2.4D]$ in order to capture the channel blockage effects on the wake and turbine development. The blade hub is at half-water depth, $8D$ from the upstream inlet and $30D$ from the downstream outlet. The blade material is set to Aluminum 6061, with properties summarized in Table 1. To acquire a consistent mesh around the complex blade geometry by virtue of the radial angle variation, the tetrahedral grids are used for the blade domain, with blade sections locally encrypted to increase the result accuracy. The boundary-layer grid is set for the blade boundary, and the height of the first-layer grid is 0.02 mm. The hexahedral grid, known for yielding higher accuracy, distortion resistance, and the number of divided grids, is used for the outflow field. In order to further reduce the influence of the outflow field calculation, the blade domain is encrypted, and the final grid structure is divided as shown in Figure 1. The eddy-viscosity model, SST $k-\omega$, accounts for turbulent shear stresses. The solution of the Navier–Stokes (NS) equations incorporates an implicit scheme. The convective components are discretized with second-order upwind schemes, owing to good convergence and stability features. The pressure–velocity linkage in the NS equation is resolved iteratively via the SIMPLE algorithm. The velocity depth variation is close to the logarithmic power law, as shown in Figure 2. The fitting formula is as follows:

$$V = 0.023\ln\left(\frac{z}{0.0015} + 57.7\right) + 0.25 \tag{4}$$

Table 1. Material properties of 6061 aluminum.

Material	Density ($\text{kg}\cdot\text{m}^{-3}$)	Young's Modulus (Pa)	Poisson's Ratio
Aluminum 6061	2750	$7e + 10$	0.33

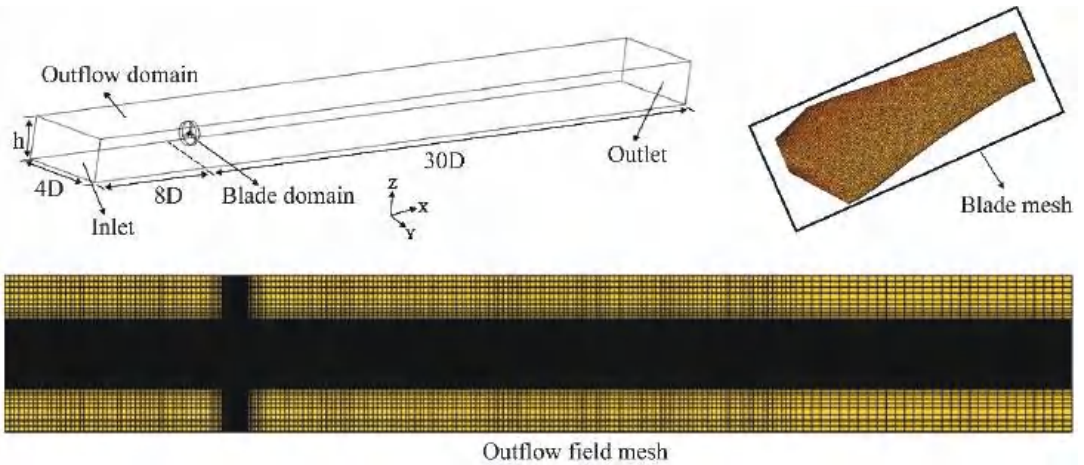


Figure 1. CFD model and the division of the mesh.

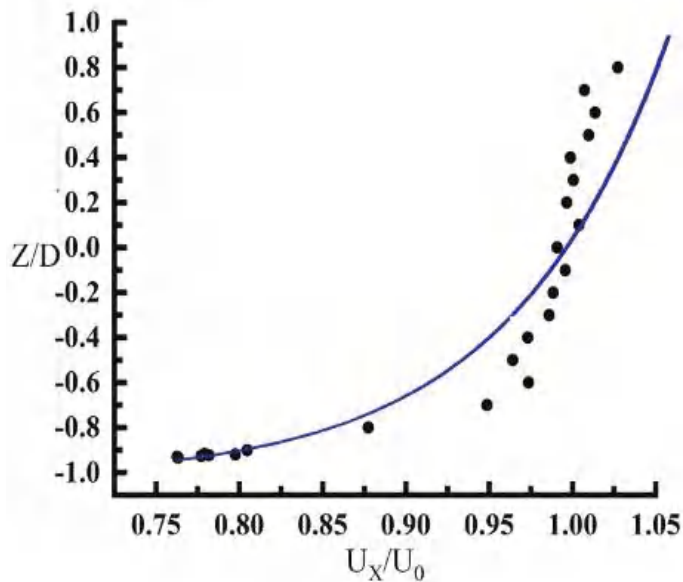


Figure 2. Vertical velocity distribution.

The mean velocity across the swept area is 0.4m/s , with a turbulence intensity of 7%. Consequently, the boundary condition at the inlet is the velocity inlet, and the velocity varies according to Equation (4), whereas at the pressure outlet, the relative atmospheric pressure is set to 0. The free liquid surface is set to symmetry, and the moving mesh is used for the non-constant solution of the fluid domain. Figure 1 shows the mesh structure and main characteristics of the domains.

The solid domain part uses a tetrahedral mesh. The radial and axial displacement constraints are applied to the blade structural body. Gravity is present, and the blade surface is the fluid–structure coupling intersection. The constraints and mesh domain of the solid part are shown in Figure 3.

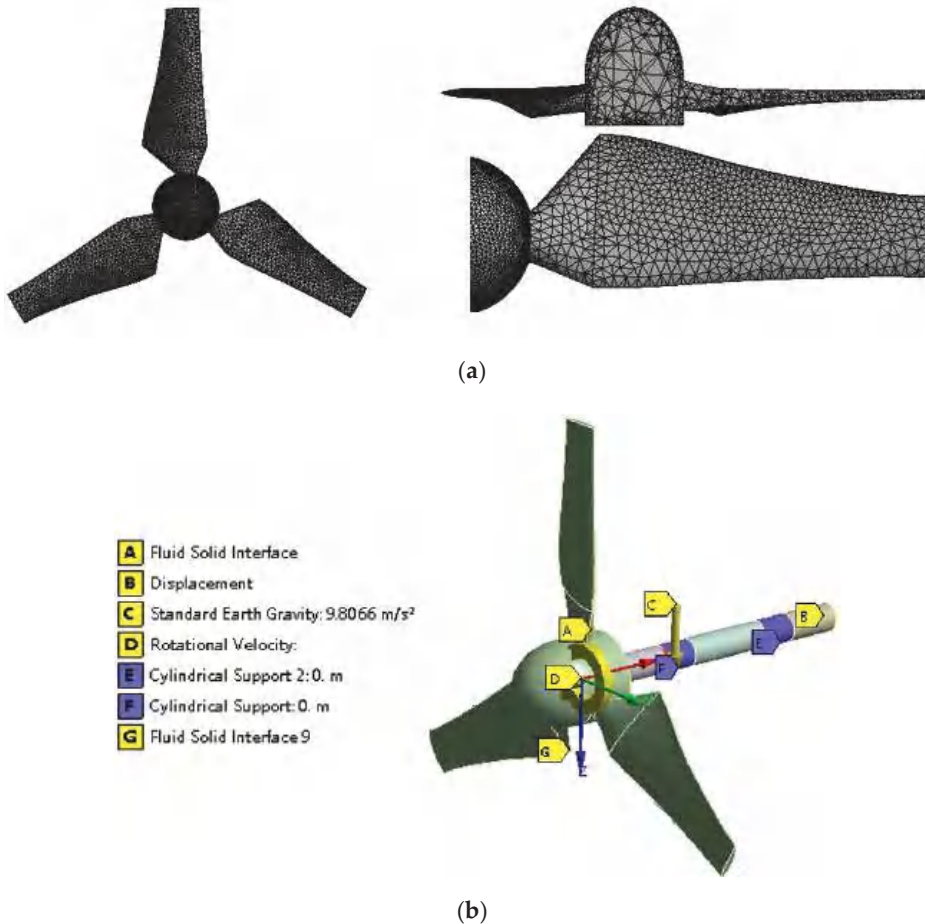


Figure 3. Mesh division and constraint setting of solid domain model: (a) mesh of solid domain and (b) constraints on solid domain.

3.2. Grid-Independence Verification

A grid-independence test investigates the method's computational resource with result accuracy. For the fluid domain, the grid number ranges from 3.5 to 7 million, whereas in the solid, the unidirectional fluid–structure coupling uses a grid size of 2 to 6 mm. The water depth is set to 0.6 m, with a blade angular speed of 100 r/min. As shown in Figure 4 and Table 2, the C_p and C_t values quickly decrease from 4.5 to 6 million grids, and then asymptote with numbers over 6 million. The maximum deformation and stress increases with grid reduction and converges with sizes less than 4 mm. Consequently, using a grid size of 3 mm for the solid and 6 million grids for the fluid saves computational resource without sacrificing accuracy level ($<0.1\%$). The bidirectional fluid–solid coupling simulation was conducted by a computer with 32-cores AMD CPU. The final computation time for each case is 132 h.

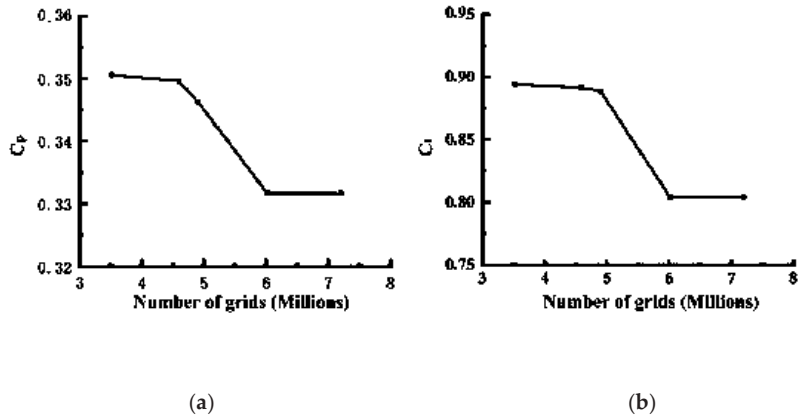


Figure 4. Grid-independence verification of fluid domain: (a) C_p and (b) C_t .

Table 2. Grid-independent verification of solid domains.

Segmentation Scheme	Grid Size (mm)	Number of Grids	Maximum Deformation (m)	Maximum Stress (MPa)
1	6	4187	0.012049	979.2
2	5	6409	0.012191	984.68
3	4	9616	0.012376	1122.3
4	3	15,337	0.012614	1307.5
5	2	43,382	0.012691	1337

3.3. Model Test Validation

The power output of the modeled 3-bladed turbine was examined in the hydrodynamic laboratory of Shandong Transportation Institute, using a flume of 50 m in length, 1.2 m in width, and 1.2 m in depth. The pumped water recirculates from the upstream inlet to the downstream via a returning underneath chamber, and the water depth (h) is 0.6 m. The piled turbine is suspended in a metal cage, confining the speed and torque controller and electric cables. This is then fixed by using a crossbeam on the flume, allowing for the adjustment of the hub height (0.3 m). Figure 5 presents the experimental setup.



Figure 5. Layout of circulation pool and turbine.

Figure 6 shows the comparison of results calculated by the FSI method and regular CFD method with the experimental results of the current study. As seen, the predicted power coefficients by BEMT, FSI, and CFD follow an inverted u-curve with a tip-speed ratio (TSR) of $TSR = \omega R/U$, culminating at $TSR = 3.9$, with $C_p = 0.332-0.345$. In general, the FSI simulations deviate more from the measurements than the CFD's do due to the non-optimal initial twist blade angle and deformation consideration; however, the error is less than 4.01% for the contemplated study's range ($TSR = 3.64-4.32$).

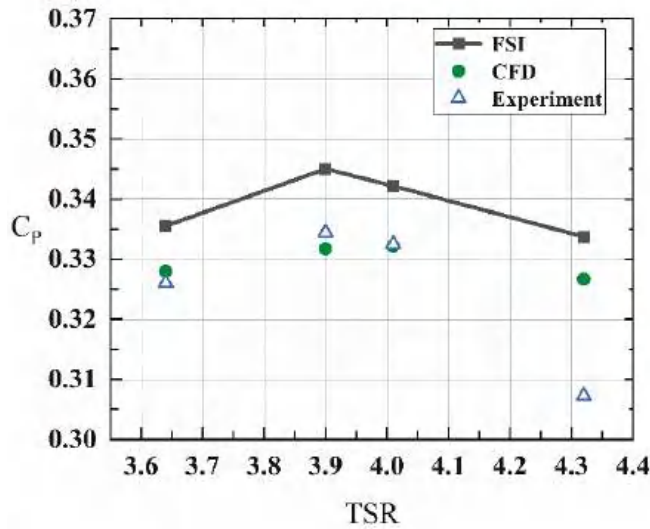


Figure 6. Graph of C_p with TSR.

4. Results Analysis

4.1. Hydrodynamic Performance of Blades

As Figure 7 demonstrates, the pressure simulations follow S-shaped curves, with upper asymptote (near the root) stretching further and lower (at the tip) shifting downwardly with radial distance. This behavior is attributed to two issues: a larger power section performance, apart from the blade root, augmenting the low–high pressure ranges; and the closer cavitation occurrence at the wingtip due to high tangential velocity ($\omega \cdot r$). The only observable simulation difference is at the rear of the blade; it is slightly more negative with than without the fluid–structure coupling condition, due to a small deformation of the blade.

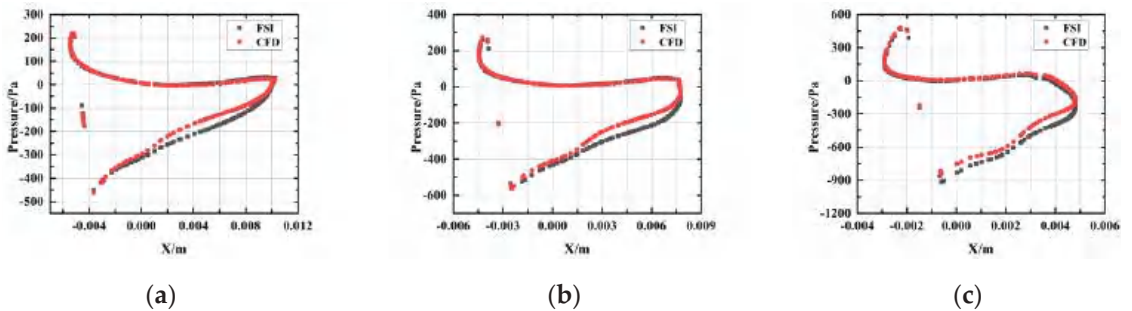


Figure 7. Cont.

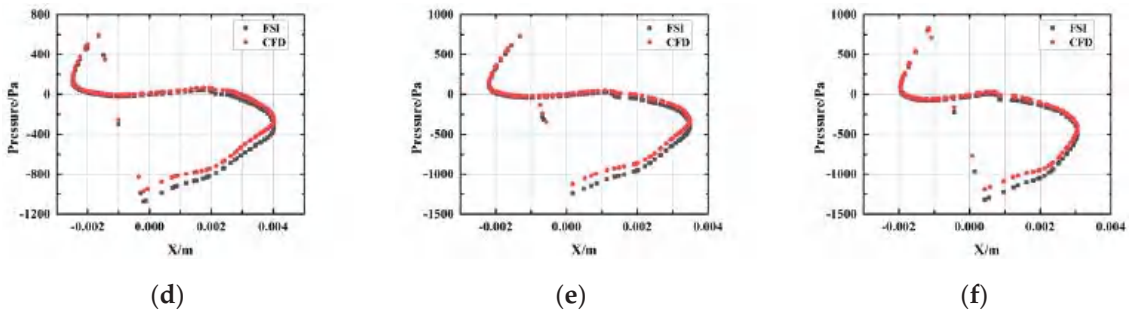


Figure 7. Pressure distribution of different blade sections: (a) span = 20%, (b) span = 40%, (c) span = 50%, (d) span = 60%, (e) span = 70%, and (f) span = 80%.

4.2. Blade Structural Stress Analysis

The structural characteristics of the blade were analyzed for a water depth of 0.6 m, an installation height of 0.3 m, and a turbine speed of 100 r/min under fluid–structure coupling conditions. The operation of the tidal-energy turbine for 3 s is calculated, and Figure 8 shows the dynamic stress distribution of the turbine blades at different times. It can be seen that the stress features similar lanceolate contours per blade, extending from the mid-root to almost all the blade, and reducing in intensity radially, reminiscent of an enlarged flame-like shape. Over time, the inner-core strength slightly augments and extends radially. This is because the blade is fixedly connected to the hub, and the blade can be regarded as a cantilever beam, and the bending moment and shear force near the blade root are maximum under the action of fluid loads, such as water thrust. The trend of the stress distribution on the three blades of the blade under each moment is that the maximum stress is at the root of the blade and decreases with an elliptical gradient toward the tip of the blade. When the blade starts to operate, the maximum stress on its surface rises rapidly, with the maximum value reaching 0.596 MPa, and the large stress-distribution area expands rapidly. As the turbine operation gradually stabilizes, the blade’s stress distribution is basically similar, and the maximum stress fluctuates in a small range, which is the result of the alternating cyclic load on the blade.

Figure 9 shows the deformation distribution of the blade at different moments. It can be clearly seen that the deformation of the blade’s surface at each moment is gradually increasing from the root to the tip of the blade. Combined with Figure 8, it can be found that the maximum blade deformation increases equally rapidly when the turbine is first started and fluctuates in a small range subsequently, due to the stable operation of the blade.

Figure 10 shows the variation of the maximum blade stress with time for 3 s operation under the water depth of 0.48 m, 0.6 m, and 0.72 m operating conditions. From the curves in the figure, it can be seen that the stress initially features an abrupt inverse u-curve before stabilizing, though in a fluctuating manner. The water depth reduces moderately the transient peak but slightly the stable stress. The maximum stress changes in all three water depth conditions show similar small amplitude periodic fluctuations. The turbine is operated under the maximum blocking ratio at the water depth of 0.48 m, and the maximum stress of the blade exists under the three water-depth conditions. Moreover, it can be observed that, under the three water-depth conditions, the maximum stress of the blade tends to decrease with the increase of water depth, but the maximum stress value is very close, so the change of water depth-conditions has little effect on the maximum stress of the blade under stable operation.

Figure 11 shows the variation of the average values of stress and deformation with the water depth during the stable operation of the turbine. It can be seen more directly that, as the water depth decreases, the average stress and average deformation of the blade show

an overall decreasing trend, and the average deformation of the blade does not change much after the water depth is lower than 0.6 m.

The influence of the tip-speed ratio (TSR) on the energy conversion of the turbine runner is relatively obvious. As the TSR increases, the runner thrust coefficient increases, and the thrust force acting on the blades also increases. Therefore, it is necessary to investigate the influence of TSR on the blade structure performance under the fluid-structure coupling condition and provide a theoretical basis for the blade strength design of tidal energy turbine. In this calculation, the incoming flow velocity of 0.4 m/s is kept constant, and the TSR is changed by changing the blade's rotational speed. The rotational speeds are 92.69 r/min, 100 r/min, 102.11 r/min, and 110.01 r/min, respectively.

Figure 12 shows the graph of stress variation of the runner at different rotational speeds. When the turbine just started, the blade was also subjected to sudden load changes, and the maximum stress showed periodic fluctuations after 1 s. The higher the rotational speed, the greater the load acting on the blade. Take the rotation speed 100 r/min and 110.01 r/min for example; when the rotation speed increases by about 10%, the sudden stress on the blade at the initial start-up increases by about 30%. Therefore, in the designed operating speed range, the abrupt load changes generated at the start of the turbine cannot be ignored.

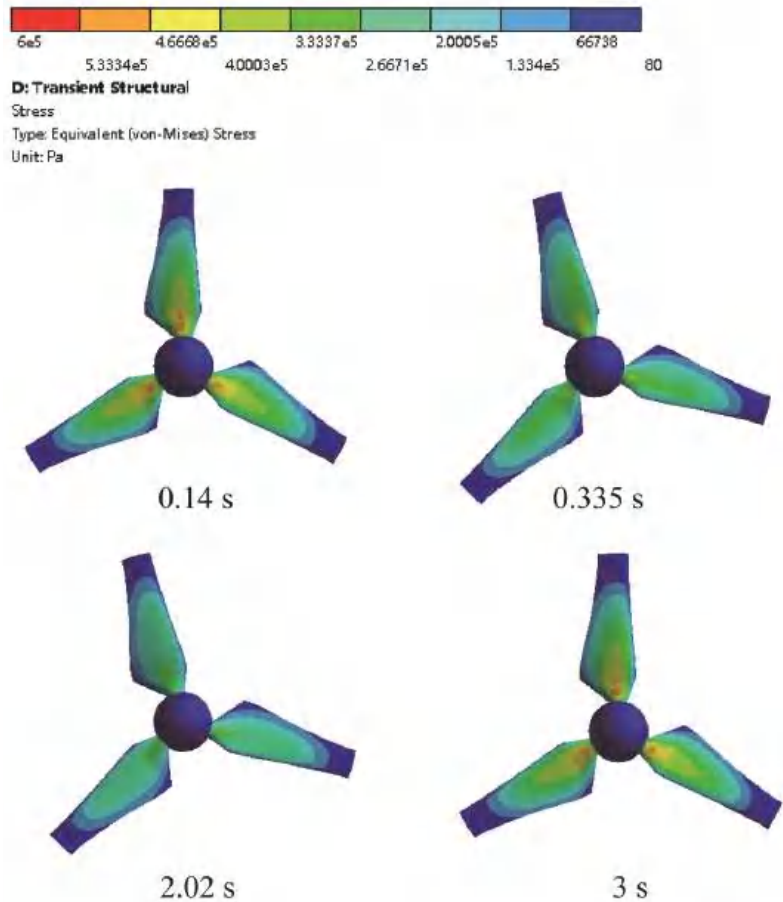


Figure 8. Distribution of blade's dynamic stress at different times (Pa).

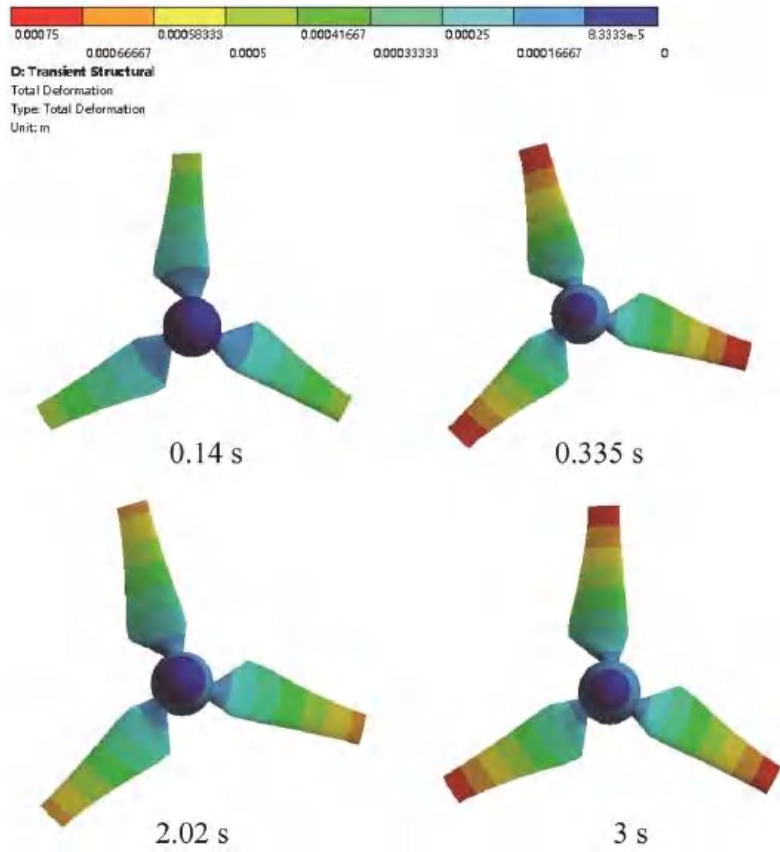


Figure 9. Distribution of blade deformation at different times (m).

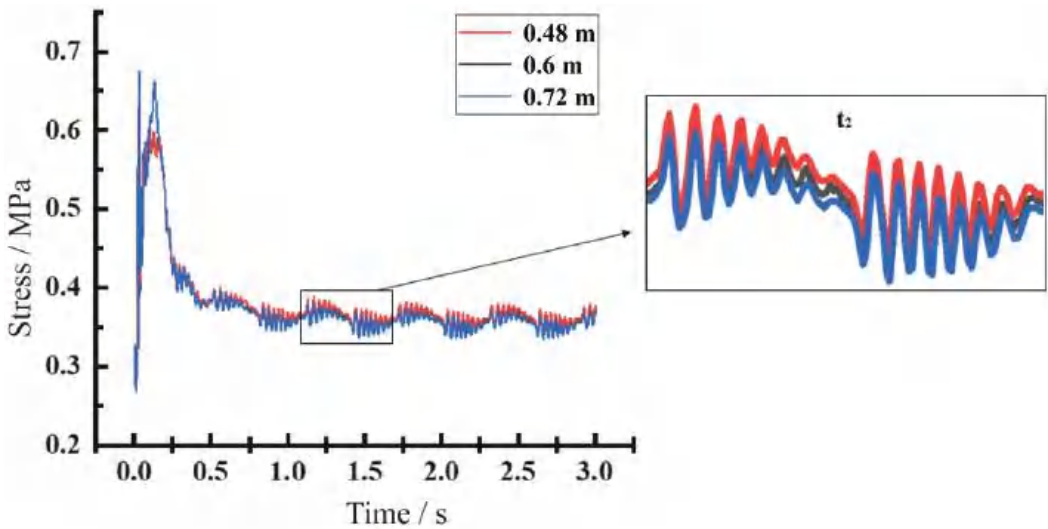


Figure 10. Variation of maximum stress of blade at different water depths.

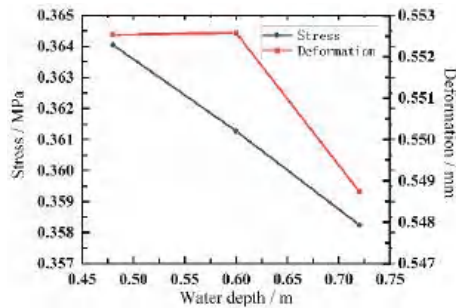


Figure 11. Stable cycle stress and deformation of the blade at different water depths.

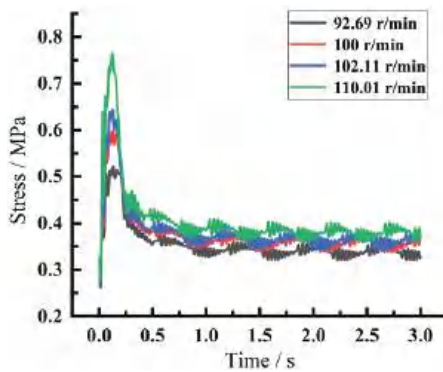


Figure 12. Variation of maximum blade stress at different rotation speeds.

When the turbine operation was stabilized, the average stress and average deformation at four rotational speeds were calculated, as shown in Table 3. It can be found that the average stress and average deformation generally increase with the increase of rotational speed. The average stress becomes larger with the increase of the rotational speed, which is consistent with the trend of the thrust load on the blade. The stress and deformation of the blade are mainly caused by the fluid load [19], and the horizontal-axis tidal-energy turbine is mainly subjected to the axial-thrust force. Moreover, as the speed increases, the axial-thrust force on the turbine increases. The average deformation of the blade decreases at the maximum speed, and this may be due to the second-order oscillation of the blades.

Table 3. Average stress and average deformation.

Rotational Speed (r/min)	Average Stress (MPa)	Average Deformation (mm)
92.69	0.339	0.543
100	0.361	0.550
102.11	0.364	0.551
110.007	0.38	0.544

4.3. Blade-Fatigue-Life Analysis

Figure 13 shows the distribution of the safety coefficient of the blade under different water-depth conditions. The safety factor is uniform, except in near the inner root section of the individual blades; it features irregular elliptical cores of the half safety factor extending along the blade’s axis. The depth both slightly affects the distribution and increases the magnitude of the safety factor.

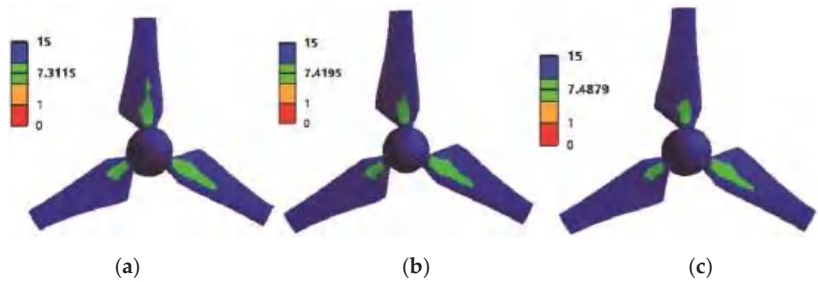


Figure 13. Blade safety factor at different water depths: (a) water depth of 0.48 m, (b) water depth of 0.6 m, and (c) water depth of 0.72 m.

Overall, the low safety coefficient of the blade is located at the root of the blade, which corresponds to the stress distribution of the blade in the previous section, where a large stress concentration occurs at the root of the blade leading to a decrease in the safety coefficient at the root. Meanwhile, with the increase of the water depth, the minimum safety coefficient increases slightly, but the influence range of the blade’s minimum safety coefficient is basically the same under different water-depth conditions, and the influence range increases only under the minimum water depth.

Figure 14 depicts the safety-factor distribution of the blade under different TSR conditions. Individually (blade), the half-safety-factor area in the root stretches along the blade axis, though irregularly, with rotational speed. Figure 14d shows the distribution of the safety coefficients on the front and back of the blade at the maximum speed, and it is found that the range of the low safety coefficients on the back of the blade is much larger and has reached the middle of the blade. If the turbine is in a more complex marine environment, the middle of the blade may break, so special attention should be paid when performing the blade’s strength calibration.

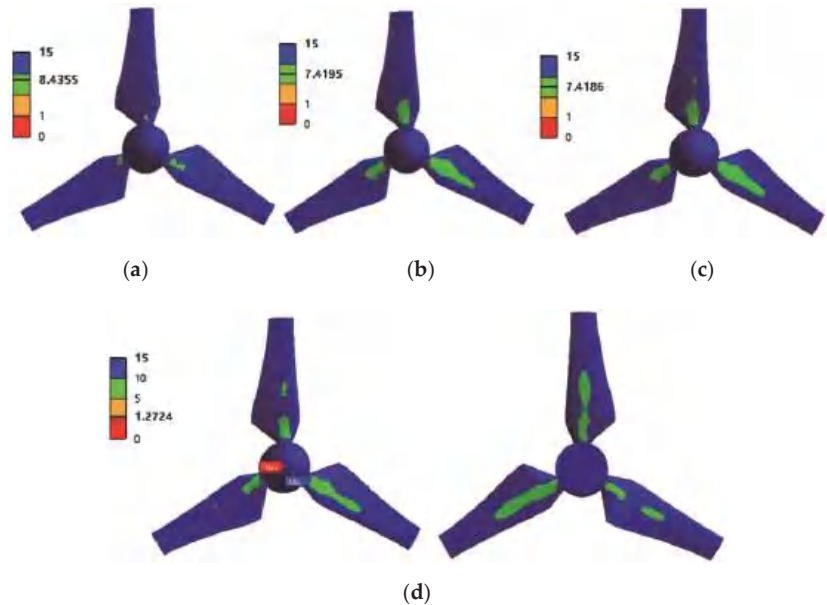


Figure 14. Blade safety factor at different rotational speeds: (a) 92.69 r/min, (b) 100 r/min, (c) 102.11 r/min, and (d) 110.01 r/min.

Considering the influence of different rotational speeds on the safety coefficient of the blade, the calculation of the number of stress cycles was carried out for different rotational speeds of the blade. The number of stress cycles of turbine blades under different rotational speeds all reach 108, indicating that the blades are in the safe range under these rotational speeds.

5. Conclusions

This paper calculated and analyzed the hydrodynamic performance and structural characteristics of the tidal stream turbine under bidirectional fluid–structure coupling conditions, and the main conclusions are as follows:

- (1) The difference between the calculated hydraulic turbine power coefficients with and without fluid–structure coupling conditions is not significant, and the deformation of the blade under the bidirectional fluid–structure coupling calculation will have a certain impact on the pressure difference on the blade’s surface.
- (2) As a cantilever beam structure, the blade has its maximum stress concentrated in the root of the leaf, and its maximum deformation is located near the tip of the leaf. The change of water depth has little influence on the stress and deformation of the blade, but the change of rotation speed has the most significant influence on it. The blade will be subjected to abrupt load when it is first started, and the increase of rotation speed will increase the abrupt load.
- (3) The fatigue-life prediction of the blade of the tidal-energy turbine was carried out. Similar to the blade stress variation, the lower safety factor of the blade is located near the root of the blade, and the blade’s rotation-speed variation has a more significant effect than water depth. The number of stress cycles of the blade at different rotational speeds is within the safety range.
- (4) During the design process of the blade, not only the hydraulic performance but also the strength of the blade situation should be taken into consideration.
- (5) These results represent an excellent initial step toward the wider use of the coupled fluid structure model due to high computational accuracy and resource efficiency; and toward further testing in more complex situations, such as incoming waves and currents, and floating turbine systems.

Author Contributions: Conceptualization, Y.Z. (Yuquan Zhang) and Z.L.; data curation, Z.L. and C.L.; funding acquisition, Y.Z. (Yuquan Zhang); investigation, Y.Z. (Yuquan Zhang) and X.W.; methodology, Y.Z. (Yuquan Zhang); resources, C.L.; supervision, Y.Z. (Yuquan Zhang); validation, Z.L., X.W. and Z.Z.; writing—original draft, Y.Z. (Yuquan Zhang) and C.L.; writing—review and editing, X.W., Z.Z., E.F.-R., and R.J.M. All authors have read and agreed to the published version of the manuscript.

Funding: The research was supported by the following funding programs: National Natural Science Foundation of China (No. 52171257) and Natural Science Foundation of Jiangsu Province (No. BK20220144).

Data Availability Statement: Not applicable.

Conflicts of Interest: The authors declare that they have no known competing financial interests or personal relationships that could have appeared to influence the work reported in this paper.

References

1. Zang, W.; Zheng, Y.; Zhang, Y.; Zhang, J.; Fernandez-Rodriguez, E. Experiments on the mean and integral characteristics of tidal turbine wake in the linear waves propagating with the current. *Ocean Eng.* **2019**, *173*, 1–11. [CrossRef]
2. Gaurier, B.; Ikhennicheu, M.; Germain, G.; Druault, P. Experimental study of bathymetry generated turbulence on tidal turbine behaviour. *Renew. Energy* **2020**, *156*, 1158–1170. [CrossRef]
3. Gaurier, B.; Carlier, C.; Germain, G.; Pinon, G.; Rivoalen, E. Three tidal turbines in interaction: An experimental study of turbulence intensity effects on wakes and turbine performance. *Renew. Energy* **2020**, *148*, 1150–1164. [CrossRef]
4. Derakhshan, S.; Ashoori, M.; Salemi, A. Experimental and numerical study of a vertical axis tidal turbine performance. *Ocean Eng.* **2017**, *137*, 59–67. [CrossRef]

5. Gaurier, B.; Druault, P.; Ikhennicheu, M.; Germain, G. Experimental analysis of the shear flow effect on tidal turbine blade root force from three-dimensional mean flow reconstruction. *Philos. Trans. R. Soc. A* **2020**, *378*, 20200001. [CrossRef]
6. Zhang, Y.; Zhang, J.; Lin, X.; Wang, R.; Zhang, C.; Zhao, J. Experimental investigation into downstream field of a horizontal axis tidal stream turbine supported by a mono pile. *Appl. Ocean Res.* **2020**, *101*, 102257. [CrossRef]
7. Zhang, Y.; Zhang, Z.; Zheng, J.; Zhang, J.; Zheng, Y.; Zang, W.; Lin, X.; Fernandez-Rodriguez, E. Experimental investigation into effects of boundary proximity and blockage on horizontal-axis tidal turbine wake. *Ocean Eng.* **2021**, *225*, 108829. [CrossRef]
8. Allmark, M.; Ellis, R.; Ebdon, T.; Lloyd, C.; Ordóñez-Sánchez, S.; Martínez, R.; Mason-Jones, A.; Johnstone, C.; O'Doherty, T. A detailed study of tidal turbine power production and dynamic loading under grid generated turbulence and turbine wake operation. *Renew. Energy* **2020**, *169*, 1422–1439. [CrossRef]
9. Myers, L.; Bahaj, A.S. Wake studies of a 1/30th scale horizontal axis marine current turbine. *Ocean. Eng.* **2005**, *34*, 758–762. [CrossRef]
10. Zhang, Y.; Zang, W.; Zheng, J.; Cappiotti, L.; Zhang, J.; Zheng, Y.; Fernandez-Rodriguez, E. The influence of waves propagating with the current on the wake of a tidal stream turbine. *Appl. Energy* **2021**, *290*, 116729. [CrossRef]
11. Peng, B.; Zhang, Y.; Zheng, Y.; Wang, R.; Fernandez-Rodriguez, E.; Tang, Q.; Zhang, Z.; Zang, W. The effects of surge motion on the dynamics and wake characteristics of a floating tidal stream turbine under free surface condition. *Energy Convers. Manag.* **2022**, *266*, 115816. [CrossRef]
12. Tian, W.; VanZwieten, J.H.; Pyakurel, P.; Li, Y. Influences of yaw angle and turbulence intensity on the performance of a 20 kW in-stream hydrokinetic turbine. *Energy* **2016**, *111*, 104–116. [CrossRef]
13. Ahmadim, H.B.; Yang, Z. The evolution of turbulence characteristics in the wake of a horizontal axis tidal stream turbine. *Renew. Energy* **2020**, *151*, 1008–1015. [CrossRef]
14. Yazicioglu, H.; Tunc, K.M.; Ozbek, M.; Kara, T. Simulation of electricity generation by marine current turbines at Istanbul Bosphorus Strait. *Energy* **2016**, *95*, 41–50. [CrossRef]
15. Gonabadi, H.; Oila, A.; Yadav, A.; Bull, S. Fatigue life prediction of composite tidal turbine blades. *Ocean Eng.* **2022**, *260*, 111903. [CrossRef]
16. Finnegan, W.; Fagan, E.; Flanagan, T.; Doyle, A.; Goggins, J. Operational fatigue loading on tidal turbine blades using computational fluid dynamics. *Renew. Energy* **2020**, *152*, 430–440. [CrossRef]
17. Mullings, H.; Stallard, T. Assessment of Dependency of Unsteady Onset Flow and Resultant Tidal Turbine Fatigue Loads on Measurement Position at a Tidal Site. *Energies* **2021**, *14*, 5470. [CrossRef]
18. Bahaj, A.S.; Myers, L.E. Fundamentals applicable to the utilisation of marine current turbines for energy production. *Renew. Energy* **2003**, *28*, 2205–2211. [CrossRef]
19. Badshah, M.; Badshah, S.; Jan, S. Comparison of computational fluid dynamics and fluid structure interaction models for the performance prediction of tidal current turbines. *J. Ocean Eng. Sci.* **2020**, *5*, 164–172. [CrossRef]
20. Hafeez, N.; Badshah, S.; Badshah, M.; Khalil, S.J. Effect of velocity shear on the performance and structural response of a small-scale horizontal axis tidal turbine. *Mar. Syst. Ocean Technol.* **2019**, *14*, 51–58. [CrossRef]
21. Liu, X.F.; Wang, J.B.; Tian, M.L.; Tang, Z.B. Efficiency and Performance Analysis of Tidal Current Energy Turbine Basing on the Unidirectional Fluid-Structure Interaction. *Appl. Mech. Mater.* **2014**, *672*, 386–391. [CrossRef]
22. Ullah, H.; Hussain, M.; Abbas, N.; Ahmad, H.; Amer, M.; Noman, M. Numerical investigation of modal and fatigue performance of a horizontal axis tidal current turbine using fluid–structure interaction. *J. Ocean Eng. Sci.* **2019**, *4*, 328–337. [CrossRef]
23. Li, C.; Zheng, Y.; Zhang, Y.; Kan, K.; Xue, X.; Fernandez-Rodriguez, E. Stability Optimization and Analysis of a Bidirectional Shaft Extension Pump. *J. Fluids Eng.* **2020**, *142*. [CrossRef]
24. Khalid, S.-S.; Zhang, L.; Zhang, X.-W.; Sun, K. Three-dimensional numerical simulation of a vertical axis tidal turbine using the two-way fluid structure interaction approach. *J. Zhejiang Univ. Sci. Appl. Phys. Eng.* **2013**, *14*, 574–582. [CrossRef]
25. Badshah, M.; Badshah, S.; VanZwieten, J.; Jan, S.; Amir, M.; Malik, S.A. Coupled Fluid-Structure Interaction Modelling of Loads Variation and Fatigue Life of a Full-Scale Tidal Turbine under the Effect of Velocity Profile. *Energies* **2019**, *12*, 2217. [CrossRef]
26. Nicholls-Lee, R.F.; Turnock, S.R.; Boyd, S.W. Application of bend-twist coupled blades for horizontal axis tidal turbines. *Renew. Energy* **2013**, *50*, 541–550. [CrossRef]
27. Badshah, M.; Badshah, S.; Kadir, K. Fluid Structure Interaction Modelling of Tidal Turbine Performance and Structural Loads in a Velocity Shear Environment. *Energies* **2018**, *11*, 1837. [CrossRef]
28. Tatum, S.C.; Frost, C.H.; Allmark, M.; O'doherty, D.M.; Mason-Jones, A.; Prickett, P.W.; Grosvenor, R.I.; Byrne, C.B.; O'Doherty, T. Wave–current interaction effects on tidal stream turbine performance and loading characteristics. *Int. J. Mar. Energy* **2016**, *14*, 161–179. [CrossRef]

Article

A Fast Singular Boundary Method for the Acoustic Design Sensitivity Analysis of Arbitrary Two- and Three-Dimensional Structures

Liyuan Lan ¹, Suifu Cheng ¹, Xiatao Sun ², Weiwei Li ³, Chao Yang ^{4,*} and Fajie Wang ^{1,*}

¹ National Engineering Research Center for Intelligent Electrical Vehicle Power System, College of Mechanical and Electrical Engineering, Qingdao University, Qingdao 266071, China

² School of Engineering and Applied Science, University of Pennsylvania, Philadelphia, PA 19104, USA

³ School of Transportation and Vehicle Engineering, Shandong University of Technology, Zibo 255049, China

⁴ College of Materials Science and Engineering, Qingdao University, Qingdao 266071, China

* Correspondence: yangchao@qdu.edu.cn (C.Y.); wfj88@qdu.edu.cn (F.W.)

Abstract: This paper proposes a fast meshless scheme for acoustic sensitivity analysis by using the Burton–Miller-type singular boundary method (BM-SBM) and recursive skeletonization factorization (RSF). The Burton–Miller formulation was adopted to circumvent the fictitious frequency that occurs in external acoustic analysis, and then the direct differentiation method was used to obtain the sensitivity of sound pressure to design variables. More importantly, RSF was employed to solve the resultant linear system obtained by the BM-SBM. RSF is a fast direct factorization technique based on multilevel matrix compression, which allows fast factorization and application of the inverse in solving dense matrices. Firstly, the BM-SBM is a boundary-type collocation method that is a straightforward and accurate scheme owing to the use of the fundamental solution. Secondly, the introduction of the fast solver can effectively reduce the requirement of computer memory and increase the calculation scale compared to the conventional BM-SBM. Three numerical examples including two- and three-dimensional geometries indicate the precision and efficiency of the proposed fast numerical technique for acoustic design sensitivity analysis associated with large-scale and complicated structures.

Keywords: recursive skeletonization factorization; Burton–Miller-type singular boundary method; fast solver; fundamental solution; acoustic design sensitivity

MSC: 65N35; 76Q05

Citation: Lan, L.; Cheng, S.; Sun, X.; Li, W.; Yang, C.; Wang, F. A Fast Singular Boundary Method for the Acoustic Design Sensitivity Analysis of Arbitrary Two- and Three-Dimensional Structures. *Mathematics* **2022**, *10*, 3817. <https://doi.org/10.3390/math10203817>

Academic Editor: Yury Shestopalov

Received: 16 September 2022

Accepted: 12 October 2022

Published: 16 October 2022

Publisher's Note: MDPI stays neutral with regard to jurisdictional claims in published maps and institutional affiliations.



Copyright: © 2022 by the authors. Licensee MDPI, Basel, Switzerland. This article is an open access article distributed under the terms and conditions of the Creative Commons Attribution (CC BY) license (<https://creativecommons.org/licenses/by/4.0/>).

1. Introduction

In recent years, various methods [1–4] have been proposed to address acoustic problems, such as transient acoustic wave propagation in unbounded domains [5], acoustic transmission across multilayered construction [6], wave diffusion in unbounded domains [7], and acoustic sensitivity analysis [8]. For these problems, numerical simulation plays an irreplaceable role. Common methods for the analysis of acoustic problems include the finite element method (FEM) [9,10], the boundary element method (BEM) [11,12], and some alternative meshless/mesh-free methods. Meshless methods can reduce or even eliminate the tasks of grid generation and numerical integration. Therefore, many scholars and engineers have developed numerous meshless approaches, such as the element-free Galerkin method [13,14], the exponential basis function method [15,16], the localized semi-analytical meshless collocation method [17–19], the method of fundamental solutions (MFS) [20,21], and the singular boundary method (SBM) [22].

Among the above methods, the SBM is a semi-analytical and boundary-type meshless approach using fundamental solutions, which is mathematically simple, numerically accurate, and easy to program. Unlike the MFS, the SBM avoids the singularity of fundamental

solutions by introducing the origin intensity factor (OIF), and circumvents the fictitious boundary issue in the traditional MFS. To overcome the influence of the fictitious eigenfrequency issue, the BM-SBM was proposed to deal with sound scattering and radiation [23,24]. Up to now, this scheme has been successfully applied to acoustic simulations [25–27], heat conduction analysis [28,29], electromagnetic problems [30], and other domains.

Similar to the traditional boundary-type methods [31–33], the resultant matrix of the BM-SBM is a dense matrix. Assuming that the number of boundary nodes is N , the storage process needs to occupy the memory of $O(N^2)$, and the operations of $O(N^3)$ are required in the direct calculation. Therefore, insufficient memory and time-consuming computation are often encountered when solving large-scale problems. In order to reduce the calculation time and increase the calculation scale, some scholars have introduced various fast algorithms. The fast multipole (FM) and adaptive cross approximation (ACA) have been used to establish a series of new fast algorithms, such as the fast multipole BEM (FM-BEM) [34–36], the fast multipole MFS (FMM-MFS) [37], the ACA-BEM [38], and the ACA-MFS [39]. Moreover, the ACA-BEM has also been successfully applied to the solution of acoustic sensitivity. The SBM, which draws inspiration from the boundary element technique, has also been combined with fast algorithms to address large-scale problems. Qu et al. [40,41] proposed the fast multipole accelerated SBM (FMM-SBM) to solve large-scale Helmholtz problems, increasing the computational scale of boundary nodes to more than one million. Wei et al. [42] developed an adaptive cross approximation SBM (ACA-SBM) to simulate 2D steady-state heat transfer problems. Li et al. [43–45] developed a precorrected-FFT SBM (PFFT-SBM) to address large-scale 3D Laplace problems, Helmholtz problems, and high-frequency acoustic radiation and scattering problems. Li et al. [46,47] proposed a fast SBM for solving the 2D steady-state heat conduction problem and large-scale 3D potential problem.

This paper aims to present a fast formulation of the BM-SBM for analyzing the acoustic sensitivity of 2D and 3D complex structures. In our earlier works [48,49], we built a BM-SBM framework for acoustic design sensitivity analysis. Benchmark numerical examples confirmed the accuracy and effectiveness of the method. However, the approach still faces the challenge of addressing a large-scale structure. Recursive skeletonization factorization (RSF) [50,51] is a fast and direct scheme based on multilevel matrix compression, and has been successfully applied to various problems. In this paper, RSF is adopted to solve the resultant system of the BM-SBM, and then a new fast method called the RSF-BM-SBM is proposed. Compared with the original BM-SBM, the calculation time is greatly reduced, and the computational scale is significantly increased.

The rest of this paper is organized as follows. In Section 2, we briefly introduce the acoustic sensitivity formula of the BM-SBM and the empirical formula of the OIFs. In Section 3, recursive skeletonization factorization is shown to solve the linear system formed in the sensitivity analysis using the BM-SBM. In Section 4, three examples, including classical models and a complex car model, are demonstrated to verify the accuracy and efficiency of the proposed RSF-BM-SBM for acoustic sensitivity analysis. In Section 5, some conclusions are drawn.

2. Burton–Miller-Type Singular Boundary Method for Acoustic Sensitivity

2.1. Acoustic Sensitivity Analysis

We consider an external sound field problem in two- and three-dimensional spaces, which can be described by the following Helmholtz equation [48,49]:

$$\nabla^2 u(x) + k^2 u(x) = 0, x \in \Omega \quad (1)$$

with the following Dirichlet and Neumann boundary conditions:

$$u(x) = \bar{u}(x), x \in \Gamma_u, \quad (2)$$

$$\frac{\partial u(\mathbf{x})}{\partial \mathbf{n}_x} = i\rho\omega\bar{v}(\mathbf{x}), \mathbf{x} \in \Gamma_q, \tag{3}$$

where ∇^2 represents the Laplace operator; $k = \omega/c$ is the wave number; ω is the angular frequency; c is the speed of sound in the propagating medium; and $\bar{u}(\mathbf{x})$ and $\bar{v}(\mathbf{x})$ are the sound pressure and the normal vibration velocity on Γ_u and Γ_q , respectively.

Considering sound propagation in an infinite field, the sound pressure should satisfy the Sommerfeld radiation condition at infinity:

$$\lim_{r \rightarrow \infty} r^{\frac{1}{2}(d-1)} \left(\frac{\partial u(\mathbf{x})}{\partial r} - iku(\mathbf{x}) \right) = 0 \tag{4}$$

where d is the spatial dimension ($d = 2, 3$) and r is the distance between point \mathbf{x} and the sound field's center. The fundamental solution employed in the BM-SBM automatically satisfies the aforementioned requirements; therefore, no additional handling is necessary in the numerical computation.

For acoustic sensitivity analysis, the most important thing is to obtain the gradient of the objective function with respect to the design variables. In many applications, the objective function is sound pressure, and the design variables are size, wave number, or frequency.

2.2. Burton–Miller-Type Singular Boundary Method

Assuming the total number of boundary nodes is N , the BM-SBM formulas can be given by [49]:

$$u(\mathbf{x}_i) = \sum_{\substack{j=1 \\ i \neq j}}^N \alpha_j (G(\mathbf{x}_i, \mathbf{s}_j) + \lambda E(\mathbf{x}_i, \mathbf{s}_j)) + \alpha_i u_{BM}, \mathbf{x}_i \in \Gamma_u, \mathbf{s}_j \in \Gamma \tag{5}$$

$$\frac{\partial u(\mathbf{x}_i)}{\partial \mathbf{n}_x} = \sum_{\substack{j=1 \\ i \neq j}}^N \alpha_j (F(\mathbf{x}_i, \mathbf{s}_j) + \lambda H(\mathbf{x}_i, \mathbf{s}_j)) + \alpha_i q_{BM}, \mathbf{x}_i \in \Gamma_q, \mathbf{s}_j \in \Gamma \tag{6}$$

$$E(\mathbf{x}_i, \mathbf{s}_j) = \frac{\partial G(\mathbf{x}_i, \mathbf{s}_j)}{\partial \mathbf{n}_s}, F(\mathbf{x}_i, \mathbf{s}_j) = \frac{\partial G(\mathbf{x}_i, \mathbf{s}_j)}{\partial \mathbf{n}_x}, H(\mathbf{x}_i, \mathbf{s}_j) = \frac{\partial^2 G(\mathbf{x}_i, \mathbf{s}_j)}{\partial \mathbf{n}_s \partial \mathbf{n}_x} \tag{7}$$

where $\lambda = \frac{i}{k+1}$ is a complex number [24]; α_j is the unknown coefficient; and \mathbf{x}_i and \mathbf{s}_j denote i th boundary node and j th source point, respectively. u_{BM} and q_{BM} are the OIFs, which can be computed by the following formulas [52,53]:

$$u_{BM} = u_{ii} - \lambda \sum_{\substack{j=1 \\ j \neq i}}^N \zeta_{ji} \frac{\partial G_0(\mathbf{x}_i, \mathbf{s}_j)}{\partial \mathbf{n}_s} \tag{8}$$

$$q_{BM} = q_{ii} + \lambda \left(\frac{k^2}{2} u_{ii} - \sum_{\substack{j=1 \\ j \neq i}}^N \zeta_{ji} \frac{\partial^2 G_0(\mathbf{x}_i, \mathbf{s}_j)}{\partial \mathbf{n}_s \partial \mathbf{n}_x} \right) \tag{9}$$

where u_{ii} and q_{ii} are given in Refs. [24,48], and $G_0(\mathbf{x}_i, \mathbf{s}_j)$ is the fundamental solution of the Laplace equation. $G_0(\mathbf{x}_i, \mathbf{s}_j) = -\frac{\ln|\mathbf{x}_i - \mathbf{s}_j|}{2\pi}$ for 2D problems; $G_0(\mathbf{x}_i, \mathbf{s}_j) = \frac{1}{4\pi|\mathbf{x}_i - \mathbf{s}_j|}$ for 3D problems.

Substituting the boundary conditions into Equations (5) and (6), the following system of equations can be obtained:

$$\mathbf{M}\boldsymbol{\alpha} = \mathbf{b} \tag{10}$$

where $\mathbf{M}_{N \times N}$ is the coefficient matrix, $\boldsymbol{\alpha}_{N \times 1}$ is the undetermined coefficient vector, and $\mathbf{b}_{N \times 1}$ is the known vector. The matrix \mathbf{M} is generated from Burton–Miller-type formulation (a combination of single- and double-layer potentials), and its condition number is related to the number of nodes. Since the method is implemented by MATLAB programming, the condition number of the matrix can be viewed by the routine *cond(M)*. By solving Equation (10), $\boldsymbol{\alpha}$ can be obtained. After that, the following formulas can be employed to determine the sound pressure and normal derivative at point \mathbf{x} :

$$u(\mathbf{x}) = \sum_{j=1}^N \alpha_j (G(\mathbf{x}, s_j) + \lambda E(\mathbf{x}, s_j)) \tag{11}$$

$$q(\mathbf{x}) = \sum_{j=1}^N \alpha_j (F(\mathbf{x}, s_j) + \lambda H(\mathbf{x}, s_j)) \tag{12}$$

Based on the formulas mentioned above, the direct differentiation approach can be used to compute the sensitivities:

$$\dot{u}(\mathbf{x}) = \sum_{j=1}^N \begin{bmatrix} \dot{\alpha}_j (G(\mathbf{x}, s_j) + \lambda E(\mathbf{x}, s_j)) \\ + \alpha_j (\dot{G}(\mathbf{x}, s_j) + \dot{\lambda} E(\mathbf{x}, s_j) + \lambda \dot{E}(\mathbf{x}, s_j)) \end{bmatrix} \tag{13}$$

$$\dot{q}(\mathbf{x}) = \sum_{j=1}^N \begin{bmatrix} \dot{\alpha}_j (F(\mathbf{x}, s_j) + \lambda H(\mathbf{x}, s_j)) \\ + \alpha_j (\dot{F}(\mathbf{x}, s_j) + \dot{\lambda} H(\mathbf{x}, s_j) + \lambda \dot{H}(\mathbf{x}, s_j)) \end{bmatrix} \tag{14}$$

where the superscript ($\dot{}$) denotes the differentiation of a function. For the differentiation calculation in the right hand sides of the above equations, one can refer to Ref. [48].

3. Recursive Skeletonization Factorization

Recursive skeleton factorization is a fast direct solver which allows fast factorization and application of the inverse in the process of solving asymmetric dense matrices.

3.1. Interpolative Decomposition

The present paper adopts interpolative decomposition (ID) to compress the low-rank blocks [46,54]. If the submatrix $\mathbf{M}_{pq} \in \mathbb{R}^{m \times n}$ of \mathbf{M} is a matrix of rank $h \leq \min(m, n)$, then there exist $\mathbf{R}_q \in \mathbb{R}^{h \times (n-t)}$ such that $\mathbf{M}_{pq'} \approx \mathbf{M}_{pq''} \mathbf{R}_q$. It should be pointed out that m and n denote the dimension of the matrix \mathbf{M} , which are set as $m = n = N$. Here, p and q represent ordered sets of indices, q' and q'' denote the skeleton and redundant indices, and they satisfy the following relationships: $q = q' \cup q''$ and $|q''| = h$. If \mathbf{R}_q satisfy $\mathbf{M}_{pq'} = \mathbf{M}_{pq''} \mathbf{R}_q$, then

$$\begin{bmatrix} \mathbf{M}_{pq'} & \mathbf{M}_{pq''} \end{bmatrix} \begin{bmatrix} \mathbf{I} \\ -\mathbf{R}_q & \mathbf{I} \end{bmatrix} = \begin{bmatrix} \mathbf{0} & \mathbf{M}_{pq''} \end{bmatrix} \tag{15}$$

It should be pointed out that ID is commonly applied to cases with an error matrix \mathbf{E} , i.e., $\mathbf{M}_{pq'} = \mathbf{M}_{pq''} \mathbf{R}_q + \mathbf{E}$, in which $\|\mathbf{E}\| \sim \sigma_{h+1}(\mathbf{M})$, and $\sigma_{h+1}(\mathbf{M})$ stands for the $(h + 1)$ th-largest singular value of \mathbf{M} . In this regard, ID can be employed to select h adaptively, so that $\|\mathbf{E}\| \leq \varepsilon \|\mathbf{M}\|$ for a given tolerance $\varepsilon > 0$. In this paper, ID is achieved by a random sampling scheme [54], which only requires $O(mn \log(h) + h^2n)$ operations.

3.2. Skeletonization

In this subsection, ID is adopted to compress a matrix with low-rank off-diagonal blocks. We consider a block matrix \mathbf{M} with index sets p and q :

$$\mathbf{M} = \begin{bmatrix} \mathbf{M}_{pp} & \mathbf{M}_{pq} \\ \mathbf{M}_{qp} & \mathbf{M}_{qq} \end{bmatrix} \tag{16}$$

where \mathbf{M}_{pq} and \mathbf{M}_{qp} are low-rank submatrices. After applying ID to \mathbf{M} with $p = p' \cup p''$, we obtain

$$\mathbf{M} = \begin{bmatrix} \mathbf{M}_{p'p'} & \mathbf{M}_{p'p''} & \mathbf{M}_{p'q} \\ \mathbf{M}_{p''p'} & \mathbf{M}_{p''p''} & \mathbf{M}_{p''q} \\ \mathbf{M}_{qp'} & \mathbf{M}_{qp''} & \mathbf{M}_{qq} \end{bmatrix} \tag{17}$$

Let

$$\mathbf{Q}_p = \begin{bmatrix} \mathbf{I} & & \\ -\mathbf{R}_p & \mathbf{I} & \\ & & \mathbf{I} \end{bmatrix} \tag{18}$$

and then

$$\mathbf{Q}_p^T \mathbf{M} \mathbf{Q}_p \approx \begin{bmatrix} \mathbf{N}_{p'p'} & \mathbf{N}_{p'p''} & \mathbf{M}_{p'q} \\ \mathbf{N}_{p''p'} & \mathbf{M}_{p''p''} & \mathbf{M}_{p''q} \\ \mathbf{M}_{qp'} & \mathbf{M}_{qp''} & \mathbf{M}_{qq} \end{bmatrix} \tag{19}$$

where

$$\mathbf{N}_{p'p'} = \mathbf{M}_{p'p'} - \mathbf{R}_p^T \mathbf{M}_{p''p'} - \mathbf{M}_{p'p''} \mathbf{R}_p + \mathbf{R}_p^T \mathbf{M}_{p''p''} \mathbf{R}_p \tag{20}$$

$$\mathbf{N}_{p'p''} = \mathbf{M}_{p'p''} - \mathbf{R}_p^T \mathbf{M}_{p''p''}, \quad \mathbf{N}_{p''p'} = \mathbf{M}_{p''p'} - \mathbf{M}_{p''p''} \mathbf{R}_p \tag{21}$$

Supposing $\mathbf{N}_{p'p'}$ is a nonsingular matrix, and $\mathbf{N}_{p'p''}$ can be decomposed into $\mathbf{L}_{p'} \mathbf{D}_{p'} \mathbf{U}_{p'}$ ($\mathbf{D}_{p'}$ is a diagonal matrix; $\mathbf{L}_{p'}$ and $\mathbf{U}_{p'}$ are unit triangular matrices), we obtain

$$\mathbf{s}_{p'}^T \mathbf{Q}_p^T \mathbf{M} \mathbf{Q}_p \mathbf{T}_{p'} \approx \begin{bmatrix} \mathbf{D}_{p'} & & \\ & \mathbf{N}_{p''p''} & \mathbf{M}_{p''q} \\ & \mathbf{M}_{qp''} & \mathbf{M}_{qq} \end{bmatrix} \equiv \Psi_p(\mathbf{M}) \tag{22}$$

where $\Psi_p(\cdot)$ is called the skeletonization operator, and

$$\mathbf{s}_{p'}^T = \begin{bmatrix} \mathbf{I} & & \\ -\mathbf{N}_{p''p'} \mathbf{U}_{p'}^{-1} \mathbf{D}_{p'}^{-1} & \mathbf{I} & \\ & & \mathbf{I} \end{bmatrix} \begin{bmatrix} \mathbf{L}_{p'}^{-1} & & \\ & \mathbf{I} & \\ & & \mathbf{I} \end{bmatrix} \tag{23}$$

$$\mathbf{T}_{p'} = \begin{bmatrix} \mathbf{U}_{p'}^{-1} & & \\ & \mathbf{I} & \\ & & \mathbf{I} \end{bmatrix} \begin{bmatrix} \mathbf{I} & -\mathbf{D}_{p'}^{-1} \mathbf{L}_{p'}^{-1} \mathbf{N}_{p'p''} & \\ & \mathbf{I} & \\ & & \mathbf{I} \end{bmatrix} \tag{24}$$

$$\mathbf{N}_{p''p''} = \mathbf{M}_{p''p''} - \mathbf{N}_{p''p'} \mathbf{N}_{p'p'}^{-1} \mathbf{N}_{p'p''} \tag{25}$$

Considering a collection of disjoint index sets C , in which \mathbf{M}_{c,c^C} and $\mathbf{M}_{c^C,c}$ are low-rank for any $c \in C$, $\Psi_C(\mathbf{M})$ can be decomposed into

$$\Psi_C(\mathbf{M}) \approx \mathbf{U}^T \mathbf{M} \mathbf{V} \tag{26}$$

where c^C denotes the complement of the index set c , $\mathbf{U} = \prod_{c \in C} \mathbf{Q}_c \mathbf{S}_{c^C}$, and $\mathbf{V} = \prod_{c \in C} \mathbf{Q}_c \mathbf{T}_{c^C}$.

3.3. Recursive Skeletonization Factorization (RSF)

Let C_j denote the collection of the skeleton index set at level j . We define the matrix at each level j by using M_j . It should be noted that $M_0 = M$. Based on the skeletonization mentioned above, we have

$$M_{j+1} = \Psi_{C_j}(M_j) \approx U_j^T M_j V_j, \quad U_j = \prod_{c \in C_j} Q_c S_{c'}, \quad V_j = \prod_{c \in C_j} Q_c T_{c'} \tag{27}$$

By using RSF, each U_j and V_j are products of unit triangular matrices, and can be simply inverted and transposed. Then, according to the same principle, the factorization can be written as

$$M_j \approx U_{j-1}^T \cdots U_0^T M V_0 \cdots V_{j-1} \tag{28}$$

Note that the inversion and transposition of matrices U_j and V_j can be easily obtained, since they are products of unit triangular matrices. Therefore, M and M^{-1} can be calculated by

$$M \approx [U_0^{-1}]^T \cdots [U_{j-1}^{-1}]^T M_j V_{j-1} \cdots V_0^{-1} \tag{29}$$

$$M^{-1} \approx V_0 \cdots V_{j-1} M_j U_{j-1}^T \cdots U_0^T \tag{30}$$

After obtaining M^{-1} from Equation (30), the unknown coefficient vector α in Equation (10) can be acquired by the following formula:

$$\alpha = M^{-1} b \tag{31}$$

4. Numerical Examples

Here, two benchmark examples are firstly investigated to demonstrate the accuracy of the RSF-BM-SBM, and then the feasibility and effectiveness of the method to solve large-scale problems are verified by calculating the sensitivity of a vehicle model. Assuming that the design variable t is divided into m equidistant nodes, the following relative-root-mean-square error (RRMSE) [24] is adopted to evaluate numerical error:

$$RRMSE = \frac{\sqrt{\sum_{j=1}^m (\dot{u}_e(t_j) - \dot{u}_n(t_j))^2}}{\sqrt{\sum_{j=1}^m \dot{u}_e(t_j)^2}} \tag{32}$$

where \dot{u}_e and \dot{u}_n denote the exact and numerical solutions of the acoustic sensitivity, respectively. In the following numerical calculation, we have fixed the air density and the sound speed to $\rho = 1.2 \text{ kg/m}^3$ and $c = 341 \text{ m/s}$.

In acoustic sensitivity analysis, the gradient of the objective function with respect to the design variables needs to be obtained. Taking the sound pressure p as the objective function, it can be expressed as $\frac{\partial p(x)}{\partial t}$, where t represents the design variable.

4.1. Example 1

In the first example, we consider an infinite pulsating cylinder [49] with radius $a = 0.1 \text{ m}$, which can be reduced to a 2D problem as shown in Figure 1.

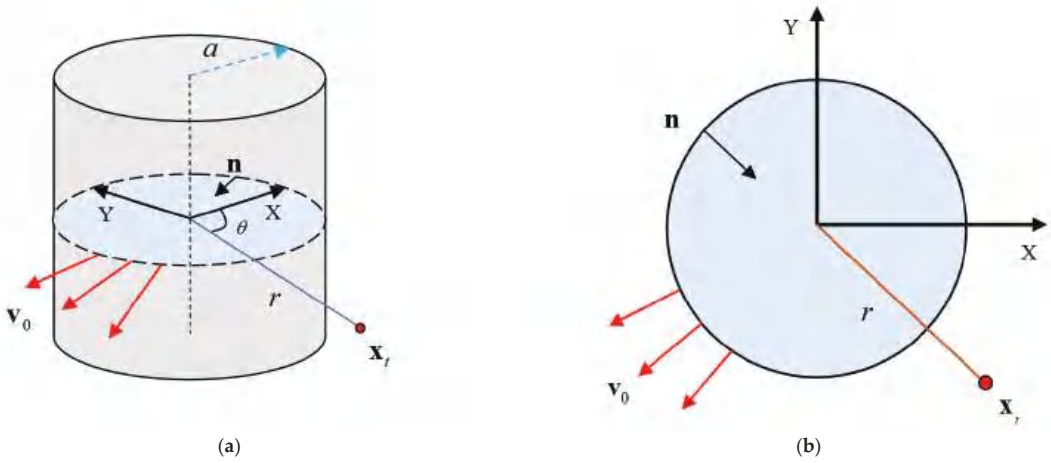


Figure 1. Infinite pulsating cylinder: (a) a pulsating cylinder; (b) simplified model.

Taking the wave number as the design variable, the analytical solution of the acoustic sensitivity at the test point x_t can be given by

$$\frac{\partial p_c(r)}{\partial k} = \frac{-i\rho cv_0}{(H_1^1(ka))^2} \left[rH_1^1(kr)H_1^1(ka) + \frac{a}{2}H_0^1(kr)(H_0^1(ka) - H_2^1(ka)) \right] \quad (33)$$

where $v_0 = 1$ m/s (Neumann boundary condition); H_0^1 and H_1^1 are first-kind zero-order and one-order Hankel functions, respectively; and r is the distance between the test point and the center of cylinder.

Firstly, we investigate the influence of compression accuracy on calculation results. Figure 2 displays error curves of sound pressure sensitivity at the test point $x_t = (3, 3)$ under various values of ID ($\epsilon = 10^{-4}$, $\epsilon = 10^{-7}$, and $\epsilon = 10^{-10}$). In this calculation, the range of the design variable is fixed at 5–6, and the traditional BM-SBM solutions are used for an intuitive comparison. We can see from Figure 2 that the numerical error of the RSF-BM-SBM increases with a decreasing value of ID. When $\epsilon = 10^{-10}$, the calculation accuracy is basically consistent with the traditional BM-SBM. Therefore, the higher compression accuracy should be chosen to obtain accurate and reliable results.

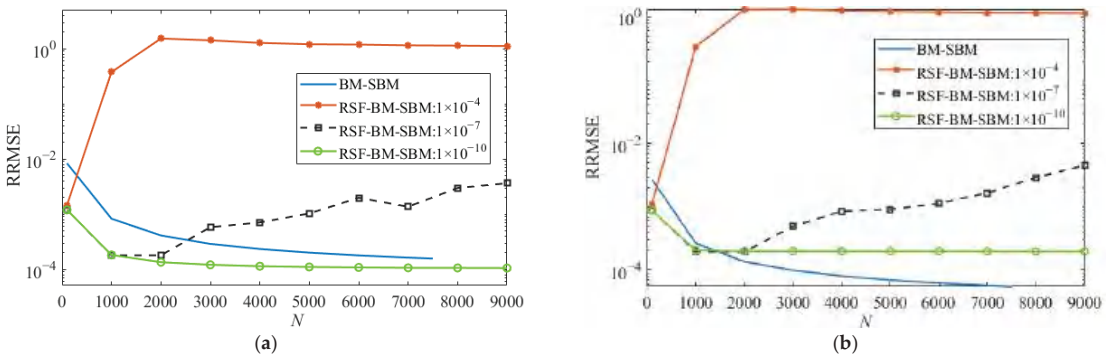


Figure 2. The RRMSEs of the RSF-BM-SBM and conventional BM-SBM: (a) real part; (b) imaginary part.

In addition, Figure 3 compares the computation times of the RSF-BM-SBM and the BM-SBM under different numbers of nodes. When the number of nodes is small, both the BM-SBM and the RSF-BM-SBM consume less time. However, with an increasing number of nodes, the RSF-BM-SBM requires significantly less time than the BM-SBM.

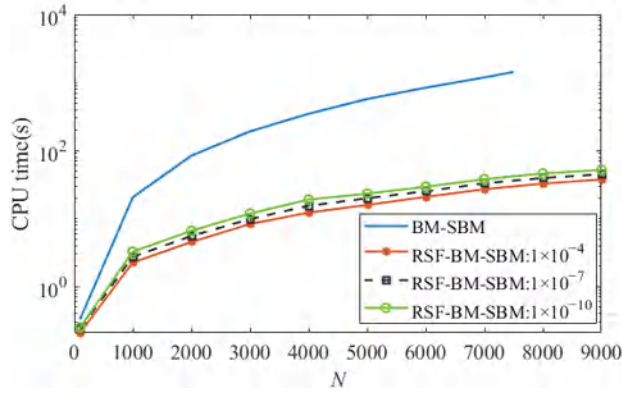


Figure 3. Comparison of CPU computation times under different numbers of nodes.

4.2. Example 2

In this example, we consider a 3D sound radiation problem on a pulsating sphere [48] with radius $a = 0.1$ m, as shown in Figure 4. This acoustic sensitivity analysis takes the wave number k as the design variable. The analytical solution of the acoustic sensitivity is

$$\frac{\partial p_e(r)}{\partial k} = \frac{i\rho c v_0 a^2 e^{ik(r-a)}}{r(1-ika)^2} [(1-ika)^2 + ikr(1-ika) + ika] \tag{34}$$

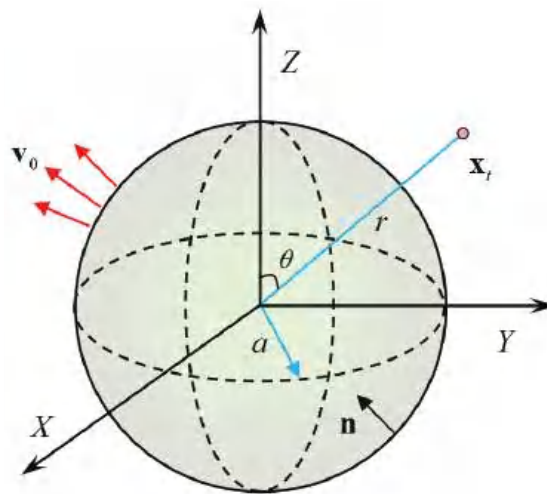


Figure 4. Acoustic radiation from a pulsating sphere.

Table 1 lists the condition numbers and the GPU memories of the conventional BM-SBM and the RSF-BM-SBM with various numbers of nodes. When the number of nodes increases, the memory required by the traditional BM-SBM increases rapidly. Therefore, when the number of nodes increases to a certain number, there will be a problem of

insufficient memory. The RSF-BM-SBM requires less memory than the BM-SBM. The traditional BM-SBM will fail when the number of boundary nodes exceeds 10,000, due to the limitation of computer memory. In addition, it should be noted that the condition number is better when using fewer nodes. As the number of nodes increases, the condition number also increases.

Table 1. Memory and condition number of the RSF-BM-SBM and the BM-SBM with various numbers of nodes.

Boundary Nodes N	Condition Number	Memory (MB)	
		Conventional BM-SBM	RSF-BM-SBM (ID: 1×10^7)
100	22.94	0.16	0.32
2000	104.37	64.00	107.82
4000	1.50×10^7	256.00	239.01
7500	3.33×10^7	900.00	530.60
9000	2.79×10^8	1296.00	589.31
58,204	—	—	6772.86
112,722	—	—	14,541.76
150,082	—	—	27,069.25

4.3. Example 3

The last example considers a scaled-down vehicle model, as shown in Figure 5. This is an acoustic scattering problem, and but there is no analytical solution for sound pressure and sensitivity. Due to the complexity of the model, a large number of boundary points need to be configured, and the traditional BM-SBM cannot be calculated, so the acoustic sensitivity of the model is established by applying the RSF-BM-SBM involving 104,896 source points. In this model, a unit amplitude plane wave of wavenumber $k = 4$ propagates in the positive x -axis direction.

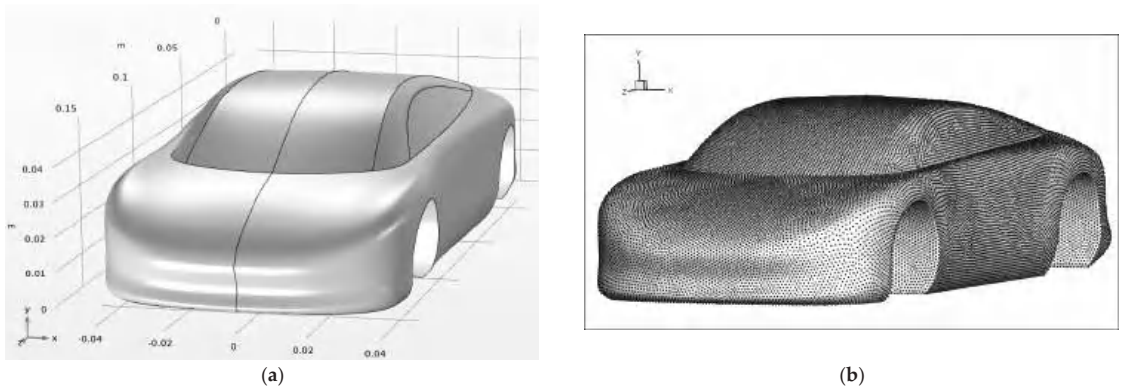


Figure 5. An irregular rigid vehicle model boundary point configuration ($N = 104,896$): (a) vehicle model; (b) boundary points.

Firstly, we chose a spherical surface with radius $r = 1$ m in order to test the accuracy of the proposed method in solving the acoustic scattering of this complex structure. The RSF-BM-SBM and COMSOL Multiphysics FEM solver were used to calculate the scattered sound pressure levels on the surface. The FEM needs to set a perfectly matched layer when solving this kind of problem. Numerical results in Figure 6 indicate the capability and reliability of the proposed method for the 3D complex structure.

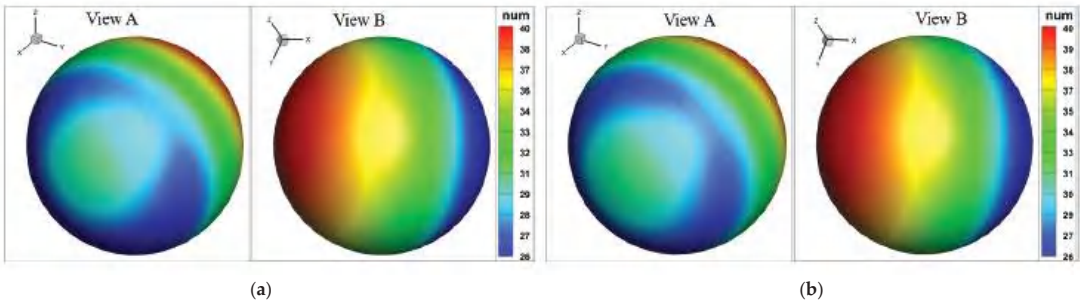


Figure 6. Distributions of the scattered sound pressure level on the investigated surface obtained by using the FEM and RSF-BM-SBM: (a) FEM; (b) RSF-BM-SBM.

We intercepted a limited domain around the car body as shown in Figure 7, and the distributions of sensitivity values with respect to the design variable k were computed by the RSF-BM-SBM. Figure 8 shows the amplitudes of sound pressure sensitivity under different wave numbers. Obvious differences can be observed, which provides a reference for the analysis of acoustic sensitivity of complex structures.

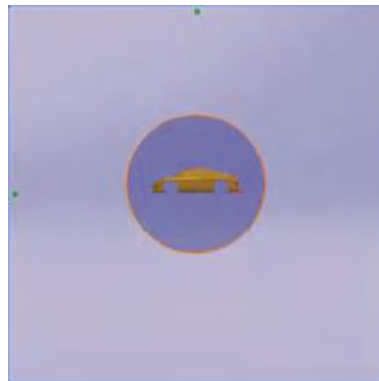


Figure 7. Distributions of boundary source points and test points.

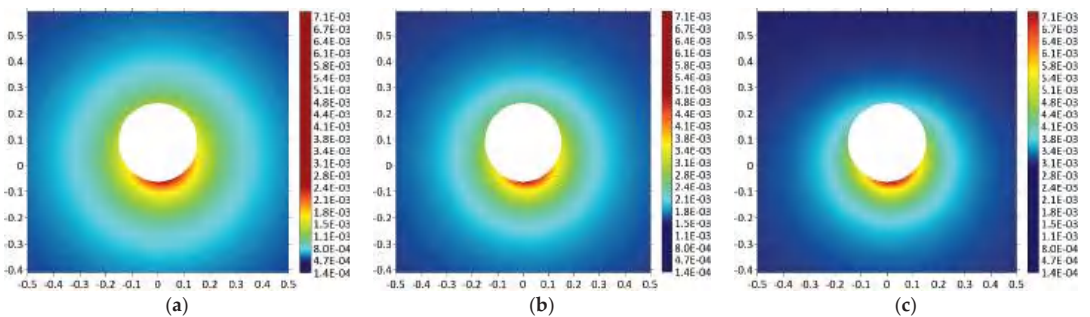


Figure 8. Acoustic pressure sensitivities ($|\partial p / \partial k|$) on $\{(x, y, z) | -0.5 \leq y \leq 0.5, -0.4 \leq z \leq 0.6, x = 0\}$ cross section under different values of k : (a) $k = 3$; (b) $k = 6$; (c) $k = 9$.

5. Conclusions

In this paper, a fast RSF-BM-SBM has been developed for the acoustic sensitivity analysis of 2D and 3D domains. The present scheme is an accurate and semi-analytical

method with the merits of being truly meshless, integration free, mathematically simple, and easy to program. As a boundary-type method based on the fundamental solution, the RSF-BM-SBM is straightforward for addressing exterior acoustic problems encountered in acoustic design sensitivity analysis. In addition, the fictitious frequency issue has been successfully overcome by using the Burton–Miller formulation. Compared with previous approaches [48,49], the proposed fast RSF-BM-SBM greatly reduces the computation time and improves the computation scale by introducing the RSF technique, which makes it possible for the method to analyze the acoustic sensitivity of high-dimensional and large-scale structures.

Through investigating the acoustic scattering problem of an infinite pulsating cylinder, the RSF-SM-SBM shows obvious advantages in solving large-scale problems. Under high compression accuracy (ID: $\varepsilon = 10^{-10}$), the CPU computation time of the RSF-SM-SBM is much shorter than that of the BM-SBM, while the calculation accuracy is basically the same. Numerical results for sound radiation from a pulsating sphere demonstrate that the traditional BM-SBM has a huge demand for memory, which limits its application in large-scale problems. Conversely, the RSF-BM-SBM has significant advantages in reducing computation time and computation cost. For the acoustic sensitivity analysis of a car-like structure, the proposed scheme is also applicable, which indicates the ability and potential of the fast method for 3D complex geometries.

Author Contributions: Conceptualization, L.L. and F.W.; Investigation, X.S. and C.Y.; Methodology, W.L. and F.W.; Resources, S.C.; Supervision, C.Y.; Validation, L.L.; Writing—original draft, S.C.; Writing—review & editing, X.S., W.L., C.Y. and F.W. All authors have read and agreed to the published version of the manuscript.

Funding: The work described in this paper was supported by the National Natural Science Foundation of China (No. 11802151).

Data Availability Statement: Not applicable.

Conflicts of Interest: The authors declare no conflict of interest.

References

- Gohari, H.; Zarastvand, M.; Talebitooti, R.; Loghmani, A.; Omidpanah, M. Radiated sound control from a smart cylinder subjected to piezoelectric uncertainties based on sliding mode technique using self-adjusting boundary layer. *Aerosp. Sci. Technol.* **2020**, *106*, 106141. [CrossRef]
- Xu, M.; Du, J.; Wang, C.; Li, Y. Hybrid uncertainty propagation in structural-acoustic systems based on the polynomial chaos expansion and dimension-wise analysis. *Comput. Methods Appl. Mech. Eng.* **2017**, *320*, 198–217. [CrossRef]
- Rahmatnezhad, K.; Zarastvand, M.; Talebitooti, R. Mechanism study and power transmission feature of acoustically stimulated and thermally loaded composite shell structures with double curvature. *Compos. Struct.* **2021**, *276*, 114557. [CrossRef]
- Chen, Q.; Fei, Q.; Wu, S.; Li, Y. Uncertainty propagation of the energy flow in vibro-acoustic system with fuzzy parameters. *Aerosp. Sci. Technol.* **2019**, *94*, 105367. [CrossRef]
- Shojaei, A.; Mossaiby, F.; Zaccariotto, M.; Galvanetto, U. A local collocation method to construct Dirichlet-type absorbing boundary conditions for transient scalar wave propagation problems. *Comput. Methods Appl. Mech. Eng.* **2019**, *356*, 629–651. [CrossRef]
- Zarastvand, M.R.; Ghassabi, M.; Talebitooti, R. Prediction of acoustic wave transmission features of the multilayered plate constructions: A review. *J. Sandw. Struct. Mater.* **2022**, *24*, 218–293. [CrossRef]
- Shojaei, A.; Hermann, A.; Seleson, P.; Cyron, C. Dirichlet absorbing boundary conditions for classical and peridynamic diffusion models. *Comput. Mech.* **2020**, *66*, 773–793. [CrossRef]
- Scarpa, F. Parametric Sensitivity Analysis of Coupled Acoustic-Structural Systems. *J. Vib. Acoust.* **2000**, *122*, 109–115. [CrossRef]
- Dong, J.; Choi, K.K.; Wang, A.; Zhang, W.; Vlahopoulos, N. Parametric design sensitivity analysis of high-frequency structural-acoustic problems using energy finite element method. *Int. J. Numer. Methods Eng.* **2005**, *62*, 83–121. [CrossRef]
- Chai, Y.; Li, W.; Liu, Z. Analysis of transient wave propagation dynamics using the enriched finite element method with interpolation cover functions. *Appl. Math. Comput.* **2022**, *412*, 126564. [CrossRef]
- Koo, B.-U.; Ih, J.-G.; Lee, B.-C. Acoustic shape sensitivity analysis using the boundary integral equation. *J. Acoust. Soc. Am.* **1998**, *104*, 2851–2860. [CrossRef]
- Kane, J.H.; Mao, S.; Everstine, G.C. A boundary element formulation for acoustic shape sensitivity analysis. *J. Acoust. Soc. Am.* **1991**, *90*, 561–573. [CrossRef]
- Belytschko, T.; Lu, Y.; Gu, L. Element-free Galerkin methods. *Int. J. Numer. Methods Eng.* **1994**, *37*, 229–256. [CrossRef]

14. Lu, Y.; Belytschko, T.; Gu, L. A new implementation of the element free Galerkin method. *Comput. Methods Appl. Mech. Eng.* **1994**, *113*, 397–414. [CrossRef]
15. Shojaei, A.; Boroomand, B.; Soleimanifar, E. A meshless method for unbounded acoustic problems. *J. Acoust. Soc. Am.* **2016**, *139*, 2613–2623. [CrossRef] [PubMed]
16. Mossaiby, F.; Shojaei, A.; Boroomand, B.; Zaccariotto, M.; Galvanetto, U. Local Dirichlet-type absorbing boundary conditions for transient elastic wave propagation problems. *Comput. Methods Appl. Mech. Eng.* **2020**, *362*, 112856. [CrossRef]
17. Chen, Z.; Wang, F. Localized Method of Fundamental Solutions for Acoustic Analysis Inside a Car Cavity with Sound-Absorbing Material. *Adv. Appl. Math. Mech.* **2022**. [CrossRef]
18. Chen, Z.; Wang, F.; Cheng, S.; Wu, G. Localized MFS for three-dimensional acoustic inverse problems on complicated do-mains. *Int. J. Mech. Syst. Dyn.* **2022**, *2*, 143–152. [CrossRef]
19. Wang, F.; Gu, Y.; Qu, W.; Zhang, C. Localized boundary knot method and its application to large-scale acoustic problems. *Comput. Methods Appl. Mech. Eng.* **2020**, *361*, 112729. [CrossRef]
20. Fairweather, G.; Karageorghis, A. The method of fundamental solutions for elliptic boundary value problems. *Adv. Comput. Math.* **1998**, *9*, 69–95. [CrossRef]
21. Poullikkas, A.; Karageorghis, A.; Georgiou, G. The method of fundamental solutions for three-dimensional elastostatics problems. *Comput. Struct.* **2002**, *80*, 365–370. [CrossRef]
22. Chen, W. Singular boundary method: A novel, simple, meshfree, boundary collocation numerical method. *Chin. J. Solid Mech.* **2009**, *30*, 592–599.
23. Burton, A.J.; Miller, G.F. The application of integral equation methods to the numerical solution of some exterior boundary-value problems. *Proc. R. Soc. London. Ser. A Math. Phys. Sci.* **1971**, *323*, 201–210. [CrossRef]
24. Fu, Z.-J.; Chen, W.; Gu, Y. Burton–Miller-type singular boundary method for acoustic radiation and scattering. *J. Sound Vib.* **2014**, *333*, 3776–3793. [CrossRef]
25. Li, J.; Chen, W. A modified singular boundary method for three-dimensional high frequency acoustic wave problems. *Appl. Math. Model.* **2018**, *54*, 189–201. [CrossRef]
26. Qu, W.; Zheng, C.; Zhang, Y.; Gu, Y.; Wang, F. A wideband fast multipole accelerated singular boundary method for three-dimensional acoustic problems. *Comput. Struct.* **2018**, *206*, 82–89. [CrossRef]
27. Wei, X.; Luo, W. 2.5D singular boundary method for acoustic wave propagation. *Appl. Math. Lett.* **2021**, *112*, 106760. [CrossRef]
28. Gu, Y.; Chen, W.; He, X. Singular boundary method for steady-state heat conduction in three dimensional general anisotropic media. *Int. J. Heat Mass Transf.* **2012**, *55*, 4837–4848. [CrossRef]
29. Wei, X.; Sun, L.; Yin, S.; Chen, B. A boundary-only treatment by singular boundary method for two-dimensional inhomogeneous problems. *Appl. Math. Model.* **2018**, *62*, 338–351. [CrossRef]
30. Li, W.; Chen, W. Band gap calculations of photonic crystals by singular boundary method. *J. Comput. Appl. Math.* **2017**, *315*, 273–286. [CrossRef]
31. Cheng, A.H.; Hong, Y. An overview of the method of fundamental solutions—Solvability, uniqueness, convergence, and stability. *Eng. Anal. Bound. Elem.* **2020**, *120*, 118–152. [CrossRef]
32. Karageorghis, A.; Johansson, B.; Lesnic, D. The method of fundamental solutions for the identification of a sound-soft obstacle in inverse acoustic scattering. *Appl. Numer. Math.* **2012**, *62*, 1767–1780. [CrossRef]
33. Jin, B.; Zheng, Y. Boundary knot method for some inverse problems associated with the Helmholtz equation. *Int. J. Numer. Methods Eng.* **2005**, *62*, 1636–1651. [CrossRef]
34. Zheng, C.; Matsumoto, T.; Takahashi, T.; Chen, H. A wideband fast multipole boundary element method for three dimensional acoustic shape sensitivity analysis based on direct differentiation method. *Eng. Anal. Bound. Elem.* **2012**, *36*, 361–371. [CrossRef]
35. Chen, L.; Liu, L.; Zhao, W.; Chen, H. 2D Acoustic Design Sensitivity Analysis Based on Adjoint Variable Method Using Different Types of Boundary Elements. *Acoust. Aust.* **2016**, *44*, 343–357. [CrossRef]
36. Xu, Y.; Zhao, W.; Chen, L.; Chen, H. Distribution Optimization for Acoustic Design of Porous Layer by the Boundary Element Method. *Acoust. Aust.* **2020**, *48*, 107–119. [CrossRef]
37. Liu, Y.; Nishimura, N.; Yao, Z. A fast multipole accelerated method of fundamental solutions for potential problems. *Eng. Anal. Bound. Elem.* **2005**, *29*, 1016–1024. [CrossRef]
38. Zheng, C.; Zhao, W.; Gao, H.; Du, L.; Zhang, Y.; Bi, C. Sensitivity analysis of acoustic eigenfrequencies by using a boundary element method. *J. Acoust. Soc. Am.* **2021**, *149*, 2027–2039. [CrossRef]
39. Godinho, L.; Soares, D.; Santos, P. Efficient analysis of sound propagation in sonic crystals using an ACA–MFS approach. *Eng. Anal. Bound. Elem.* **2016**, *69*, 72–85. [CrossRef]
40. Qu, W.; Chen, W.; Gu, Y. Fast multipole accelerated singular boundary method for the 3D Helmholtz equation in low frequency regime. *Comput. Math. Appl.* **2015**, *70*, 679–690. [CrossRef]
41. Qu, W.; Chen, W.; Zheng, C. Diagonal form fast multipole singular boundary method applied to the solution of high-frequency acoustic radiation and scattering. *Int. J. Numer. Methods Eng.* **2017**, *111*, 803–815. [CrossRef]
42. Wei, X.; Chen, B.; Chen, S.; Yin, S. An ACA-SBM for some 2D steady-state heat conduction problems. *Eng. Anal. Bound. Elem.* **2016**, *71*, 101–111. [CrossRef]
43. Li, W.; Chen, W.; Fu, Z. Precorrected-FFT Accelerated Singular Boundary Method for Large-Scale Three-Dimensional Potential Problems. *Commun. Comput. Phys.* **2017**, *22*, 460–472. [CrossRef]

44. Li, W. A fast singular boundary method for 3D Helmholtz equation. *Comput. Math. Appl.* **2019**, *77*, 525–535. [CrossRef]
45. Li, W.; Wang, F. Precorrected-FFT Accelerated Singular Boundary Method for High-Frequency Acoustic Radiation and Scattering. *Mathematics* **2022**, *10*, 238. [CrossRef]
46. Li, W.; Xu, S.; Shao, M. Simulation of two-dimensional steady-state heat conduction problems by a fast singular boundary method. *Eng. Anal. Bound. Elem.* **2019**, *108*, 149–157. [CrossRef]
47. Li, W.; Wu, B. A fast direct singular boundary method for three-dimensional potential problems. *Eng. Anal. Bound. Elem.* **2022**, *139*, 132–136. [CrossRef]
48. Cheng, S.; Wang, F.; Wu, G.; Zhang, C. A semi-analytical and boundary-type meshless method with adjoint variable formulation for acoustic design sensitivity analysis. *Appl. Math. Lett.* **2022**, *131*, 108068. [CrossRef]
49. Cheng, S.; Wang, F.; Li, P.-W.; Qu, W. Singular boundary method for 2D and 3D acoustic design sensitivity analysis. *Comput. Math. Appl.* **2022**, *119*, 371–386. [CrossRef]
50. Ho, K.L.; Greengard, L. A Fast Direct Solver for Structured Linear Systems by Recursive Skeletonization. *SIAM J. Sci. Comput.* **2012**, *34*, A2507–A2532. [CrossRef]
51. Ho, K.L.; Ying, L. Hierarchical Interpolative Factorization for Elliptic Operators: Differential Equations. *Commun. Pure Appl. Math.* **2016**, *69*, 1415–1451. [CrossRef]
52. Xing, W.; Wen, C.; Sun, L.; Chen, B. A simple accurate formula evaluating origin intensity factor in singular boundary method for two-dimensional potential problems with Dirichlet boundary. *Eng. Anal. Bound. Elem.* **2015**, *58*, 151–165.
53. Li, J.; Chen, W.; Fu, Z.; Sun, L. Explicit empirical formula evaluating original intensity factors of singular boundary method for potential and Helmholtz problems. *Eng. Anal. Bound. Elem.* **2016**, *73*, 161–169. [CrossRef]
54. Cheng, H.; Gimbutas, Z.; Martinsson, P.G.; Rokhlin, V. On the Compression of Low Rank Matrices. *SIAM J. Sci. Comput.* **2005**, *26*, 1389–1404. [CrossRef]

Article

Transient Dynamic Response Analysis of Two-Dimensional Saturated Soil with Singular Boundary Method

Dongdong Liu ¹, Xing Wei ^{1,*}, Chengbin Li ², Chunguang Han ², Xiayi Cheng ¹ and Linlin Sun ^{3,*}

¹ Jiangxi Key Laboratory of Disaster Prevention, Mitigation and Emergency Management, School of Civil Engineering & Architecture, East China Jiaotong University, Nanchang 330013, China

² China Railway Construction Bridge Engineering Bureau Group Co., Ltd., Tianjin 300000, China

³ School of Science, Nantong University, Nantong 226019, China

* Correspondence: weix911@126.com (X.W.); rudong9110@163.com (L.S.); Tel.: +86-791-87046046 (X.W.); +86-513-55003300 (L.S.)

Abstract: In this paper, the singular boundary method (SBM) in conjunction with the exponential window method (EWM) is firstly extended to simulate the transient dynamic response of two-dimensional saturated soil. The frequency-domain (Fourier space) governing equations of Biot theory is solved by the SBM with a linear combination of the fundamental solutions. In order to avoid the perplexing fictitious boundary in the method of fundamental solution (MFS), the SBM places the source point on the physical boundary and eliminates the source singularity of the fundamental solution via the origin intensity factors (OIFs). The EWM is carried out for the inverse Fourier transform, which transforms the frequency-domain solutions into the time-domain solutions. The accuracy and feasibility of the SBM-EWM are verified by three numerical examples. The numerical comparison between the MFS and SBM indicates that the SBM takes a quarter of the time taken by the MFS.

Keywords: singular boundary method; meshless methods; exponential window method; saturated soil; transient dynamic response analysis

MSC: 65N35; 65N80; 74H15

Citation: Liu, D.; Wei, X.; Li, C.; Han, C.; Cheng, X.; Sun, L. Transient Dynamic Response Analysis of Two-Dimensional Saturated Soil with Singular Boundary Method. *Mathematics* **2022**, *10*, 4323. <https://doi.org/10.3390/math10224323>

Academic Editor: Ravi P. Agarwal

Received: 27 October 2022

Accepted: 15 November 2022

Published: 17 November 2022

Publisher's Note: MDPI stays neutral with regard to jurisdictional claims in published maps and institutional affiliations.



Copyright: © 2022 by the authors. Licensee MDPI, Basel, Switzerland. This article is an open access article distributed under the terms and conditions of the Creative Commons Attribution (CC BY) license (<https://creativecommons.org/licenses/by/4.0/>).

1. Introduction

The transient dynamic analysis is of great importance in the geotechnical and mechanical engineering to observe the time-history mechanical response caused by the dynamic loads [1,2]. Although there are some analytical solutions for the regular geometric shapes with isotropic and homogeneous material properties and simple boundary conditions, the numerical tools are usually more flexible and effective for general real-world problems. The transient analysis is usually divided into two parts, viz. spatial discretization and temporal discretization.

For the spatial discretization, the finite element method (FEM) is one of most powerful numerical methods. In light of its theoretical completeness and well-established commercial software, the FEM is robust to different engineering applications [3,4]. Nevertheless, the FEM requires the artificial boundary [5] to analyze the infinite and semi-infinite medium. Besides the FEM, the other domain-type methods [6] encounter the same difficulty. The boundary element method (BEM) has been boosted as an effective alternative in infinite and semi-infinite problems because the fundamental solutions used in the BEM automatically satisfy the Sommerfield radiation condition at infinity. The utilization of the fundamental solutions makes the BEM avoid domain discretization, because the kernel function satisfies governing equations. The superiority of the BEM motivated researchers to develop novel numerical methods based on analytical solutions, such as the fundamental solutions [7–9], the general solutions [10–12] and the particular solutions [13–16]. Among them, most

of numerical methods are pertinent to the fundamental solutions, including the method of fundamental solutions (MFS) [8,17], modified method of fundamental solutions [18] and singular boundary method (SBM) [19–21], to just name a few. The SBM was firstly proposed by Chen [19] with introducing the concept of the origin intensity factor (OIF) to desingularize the fundamental solutions. Originally, the OIF was evaluated via a tedious inverse interpolation technique [22]. Later, simple analytical and empirical formulas were developed and extended the application of the SBM to different problems [23–32]. The abovementioned boundary-type methods required expensive operation counts and memory storage in real-world large-scale problems. This promotes the development of fast algorithms accelerated techniques [33–37] and localized methods [38–41]. It is worth noting that the localized variant of the boundary-type method is a domain-type method.

To implement the transient analysis, the boundary methods require special treatment to deal with time-dependent terms, including the direct time integration methods [42–44], transform methods [45–47] and time-domain fundamental solutions [48]. Except the transform method, the other methods require a proper time-step for numerical stability. Nevertheless, the long-time solution may deteriorate as the time increases. The Krylov deferred correction method (KDC) [49] allows larger time step size for the long-time analysis with acceptable temporal accumulation errors. In the transform methods, the frequency-domain governing equation is solved at some discrete sampling frequencies, and then the frequency-domain solutions are transformed back to the time-domain solutions via the inverse transform, namely the Laplace transform or Fourier transform. The inverse transform is carried out by numerical methods, which may consume a lot of time. The Fourier transform is more attractive because its inverse process can be accelerated by the fast Fourier transform (FFT). However, in lightly damped systems or undamped systems, the FFT is inefficient, or even not applicable without the desired attenuation. This problem was circumvented by introducing an artificial damping to the system by the exponential window method (EWM) [50].

There are few works related to the transient dynamic response analysis of saturated soil. In this study, the SBM in conjunction with the EWM is firstly established to solve the transient dynamic problems in two-dimensional saturated soil. The SBM is formulated in the frequency domain (Fourier space). Thanks to the fundamental solutions, the SBM can be directly applied to finite-, semi-infinite and infinite domains. The source singularity of the fundamental solution is bypassed with simple formulas. Subsequently, the frequency-domain SBM solutions are transformed by the EWM. The selection of the parameters in the EWM will be discussed. The stability and accuracy of the SBM will be investigated via three numerical examples.

2. Governing Equations

For the saturated soil, it is better to take the coupling effect of two phases into consideration [51,52]. Thus, the coupling effect is taken into account in the constitute equation [53,54]:

$$\sigma_{ij} = \lambda \delta_{ij} u_{k,k} + 2\mu \varepsilon_{ij} - \alpha \delta_{ij} p, \quad i = 1, 3, j = 1, 3, \tag{1}$$

$$p = -\alpha M u_{i,i} - M w_{i,i}, \tag{2}$$

where σ_{ij} is the effective stress; δ_{ij} the Kronecker delta; $\varepsilon_{ij} = (u_{i,j} + u_{j,i})/2$ the strain tensor; w_i the fluid displacement with respect to the solid skeleton; p the pore pressure; u_i the average skeleton displacement; λ and μ the solid skeleton Lamé constants; and α and M the Biot parameters describing the compressibility of the fluid-saturated two-phase material.

Taking Equations (1) and (2) into the equilibrium equations, we obtained the equations of motion for the bulk porous medium and the pore fluid without body forces as [53,54]

$$\mu u_{i,jj} + (\lambda + \alpha^2 M + \mu) u_{j,ji} + \alpha M w_{j,ji} = \rho \ddot{u}_i + \rho_f \ddot{w}_i, \tag{3}$$

$$\alpha M u_{j,ji} + M w_{j,ji} = \rho_f \ddot{u}_i + m \ddot{w}_i + \frac{\eta}{k} K(t) * \dot{w}_i, \tag{4}$$

where a dot ($\dot{\bullet}$) denotes the time derivative and a star (\ast) denotes the time convolution; $\rho = (1 - \phi)\rho_s + \phi\rho_f$ is the density of the saturated poroelastic medium; ρ_s and ρ_f are the density of the skeleton and fluid; ϕ the porosity; η the viscosity of the pore fluid; k the permeability of the saturated poroelastic medium; $m = \alpha_\infty\rho_f/\phi$; α_∞ is the tortuosity; and $K(t)$ is a time-dependent viscosity correction factor which describes the transition between the viscous flow in the low-frequency range and the inertia-dominated flow in the high-frequency range.

The initial boundary conditions and boundary conditions are given as

$$\mathbf{u}^s|_{t=0} = \frac{\partial \mathbf{u}^s}{\partial t}\Big|_{t=0} = 0, \mathbf{w}|_{t=0} = 0, \text{ and } p|_{t=0} = 0, \tag{5}$$

$$u_i^s = \hat{u}_i^s, \text{ on } \Gamma_u^s, \tag{6}$$

$$t_i^s = \sigma_{i1}^s n_1 + \sigma_{i3}^s n_3 = \hat{t}_i^s, \text{ on } \Gamma_t^s, \tag{7}$$

$$w_i = \hat{w}_i, \text{ on } \Gamma_w^f, \tag{8}$$

$$p = \hat{p}, \text{ on } \Gamma_p^f, \tag{9}$$

where $\mathbf{n} = (n_1, n_3)$ is the normal vector to the boundary, and $\hat{u}_i^s, \hat{t}_i^s, \hat{w}_i$ and \hat{p} are the prescribed solid displacements, tractions, relative fluid displacements and pore pressure on the boundary, respectively.

We introduce the Fourier transform with respect to time and frequency as

$$\tilde{f}(\omega) = \int_{-\infty}^{+\infty} f(t)e^{-j\omega t} dt, f(t) = \frac{1}{2\pi} \int_{-\infty}^{+\infty} \tilde{f}(\omega)e^{j\omega t} d\omega, \tag{10}$$

where $j = \sqrt{-1}$ is the imaginary unit.

After Fourier transform on Equations (3) and (4), the frequency-domain governing equations in terms of solid displacement and fluid pressure [54] are recast as

$$\mu \tilde{u}_{i,jj} + (\lambda + \mu) \tilde{u}_{j,ji} + \rho_g \omega^2 \tilde{u}_i - \alpha_g \tilde{p}_{,i} = 0, \tag{11}$$

$$\tilde{p}_{,jj} + \beta_2 \omega^2 \tilde{p} - \beta_3 \tilde{u}_{i,j} = 0, \tag{12}$$

where $\rho_g = \rho - \beta_4 \rho_f, \alpha_g = \alpha - \beta_4, \beta_1 = M/[m\omega^2 - j\omega(\eta/k)\tilde{K}(\omega)], \beta_2 = 1/(\beta_1 \omega^2), \beta_4 = \rho_f \omega^2 \beta_1/M; \beta_3 = \rho_f \omega^2 - \alpha[m\omega^2 - j\omega(\eta/k)\tilde{K}(\omega)], \tilde{K}(\omega)$ is the Fourier transform of $K(t)$, and “ \sim ” denotes the representation in the frequency-domain.

3. Singular Boundary Method in Frequency-Domain

In this section, the SBM formulation is established for the frequency-domain governing equations. The SBM evaluates the frequency-domain solution with a linear combination of fundamental solutions in terms of the source points as [55]

$$\tilde{u}_i^s(\mathbf{x}_m) = \sum_{n=1}^N \beta_{1n} \tilde{u}_{i1}^s(\mathbf{x}_m, \mathbf{s}_n) + \sum_{n=1}^N \beta_{3n} \tilde{u}_{i3}^s(\mathbf{x}_m, \mathbf{s}_n) + \sum_{n=1}^N \beta_{4n} \tilde{u}_{i4}^s(\mathbf{x}_m, \mathbf{s}_n), \quad i = 1, 3, \tag{13}$$

$$\tilde{p}(\mathbf{x}_m) = \sum_{n=1}^N \beta_{1n} \tilde{p}_1(\mathbf{x}_m, \mathbf{s}_n) + \sum_{n=1}^N \beta_{3n} \tilde{p}_3(\mathbf{x}_m, \mathbf{s}_n) + \sum_{n=1}^N \beta_{4n} \tilde{p}_4(\mathbf{x}_m, \mathbf{s}_n), \tag{14}$$

$$\tilde{t}_i^s(\mathbf{x}_m) = \sum_{n=1}^N \beta_{1n} \tilde{t}_{i1}^s(\mathbf{x}_m, \mathbf{s}_n) + \sum_{n=1}^N \beta_{3n} \tilde{t}_{i3}^s(\mathbf{x}_m, \mathbf{s}_n) + \sum_{n=1}^N \beta_{4n} \tilde{t}_{i4}^s(\mathbf{x}_m, \mathbf{s}_n), \quad i = 1, 3, \tag{15}$$

$$\tilde{q}_n(\mathbf{x}_m) = \sum_{n=1}^N \beta_{1n} \tilde{q}_1(\mathbf{x}_m, \mathbf{s}_n) + \sum_{n=1}^N \beta_{3n} \tilde{q}_3(\mathbf{x}_m, \mathbf{s}_n) + \sum_{n=1}^N \beta_{4n} \tilde{q}_4(\mathbf{x}_m, \mathbf{s}_n). \tag{16}$$

where x_m, s_n are the m th field point and n th source point; N is the total number of boundary source points; $\{\beta_{kn}\}_{n=1}^N (k = 1, 3, 4)$ are the coefficients to be determined; and $\tilde{u}_{ik}^s, \tilde{t}_{ik}^s, \tilde{p}_k$ and $\tilde{q}_k (i = 1, 3, k = 1, 3, 4)$ are the fundamental solutions of solid displacements, traction, pore pressure and flux, which are given as

$$\tilde{u}_{ik}^s = A\delta_{ik} - Br_{,i}r_{,k}, \tilde{u}_{i4}^s = Dr_{,i}, i, k = 1, 3, \tag{17}$$

$$\begin{aligned} \tilde{t}_{ik}^s &= \lambda \left[A' - B' - \frac{B}{r} \right] r_{,k}n_i + \mu \left[\left(A' - \frac{B}{r} \right) (r_{,n}\delta_{ik} + r_{,i}n_k) \right. \\ &\quad \left. - \frac{2B}{r} r_{,k}n_i + 2 \left(-B' + \frac{2B}{r} \right) r_{,i}r_{,k}r_{,n} \right], i, k = 1, 3, \tag{18} \\ \tilde{t}_{i4}^s &= \left[(\lambda + 2\mu) \frac{D}{r} + \lambda D' \right] n_i + 2\mu \left(-\frac{D}{r} + D' \right) r_{,i}r_{,n}, i = 1, 3, \end{aligned}$$

$$\tilde{p}_k = Cr_{,k}, \tilde{p}_4 = \frac{1}{2\pi} \sum_{d=1,2} r_d h_d K_0(z_d), k = 1, 3, \tag{19}$$

$$\tilde{q}_k = \begin{cases} \frac{-\alpha_g}{\beta_3} \left[\frac{C}{r} n_k + \left(C' - \frac{C}{r} \right) r_{,k}r_{,n} \right], k = 1, 3, \\ \frac{j\alpha_g r_{,n}}{2\pi\beta_3} \sum_{d=1,2} r_d h_d k_d K_1(z_d), k = 4, \end{cases} \tag{20}$$

where

$$A = \frac{1}{2\pi} \left[- \sum_{d=1,2} g_d \frac{K_1(z_d)}{z_d} + g_3 \left(K_0(z_3) + \frac{K_1(z_3)}{z_3} \right) \right], C = \frac{j}{2\pi} \left[\sum_{d=1,2} \frac{r_d g_d}{k_d} K_1(z_d) \right]$$

$$B = \frac{1}{2\pi} \left[- \sum_{d=1,2} g_d K_2(z_d) + g_3 K_2(z_3) \right], D = \frac{-j}{2\pi} \sum_{d=1,2} k_d h_d K_1(z_d) z_3 = jk_3 r$$

$$z_d = jk_d r, r_d = \frac{\omega^2 \rho_g - (\lambda + 2\mu)k_d^2}{\alpha_g} (d = 1, 2), g_1 = \frac{\beta_3 - r_2}{(\lambda + 2\mu)(r_1 - r_2)},$$

$$g_2 = \frac{\beta_3 - r_1}{(\lambda + 2\mu)(r_2 - r_1)}, g_3 = \frac{1}{\mu}, h_1 = -\frac{\beta_3}{\alpha_g(r_1 - r_2)}, h_2 = -\frac{\beta_3}{\alpha_g(r_2 - r_1)}$$

in which $r = \sqrt{(x_1 - y_1)^2 + (x_3 - y_3)^2}$ is the distance between field point $x = (x_1, x_3)$ and source point $y = (y_1, y_3)$. K_n is the modified Bessel function of the second kind of order n , and k_d is

$$k_1 = \sqrt{\frac{\beta_2 \omega^2}{2} + \frac{\rho_g \omega^2 - \alpha_g \beta_3 + \sqrt{H}}{2(\lambda + 2\mu)}}, k_2 = \sqrt{\frac{\beta_2 \omega^2}{2} + \frac{\rho_g \omega^2 - \alpha_g \beta_3 - \sqrt{H}}{2(\lambda + 2\mu)}}, k_3 = \sqrt{\omega^2 \rho_g / \mu}$$

where

$$H = (\lambda \beta_2 \omega^2 - \alpha_g \beta_3 + \rho_g \omega^2)^2 + 4(\lambda + \mu) \beta_2 \omega^4 (\mu \beta_2 - \rho_g) - 4\mu \alpha_g \beta_2 \beta_3 \omega^2$$

The derivation of the fundamental solutions is detailed in Appendix A.

With the fundamental solutions, Equations (13)–(16) are forced to satisfy the boundary conditions for the determination of the unknown coefficients. Then the boundary conditions with Equations (13)–(16) are formulated as

$$\tilde{u}_i^s(\mathbf{y}_m) = \sum_{k=1,3,4} \sum_{n \neq m}^N \beta_{kn} \tilde{u}_{ik}^s(\mathbf{y}_m, \mathbf{y}_n) + \sum_{k=1,3,4} \beta_{km} \tilde{U}_{ik}^s(\mathbf{y}_m, \mathbf{y}_m), i = 1, 3, \tag{21}$$

$$\tilde{t}_i^s(\mathbf{y}_m) = \sum_{k=1,3,4} \sum_{n \neq m}^N \beta_{kn} \tilde{t}_{ik}^s(\mathbf{y}_m, \mathbf{y}_n) + \sum_{k=1,3,4} \beta_{km} \tilde{T}_{ik}^s(\mathbf{y}_m, \mathbf{y}_m), i = 1, 3, \tag{22}$$

$$\tilde{p}(\mathbf{y}_m) = \sum_{k=1,3,4} \sum_{n \neq m}^N \beta_{kn} \tilde{p}_k(\mathbf{y}_m, \mathbf{y}_n) + \sum_{k=1,3,4} \beta_{km} \tilde{p}_k(\mathbf{y}_m, \mathbf{y}_m), \tag{23}$$

$$\tilde{q}_n(\mathbf{y}_m) = \sum_{k=1,3,4} \sum_{n \neq m}^N \beta_{kn} \tilde{q}_k(\mathbf{y}_m, \mathbf{y}_n) + \sum_{k=1,3,4} \beta_{km} \tilde{q}_k(\mathbf{y}_m, \mathbf{y}_m). \tag{24}$$

The singular terms, namely, $\tilde{u}_{ik}^s(\mathbf{y}_m, \mathbf{y}_m)$, $\tilde{t}_{ik}^s(\mathbf{y}_m, \mathbf{y}_m)$, $\tilde{p}_k(\mathbf{y}_m, \mathbf{y}_m)$ and $\tilde{q}_k(\mathbf{y}_m, \mathbf{y}_m)$, are involved when the boundary data points overlaps the source points. To deal with this issue, some numerical or analytical methods are introduced to desingularize these terms. In the SBM, the diagonal terms are called the origin intensity factors (OIFs), as $\tilde{U}_{ik}^s(\mathbf{y}_m, \mathbf{y}_m)$, $\tilde{T}_{ik}^s(\mathbf{y}_m, \mathbf{y}_m)$, $\tilde{P}_k(\mathbf{y}_m, \mathbf{y}_m)$ and $\tilde{Q}_k(\mathbf{y}_m, \mathbf{y}_m)$ in Equations (21)–(24). The OIFs for 2D saturated poroelastic problems [20,21,56], as shown in Equations (21)–(24) are calculated as

$$\tilde{U}_{ik}^s(\mathbf{y}_m, \mathbf{y}_m) = \begin{cases} [\hat{g}(\mathbf{y}_m, \mathbf{y}_m)\chi_1 - \chi_2]\delta_{ik} + \chi_3\Lambda_{ik}, & i, k = 1, 3, \\ 0, & k = 4, i = 1, 3, \end{cases} \tag{25}$$

$$\tilde{T}_{ik}^s(\mathbf{y}_m, \mathbf{y}_m) = \begin{cases} \hat{t}_{ik}(\mathbf{y}_m, \mathbf{y}_m), & i, k = 1, 3, \\ [\hat{g}(\mathbf{y}_m, \mathbf{y}_m)\chi_4 + \chi_5]n_i, & k = 4, i = 1, 3, \end{cases} \tag{26}$$

$$\tilde{P}_k(\mathbf{y}_m, \mathbf{y}_m) = \begin{cases} 0, & k = 1, 3, \\ \hat{g}(\mathbf{y}_m, \mathbf{y}_m)\chi_6 + \chi_7, & k = 4, \end{cases} \tag{27}$$

$$\tilde{Q}_k(\mathbf{y}_m, \mathbf{y}_m) = \begin{cases} [\hat{g}(\mathbf{y}_m, \mathbf{y}_m)\chi_8 + \chi_9]n_k, & k = 1, 3, \\ \hat{q}(\mathbf{y}_m, \mathbf{y}_m)\chi_{10}, & k = 4, \end{cases} \tag{28}$$

where χ_1, \dots, χ_{10} are provided in Appendix B; $\Lambda_{ik} = \lim_{x \rightarrow y, x \in \Gamma} r_i r_k = \frac{\tau_i \tau_k}{\tau_1 + \tau_3}$, $\boldsymbol{\tau} = (\tau_1, \tau_3)$ is the tangent vector of point x on the boundary, $\hat{g}(\mathbf{y}_m, \mathbf{y}_m)$ and $\hat{q}(\mathbf{y}_m, \mathbf{y}_m)$ are the OIFs for the fundamental solution of the Laplace operator for Dirichlet and Neumann boundary conditions, and $\hat{t}_{ik}(\mathbf{y}_m, \mathbf{y}_m)$ is the OIF for the fundamental solution of the traction boundary condition. These terms are computed as

$$\hat{g}(\mathbf{y}_m, \mathbf{y}_m) = -\frac{1}{2\pi} \ln\left(\frac{l_m}{2\pi}\right), \hat{q}(\mathbf{y}_m, \mathbf{y}_m) = -\frac{1}{2l_m}, \hat{t}_{ij}(\mathbf{y}_m, \mathbf{y}_m) = -\frac{\delta_{ij}}{2l_m} \tag{29}$$

where l_m is a half-length of the arc between source points \mathbf{y}_{m+1} and \mathbf{y}_{m-1} .

Finally after obtaining the coefficients, the frequency-domain solutions of the variables within the domain can be evaluated via Equations (13)–(16).

4. Exponential Window Method

The frequency-domain solutions can be converted to the transient solutions via the inverse Fourier transform, which is accelerated by the fast Fourier transformation (FFT) [47,57]. It should be noted that the time responses decay slowly in lightly damped systems, and even never decay in undamped systems. In these two cases, the FFT is inefficient. Thus, a powerful numerical technique, the exponential window method (EWM) [58], is introduced. In the EWM, artificial damping is created to produce the desired attenuation, and the artificial damping is removed by scaling back in the final. The detail of the EWM is summarized as follows:

- (1) Determine the total calculation time T and the number of sampling frequencies N_ω , then to determine the angular frequency resolution $\Delta\omega = 2\pi/T$ with $\Delta t = T/N_\omega$;
- (2) Determine the shifting constant according to the numerical experiments and experience as

$$\vartheta = \frac{\kappa \ln 10}{T}, \tag{30}$$

where κ denote the damping coefficient, and $2 \leq \kappa \leq 3$ is recommended;

- (3) Construct a desired damping system with scaling the variables $\zeta(\mathbf{x}, t)$ ($u_i^s, \sigma_{ik}^s, w_i$ and p) with the scaling function $e^{-\theta t}$ as $\zeta_{ew}(\mathbf{x}, t) = \zeta(\mathbf{x}, t)e^{-\theta t}$. Bring new variables ζ_{ew} into the governing equations, and a novel frequency-domain boundary value problem Equations (6) and (7) with $\bar{\omega} = \omega - j\theta$ is obtained.
- (4) Simultaneously, the boundary condition $P(\mathbf{x}, t)$ is scaled into $P_{ew}(\mathbf{x}, t) = P(\mathbf{x}, t)e^{-\theta t}$, and the frequency-domain boundary condition can be obtained via discretized Fourier transform

$$\hat{P}_{ew}(\mathbf{x}, \bar{\omega}_k) = \frac{1}{N_\omega} \sum_{n=0}^{N_\omega-1} P_{ew}(\mathbf{x}, n\Delta t) e^{-2\pi jnk/N_\omega} = \frac{1}{N_\omega} \sum_{n=0}^{N_\omega-1} e^{-\theta n\Delta t} P(\mathbf{x}, n\Delta t) e^{-2\pi jnk/N_\omega}, \tag{31}$$

where $\bar{\omega}_k = k\Delta\omega - j\theta (k = 0, 1, \dots, N_\omega - 1)$.

- (5) Perform the SBM to evaluate the solutions of the frequency-domain problems $R_{ew}^*(\bar{\omega}_k)$ at the frequencies $\bar{\omega}_k = k\Delta\omega - j\theta (k = 0, 1, \dots, N_\omega/2)$. The remaining of results can be obtained through conjugate symmetric property as

$$R_{ew}^*(\bar{\omega}_k) = \text{conj}(R_{ew}^*(\bar{\omega}_{N_\omega-k})), k = N_\omega/2 + 1, \dots, N_\omega - 1. \tag{32}$$

- (6) Perform the IFFT with the inverse DFT with Hanning window function W_k , and obtain the time-domain solutions as

$$R_{ew}(n\Delta t) = \sum_{k=1}^{N_\omega-1} W_k R_{ew}^*(\bar{\omega}_k) e^{2\pi jnk/N_\omega}, \tag{33}$$

The Hanning window function $W_k = 0.5[1 + \cos(2\pi k/N_\omega)]$ is used to alleviate the Gibbs oscillations.

- (7) Descale the time-domain solutions and obtain the solutions of the original problems as

$$R(n\Delta t) = e^{\theta n\Delta t} R_{ew}(n\Delta t). \tag{34}$$

5. Numerical Examples

In this section, three numerical examples are used to verify the accuracy and effectiveness of the proposed method for the transient dynamic response of two-dimensional saturated soil. The accuracy of the SBM-EWM is evaluated by the absolute error of variable ζ versus time at point \mathbf{x} as

$$AE(\zeta) = \left| \bar{\zeta} \left(\frac{kT}{N_\omega}, \mathbf{x} \right) - \zeta \left(\frac{kT}{N_\omega}, \mathbf{x} \right) \right|, \tag{35}$$

where $\bar{\zeta}$ represents the exact solution, ζ denotes the numerical result obtained by the SBM.

Unless otherwise specified, the parameters of the saturated soil are set as $\lambda = 4.0 \times 10^7$ Pa, $\mu = 2.0 \times 10^7$ Pa, $\rho_s = 2500$ kg/m³, $\rho_f = 1.0 \times 10^3$ kg/m³, $a_\infty = 3$, $\alpha = 0.95$, $M = 4.0 \times 10^8$ Pa, $\phi = 0.3$, $\eta = 1.0 \times 10^{-3}$ Pa·s, $k = 1.0 \times 10^{-12}$ m². All calculations of this paper are fulfilled on a desktop with an Intel Core (TM) I7-6500U at 2.50 GHz on a 64-bit Windows server with a total of 12GB DDR4 memory. The SBM is implemented via MATLAB software.

5.1. Verification of the Proposed SBM-EWM Method

In the section, a saturated poroelastic column problem (Figure 1) is considered. A uniform normal load on the upper boundary and the rest boundaries is sliding:

$$\begin{cases} t_n^s = -H(t)N/m^2, t_\tau^s = 0N/m^2, p = 0Pa, & \text{on the top boundary,} \\ u_n^s = 0m, t_\tau^s = 0N/m^2, w_n = 0m, & \text{on the other boundaries,} \end{cases} \tag{36}$$

where $H(t)$ is the Heaviside step function.

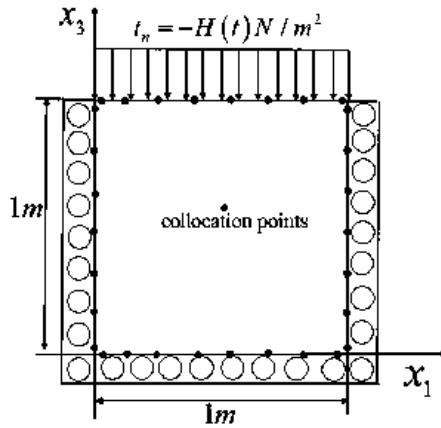


Figure 1. Computational model of saturated column.

Firstly, the transient problem is transformed into the frequency domain. The frequency-domain exact solution for the problem can be constructed as

$$\begin{aligned} \tilde{u}_3^s &= a_1 j k_1 e^{j k_1(x_3-h)} + a_2 j k_2 e^{j k_2(x_3-h)} - a_3 j k_1 e^{-j k_1 x_3} - a_4 j k_2 e^{-j k_2 x_3}, \\ \tilde{p} &= a_1 r_1 e^{j k_1(x_3-h)} + a_2 r_2 e^{j k_2(x_3-h)} + a_3 r_1 e^{-j k_1 x_3} + a_4 r_2 e^{-j k_2 x_3}, \end{aligned} \tag{37}$$

in which $h = 1\text{ m}$, and the unknown coefficients a_1, a_2, a_3 and a_4 can be derived from

$$\begin{bmatrix} -k_1^2 & -k_2^2 & -k_1^2 e^{-j k_1 h} & -k_2^2 e^{-j k_2 h} \\ r_1 & r_2 & r_1 e^{-j k_1 h} & r_2 e^{-j k_2 h} \\ j k_1 e^{-j k_1 h} & j k_2 e^{-j k_2 h} & -j k_1 & -j k_2 \\ j k_1 (r_1 - \omega^2 \rho_f) e^{-j k_1 h} & j k_2 (r_2 - \omega^2 \rho_f) e^{-j k_2 h} & j k_1 (r_1 - \omega^2 \rho_f) & j k_2 (r_2 - \omega^2 \rho_f) \end{bmatrix} \begin{bmatrix} a_1 \\ a_2 \\ a_3 \\ a_4 \end{bmatrix} = \begin{bmatrix} \frac{-1}{\lambda + 2\mu} \\ 0 \\ 0 \\ 0 \end{bmatrix}$$

Then the transient exact solution is retrieved via the EWM.

The SBM discretizes the boundary into 400 boundary nodes. The EWM-SBM is employed for the numerical solutions in a duration of $T = 18\text{ ms}$. In the EWM, N_ω and κ are set as 128 and 3.

In Figure 2, some numerical results are picked up to show the accuracy of the present method, including u_3^s at (0.5, 0.8), p at (0.5, 0.5), w_3 at (0.5, 0.7) and σ_{33}^s at (0.5, 0.3). It is shown that the numerical results are in good agreement with the exact solutions. Nevertheless, the results without the Hanning window function drastically oscillate in the end of the duration, which is called Gibbs oscillations. The problem is ameliorated by the Hanning window function. The application of the Hanning window functions does not bring much time. For example, in Figure 2a, the SBM-EWM without and with the Hanning window functions, respectively, take 57.08 s and 56.48 s. As a consequence, it is essential to employ the window function in the EWM-SBM.

It is obvious that the selection of the parameters N_ω, κ has an influence on the accuracy and the stability of the solutions. In the following, the influence is studied.

N_ω is the number of the sample frequencies. More sample frequencies enhance the accuracy of the results but in the meantime bring more operation counts. If the sample frequencies are not enough, the numerical methods may yield inaccurate results. Figure 3 shows the effect of N_ω on the numerical methods via σ_{33}^s at (0.5, 0.8) and p at (0.5, 0.5). In this figure, the number of boundary points is 400 and $\kappa = 2.7$. As the number of sampling frequencies increases, the numerical solutions converge to the exact solutions. The solution with $N_\omega = 64$ deviates from the exact solutions most in comparison with $N_\omega = 128$ and 256. However, the case with $N_\omega = 256$ takes 111.7 s in total, which is nearly two times that

of the case with $N_\omega = 128$, which consumes 59.3 s. Overall, $N_\omega = 128$ is considered in the following numerical experiments.

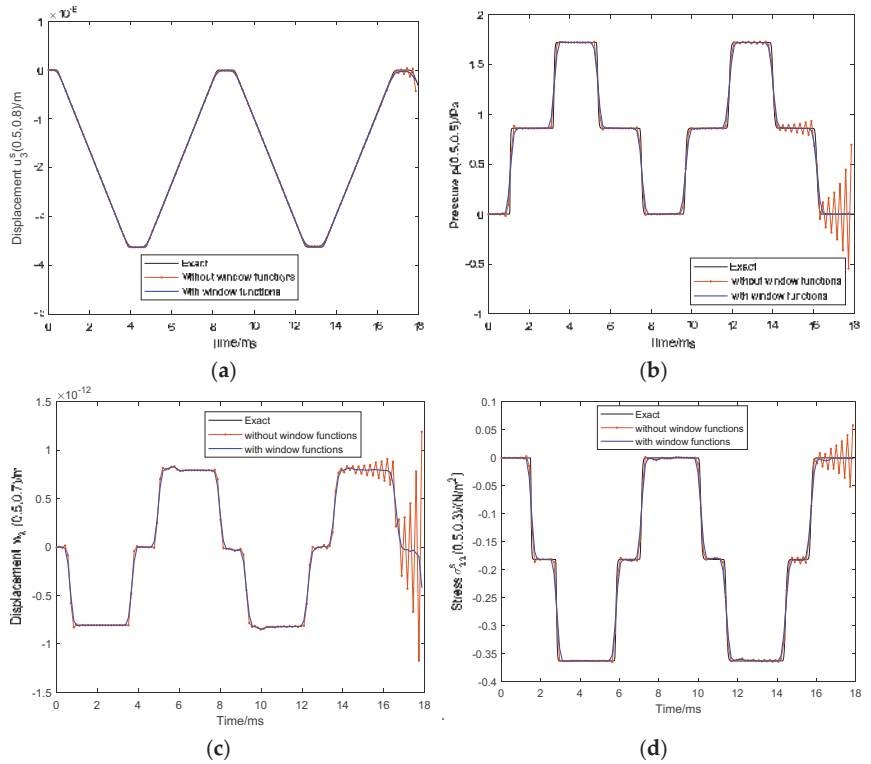


Figure 2. Time history of (a) u_3^s at (0.5, 0.8), (b) p at (0.5, 0.5), (c) w_3 at (0.5, 0.7), (d) σ_{33}^s at (0.5, 0.3).

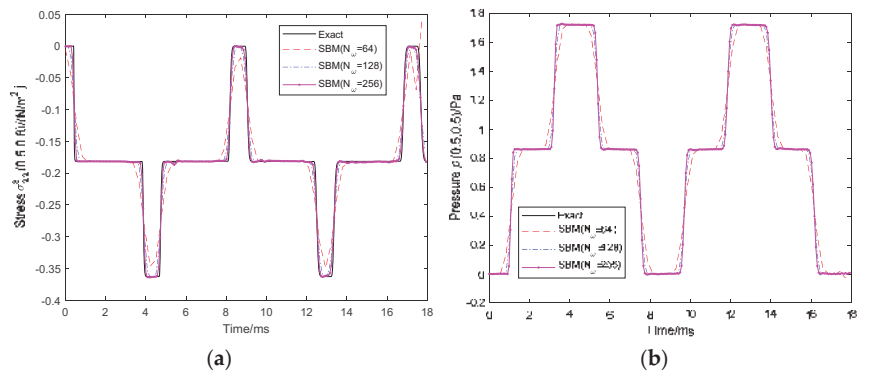


Figure 3. Time history of (a) σ_{33}^s at (0.5, 0.8) and (b) p at (0.5, 0.5) with respect to the number of sampling frequencies N_ω .

κ is the damping coefficient to determine the artificial damping. A numerical investigation on the κ is given in Figure 4 via the absolute error of u_3^s at (0.5, 0.5) under different damping coefficients. $\kappa = 1.5, 2, 2.5, 3$ and 3.5 are selected. The method with $\kappa = 1.5$ results in the worst solutions. The reason lies in that more sampling frequencies are required in

lightly damped systems. In Figure 4, the results with $\kappa = 2, 2.5, 3$ and 3.5 are acceptable. Nevertheless, an arbitrary large damping coefficient may lead to loss of numerical precision. As a trade-off, the $\kappa = 2.5$ is applied in the subsequent examples.

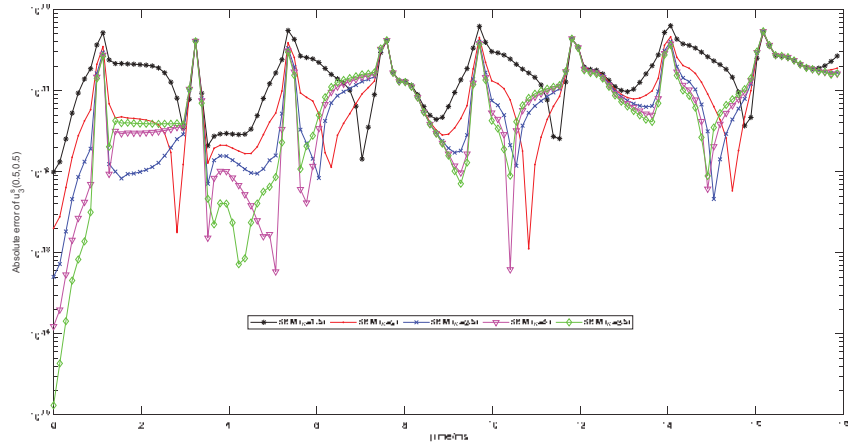


Figure 4. Time history of absolute error of u_3^s at point $(0.5, 0.5)$ under different κ .

In general, the numerical transient results are limited to a short time duration because the results deteriorate if the calculation duration is too long. In this study, the long time behavior of the present method is investigated. In this case, $T = 140$ ms and $N_\omega = 1024$. Figure 5 plots the history of u_3^s at $(0.5, 0.8)$ and p at $(0.5, 0.5)$. In the entire calculation time, no obvious differences can be observed between the SBM-EWM and exact solutions, which verifies the accuracy and stability of the SBM-EWM in the long-term dynamic simulation.

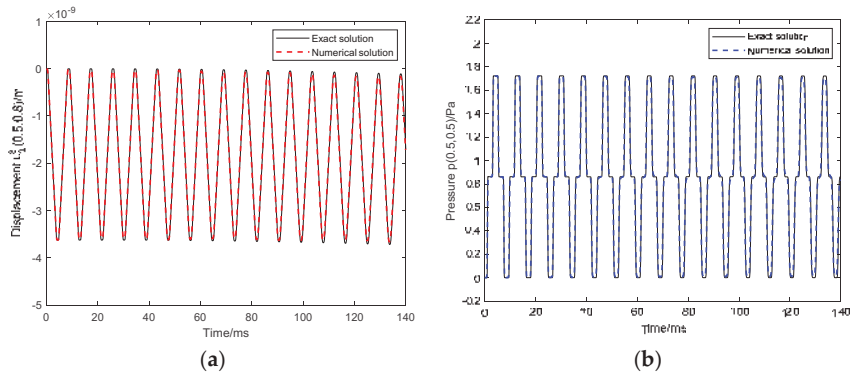


Figure 5. A long time dynamic response of saturated column (a) u_3^s at $(0.5, 0.8)$ and (b) p at $(0.5, 0.5)$.

5.2. A Half-Space Problem Subjected to a Transient Load

In the section, a saturated poroelastic half-space subjected to transient loads on the ground is shown in Figure 6. Thus, the saturated poroelastic half-space is subjected to the boundary condition expressed as

$$\begin{cases} t_3^s = -H(t)\text{N/m}^2, t_1^s = 0\text{N/m}^2, p = 0\text{Pa}, x_1 \in [-1, 1], x_3 = 0, \\ t_3^s = 0\text{N/m}^2, t_1^s = 0\text{N/m}^2, p = 0\text{Pa rest} \end{cases}$$

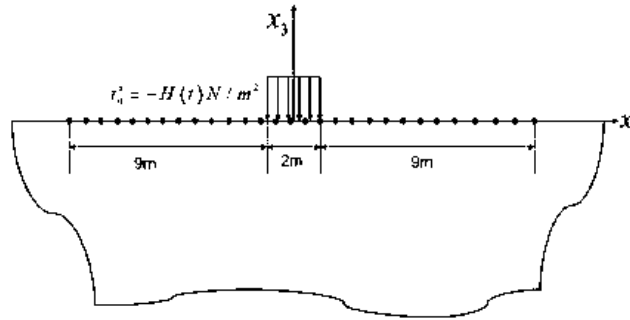


Figure 6. The sketch of the semi-infinite domain.

The boundary is discretized into 500 points. The parameters N_ω , κ are respectively 128 and 2.5 for the SBM. The analytical solution of this problem in frequency-domain is derived by Ba [59]. Then the transient analytical solution is obtained by the EWM with $N_\omega = 256$ and $\kappa = 2.5$. The mesh plots of the analytical solutions and SBM solutions are displayed in Figures 7 and 8. The solutions at different times at different depths are plotted. Good agreement indicates that the SBM is successfully applied to the half-space transient problem.

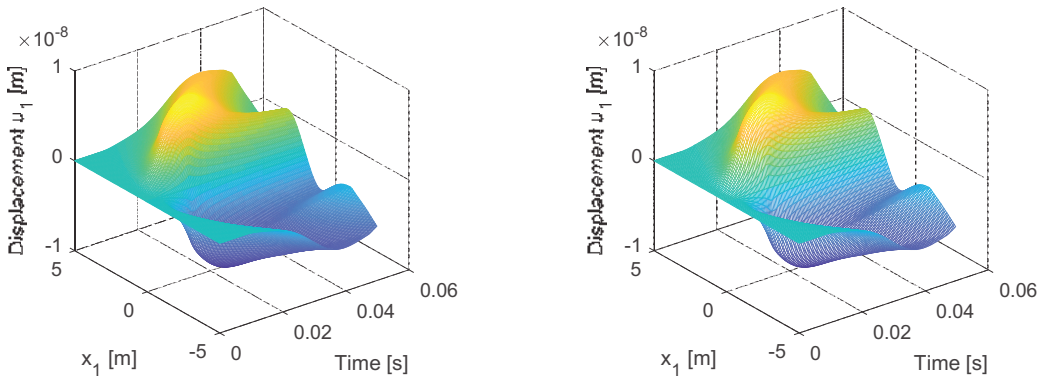


Figure 7. Time history of u_1 at $x_3 = -1$ generated by the analytical solution (left) and the SBM-EWM (right).

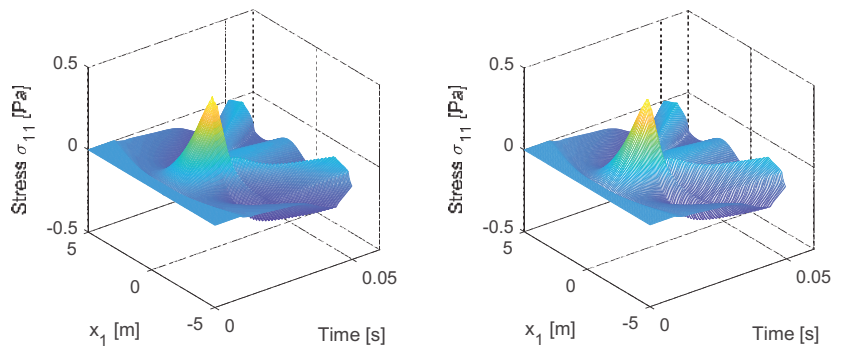


Figure 8. Time history of σ_{11} at $x_3 = -2$ generated by the analytical solution (left) and the SBM-EWM (right).

Furthermore, the MFS is introduced for comparison with the SBM in Figure 9. All the parameters for the MFS and SBM are the same as the above. The MFS avoids the origin singularity via the artificial boundary outside the computational domain. d is the distance between the artificial boundary and physical boundary. To obtain stable solutions, the MATLAB built-in function `pinv` is used to solve the linear system of the MFS. As shown in the figure, the MFS and SBM could obtain acceptable solutions. Nevertheless, the results of the MFS are influenced by the location of the artificial boundary. Only the MFS with $d = 0.1$ converges to the analytical solutions. Otherwise, because of the application of `pinv`, the MFS takes 357.34 s for the whole process, while the SBM takes 92.96 s. It can be observed that the MFS takes a much longer time than the SBM.

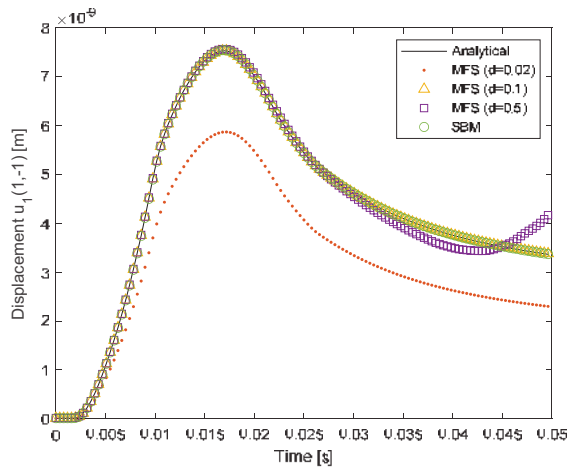


Figure 9. Numerical comparison between the MFS and SBM.

5.3. A Tunnel Embedded in a Saturated Poroelastic Half-Space

In this example, a model of a semi-circular tunnel embedded in a saturated poroelastic half-space in Figure 10 is considered. The radius of the tunnel is $R = 3$ m and the depth of invert of the tunnel is $H = 6$ m. A triangularly distributed transient load is imposed at the invert of the tunnel. The ground and the surface of the tunnel are set as permeable. Thus, the boundary conditions are expressed as

$$\begin{cases} t_3^s = ((|x| - 3)P(t))\text{N/m}^2, t_1^s = 0\text{N/m}^2, p = 0\text{Pa}, x_1 \in [-3, 3], x_3 = -6 \\ t_3^s = 0\text{N/m}^2, t_1^s = 0\text{N/m}^2, p = 0\text{Pa}, \text{ otherwise} \end{cases}$$

where

$$P(t) = \begin{cases} 100t & 0 \leq t \leq 0.01 \\ 1 & 0.01 < t \leq 0.03 \\ 4 - 100t & 0.03 < t \leq 0.04 \\ 0 & \text{otherwise} \end{cases}$$

In this case, no analytical solution is available. Thus, the accuracy of the SBM-EWM is presented with different parameters. The total time of tunnel transient response T is 90 ms, and the damping coefficient κ is 2.5. Figure 11 gives σ_{33}^s at $(-2, -7)$ and p at $(1, -7)$ calculated by the SBM-EWM with different numbers of sampling frequencies N_ω (128, 256) and numbers of boundary points N (471, 786). It is observed that the SBM-EWM with different parameters obtains identical results.